The Hashemite Kingdom of Jordan
Scientific Research Support Fund
The Hashemite University

JJEES

Jordan Journal of Earth and Environmental Sciences

Indexed by Scopus
ELSEVIER

Volume (17) Number (1)

JJEES is an International Peer-Reviewed Research Journal

ISSN 1995-6681 jjees.hu.edu.jo March 2026

Jordan Journal of Earth and Environmental Sciences (JJEES)

JJEES is an International Peer-Reviewed Research Journal, Issued by Deanship of Scientific Research, The Hashemite University, in corporation with, the Jordanian Scientific Research Support Fund, the Ministry of Higher Education and Scientific Research.

Editorial Board:

Associate Editorial Board: (Arranged Alphabetically)

International Advisory Board: (Arranged Alphabetically)

Editorial Board Support Team:

Submission address:

Manuscripts should be submitted electronically to the following e-mail:

jjees@hu.edu.jo

For more information and previous issues:

www.jjees.hu.edu.jo

Hashemite Kingdom of Jordan

Scientific Research Support Fund

Hashemite University

Jordan Journal of Earth and Environmental Sciences

JJEES

An International Peer-Reviewed Scientific Journal

Financed by the Scientific Research Support Fund

Volume 17 Number (1)

http:// jjees.hu.edu.jo/

ISSN 1995-6681

Flash Flood at Eastren Basaltic Platue - Jordan.
By Mariam Najajreh

JJEES
Jordan Journal of Earth and Environmental Sciences

JJEES

JJEES (2026) 17 (1): 1-6
ISSN 1995-6681

Jordan Journal of Earth and Environmental Sciences

Assessment of Heavy Metal Pollution in Agricultural Soils around Abandoned Kettara Mine in Marrakech, Morocco

Yassir Barkouch[1*], Flata Khadija[2], El Kherchi Ouassil[3], El Fadeli Sana[4], Pineau Alain[5]

[1] Faculty of Sciences and Techniques Gueliz - Marrakech, Cadi Ayyad University, Marrakech, Morocco.
[2] Regional Laboratory for Epidemiological Diagnosis and Environmental Hygiene, Boulevard des Hôpitaux, Gueliz-Marrakesh, Morocco.
[3] Laboratory of Sciences and Health Technologies, Epidemiology and Biomedical Unit, Higher Institute of Health Sciences, Hassan First University of Settat, PB 26000, Settat, Morocco.
[4] Higher Institute of Nursing Professions and Health Technology, ISPITS - Essaouira - Morocco.
[5] UFR de Sciences Pharmaceutiques et Biologiques, Centre de Dosage des Eléments Minéraux (CDEM), 9 rue Bias, BP 53508, 44035 Nantes, France.

Received on 6 March 2025; Accepted on 13 June 2025

Abstract

This study evaluates heavy metal contamination in agricultural soils surrounding the abandoned Kettara mine near Marrakech, Morocco. A total of 120 soil samples were collected in the impacted zone, along with 6 background samples located 20 km from the mine site. Soil's physicochemical parameters showed slightly acidic pH values (6.7 in KC1 and 6.9 in KC2), elevated electrical conductivity (1706.2 and 1830.4 µS/cm), and increased sulfur content (1.3% and 0.9%), all indicating a potential for enhanced metal mobility. Cadmium, copper, lead, and zinc concentrations reached 2.6, 427.8, 384.0, and 756.4 $mg \cdot kg^{-1}$ respectively in KC1 and remained substantially elevated in KC2 compared to background levels. Contamination factors and pollution index values, ranging from 5.2 to 32.5 for CF and from 55.1 to 48.9 for PI in KC1 and KC2, respectively, confirm significant anthropogenic pollution. The lack of mitigation measures for mine tailings has contributed to ongoing soil contamination, posing risks to surrounding rural communities with serious implications for environmental and agricultural sustainability. These findings emphasize the urgent need for effective environmental management and remediation strategies .to address the ecological and public health impacts of mining pollution

Keywords: *Contamination factors, heavy metals, Kettara mine, Marrakech, mining contamination, pollution index, soil pollution.*

1. Introduction

As a result of human and natural activities, the introduction of metallic pollutants into the environment has become a major concern due to their adverse effects globally (Sumanta et al., 2023; Briffa et al., 2020). The expanding industrialization and economic growth, coupled with the production and consumption of various compounds and chemicals, have led to the generation of dangerous pollutants that pose serious risks to the environment and human health (Ranjeet et al., 2023; Md Golam et al., 2023). Natural events, such as soil and rock weathering, earthquakes, and floods, also contribute to environmental pollution (Anthony and Rusyn, 2016; Espinoza-Quiñones et al., 2005). Additionally, the improper disposal of municipal, industrial, and agricultural waste further exacerbates environmental pollution caused by human activities (Al-Hanini et al., 2024).

Industrial processes, including mining and smelting operations, have been identified as significant sources of hazardous metals in the environment (Muhammad et al, 2024; Barkouch et al., 2024; Pruvot et al., 2006). Mining operations, encompassing mineral excavation, ore transportation, smelting and refining processes, and the disposal of tailings and waste water, are significant sources of heavy metal contamination in the vicinity of mines (Haghighizadeh et al., 2024; Hosseinpour et al., 2022). Mine residues, deposited on surrounding soils, are exposed to abiotic environmental factors, such as rain and wind, which mobilize the metallic content of the waste into the environment (Guillevic et al., 2023; Ping et al, 2019). This mobilization can lead to soil contamination with trace metals and the generation of acid mine drainage, disrupting the stability and renewal of natural ecosystem resources. Consequently, contamination from mine tailings can impact not only the immediate mining sites but also extend to larger areas, including surface waters and agricultural soils (Ifeanyi and Yusuf, 2023).

Several studies have examined the impact of mining on environmental pollution in Morocco, particularly in regions near abandoned mining sites. For instance, a study identified significant contamination of soils and crops with metals such as lead, cadmium, and zinc in areas surrounding mining operations (Valiente et al., 2012). Its findings support the need for continued monitoring and management of mining activities in these regions. Similar studies have reported high concentrations of heavy metals in soils near mining districts in Morocco, reinforcing the potential risks posed by such activities to both the environment and human health (El Haya et al., 2023; Barkouch and Pineau, 2016).

The environmental consequences of excessive heavy-metal dispersion from mine and smelter sites include water and soil contamination, phytotoxicity, soil erosion, and potential risks to human health. These pollution consequences arise

* Corresponding author e-mail: yassirbark@yahoo.fr

when mobilized and bioavailable trace metals are absorbed by plants or transported to groundwater aquifers (Kafle et al., 2022).

Abandoned and active mines are often linked to elevated concentrations of heavy metals in surrounding areas due to the discharge and dispersion of untreated waste materials into nearby agricultural soils, food crops, riverine waters, and stream sediments (Bany Yaseen and Al-Hawari, 2019; González-Martíne et al., 2019; Liu et al., 2005; Lu and Zhang, 2005). This widespread soil contamination with heavy metals from mines has raised significant environmental concerns (Kachenko and Singh, 2006). In this context, high soil metal contamination and severe accumulation of trace elements in crops have been reported in both operational and abandoned mining districts in the Marrakech region of Morocco (El Haya et al., 2023; Barkouch and Pineau, 2016). Similarly, certain crops, cultivated near mining sites in this region, have been found to contain lead and cadmium at concentrations exceeding permissible limits. This contamination impacts the food chain, leading to health problems in both humans and animals (El Haya et al., 2023; Mashal et al., 2017; Barkouch and Pineau, 2016).

Given the urgency of the situation, it is essential to assess the distribution of heavy metals in surface soils, which serve as crucial sinks for pollutants, to understand the overall status of heavy metal pollution and its associated ecological risks in the region. The results of such assessments are vital for effective environmental management in areas undergoing rapid industrial transformation.

The objective of this study is to evaluate the impact of mining activities on heavy metal concetrations in agricultural soils in the vicinity of the Kettara mine in Marrakech,Morocco and to compare the findings with those from a control site. By shedding light on the potential impacts of pollutants, this study aims to raise awareness and provide valuable insights for the efficient management of surface soil quality in the mining area.

2. Materials and Methods

2.1. Site description

The abandoned Kettara mine is situated approximately 30 km northwest of Marrakech, within the heart of the central Jebilet Mountains in Southern Morocco (Figure 1) (Hakkou et al., 2008).

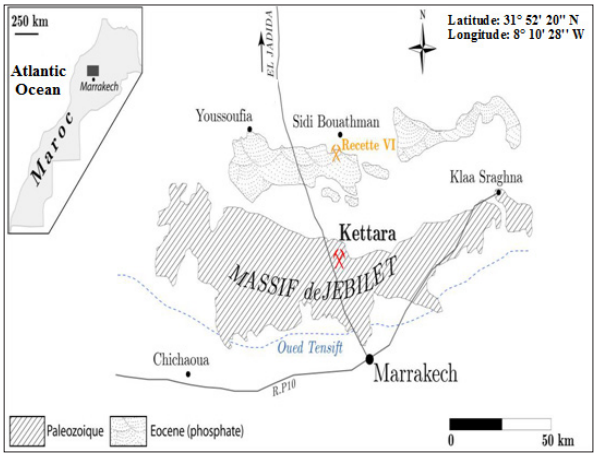

Figure 1. Geographic situation of the Kettara mine in the Marrakech region.

Active mining operations at the Kettara mine occurred between 1964 and 1981, primarily extracting pyrrhotite, with a total production exceeding 5.2 million tons. The mine was closed in 1982 (Hakkou et al., 2008).

During its operation, more than 3 million tons of mine waste accumulated over an area of 16 hectares, without due consideration for environmental implications (Figure 2). The ore extracted from the Kettara mine contained various minerals, including pyrrhotite, sphalerite, galena, chalcopyrite, pyrite, arsenopyrite, and glaucodot. The main elements targeted for extraction were Cu, Fe, and S. Regrettably, the large quantities of waste materials, including tailings, were left untreated. Consequently, these materials were dispersed downslope by surface erosion and wind action, as well as through effluent drainage into lower-lying land used for the cultivation of paddy rice and household garden crops.

Notably, the abandoned Kettara mine is near two rural communities, known as Kettara Rural Center 1 and 2 (Figure 2), which together encompass approximately 7000 hectares, of which 72% is devoted to farmland. The region experiences a Mediterranean climate, bordering on arid and semi-arid conditions, with an average annual precipitation of 227 mm over a 10-year period. The temperatures exhibit significant daily and seasonal variations, with an average of 10.3°C in January and 37.2°C in July.

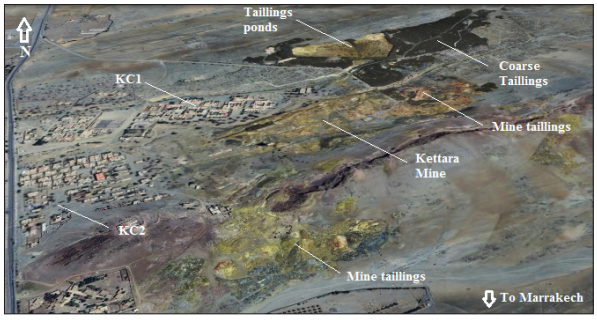

Figure 2. Geographic situation of Kettara rural communities KC1 and KC_2, and tailings ponds covering a large area in the Kettara region.

2.2. Sampling Description

To evaluate the spatial distribution of heavy metal contamination, 120 soil samples were systematically collected from agricultural lands within a 30-hectare area surroundingthe Kettara mine. Sampling points were spaced at regular 50-meter intervals, along a grid pattern to ensure homogeneous spatial coverage. At each point, soil was sampled from the 0–20 cm depth layer, after discarding the top 2 cm to eliminate surface contamination.

Each sample was collected with a clean garden shovel over a 100 cm² surface area and stored in pre-acid-washed polyethylene containers. Additionally, 6 background soil samples were collected 20 km upwind of the mining area, in an unaffected zone with similar soil characteristics, to serve as controls.

2.3. Soil samples analysis

The soil samples were collected from various sampling sites, including Kettara Rural Center 1 (KC_1), Kettara Rural Center 2 (KC_2), and Kettara mine tailings (KT). Each sample was collected at a depth of 0 to 0.2 meters, using a garden

shovel that had been thoroughly cleaned with concentrated nitric acid to eliminate any potential heavy-metal contaminants (Jung, 2001). Over 12 months, five samples were collected from each sampling site.

Soil samples were prepared for particle size distribution analysis by drying at 60°C for 75 hours, crushing, sieving (< 325 µm), homogenizing, and weighing. The hydrometer method was used to measure the soil particle size distribution.

To ensure accurate analysis, the soil samples were placed in pre-cleaned plastic containers that had been treated with concentrated nitric acid to prevent any trace of heavy metal contamination. Subsequently, the samples were dried and passed through a 2-mm sieve.

The pH of each sample was measured in a soil-water suspension (1:2.5, w/w), and electrical conductivity was measured in a 1:5 soil-to-water suspension utilizing an HI 9828 multiparameter portable instrument from HANNA Instruments (Badmus et al., 2014). The organic matter content was determined using the Walkley and Black procedure (Walkley and Black, 1934; Nelson and Sommers, 1982).

10 g of sieved sample was placed in a 500 ml wide-mouthed Erlenmeyer flask. To this, 10 ml of 1 N $K_2Cr_2O_7$ was added, and the flask was swirled gently to disperse the soil in the solution. 20 ml of Concentrated H_2SO_4 was then added slowly, followed by vigorous shaking for 1 min. Distilled water (200ml) was added to the flask, and the suspension was filtered. A few drops of ophenanthroline indicator were then added to the filtered solution and titrated against 0.5 N $FeSO_4$ H_2O. The sample without tailings was kept as a blank. The amount of organic carbon in the soil sample was calculated by using the following formula:

$$Organic\ content\ (\%) = \frac{(\text{milliequivalents of K2Cr2O7} - \text{milliequivalents of FeSO4}) \times 0.003 \times 100}{Masse\ of\ \text{taillings sample}}$$

% Organic Matter = % Organic Carbon 1.724.

Before analysis, the tailings samples were homogenized. Subsequently, these homogenized samples were stored in hermetically sealed polyethylene bags at 4°C until the commencement of the analysis (Barkouch et al., 2016; Wufem et al., 2013).

Aliquots of approximately 1 gram from each sample were digested with 5 mL of 65% HNO3 using a microwave digestion system to determine the HNO3-soluble fraction of heavy metals. The concentrations of Cd, Cu, Pb, and Zn were measured by a graphite furnace atomic absorption.

These comprehensive analytical procedures were conducted to obtain precise and reliable data on soil properties and heavy-metal concentrations, facilitating a thorough evaluation of the environmental impact of the Kettara mine and its surrounding areas.

3. Results and discussion

The textural characteristics of the soils under investigation are presented in Table 1, following the classification method by Shepard. The results revealed that coarse sand (2.0-1.0 mm) and fine sand (0.250-0.125 mm) were the dominant fractions in all agricultural soil samples, with a range from 25.6 to 21.2% and 26.0 to 23.0% in Kettara Center 1 (KC_1) and 2 (KC_2) soils, respectively.

Table 1. Average percentages grain-size (%) of different soils in Kettara region.

	KC_1	KC_2	MTK	Background soil
Clay	15.0 ± 3.1	18.6 ± 4.3	29.0 ± 3.0	15.5 ± 2.6
Fine silt	16.9 ± 2.8	20.0 ± 1.9	13.4 ± 2.6	19.5 ± 3.6
Coarse silt	11.0 ± 1.3	12.6 ± 2.0	13.7 ± 1.4	11.0 ± 1.2
Fine sand	26.0 ± 3.3	23.0 ± 3.5	19.8 ± 3.2	25.1 ± 0.6
Coarse sand	25.6 ± 3.4	21.2 ± 3.7	24.0 ± 2.9	25.0 ± 0.4

The geochemical soil characteristics, including pH, electrical conductivity (EC), and carbonate ($CaCO_3$) content, play a crucial role in understanding the soil's capacity to retain heavy metal pollutants (Barakat et al, 2022). Detailed numerical values for pH, EC, OM, OCC, $CaCO_3$, Cl^- and S^- for each sample are presented in Table 2.

The results of the soil pH measurements indicated that, overall, all sampled points exhibited slightly acidic to neutral pH levels, ranging from 6.7 to 6.9, which were lower than the background soil (7.7), except for the tailing sample, which displayed a very acidic pH of 5.2.

The observed variations in soil pH appeared to be influenced by the heterogeneous deposition of sulfuric residues from mine tailings in the vicinity of the studied mine. The oxidation of these residues and the subsequent formation of sulfuric acid (approximately 0.9 to 1.3% of S^-) from these residues seemed to contribute to the decrease in pH, particularly in the tailing sample.

These findings suggest that mine tailings and associated sulfidic residues can affect soil pH, potentially influencing the soil's ability to retain heavy-metal pollutants. Such insights are critical for understanding the environmental implications of the Kettara mine and its surrounding areas and can aid in devising appropriate remediation strategies to address the potential risks posed by heavy metal contamination in the soil.

Table 2. Geochemical characteristics of different Kettara region soils

Parameters	KC_1	KC_2	MTK	Background soil
PH	6.7 ± 0.4	6.9 ± 0.4	5.1 ± 0.3	7.7 ± 0.3
E.C (µS/cm)	1706.2 ± 37.5	1830.4 ± 52.6	7569.7 ± 159.4	960.5 ± 81.9
OM (%)	4.6 ± 0.9	5.4 ± 0.8	3.3 ± 1.6	4.2 ± 0.9
OCC (%)	2.6 ± 0.5	3.3 ± 0.5	2.5 ± 0.9	2.9 ± 0.5
$CaCO_3$ (mg/g)	160.1 ± 29.2	120.9 ± 26.4	159.2 ± 19.4	129.8 ± 18.5
S %	1.3	0.9	4.1	0.3

The electrical conductivity (EC) exhibited greater variability than pH, with EC values ranging from 1706.2 to 1830.4 µS/cm. These values are significantly higher than those observed in background samples, indicating an increasing salinity gradient and high concentrations of labile ions near the mine area. The mine tailings area showed an exceptionally high EC value of 7569.7 µS/cm, primarily attributed to the elevated metal content in this region.

Particle size was found to be a significant factor influencing metal accumulation. Fine-grained soils showed higher nutrient concentrations due to their larger surface-to-volume ratio and enrichment in organic matter (OM) (Koiter et al., 2017).

The average organic matter content in the studied soils ranged from 4.6% in KC_1 to 5.4% dw in KC_2. This can be attributed to anthropogenic contributions, such as the discharge of domestic sewage in the Kettara region, which was an important source of organic matter in the mining zone. Additionally, agricultural activities in the vicinity of the mine contributed to the high organic content.

The organic carbon content (OCC) ranged from 2.6% dw in KC_1 to 3.3% dw in KC_2. OCC increased in KC_2 soils, corresponding to a decrease in soil grain size. The highest OCC was observed in soils with the lowest sand content and the highest silt and clay contents (Table 1).

Table 3 presents the estimated total concentrations (mg/kg) of heavy metals, namely Cd, Cu, Pb, and Zn, in the soils. The concentrations of these heavy metals were higher in KC_1 soils than in KC_2 soils. Local geology and anthropogenic influences were found to strongly determine the heavy metal concentrations in these soils.

Table 3. Mean concentrations of heavy metals in different Kettara region soils.

Metals	KC_1	KC_2	MTK	Background soil
Cd (mg/kg)	2.6 ± 0.7	2.2 ± 0.2	157.2 ± 8.8	0.4 ± 0.1
Cu (mg/kg)	427.8 ± 25.3	330.5 ± 22.8	969.1 ± 38.7	40.7 ± 0.7
Pb (mg/kg)	384.0 ± 27.1	355.3 ± 24.0	2640.7 ± 42.7	11.8 ± 1.4
Zn (mg/kg)	756,4 ± 74,3	690,5 ± 51,0	2846,8 ± 84,6	133,9 ± 2,0

Mineral weathering is a significant natural source of contamination, alongside various anthropogenic activities such as the use of fertilizers, herbicides, irrigation, and industrial effluents. In this agricultural region, the Kettara, abandoned mine tailings, are a prominent and likely major source of contamination.

Cu is widely distributed in aquatic ecosystems because it is a naturally occurring element. However, Cu and Zn concentrations are greatly influenced by anthropogenic sources.

Total Cu showed higher concentrations in CK_1 with 427.8 ± 25.3 mg/kg. Total Zn also showed similar trends with the highest level at the same soils with 756,4 ± 74,3 mg/kg. The results showed an increase in zinc in the soil due to domestic and industrial wastewater and agricultural runoff.

The results also showed significant spatial variations. Compared with the background soil, the concentrations of other heavy metals, in the studied soils showed a significant increase. The highest levels were observed in CK_1.

The calculated contamination factors (CF) (Table 4) indicate the extent of this increase in metallic contamination. The pollution index (PI) is the arithmetic mean of the CFs of the analyzed metals (Moghadam et al, 2024; Ferreira et al., 2022; Li et al., 2022; Boroujerdnia et al., 2020), and it allows an assessment of the degree of polymetallic pollution of the analyzed soil samples. A value greater than 1 indicates that the analyzed sample had a metallic contamination caused by human activities.

Table 4. Contamination factors (CFs) and pollution index (PI) of different Kettara region soils.

		Soil samples		
Contamination factors	Eléments	KC_1	KC_2	MTK
	Cd	6.5	5.5	393
	Cu	10.5	8.1	23.8
	Pb	32.5	30.1	223.8
	Zn	5.6	5.2	21.3
Pollution Index		**55.1**	**48.9**	**661.9**

The pollution index (Table 4) shows that the soils of CK_1 and CK_2 exhibit high levels of metal contamination, as their IP values significantly exceed the legal pollution limit of 1. Moreover, the respective IP values for CK_1 (55.1) and CK_2 (48.9) further indicate that these areas are highly polluted (Table 4).

Statistical comparisons between the two rural communities (KC1 and KC2) and the background soil show that differences in heavy metal concentrations are highly significant ($p < 0.05$), indicating a strong anthropogenic influence linked to historical mining activities. For example, cadmium levels in KC1 (2.6 mg/kg) and KC2 (2.2 mg/kg) are significantly elevated compared to the control soil (0.4 mg/kg), with similar trends observed for Cu (427.8 and 330.5 vs. 40.7 mg/kg), Pb (384.0 and 355.3 vs. 11.8 mg/kg), and Zn (756.4 and 690.5 vs. 133.9 mg/kg). These differences are further supported by contamination factors and pollution

indices, which confirm a high degree of soil enrichment in both villages. In addition, physicochemical parameters such as pH and electrical conductivity also show statistically significant deviations from the background soil. The pH in KC1 (6.7) and KC2 (6.9) is significantly lower than that of the control site (7.7), indicating increased acidity likely driven by sulfuric residues. Electrical conductivity values in KC1 (1706.2 µS/cm) and KC2 (1830.4 µS/cm) are approximately twice those of the control soil (960.5 µS/cm), indicating higher salinity and potential metal mobility. These statistically supported differences strengthen the interpretation that the elevated contamination in agricultural soils is not incidental but a direct consequence of proximity to the abandoned mine site.

Although no effective mitigation measures are currently at the Kettara site, several strategies could be considered to address heavy-metal contamination in soils. Potential remediation approaches include phytoremediation with tolerant plant species (Mahendra, 2024), soil washing techniques (Lianwen et al., 2018), and the use of stabilizing amendments such as lime or biochar to immobilize metals and improve soil pH (Lina et al., 2021). Additionally, policy interventions may include enforcing land-use regulations in contaminated areas, establishing long-term environmental monitoring programs, and developing rehabilitation plans for abandoned mining zones through coordinated efforts among governmental agencies, researchers, and local stakeholders. These general recommendations offer a framework for reducing environmental and health risks in affected regions.

4. Conclusion

The study demonstrated that soils in the Kettara rural communities exhibit altered physicochemical properties, with pH values ranging from 6.7 in KC1 to 6.9 in KC2, compared with 7.7 in the control soil. Electrical conductivity reached 1706.2 $\mu S \cdot cm^{-1}$ in KC1 and 1830.4 $\mu S \cdot cm^{-1}$ in KC2, notably higher than the control value of 960.5 $\mu S \cdot cm^{-1}$. Sulfur contents were also elevated (1.3% in KC1 and 0.9% in KC2), reflecting the influence of mine tailings on soil acidification and metal mobility. Heavy-metal concentrations in KC1 reached 2.6 $mg \cdot kg^{-1}$ for Cd, 427.8 $mg \cdot kg^{-1}$ for Cu, 384.0 $mg \cdot kg^{-1}$ for Pb, and 756.4 $mg \cdot kg^{-1}$ for Zn, while in KC2 the respective values were 2.2, 330.5, 355.3, and 690.5 $mg \cdot kg^{-1}$—substantially exceeding those in the background soil (0.4, 40.7, 11.8, and 133.9 $mg \cdot kg^{-1}$). Contamination factors in KC1 ranged from 5.6 (Zn) to 32.5 (Pb), and in KC2 from 5.2 to 30.1, while pollution index values reached 55.1 and 48.9, respectively, confirming a high level of polymetallic contamination. These results clearly indicate that mining residues have significantly contributed to the degradation of agricultural soils in both communities, emphasizing the urgent need for targeted remediation and risk mitigation strategies.

Acknowledgments

The present research did not receive any financial support.

Conflict of Interest

The authors declare that there are no conflicts of interest regarding the publication of this paper.

References

Al-Hanini, M., Makhamreh, Z., Al Bakain, R. (2024). Chemometric Evaluation of Residual Soil Contents: Application to Heavy Metals at Public Parks in Amman Jordan. Jordan Journal of Earth and Environmental Sciences, 15 (2): 115–122.

Anthony, H.K., Rusyn, I. (2016). Environmental Exposures due to Natural Disasters. Review in Environmental Health, 31(1): 89–92.

Badmus, B.S., Ozebo, V.C., Idowu, O.A., Ganiyu, S.A., Olurin, O.T. (2014). Physico-chemical Properties of Soil Samples and Dumpsite Environmental Impact on Groundwater Quality in Southwestern Nigeria. African Review in Physics, 9:103-114.

Bany Yaseen, I., Al-Hawari, Z. (2019). Assessment of Metal Pollution of the Surface Sediments along the Wadi Al Rayyan Area, Jordan. Jordan Journal of Earth and Environmental Sciences, 10(2): 75-84.

Barakat, A., Khellouk, R., Ennaji, W., Mosaid, H. (2022). Investigation of Heavy Metal Contamination and Ecological and Health Risks in Farmland Soils From Southeastern Phosphate Plateaus of Khouribga (Morocco). Ecological Questions, 33(4): 61-75.

Barkouch, Y., El Fadeli, S. (2024). Acid-Base Accounting Test as a Tool for Prediction of Mine Drainage Acid Risk at a Still Functional Mine Site: Case of Draasfar Mine in Marrakech (Morocco). Pollution, 10 (3): 929-940.

Barkouch, Y., Pineau, A. (2016). Evaluation of the Impact of Mine Activity on Surrounding Soils of Draa Lasfar Mine in Marrakech-Morocco. African Journal of Environmental Sciences and Technology, 10(1): 44-49.

Boroujerdnia, A., Mohammadi Roozbahani, M., Nazarpour, A., Ghanavati, N., Payandeh, K. (2020). Heavy Metal Pollution in Surface Soils of Ahvaz, Iran, Using Pollution Indicators and Health Risk Assessment. Archives of Hygiene Sciences, 9(4): 299–310.

Briffa, J., Sinagra, E., Blundell, R. (2020). Heavy Metal Pollution in the Environment and their Toxicological Effects on Humans. Heliyon, 6(9): e04691.

El Haya, N., Ait Melloul, A., Flata, K., El-Fadeli, S., Pineau, A., Barkouch, Y. (2023). Impact of Mining Activity on Soils and Plants in the Vicinity of a Zn-Pb Mine (Draa Lasfar, Marrakech - Morocco). Pollution, 9 (2): 615-627.

Espinoza-Quiñones, F.R., Zacarkim, C.E., Palacio, S.M. (2005). Removal of Heavy Metal from Polluted River Water Using Aquatic Macrophytes Salvinia Sp. Brazilien Journal of Physics, 35(3): 744–746.

Ferreira, S., Da Silva, J., Dos Santos, I., De Oliveira, O., Cerda, V., Queiroz, A. (2022). Use of Pollution Indices and Ecological Risk in the Assessment of Contamination from Chemical Elements in Soils and Sediments – Practical Aspects. Trends in Environmental Analytical Chemistry, 35: e00169.

González-Martínez, M., Huguet, C., Pearse, J., McIntyre, N., Camacho, L. (2019). Assessment of Potential Contamination of Paramo Soil and Downstream Water Supplies in a Coal-Mining Region of Colombia. Applied Geochemistry, 108: 104382.

Guillevic, F., Rossi, M., Develle, A., Spadini, L., Martins, J., Arnaud, F., Poulenard, J. (2023). Pb Dispersion Pathways in Mountain Soils Contaminated by Ancient Mining and Smelting Activities. Applied Geochemistry, 150: 105556.

Haghighizadeh, A., Rajabi, O., Nezarat, A., Hajyani, Z., Haghmohammadi, M., Hedayatikhah, S., Delnabi, S., Aghababai, A. (2024). Comprehensive Analysis of Heavy Metal Soil Contamination in Mining Environments: Impacts, Monitoring Techniques, and Remediation Strategies. Arab Journal Chemistry, 17(6): 105777.

Hakkou, R., Benzaazoua, M., Bussiere, B. (2008). Acid Mine Drainage At The Abandoned Kettara Mine (Morocco): 1. Environmental Characterization. Mine Water and the Environment, 27: 145-159.

Hosseinpour, M., Morteza, O., Azimi, Y. (2022).

Evaluation of Positive and Negative Impacts of Mining on Sustainable Development by a Semi-Quantitative Method. Journal of Cleaner Production, 336: 132955.

Ifeanyi, M., Yusuf, M. (2023). Bioremediation of Acid Mine Drainage – Review. Alexandria Engineering Journal, 65: 1047-1075.

Jung M.C. (2001). Heavy Metal Contamination of Soil and Water in and around the Imcheon Au-Ag Mine, Korea. Applied Geochemistry, 16:1369–1375.

Kachenko, A.G., Singh, B. (2006). Heavy Metals Contamination in Vegetables Grown in Urban and Metal Smelter Contaminated Sites in Australia. Water, Air and Soil Pollution, 169: 101–123.

Kafle, A., Timilsina, A., Gautam, A., Adhikari, K., Bhattarai, A., Aryal, N. (2002). Phytoremediation: Mechanisms, Plant Selection and Enhancement by Natural and Synthetic Agents. Environmental Advanced, 8: 100203.

Koiter, A., Owens, P., Petticrew, E., Lobb, D. (2017). The Role of Soil Surface Properties on the Particle Size and Carbon Selectivity of Interrill Erosion in Agricultural Landscapes. CATENA, 153: 194-206.

Li, W., Qian, H., Xu, P., Zhang, Q., Chen, J., Hou, K., Ren, W., Qu, W., Chen, Y. (2022). Distribution Characteristics, Source Identification and Risk Assessment of Heavy Metals in Surface Sediments of the Yellow River, China. CATENA, 216: 106376.

Lianwen, L., Wei, L., Weiping, S., Mingxin, G. (2018). Remediation Techniques for Heavy Metal-Contaminated Soils: Principles and Applicability. Science of the Total Environment, 633: 206-219.

Liu, H., Probst, A., Liao, B. (2005). Metal Contamination of Soils and Crops Affected by the Chenzhou Lead/Zinc Mine Spill (Hunan, China). Science of Total Environment, 339:153–166.

Lina, G., Rumi, N., Rahul, C., Bikram, B., Nirmali, G., Rupam, K. (2021). Remediation of Heavy Metal Contaminated Soil: Role of Biochar. Advances in Chemical Pollution, Environmental Management and Protection, 7: 39-63.

Lu, A., Zhang, X. (2005). Environmental Geochemistry Study of Arsenic in Western Hunan Mining Area P.R. China. Environmental Geochemistry and Health, 27:313–320.

Mahendra, A. (2024). Phytoremediation Strategies for Mitigating Environmental Toxicants. Heliyon, 10(19): e38683.

Mashal, K., Salahat, M., Al-Qinna, M., Ali, Y. (2017). Assessment of Heavy Metals in Urban Areas of Al Hashmiyya City of Jordan. Jordan Journal of Earth and Environmental Sciences 8(2): 61-67.

Md Golam, K., Nahid, I.M., Rafat, S., Huy, Q.N., Monjur, M. (2023). Plastic Waste: Challenges and Opportunities to Mitigate Pollution and Effective Management. International Journal of Environmental Research, 17: 1-37.

Moghadam, S., Payandeh, K., Koushafar, A., Goosheh, M., Rouzbahani, M. (2024). Level of Heavy Metals and Environmental Pollution Index in Ahvaz, Southwest Iran. Scientific Reports, 14: 14754.

Muhammad, A., Baohua, X., Muhammad, U., Peiwen, X., Peng, Z., Haiyan, W., Shaheen, B. (2024). Heavy Metals Pollution from Smelting Activities: A Threat to Soil and Groundwater. Ecotoxicology and Environment Safety, 274: 116189.

Nelson, D.W., Sommers, L.E. (1982). Total Carbon, Organic Carbon and Organic Matter. In Page, L. (Ed.), Methods of Soil Analysis. Part 2. Agronomy 9. American Society of Agronomy, Madison, WI. 279-539 pp. 1982.

Ping, W., Zehang, S., Yuanan, H., Hefa, C. (2019). Leaching of Heavy Metals from Abandoned Mine Tailings Brought by Precipitation and the Associated Environmental Impact. Science of the Total Environment, 695: 133893.

Pruvot, C., Douay, F., Herve, F., Waterlot, C. (2006). Heavy Metals in Soil, Crops and Grass as a Source of Human Exposure in The Former Mining Areas. Journal of Soils and Sediments, 6: 215–220.

Ranjeet, K.M., Spandana, S.M., Yash, M., Naveen, D. (2023). Emerging Pollutants of Severe Environmental Concern in Water and Wastewater: A Comprehensive Review on Current Developments and Future Research. Water-Energy Nexus, 6: 74-95.

Sumanta, D., Kaniz, W.S., Ashwell, R.N., Moupriya, M., Indrani, C. (2023). Heavy Metal Pollution in the Environment and its Impact on Health: Exploring Green Technology for Remediation. Environ Health Insights, 17: 1–10.

Valiente, M., Perez, G., Avila, M., Ouazzani, N., Esshaimi, M. & Mandi, L. (2012). Heavy Metal Contamination of Soils and Water Resources Kettara Abandoned Mine. American Journal of Environmental Sciences, 8(3): 253-261.

Walkley, A.J., Black, I.A. (1934). Estimation of Soil Organic Carbon by the Chromic Acid Titration Method. Soil Science, 37, 29-38.

Wufem, M.B., Ibrahim, A.Q., Maina, M.H., Nangbes, J., Gungsat, J.B. (2013). Speciation of Some Heavy Metals in Soils around a Cement Factory in Gombe State, Nigeria. International Journal of Engineering Sciences, 2(9):110-115.

JJEES

JJEES (2026) 17 (1): 7-15
ISSN 1995-6681

Jordan Journal of Earth and Environmental Sciences

Dakhla Sand Dunes in Southern Morocco: Using Grain Size Analysis to Understand Wind Dynamics

Smail Harchane*, Nassareddine Azzouzi, Fatima El Hammichi, Hassan Tabyaoui, Abderrahim Lahrach, Naoual El Hammouch.

Geo-resources and Environment laboratory, Sidi Mohammed Ben Abdellah University, Fez, Morocco

Received on 12 January 2025; Accepted on 13 June 2025

Abstract

Morocco is affected by desertification in its southern and southeastern territories. A visible manifestation of desertification in southern Morocco is the movement of dune sands shaped by wind dynamics. This paper investigates the characteristics and distribution of sand in the study area using granulometric analysis to determine physical properties and textural parameters such as mean grain size, sorting, skewness, and kurtosis. To better understand the dynamics of sandy deposit emplacement in the Dakhla region, a dynamic and sedimentological study was conducted. This study constituted the second phase of the research and involved laboratory analyses, particularly granulometric measurements, to determine grain-size distributions.

Sand samples were collected from various locations across the region extending from the bay through the Dakhla area to the Awserd region. Aeolian dynamics responsible for the formation of Dakhla dunes produced sand stocks composed of one or more grain-size fractions, with modes at 113–143 µm, 225–283 µm, and 358–450 µm. Most of the analyzed samples exhibited bimodal distributions, with clearly distinguishable modes corresponding to mixtures of two homogeneous particle-size populations.

Three distinct particle-size distributions characterize these sand deposits. The first is a minor unimodal distribution of well-sorted medium grains, reflecting an aeolian evolution toward unimodal "old barchan sands" through mobilization, deposition, and stabilization under a moderate-energy wind regime with minimal fluctuations. The second is a dominant bimodal distribution, comprising a well-sorted fine-grained mode mobilized and deposited by low-energy winds with minimal fluctuations, and a well-sorted mode with negative skewness characterized by a developed tail of fine to medium grains mobilized and deposited by medium-energy winds with significant fluctuations. This group includes "slick sands," "deflated sands," and "ridge sands." The third type, which is occasionally observed, is polymodal and very poorly sorted. It is dominated by medium-sized grains accumulated under highly variable wind dynamics or in settings sheltered from remobilization and corresponds to basement sands.

The findings of this paper contribute to ongoing research on wind dynamics in southern Morocco by offering insight into the processes associated with desertification, ranging from bedrock weathering to erosion, transport, and sand deposition.

Keywords: Desertification, Dune Sands, Wind Dynamics, southern Morocco, granulometric analysis.

1. Introduction

Aeolian processes generate extensive sand sheets and dune fields in arid regions. These sandy deposits require close monitoring, as they may advance more rapidly than desertification, land encroachment, or even the degradation of industrial infrastructure (Gomez et al., 2018; Sur & Chau, 2019). Understanding these deposits is crucial, not only for managing environmental and infrastructural impacts but also for gaining insight into sedimentary processes. As primary aeolian landforms, dunes preserve a record of wind-driven transport and sediment sorting within their source areas. The granulometric and geochemical characteristics of these sediments are essential in aeolian research, providing valuable information on sedimentary processes and provenance (Garzanti et al., 2015; Kalinska-Nartisa et al., 2017; Muhs, 2017; Kasper-Zubillaga et al., 2022). In particular, grain size serves as a key indicator of sediment transport dynamics and offers insights into the origin and composition of sand grains.

Sand grains are fine particles resulting from the fragmentation of rocks or minerals, and they bear witness to the origin and nature of the parent rock from which they originate. They are found in various environments throughout the Earth's crust (Dahnoun and Djadouni, 2020). Grain size analysis is commonly used because it plays a fundamental role in dune ecosystem dynamics, influencing wind transport efficiency and sediment stability. It is also used to assess the shear stress required to initiate and maintain particle movement.

The statistical distribution of granulometric characteristics, such as mean size and asymmetry, also provides a good indicator of how wind dynamics control sand movement patterns. These characteristics are also commonly

* Corresponding author e-mail: smailharchane@gmail.com

used to infer the aeolian sedimentary environment, given the wide size range. The mixing and sorting of sediment populations vary systematically in response to sedimentary processes, their dynamics , sediment quality, and sediment provenance (Visher, 1969).

Granulometric analysis is a fundamental and widely used method for determining the sedimentary environment, dynamics, depositional mechanisms, and the development of aeolian landforms, as well as the transport and sorting of aeolian particles (Sahu, 1964; Visher, 1969; Wang et al., 2003; Guan et al., 2025). In this paper, we attempted to address some of the above problems by systematically collecting surface sediment samples from the entire Dakhla-Awserd region.

2. Geographical and Climatic Context

The study area liesbetween Dakhla and Awserd in the Saharan provinces of southern Morocco(Figure 1). It is crossed by a north-west-south-east road linking the two towns and is divided into two geographically distinct zones. The first, located in the coastal region of Dakhla, encompasses the bay and peninsula of Dakhla and is characterized by a desert climate tempered by the ocean, which reduces annual temperature variations, allowing mean annual temperatures to range from17°C to 26°C (Sanchez & Martin, 2019).

Coastal areas, softened by oceanic influence, enjoy a generally more moderate climate, while continental regions are subject to harsher climatic conditions. This climatic divergence leads to adaptive responses specific to each environment, both ecological and socio-economical. In the first zone, winds actively shape the relief, constantly reshaping it, and promoting the formation of vast dune fields in perpetual motion (Barcellos et al., 2022). Plant cover is very sparse, dominated by xerophytic and halophytic species, and adapted to saline soils and high evapotranspiration, typical of desert environments (Barbero et al., 1994).

The second zone, the Continental and Saharan region, corresponds to Awserd, located inland and characterized by an extreme desert climate classified as BWh (hot desert climate in the Köppen system). Deprived of the ocean's moderating influence, summer temperatures frequently exceed 45 °C during the day, with high diurnal temperature ranges and annual precipitation below 50 mm (Benattia & Hassan, 2020). Although atmospheric humidity can occasionally enhance water retention, it does not offset the chronic rainfall deficit necessary to support plant life. These harsh conditions, compounded by hot, dry winds, intensify aridity, severely limiting vegetation and making living conditions challenging for local populations (Laurent & Benhammou, 2021).

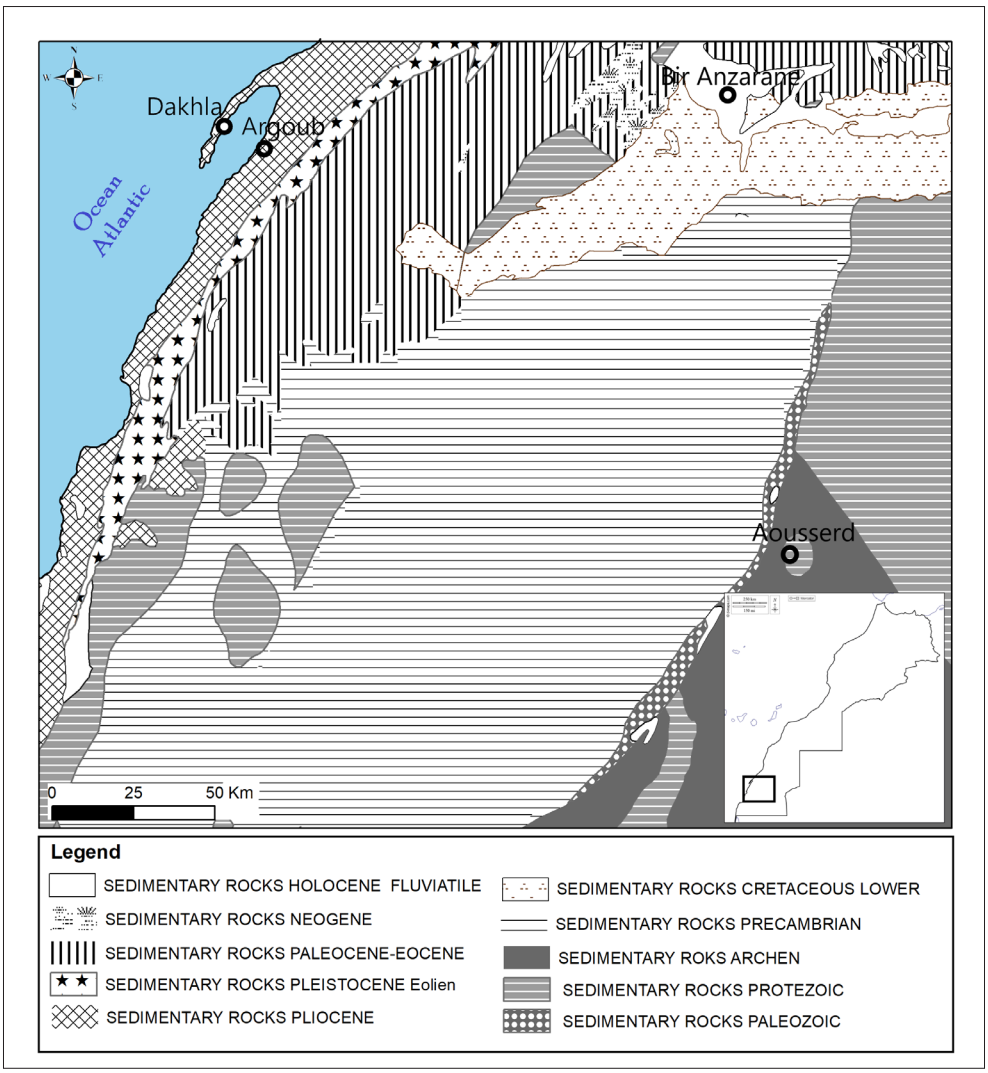

Figure 1. (a) map of Africa locating the Dakhla Peninsula in the westernmost part of the Sahara (Morocco) ; (b) location of surveyed areas in a red square

3. Geological Context

The Dakhla-Awserd region (Figure 2) is organized into four major stratigraphic units. Among these, the Archean formations of the Réguibat ridge are composed mainly of granite, migmatite, and gneiss, with notable concentrations of quartz, feldspar, and mica (Villeneuve, 2008). Wind erosion, active over the long term, has shaped these landscapes by incising the plateaus with ravines and depressions. This process has producedbuttes and cuestas with angular edges, the result of differential erosion: the harder rock layers resist abrasion, while the softer ones disintegrate more rapidly (Fabre, 2005).

The Dakhla region is underlain by an ancient basement known as the R'guibat Ridge, composed of very old rocks such as sandstone, quartzite, and granite (Fabre, 2005; Theveniaut and Dallmeyer, 2009). This basement is overlain by layers of younger sediments, deposited in shallow marine or continental environments (Caby & Kienast, 2009). These sediments are rich in a lot of quartz, which facilitates the formation of sands that are easily transported by the wind. Wind shapes a variety of dunes in the region (Bouziani & Khouja, 2009). Depending on wind strength and direction, dunes can be mobile or more stable, with shapes such as barchanes or ripples (Besler, 1983; Besler, 2008; Pye & Tsoar, 2009). Consequently, local geology and wind dynamics explain the presence and diversity of dunes around Dakhla.y

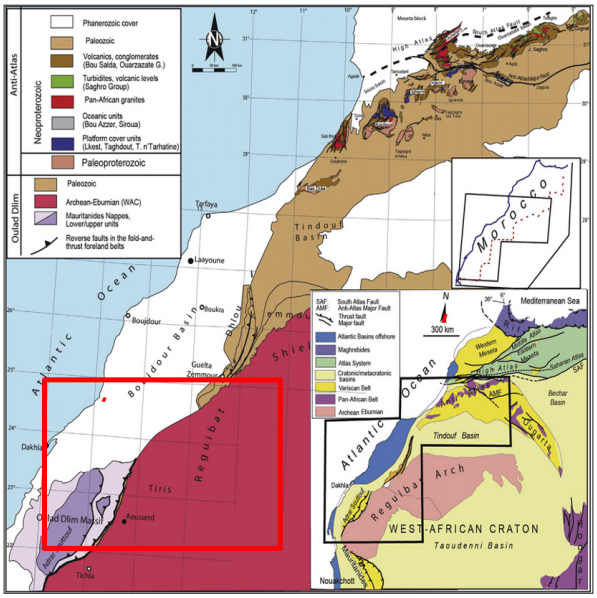

Figure 2. Geological map of the southern part of Morocco, showing the western margin of the R'guibat Shield, its sedimentary cover, and the Precambrian inliers of the Anti-Atlas. The study area is outlined by the red square.

4. Materials and Methods

Sampling sites are shown in Figure 3. For the study and characterization of the granulometric and mineralogical properties of the sandy accumulations in the Dakhla region, two approaches were used. The first approach involved sampling and facies observation: field samples were collected alongside facies identification within and at the periphery of the study area. These missions focused on geological prospecting, facies recognition, and sample collection for laboratory analysis. Each sample was packaged in a labelled plastic bag, allowing rigorous separation and systematic categorization based on criteria such as geographical location, sampling depth, substrate type, and collection date. A Global Positioning System (GPS) was used to locate the sampling sites.

The Quaternary landscapes of the study area are also marked by a wide variety of dune formations: longitudinal dunes aligned with the dominant winds, transverse dunes perpendicular to the prevailing winds, and star-shaped dunes formed by winds with changing directions. Finally, deflation surfaces, where wind erosion removes finer sediments, leaving behind a residual gravel and pebble layer located around the reliefs and plateaus, These surfaces result from strong aeolian erosion, which strips away finer sediments, exposing gravels on the surface. (Bouziani and Khouja, 2009)

4.1. Grain size analysis

Grain-size analysis was performed using the traditional method described by Berthois and Le Calez (1966). The samples were washed, dried in an oven, weighed, and sieved on a column of 12 sieves ranging from 0.5 to 0.063 mm for 20 minutes, following the standard (AG) NF P 18-560. The results of the grain-size analysis for each sample were presented asfrequency curves. The graphical representation used in this study follows the model proposed by Besler (2008) to classify dune sands based on their granulometric evolution using the position and amplitude of their modes. On the x-axis, grain sizes were arranged from the finest to the coarsest using an arithmetic scale, rather than the conventional logarithmic scale. Two units of measurement were used: millimeters (d) and phi (ϕ), which is defined by (Krumbein and Pettijohn, 1938) as $\phi = -\log_2(d)$. The y-axis differed from the traditional approach by weighting the frequency of each grain-size class by its amplitude, defined as the difference between the maximum and minimum sizes of the class in millimeters. (f (%)/(Δd (mm)). This difference allowed for the derivation of the differential frequencies proposed by Besler (2008), who adjusted raw frequencies based on the size of each class, providing balanced frequencies according to individual sizes. This approach proved more suitable for aeolian processes by correcting the emphasis on coarse grains imposed by the arithmetic scale, allowing the distinction and characterization of various granulometric types of aeolian sands (Besler, 2008). Additionally, the differential frequencies were normalized to represent density curves.

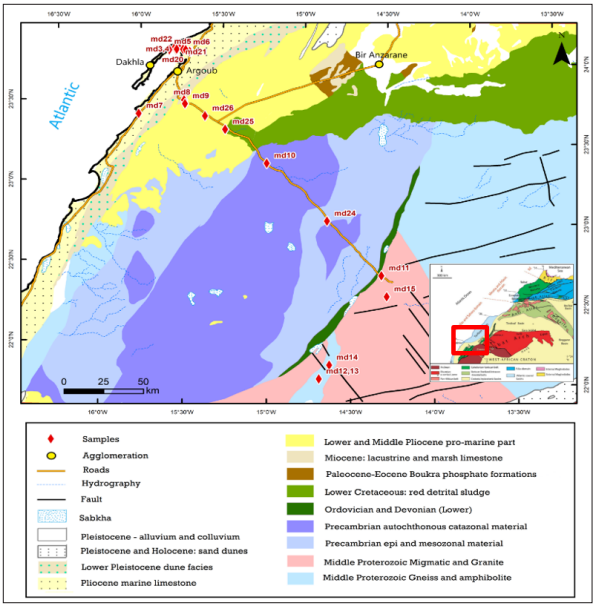

Figure 3. Sampling sites for mineralogical analysis.

The statistical parameters of the grain-size distributions (Folk & Ward, 1957; Folk, 1971) were employed to interpret the transport and sorting characteristics of the dune sands in Dakhla. The parameters expressed in phi (ϕ) are defined as follows:

- Modal size (Mo): The most frequently occurring grain size, indicating the central tendency and homogeneity of the distribution.
- Median size (M): Also referred to as the 50th percentile (ϕ50) or second quartile (Q2), it divides the distribution into two equal parts and provides a robust measure of central tendency, especially for asymmetric distributions.
- Quartiles (Q1 and Q3): On the coarser side of the distribution, grain sizes correspond to cumulative frequencies of 25% and 75%, respectively.
- Centiles (ϕ5, ϕ16, ϕ84, ϕ95): Grain sizes associated with cumulative frequencies of 5%, 16%, 84%, and 95%, respectively, on the coarser side of the distribution

The calculated parameters (Folk and Ward, 1957; Folk, 1971) are as follows:

- Mean size in phi (ϕ): $Mz = \frac{(\phi 16+\phi 50+\phi 84)}{3}$, which is a good measure of the center of a nearly normal and symmetric distribution;
- Standard deviation in phi (ϕ): $\sigma = \frac{(\phi 84-\phi 16)}{4} + \frac{(\phi 95-\phi 5)}{6{,}6}$, also called sorting index, is a good measure of the dispersion around the mean and, consequently, the overall sorting of the grains. It averages the sorting of the 68% of the population centered on the median with that of the 90%;
- Kurtosis coefficient (dimensionless): $KG = \frac{(\phi 95-\phi 5)}{2{,}44(\phi 75-\phi 25)}$ which is a good measure of the shape of the distribution, indicating whether it is more or less pointed or flat. It measures the proportion of the relative deviation in sorting at the tail of the curve compared to its center.
- Skewness coefficient (dimensionless): $Sk = \frac{(\phi 16+\phi 84-2\phi 50)}{2(\phi 84-\phi 16)} + \frac{(\phi 5+\phi 95-2\phi 50)}{2(\phi 95-\phi 5)}$, which is a good measure of the symmetry of the distribution. It averages the skewness of the 68% of the population centered on the median with that of the 90%.

The interpretation of the grain-size indices (Table1) is based on the terminology defined by Folk and Ward (1957).

Table 1. Terminology of the granulometric parameters (Folk and Ward, 1957).

Storting index (σ)		Skewness (SK)		Kurtosis (K_G)	
< ø 0.35	Very well sorted	ϕ 1.0 to ϕ 0.3	Strongly fine-skewed	< ø 0.67	Very platykurtic curve
ϕ 0.35 to ϕ 0.5	Well sorted	ϕ 0.3 to ϕ 0.1	Fine skewed	ø 0.67 to ø 0.90	Platykurtic curve
ϕ 0.50 to ϕ 0.71	Moderately well sorted	ϕ 0.1 to ϕ -0.1	Symmetrical	ø 0.90 to ø 1.11	Mesokurtic curve
ϕ 0.71 to ϕ 1.0	Moderately sorted	ϕ -0.1 to ϕ -0.3	Coarse skewed	ø 1.11 to 1.50	Leptokurtic curve
ϕ 1.0 to ϕ 2.0	Poorly sorted	ϕ -0.3 to ϕ -1.0	Strongly coarse-skewed	ø 1.50 to 3.00	Very leptokurtic curve
ϕ 2.0 to ϕ 4.0	Very poorly sorted			> ø 3.00	Extremely leptokurtic curve

5. Results and discussion

5.1. Grain size and aeolian evolution

The approach to the grain-size analysis of the sands from Dakhla follows the methodology used for the sands of Merzouga-Tafilalet (Harchane et al., 2025). Specifically, the methodology developed by Besler (2008) for constructing frequency distribution graphs was used and explained. Based on this methodology, Besler (2008) defined and classified aeolian sands according to the position of the mode and the shape of the distribution, allowing for the interpretation of the aeolian evolution of sandy deposits, originating from alluvial sources primarily from endorheic rivers or other sources such as coastal sands or sands resulting from the weathering of pre-existing rocks, such as granite sands. The various stages of this aeolian evolution, also referred to as aeolian ages, are described by Besler (2008) as follows:

The "young dune sands" represent the first stage in the evolution of the initial sandy stock, which has been mobilized and cleared of silt-clay dust by deflation. They consist of the 63-125 µm fraction mobilized by the winds inland to form small longitudinal dunes and young barkhanes. The second aeolian age is the "active crest sands," which correspond to the active dune crests formed after the deflation of the very fine sandy fraction (63-125 µm) and the concentration of the fine fraction (125-250 µm). Active crests are found on primary longitudinal and transverse dunes, on barkhanes, and on secondary dunes in the Draa areas after reactivation. The mixture of the preceding two fractions may form "dome sands" through the replenishment of very fine grains. The third aeolian age is the "inactive crest sands," which corresponds to the inactivation of the dune sands by the progressive loss of the 125-250 µm fraction in favor of the 250-500 µm fraction. This stage is primarily found in the lower parts of longitudinal and transverse dunes, as well as at the edges of barkhane dunes. The preceding stages characterize quasi-stationary dunes in which only the crest is in continuous motion.

The fourth aeolian age is that of the "old barchan sands," where the 250-500 µm fraction predominates over the fine fractions of the "inactive crest sands." This aeolian evolution characterizes migrating banchan dunes. According to Besler (2008), the final stage of this aeolian evolution corresponds to a sand with a single mode between 250 and 500 µm, representing the last step in the granulometric evolution of dunes in modern aeolian systems.

Several possibilities for degeneration within this aeolian evolution were highlighted by Besler (2008). These occur when a certain wind stability takes over from mobility. “Sand sheet sands” are characterized by a long tail and a reduced mode of residual coarser grains, which may exceed 1000 µm, associated with a modal 63-125 µm fraction that protects them from deflation. “Deflated sands” are bimodal mixtures between a fine fraction trapped because the sandy stock is no longer mobilized and another medium fraction. “Plinth sands” are characterized by a broad plateau from 63 to 500 µm, sometimes with a slight peak in the fine fractions. These represent a stage of maximal stability, where all deflation is absent, and all imported fractions accumulate.

The analysis of the dune sands of Dakhla is almost devoid of silt-clay fractions (maximum 1.10%), revealing grain size distributions falling into three distinct configurations:

Grain-size homogeneous unimodal sands are rare. Only three samples (Figure 4) with a single mode at 285 µm, were observed. The median grain size for one is 295 µm, and for the other two, it is 342 µm. Their interquartile range is 80110 µm, indicating good sorting. The well-sorted nature is also confirmed by a tight standard deviation, ranging from 75 to 140 µm. These samples exhibit slight positive skewness, indicateded by a flattened tail toward finer grains. Their distribution is leptokurtic to mesokurtic, with an average kurtosis coefficient of 1. These sands indicate good dynamic sorting and consist of a dominant modal fraction of well-sorted medium grains (180-460 or 220-560 µm), with a more or less developed tail of fine to very fine grains (65-180 µm). This distribution suggests mobilization, deposition, and stabilization under a moderate wind regime with little fluctuation.

The correlation of these few unimodal aeolian sands from Dakhla with the types defined by Besler (2008) allows their interpretation as the result of ongoing aeolian evolution, transitioning from “inactive crest sands” to “old barchan sands” in a unimodal state.

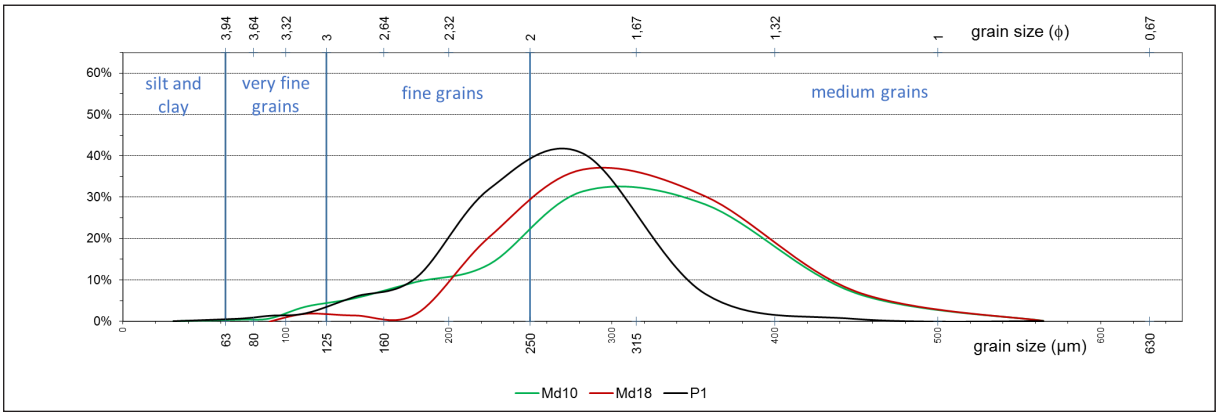

Figure 4. Typical unimodal frequency curves for Dakhla dune sands.

The majority of the analyzed sands exhibit bimodal distributions with distinct well-separated modes, corresponding to mixtures of two homogeneous grain-size subpopulations (Fig. 6a). These two subpopulations were separated for the same reasons and in the same manner as the sands of Merzouga-Tafilalet (Harchane et al., 2025), assuming that any heterogeneous grain population consists of homogeneous subpopulations in terms of their origin or nature (Folk, 1971). The total bimodal samples were thus graphically segmented, around 180 µm, into homogeneous unimodal sub-samples (Figure 5) with significant representative statistical parameters and distributions reflecting their individual origins and evolutions.

These two modes , with few exceptions, occupy well-defined and relatively stable positions (Fig. 6a): the first around 142 µm, and the second around 225 µm. They thus represent two grain fractions: the fine grain fraction (90-180 µm) and the fine-to- medium grain fraction (180-350 µm), with, in addition, a more or less developed tail, extending to 600 µm and a very reduced and minor tail of very fine grains (65-90 µm). The main fractions are mixed in various proportions, with each fraction potentially being minor or major. Only one sample exhibits a predominant very fine mode of 112 µm, associated with a very reduced fine–to-medium mode at 225 µm and a long low tail extending to 500 µm.

The analysis of the fine-grain fraction, with a mode of 142 µm, showed a median size, ranging between 130 and 165 µm, and an average of 158 µm. The average grain size in this fraction ranges from 131 to 165 µm, with an average of 157 µm and a mean standard deviation of 17.5,ranging from 10 to 27 µm, and an interquartile range of 15 µm. The distribution is leptokurtic to very leptokurtic, with a mean kurtosis coefficient of 1.8. It is symmetrical to slightly asymmetrical toward coarser or finer grains. These grains would therefore be very well-sorted sands, mobilized and deposited by low-energy winds with minimal fluctuations.

The grains in the fine–to-medium fraction, with a mode of 225 µm, have median sizes ranging from 250 to 340 µm, with an average of 296 µm. Their average sizes range from 257 to 341 µm, with an average of 302 µm, a mean standard deviation of 80 µm (ranging from 47 to 106), and an interquartile range of 85 µm. Their distribution can be leptokurtic, mesokurtic, or platykurtic, with a mean kurtosis coefficient of 1.2. It is weakly or strongly skewed toward the coarser grains, due to the more or less developed tail of coarse grains. These characteristics correspond to well-

sorted sands, mobilized and deposited by winds of medium energy, with noticeable fluctuations.

Correlating the segmented distributions of the bimodal aeolian sands of Dakhla with the types defined by Besler (2008) indicates that they represent a mixture of two dominant components (Figure 5). The very fine to fine modal fraction corresponds to the "active crest sands" type in most cases. Only one sample shows a very fine fraction of the "young dune sands" type (Md11), and another shows the "dome sand" type (Md3), indicating a replenishment of very fine sands. The fine–to-medium modal fraction results from a gradual evolution from the "inactive crest sands" (Md3 and Md25) to the "old barchan sands" (Md19 and Md22) and the "ridge sands" (Md11 and Md24), with stages visible from one sample to another.

These fractions form a heterogeneous mixture in varying proportions (Figure 5). Each fraction represents a specific wind kinetic energy responsible for its mobilization. The lowest energy in the studied area is responsible for the deposition of the "young dune sands," while the highest energy brings the "ridge sands," passing through the "active crest sands," then "inactive crest sands," and finally the "old barchan sands." The following mechanisms could act jointly or differentially to generate these two-mode mixtures, which are characteristic of the aeolian sands in the study area:

1- Simultaneous deposition of the two modal fractions due to alternating wind dynamics over short durations, explaining their coexistence (Figure 5, all samples).

2- Gradual evolution between stages during a change in wind regime, with winds becoming increasingly stronger, incomplete deflation of the finer fraction, and deposition of the coarser fraction. This mechanism would explain the observed differences between samples for modal fractions of the same category (Figure 5, all samples).

3- Degeneration of aeolian evolution, from "old barchan sands" to fine sands undergoing deflation (Fig. 5a, Md19 and Md22), toward aeolian ages characteristic of wind stability, where fine sands are no longer swept away, while stronger winds continue to bring coarser grains and readjust the distributions. Sample Md11, with a very fine mode at 112 µm, would likely be a "sand sheet sand," while Md3 and Md25 would correspond to "deflated sands."

4- If the occasional stronger winds responsible for the coarse tails become more regular, the coarse mode increases in amplitude, and the sand would become a "ridge sand" (Figure 5a, Md24).

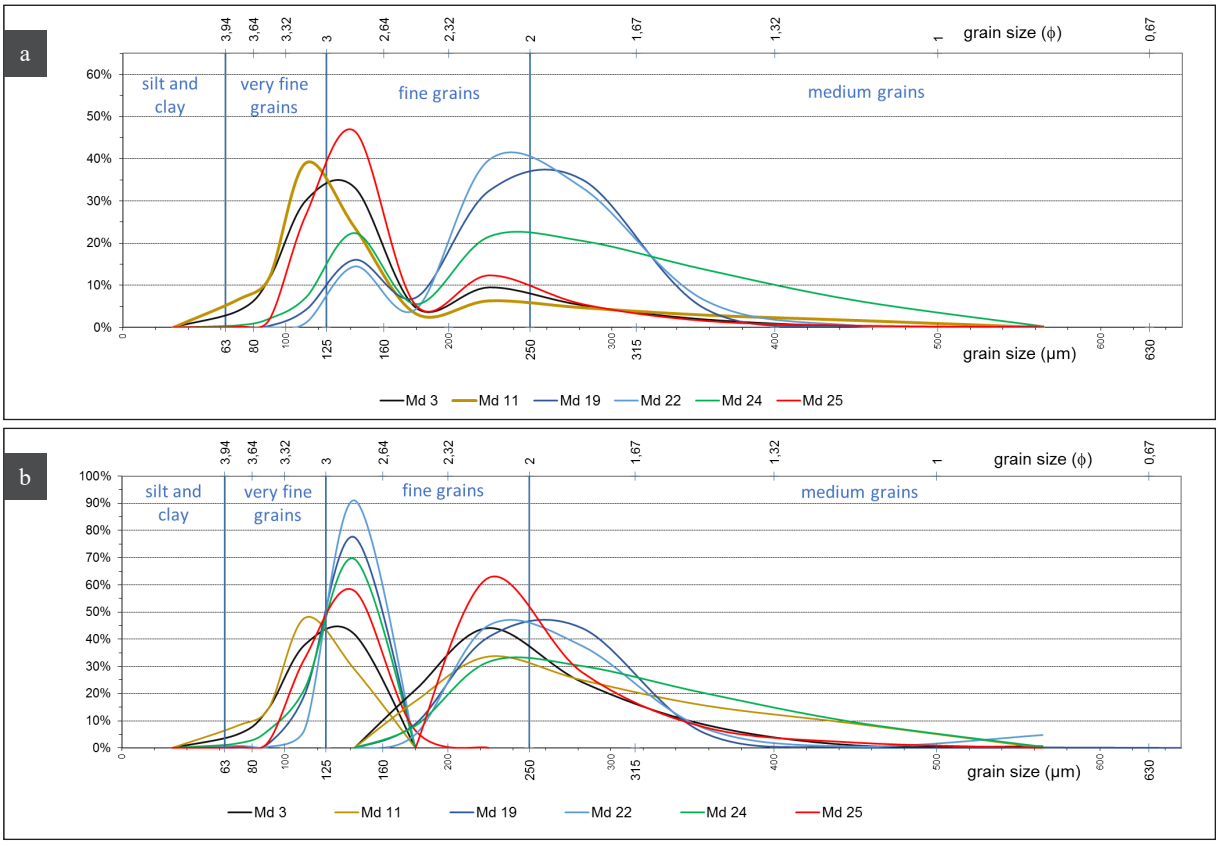

Figure 5. (a) typical bimodal frequency curves for Dakhla dune sands. (b) Segmented modes of the same sands.

Some sands from the study area (Figure 6) exhibited a highly heterogeneous grain-size distribution with a multimodal frequency curve that is very platykurtic, indicating a near absence of genetic sorting. These distributions range from 63 µm to 700 µm, with a median of 300-480 µm, an average of 380 µm, a first quartile of 400-550 µm, and a third quartile of 240-380 µm. Their interquartile range is very wide, from 135 to 270 µm, with an average of 185 µm, indicating poor sorting of these sands. These sands are thus composed of a large, poorly sorted fraction of

medium grains (250-700 µm), followed by an equally poorly sorted fraction of fine grains (125-250 µm), in addition to a very small amount of very fine grains (65-125 µm). These sands were likely accumulated under the influence of vortex, multidirectional winds, or winds with highly variable dynamics acting simultaneously. The presence of obstacles could also explain this lack of sorting. They likely correspond to the "plinth sands" of Besler (2008).

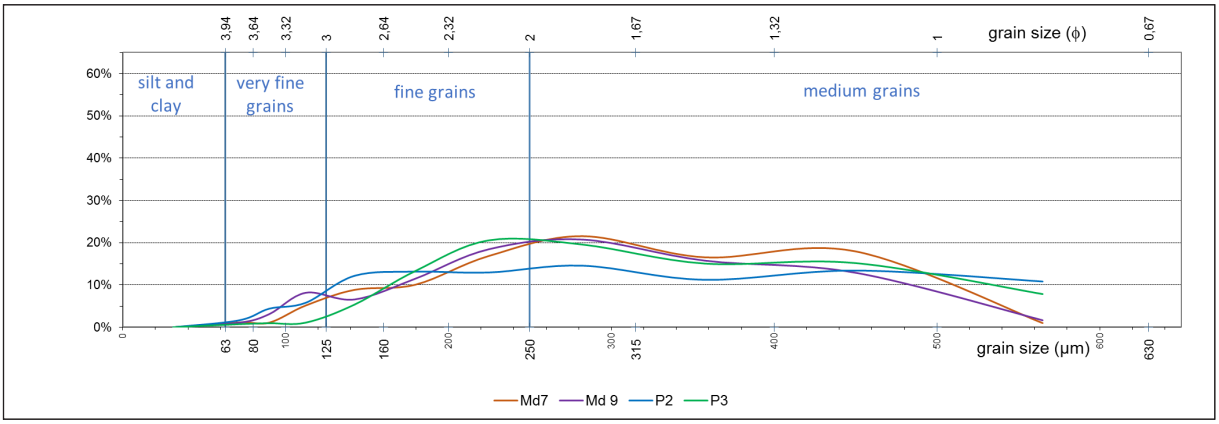

Figure 6. Typical multimodal frequency curves for Dakhla dune sands.

The analysis of the very fine–to-fine sand fractions of the heterogeneous samples (Figure 5) revealed sharp-peaked sand curves, indicating the mobility of thesesands. The aeolian ages of these sand fractions also supported the mobility of the studied sands, as it is well known that sands from young dunes with active and inactive crests are always in aeolian mobility, that is, a sorting factor responsible for the good classification of transported and deposited sands, and it is especially effective when it acts on fine grains (Besler, 1983).

In contrast, the frequency analysis of the homogeneous samples (Figure 4) and the fine-to-medium sand fractions of the heterogeneous samples (Figure 5) showed broader, more peaked curves for fine-to-medium sand, with a coarser sand tail, indicating lower mobility. The aeolian ages of these samples and sand fractions are also consistent with the relative stability of the wind regime under which they were accumulated.

For confirmation, the response diagram from Besler (1983) was used in Figure 7. This diagram, derived from the diagram of Friedman (1961), allows a quantitative distinction between mobile, stabilized, and residual aeolian sands, as well as fluvial sands. It is a binary diagram that plots the mean grain size (Mz) in Φ, against the sorting index (σ) in Φ. The mean size indicates the average kinetic energy of the transport and deposition agent, the sorting index, or standard deviation. It represents the variability of this energy around the mean. Because these two parameters can be strongly influenced by sample heterogeneity, meaning the association of several transport and deposition agents or grain sources (Besler, 1983), the parameters calculated fromthe segmented fractions were used for the heterogeneous samples in the diagram.

Overall, the mean grain sizes of Dakhla sands (Figure 5a) align with those observed in the Moroccan desert by Benalla (2003), Boudad (2004), and Harchane et al. (2025). Their sorting index is also in agreement with those of well-sorted continental dune sands (less than 0.5) described by Friedman (1961).

5.2. The Response Diagram

The response diagram (Figure 7), thanks to the small size and strong sorting of the fractions, confirmed that the very fine fractions are indeed aeolian sediments in the process of mobilization. The fine fractions lie between mobility and aeolian stability, with their sizes corresponding to the threshold for sand movement. The medium fractions are clearly within the stability zone, on the edge of the residual zone, given their sizes that exceed the threshold mobilization speed.

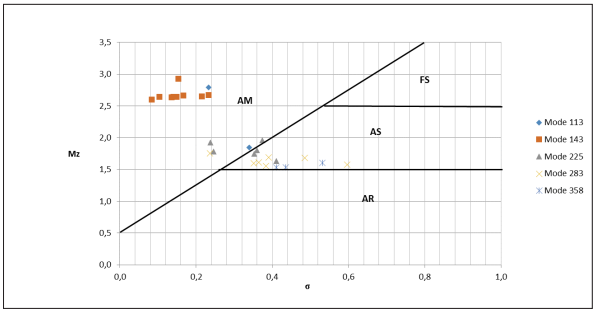

Figure 7. The response diagram (Besler, 1983) of Dakhla dune sand segments: Fluvial Sands (FS), Aeolian Mobility Sands (AM), Aeolian Stability Sands (AS), Aeolian Residuals (AR).

6. Conclusion

The aeolian evolution of the sands in the Dakhla region has been interpreted through detailed granulometric analysis, highlighting the dominance of wind-driven processes in forming of dune complexes. Although various modes of sediment transport have contributed to sand accumulation, aeolian activity remains the principal agent, sorting the grains into distinct fractions: very fine-grained (63–100 µm), fine (100–180 µm), and fine–to-medium (180–350 µm and beyond).

These findings highlight distinct granulometric distribution types within the Dakhla sands, reflecting differences in sediment transport and depositional conditions. Based on Besler's (1983, 2008) response diagrams, the observed grain-size fractions correspond to varying degrees of aeolian mobility and stability: the very fine sands indicate active wind transport, the fine fraction marks the transitional threshold between mobility and stability, and the

coarser fractions are largely stable, representing residual, relict accumulations. This interpretation clarifies how wind dynamics shape dune evolution and the spatial variability of sediment deposits in the region. Three main granulometric distribution types were identified:

1. Unimodal distributions, relatively rare, show well-sorted medium grains and slight positive skewness, corresponding to stabilized "old barchan sands" shaped by moderate, steady winds.

2. Bimodal distributions, the most common, combine fine and fine-to-medium fractions, indicating alternating wind regimes of varying energy. These sands represent transitional aeolian ages between "old barchan sands" and "ridge sands."

3. Polymodal distributions, less common, consist of poorly sorted grain mixtures ranging from 65 to 700 µm. Their chaotic structure suggests deposition under turbulent, multidirectional winds or in sheltered environments, consistent with Besler's "plinth sands."

These findings underscore the complexity of aeolian processes in shaping the sandy Dakhla's landscape. The diverse grain-size distributions and sedimentary structures reflect both past and present wind dynamics. Overall, the dune sands preserve a detailed archive of aeolian activity over time, illustrating stages of mobilization, deposition, and stabilization that define their "aeolian ages."

Acknowledgment:

The authors sincerely thank the anonymous reviewers for their valuable comments, which helped improve the quality of this paper. This work is sponsored by the Académie Hassan II des Sciences et Techniques. The authors extend special thanks to the team at the Laboratoire des Géo-Ressources et de l'Environnement in Fez, as well as to the technicians in the Geology and Chemistry laboratories at the Faculté Polydisciplinaire in Taza. The authors also gratefully acknowledge the staff of the Fez Innovation Center at Sidi Mohamed Ben Abdellah University for their invaluable collaboration and support.

Conflict of Interests

The authors declare that they have no conflicts of interest concerning the publication of this paper.

References

Barbero, M., Loisel, R., & Quézel, P. (1994). Écologie et adaptations des plantes en zone saharienne. Actes du Congrès de l'Écologie Méditerranéenne, 23–30.

Barcellos, A. F., Tavares, A. C., Oliveira, P. T. S., & Sano, E. E. (2022). A global Köppen–Geiger climate classification map based on remote sensing data. International Journal of Climatology, 42(1), 186–202. https://doi.org/10.1002/joc.7253

Benalla, M., et al. (2003). Les dunes du Tafilelt (Maroc): dynamique éolienne et ensablement des palmeraies. Sécheresse, 14, 73–83.

Benattia, M., & Hassan, A. (2020). Impact des changements climatiques sur le climat saharien d'Awserd. Bulletin de la Société Météorologique du Maroc, 12(4), 87–98.

Berthois, L., & Le Calez, Y. (1966). Etude sédimentologique des dépôts à « Jullienella fœtida » de la région d'Abidjan. Bulletin du B.R.G.M., 1, 44–55.

Besler, H. (1983). The response diagram: Distinction between aeolian mobility and stability of sands and aeolian residuals by grain size parameters. Zeitschrift für Geomorphologie N.F., Suppl-Bd., 45, 287–301.

Besler, H. (2008). The Great Sand Sea in Egypt. Developments in Sedimentology, 59. Elsevier.

Boudad, L. (2004). Les formations sédimentaires du pléistocène supérieur et de l'holocène du Tafilelt (Sud-Est du Maroc): Géochronologie, stratigraphie et paléoenvironnement (Thèse de 3ème cycle). Université Moulay Ismail, Meknès, Maroc.

Bouziani, A., & Khouja, M. (2009). Formations quaternaires et systèmes dunaires de la région de Dakhla-Awserd. Revue Marocaine de Géomorphologie, 4(1), 33–47.

Caby, R., & Kienast, J. R. (2009). Neoproterozoic and Hercynian metamorphic events in the Central Mauritanides: Implications for the geodynamic evolution of West Africa. Journal of African Earth Sciences, 53, 122–136. https://doi.org/10.1016/j.jafrearsci.2008.09.004

Dahnoun, K., & Djadouni, F. (2020). Effects of heavy-metal pollution on soil microbial community, plants, and human health. Jordan Journal of Earth and Environmental Sciences, 11(3), 234–240. http://jjees.hu.edu.jo/files/Vol11No4/JJEES_Vol_11_No_4_P1.pdf

Fabre, J. (2005). Géologie du Sahara occidental et central. Tervuren African Geosciences Collection, MRAC Tervuren, Belgique.

Folk, R. L. (1971). Longitudinal dunes of the northwestern edge of the Simpson Desert, Northern Territory, Australia. I. Geomorphology and grain size relationships. Sedimentology, 16, 5–54.

Folk, R. L., & Ward, W. C. (1957). Brazos River bar (Texas): A study in the significance of grain size parameters. Journal of Sedimentary Research, 27, 3–26.

Friedman, G. M. (1961). Distinction between dune, beach, and river sands from their textural characteristics. Journal of Sedimentary Research, 31(4), 514–529. https://pubs.geoscienceworld.org/sepm/jsedres/article/31/4/514/95526

Garzanti, E., Resentini, A., Andò, S., Vezzoli, G., Pereira, A., & Vermeesch, P. (2015). Physical controls on sand composition and relative durability of detrital minerals during ultra-long-distance littoral and aeolian transport (Namibia and southern Angola). Sedimentology, 62, 971–996. https://doi.org/10.1111/sed.12169

Gomez, C., Garcia, A., & Smith, J. (2018). Aeolian processes and dune dynamics in arid environments: A global synthesis. Geomorphology, 312, 1–15. https://doi.org/10.1016/j.geomorph.2018.04.005

Guan, C., Hasi, E., & Tang, K. S. (2025). Grain size characteristics of the reticulate dunes of the Hobq Desert. Journal of Arid Environments, 226. https://doi.org/10.1016/j.jaridenv.2024.105279

Harchane, S., Azzouzi, N., El Hammichi, F., Tabyaoui, H., & El Hammouch, N. (2025). Mineral composition and aeolian evolution of dune deposits in Merzouga-Tafilalet, South-Eastern Morocco. Studia Quaternaria, 42, 27–40. https://doi.org/10.24425/sq.2025.154324

Muhs, D. R. (2017). Evaluation of simple geochemical indicators of aeolian sand provenance: Late Quaternary dune fields of North America revisited. Quaternary Science Reviews, 171, 260–296. https://doi.org/10.1016/j.quascirev.2017.07.007

Kasper-Zubillaga, J. J., Arellano-Torres, E., Alvarez Sánchez, L. F., Carlos-Delgado, L., Martínez-Serrano, R., & Jiménez,

P. B. (2022). Implications of polymodal distributions in the grain size parameters of coastal dune sands (Oaxaca, Mexico). Sedimentary Geology, 437, 106189. https://doi.org/10.1016/j.sedgeo.2022.106189

Kalinska-Nartisa, E., Alexanderson, H., Nartiss, M., Stevic, M., & Kaiser, K. (2017). Sedimentary features reveal transport paths for Holocene sediments on the Kristianstad coastal plain, SE Sweden. GFF, 139(2), 147–161. https://doi.org/10.1080/11035897.2017.1290675

Krumbein, W. C., & Pettijohn, F. J. (1938). Manual of sedimentary petrography. Appleton-Century-Crofts.

Laurent, C., & Benhammou, F. (2021). Conditions de vie dans le désert saharien: Études socio-environnementales. Sociologie du Maroc, 19(2), 99–115.

Pye, K., & Tsoar, H. (2009). Aeolian sand and sand dunes (2nd ed.). Springer. https://doi.org/10.1007/978-3-540-85910-9

Sanchez, J., & Martin, L. (2019). Les dynamiques climatiques du littoral de Dakhla. Annales Marocaines de Climatologie, 14, 65–78.

Sur, R., & Chauhan, P. (2019). Aeolian transport and dune migration using remote sensing and GIS techniques: Case study from the Thar Desert, India. Aeolian Research, 39, 24–34. https://doi.org/10.1016/j.aeolia.2019.02.002

Theveniaut, H., & Dallmeyer, R. D. (2009). Chronologie et déformation des reliefs de l'Adrar Souttouf et du massif de Réguibat. Precambrian Research, 167(1–2), 104–118. https://doi.org/10.1016/j.precamres.2008.10.003

Villeneuve, M. (2008). Review of the orogenic belts on the western side of the West African craton: The Bassarides, Rokelides and Mauritanides. In N. Ennih & J.-P. Liegeois (Eds.), The boundaries of the West African craton (Geological Society of London, Special Publications, 297, pp. 169–201). https://doi.org/10.1144/sp297.8

Visher, G. S. (1969). Grain size distributions and depositional processes. Journal of Sedimentary Research, 39(3), 1074–1106. https://doi.org/10.1306/74D71D9D-2B21-11D7-8648000102C1865D

Sahu, B. K. (1964). Depositional mechanisms from the size analysis of clastic sediments. Journal of Sedimentary Research, 34(1), 73–83. https://doi.org/10.1306/74D70FCE-2B21-11D7-8648000102C1865D

Wang, X., Dong, Z., Zhang, J., Qu, J., & Zhao, A. (2003). Grain size characteristics of dune sands in the central Taklimakan Sand Sea. Sedimentary Geology, 161(1–2), 1–14. https://doi.org/10.1016/s0037-0738(02)00380-9

JJEES

JJEES (2026) 17 (1): 16-25
ISSN 1995-6681

Jordan Journal of Earth and Environmental Sciences

Pollution Assessment and Source Identification of Heavy Metals in Groundwater on Mosul's Left Bank, Iraq.

Hazim J. Mahmood[1*], Mohammed F. O. Khattab[2]

[1] College of Environmental Sciences, University of Mosul, Mosul, Iraq
[2] Remote Sensing Center, University of Mosul, Mosul, Iraq

Received on 8 September 2024; Accepted on 23 June 2025

Abstract

The occupation of Mosul by the terrorist organization ISIS and the subsequent military operations to liberate the city forced residents to resort to dig wells randomly and rely on the water from these wells for various uses, without conducting any tests to determine their suitability. Some of these wells are still used in some situations. The current study aims to determine the content and sources of trace elements in groundwater on the left bank of the city and to assess the risks associated with using this water for drinking purposes. Sixteen trace elements (Al, As, B, Ba, Cd, Cr, Cu, Fe, Mn, Mo, Ni, Pb, Sb, Se, U, and Zn) were analyzed in well water using Inductively Coupled Plasma Mass Spectrometry (ICP-MS). Fe, Mn, and Al had concentrations above the recommended limits at two locations among all the trace elements analyzed and assessed. The results of the pollution indices showed that the groundwater under investigation, excluding one sample (M5), isn't polluted by heavy metals. For the M5 sample, the pollution indices yielded different classifications: the sample was classified as highly polluted, non-polluting, and moderately polluted according to the Contamination Index, Heavy-Metal Evaluation Index, and Nemerow Pollution Index, respectively. Factor analysis and cluster analysis findings generally agree that redox reactions, mineral composition of reservoir materials, geochemical behavior, and anthropogenic influences are all involved in controlling the groundwater content of heavy metals. Overall, the Nemerow Pollution Index was the best way to express the state of groundwater pollution by heavy metals, and the source of these heavy metals is primarily geogenic and secondary anthropogenic.

Keywords: *pollution indices, heavy metals, trace elements, Mosul, Groundwater*

1. Introduction

Groundwater is a major source of drinking water globally and the only source in arid regions. In Iraq, given the growing environmental pressures on freshwater, particularly in recent years, water resources have been under considerable stress in terms of both water quality and quantity for various reasons. This stress is due to dams constructed on the Tigris and Euphrates in the riparian countries, global climate change, a significant local decline in annual precipitation rates, and inappropriate planning of water use in Iraq (Adamo et al., 2018; Al-Ansari et al., 2018; Alobaidy et al., 2010; Jones et al., 2008; M. J. Trondalen, 2009; Rahi & Halihan, 2010) Kurdistan region, Iraq using ten water quality pa-rameters (pH, Dissolved Oxygen, Turbidity, Conductivity, Hardness, Alkalinity, Sodium, Biochemical Oxy-gen Demand, Nitrate and Nitrite. As a result, groundwater has been used as the most convenient and easiest option to supply freshwater in many areas, and it is the only option in arid regions. In fact, it is the only refuge in some cases and emergency conditions, as happened in the city of Mosul during the terrorist organization ISIS,s occupation of the city and the difficult periods that followed during the liberation operations and the accompanying military operations that led to the cessation or destruction of water treatment plants and water supply lines in almost all Mosul areas(Khattab et al., 2021; Lead IG, 2017). Most groundwater is of phenomenal natural microbiological quality and has the appropriate chemical quality for most applications. Indeed, many people buy bottled water from natural groundwater sources at considerable cost in preference to public tap water, which may be sourced from treated river water (Smith et al., 2016). This is because groundwater is less susceptible to pollution than surface water, but this does not mean that groundwater can be used for particular purposes without assessing its appropriateness of use. It is therefore important to evaluate its quality characteristics and compare them with international determinants and standards in order to consider the possibility of using it for different uses. One of the essential criteria for assessing groundwater is the contamination of groundwater with trace elements, especially heavy metals, as they pose a direct risk to human health and are difficult to handle when they occur.

Based on the above, groundwater samples were collected from some wells on the left side of Mosul City to examine and evaluate their heavy metal content and other trace elements. Mosul is Iraq›s second-largest city, located in the northwest of Iraq and is the main commercial city in the country›s northwestern part (Augustin et al., 2019). The city of Mosul is divided into two sides by the Tigris River: right and left sides, with an approximate population of 1.5 million inhabitants, more than half of who live on the left bank (Al-Sabawi, 2008; UNAMI, 2017). During the ISIS occupation and the ten-month military operations to retake

* Corresponding author e-mail: hazimjm@uomosul.edu.iq

the city, citizens suffered from water shortages. To address this situation, the residents of the city dug wells in each area and used the water from wells for different purposes without any testing.

Accordingly, the current study focuses on groundwater on Mosul›s left bank, as the city relied on well water for various purposes during the emergency period of city life, and some of these wells are still used for domestic and irrigation purposes. Therefore, the objectives of this study are to: (i) determine the concentrations of trace elements in groundwater and compare them with international drinking-water guideline values, (ii) assess the potential human health risks associated with heavy-metal contamination, and (iii) identify the sources of these elements and evaluate the influence of anthropogenic activities on groundwater quality using multivariate statistical methods.

2. Materials and methods

2.1. Study area

Mosul is located approximately 465 kilometers northwest of Baghdad in the northwestern part of Iraq (Figure 1). It is situated at 36.3388° N latitude, 43.1349° E longitude, and 228 m altitude (AtlasWorld, 2019). The Tigris River divides Mosul into two sides, with the left side being the northeastern side of the city and the right side the southwestern side. The left side covers approximately 140 square kilometers and is divided into 51 residential neighborhoods, with a population of over 750000 (UN-Habitat, 2016).

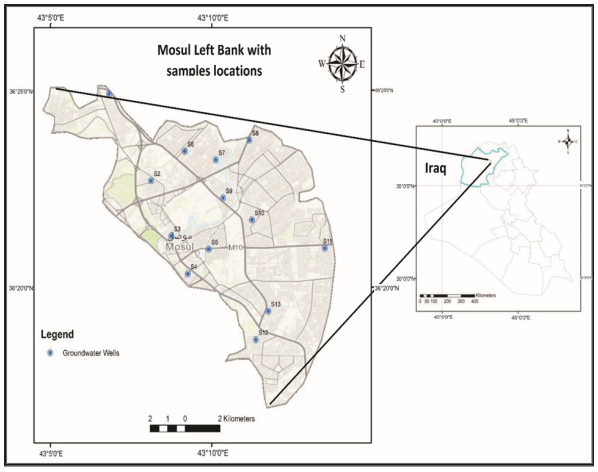

Figure 1. Study area location map with current study wells locations.

2.2. Geological and hydrogeological setting

The study area is situated in a semi-arid region, with hot, dry, sunny summers, and cold and partly cloudy winters. The climate in Mosul is classified as warm and temperate, with an average annual rainfall of approximately 370.4 mm. Temperatures peak in July, reaching up to 46°C, while January is the coldest month, with average lows of 3.3°C and highs of 12.2°C (Climate-Data.Org, 2024; WeatherSpark, 2024).

Geologically, the study area is predominantly characterized by sedimentary deposits ranging in age from the Late Miocene to the Recent (Figure 2). These deposits are stratigraphically arranged in the following order, from oldest to youngest as follows: Fat'ha Formation (Late Miocene), composed of layers of anhydrite, gypsum, limestone, marl, sandstone, and mudstone, often overlain by recent sedimentary layers (Al-Naqib et al., 2018; Mahder-Bashi & Khattab, 2009). Injana Formation, located in the northern part of the study area, is primarily composed of sandstone, siltstone, and mudstone, with evidence of fluvial and deltaic depositional environments. The clastic sediments of the Fat'ha and Injana Formations contain a variety of minerals, including feldspar, pyroxene, quartz, magnetite, chromite, rutile, titanite, and clay minerals. These minerals are derived from the weathering of exposed igneous, metamorphic, and older sedimentary rocks located in the northern and northeastern regions of Iraq. Although these sediments include heavy minerals, such as magnetite, chromite, rutile, and titanite, their overall mineral composition is diverse and reflects the complex processes of sedimentation and transport from the source rocks (Al-Nuaimi & Al-Sayegh, 2004). The Quaternary deposits, which include river terraces and alluvial sediments, are also rich in a diverse array of clasts and minerals, including feldspar, mica, rutile, magnetite, almandite, chromite, and various clay minerals. These deposits, primarily covering the left bank of the Mosul region, consist of conglomerates, gravel, sand, silt lenses, and residual soils, reflecting a dynamic fluvial environment. The floodplain areas along the Al-Khoser and Tigris Rivers further highlight the role of modern hydrological processes, which continue to shape the sedimentary landscape through periodic flooding and sediment deposition. Groundwater movement in the region predominantly follows a flow pattern from the north and northeast toward the south and southwest, particularly to the east of the Tigris River, with some localized exceptions (Al-Jiburi & Al-Basrawi, 2015).

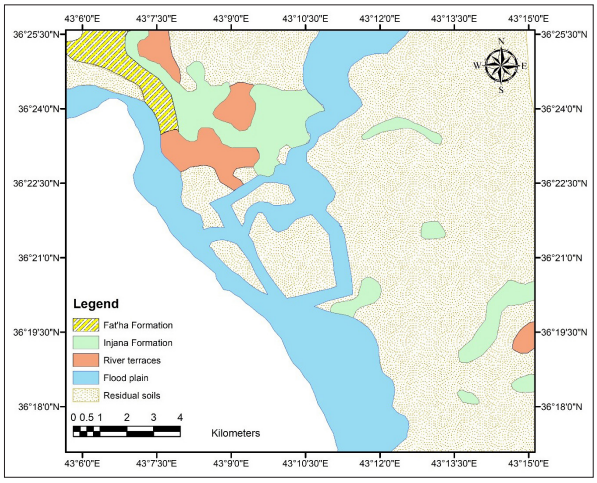

Figure 2. Geological map of the study area (modified from Sissakian et al., 1995)

2.3. Sampling and analytical procedure

Thirteen wells, distributed across the left side of Mosul city, were carefully selected for water sample collection (Figure 1). Samples were collected in November 2019, and well locations were determined using GPS. The depths of the wells examined ranged from 12 to 60 m. Electrical conductivity (EC) was measured in the field using a portable Hanna EC meter. After pumping, samples were collected once EC had stabilized. Samples were collected in 60 ml pre-washed polyethylene bottles, filtered in situ through a

0.2 µm membrane filter, and then acidified with ultrapure HNO_3. Trace elements (Al, As, B, Ba, Cd, Cr, Cu, Fe, Mn, Mo, Ni, Pb, Sb, Se, U, and Zn) were determined by ICP-MS at TU Bergakademie Freiberg in Germany. To confirm the accuracy of the results, an internal standard containing three elements was added to the samples. Measurements were performed in direct, interaction, or collision mode, depending on the element being measured.

2.4. Groundwater pollution assessment

To evaluate heavy-metal contamination in groundwater in the study area, three heavy-metal pollution assessment models were applied, as indicated below:

2.4.1. Contamination index (Cd)

The Cd accounts for both the sum of parameters exceeding the acceptable upper limits or guideline values of potentially hazardous elements and the concentrations above those limits (Backman et al., 1998). It is calculated separately for each water sample analyzed as the sum of the water contaminant factor for the individual components that exceed the upper permissible limits.

Generally, the Cd summarizes the cumulative effects or degree of pollution across several parameters considered potentially harmful to household water. It is calculated using the following equation:

$$C_d = \sum_{i=1}^{n} C_{fi}$$

$$C_{fi} = \frac{C_{Ai}}{C_{Ni}} - 1$$

Where:

C_{fi}= contamination factor for the *i*th component, C_{Ai} = analytical value for the *i*th component and C_{Ni}= upper permissible concentration of the ith component.

The Cd values are classified as follows into three categories: low (Cd < 1), medium (1 < Cd < 3), and high (Cd > 3)(Backman et al., 1998; Edet & Offiong, 2002; Prasad Ahirvar et al., 2023)

2.4.2. Heavy metal evaluation index (HEI)

The Heavy Metal Evaluation Index (HEI) is a quantitative tool used to assess the overall contamination level of heavy metals in water, soil, or sediment. It provides a single value that represents the cumulative impact of multiple heavy metals, making it easier to evaluate pollution levels and compare different samples or sites. This approach provides an overall water quality concerning heavy metals (Bhuiyan et al., 2010; Edet & Offiong, 2002; Singh Brraich & Jangu, 2015) and is measured using the following equation:

$$HEI = \sum_{i=1}^{n} \frac{H_c}{H_{mac}}$$

where H_c and H_{mac} are the measured value and the maximum allowable concentration of the *i*th parameter, respectively.

The level of the heavy metal evaluation index is divided into three categories, as follows: low (HEI < 10), medium (10 < HEI < 20), and high (HEI >20) (Bodrud-Doza et al., 2016; Edet & Offiong, 2002).

2.4.3. Nemerow Pollution Index (NI).

This index is used to assess the extent of contamination of groundwater by several heavy metals at a given sampling location. It considers the average and maximum values of the single-factor pollution index and focuses on pollutants with high pollution rates (Zhong et al., 2015). It is calculated as follows:

$$NI = \sqrt{\frac{\left[\left(\frac{1}{n}\right)\sum\left(\frac{Ci}{Si}\right)\right]^2 + \left[\max\left(\frac{Ci}{Si}\right)\right]^2}{2}}$$

Where:

n = the number of indices; *Ci* = the measured content of heavy metal *i*; *Ci* = the standard value. The groundwater is divided by Nemerow Pollution Index into six degrees (Li et al., 2001) (Table1).

Table 1. Classification of Nemerow Pollution Index (NI).

Class	Pollution degree	NI
1	No pollution	≤0.5
2	Clean	0.5–0.7
3	Warm	0.7–1.0
4	Polluted	1.0–2.0
5	Medium pollution	2.0–3.0
6	Severe pollution	>3.0

2.5. Multivariate statistical analysis:

Multivariate statistical techniques, such as factor analysis (FA) and cluster analysis (CA), are effective ways of manipulating, interpreting, and representing data concerning groundwater pollutants and geochemistry and are often used to distinguish groundwater quality(Alaarajy et al., 2023; Chen et al., 2007a; Dmitrijeva et al., 2020; Liu et al., 2003).

2.5.1. Factor analysis

Factor analysis was used to identify and interpret the underlying structure of the data set by reducing it it to smaller set of new orthogonal (uncorrelated) variables (principal components), ordered by decreasingimportance. In addition to significant data reduction, principal components can capture the full variability of the multidimensional data set without losing much of the original information(Dhannoun & Mahmood, 2019). Factor analysis with Varimax rotation of standardized component loadings for extracting and deriving factors, respectively, were carried out and those principal components with eigenvalues greater than 1 were retained(Belkhiri et al., 2018; Li & Zhang, 2010).

2.5.2. Hierarchical cluster analysis

Cluster analysis is one an important multivariate method used to identify correlated data sets. Objects are grouped into clusters so that related objects fall into the same class (Chen et al., 2007a; Danielsson et al., 1999; Xu et al., 2020). Hierarchical clustering combines the most similar observations, followed by the next most similar observations. A dendrogram is constructed based on the degree of similarity at which observations are combined. In this study, cluster analysis was carried out on the standardized data set using Euclidean distances as a measure of similarity and Ward›s linkage method to obtain a dendrogram.

3. Results and discussion

Table 2 presents the statistical summary of trace element concentrations in the groundwater samples from the current study, including key statistical metrics such as the maximum, minimum, standard deviation, mean, and median values. Additionally, it includes the maximum permissible limits (MPL) for these elements in drinking water, as specified by the World Health Organization (WHO, 2011). Table 3 provides a detailed list of the analytical results for the trace element concentrations in each groundwater sample. All pollution indices and statistical analyses were based on this dataset.

Table 2. Statistical summary of trace element concentrations in the current study samples and their maximum permissible limits(MPL)

Element	Mean	Median	Minimum	Maximum	St. Dev.	MPL (WHO, 2011).
Al	62.69	41.57	26.35	271.50	65.22	200
As	0.30	0.28	0.04	0.72	0.18	10
B	538.37	418.20	278.50	1314.00	283.77	500
Ba	32.05	24.35	12.08	108.50	26.12	700
Cd	0.05	0.05	0.01	0.12	0.03	3
Cr	5.12	4.90	2.81	10.66	2.41	50
Cu	9.35	8.95	7.50	16.49	2.32	2000
Fe	156.04	44.29	20.36	1109.00	298.60	300
Mn	113.24	10.70	0.99	971.80	266.34	400
Mo	5.08	5.22	1.82	10.87	2.91	70
Ni	3.92	2.91	0.93	12.72	3.06	70
Pb	0.70	0.65	0.33	1.66	0.38	10
Sb	0.11	0.10	0.08	0.17	0.03	20
Se	0.63	0.47	0.18	1.58	0.47	40
U	10.83	11.61	2.49	18.97	5.45	30
Zn	29.43	15.95	8.30	145.80	36.67	3000

Table 3. EC (µmhos/cm) and trace element (ppb) of studied groundwater samples

Parameters	Sample No.												
	1M	2M	3M	4M	5M	6M	7M	8M	9M	10M	11M	12M	13M
EC	2922	2116	1310	1814	2721	1612	1814	2015	3829	1612	1008	1310	1914
Al	50.93	36.35	48.22	33.96	60.89	271.5	35	40.04	44.54	41.57	95.99	29.61	26.35
As	0.336	0.382	0.18	0.721	0.043	0.496	0.168	0.256	0.28	0.15	0.45	0.313	0.165
B	418.20	720.50	302.50	365.70	670.40	516.90	359.20	733.30	1314	616.70	278.50	344	358.90
Ba	14.40	14.73	37.00	24.35	108.50	29.27	16.60	17.76	12.08	29.4	58.48	31.40	22.62
Cd	0.049	0.048	0.076	0.117	0.081	0.081	0.007	0.044	0.037	0.065	0.069	0.012	0.016
Cr	5.927	5.275	3.072	2.812	3.722	7.296	3.084	3.119	5.865	10.66	4.902	2.857	8.016
Cu	7.676	7.499	9.559	8.551	9.514	9.27	7.853	8.706	8.949	9.181	10.5	16.49	7.856
Fe	44.24	115.6	44.29	26.85	1109	341.8	34.91	42.66	69.22	48.01	101.5	30.11	20.36
Mn	0.994	227	22.06	131.2	971.8	7.1	13.33	6.981	61.66	10.7	3.561	9.211	6.544
Mo	5.723	10.87	5.338	2.484	2.179	3.314	10.14	5.265	6.847	5.216	1.974	4.91	1.82
Ni	2.925	6.115	2.627	2.906	12.72	3.528	2.362	6.604	2.772	2.647	2.911	0.925	1.92
Pb	0.421	0.361	0.707	1.005	0.92	0.78	0.374	0.483	0.654	1.004	1.659	0.429	0.326
Sb	0.131	0.098	0.144	0.142	0.171	0.104	0.115	0.083	0.123	0.077	0.088	0.089	0.081
Se	1.580	0.190	0.469	0.444	0.176	0.501	0.237	1.022	1.495	0.394	0.35	0.796	0.598
U	9.034	9.301	2.494	5.94	16.83	12.4	11.61	17.46	4.442	15.97	11.83	4.505	18.97
Zn	8.299	145.8	12.04	9.981	43.97	15.83	8.719	13.25	23.08	29.36	19.36	36.98	15.95

3.1 pollution assessment

The computed results for the pollution evaluation indices (Cd, HEI, and NI) are presented in Tables 4 and 5. The study considered the following trace elements (Al, As, B, Ba, Cd, Cr, Cu, Fe, Mn, Mo, Ni, Pb, Sb, Se, U, and Zn). The calculated contamination factor (*Cfi*) values indicate that the analytical values for almost all trace elements are below the maximum permissible concentration (WHO, 2011), except for iron and manganese in a single sample (5M). Thus, considering only analytical values that exceed the maximum permissible limit for the pollution index (Cd) calculation (Backman et al., 1998; Edet & Offiong, 2002), all samples in the current study, except sample 5M, fall within the low contamination field (Cd < 1). Sample 5M, with a Cd value of 4.13, falls within the high contamination field (Cd > 3).

The calculated heavy metal evaluation index (HEI) for

the current study ranges from 1.02 to 7.87 (Table 5). The classification is based on the procedure followed in Bodrud-Doza et al. (2016) and Edet & Offiong (2002)Contamination index (Cd, which divides the Heavy Metal Evaluation Index into three categories: low (HEI < 10), medium (10 < HEI < 20) and high (HEI > 20). All samples of the current study fall under the low HEI category (HEI < 10).

The calculated values of the Nemerow Pollution Index (NI) indicated that the sample 5M was categorized as medium-polluted and the sample 6M was at warming level while the rest of the samples were all at no-pollution level (Table 5). Figure 3 illustrates that the highest value of the Nemerow Pollution Index was observed approximately in the central area of the left bank of Mosul, an old and commercial zone that is also one of the most densely populated areas in the city. This likely reflects the impact of human activities on groundwater contamination

Table 4. Contamination factors of individual components (*Cfi*) and Contamination index (Cd) of the studied samples

Heavy metals	Sample No.												
	1M	2M	3M	4M	5M	6M	7M	8M	9M	10M	11M	12M	13M
	contamination factors of individual components (*Cfi*)												
Al	-0.75	-0.82	-0.76	-0.83	-0.70	0.36	-0.83	-0.80	-0.78	-0.79	-0.52	-0.87	-0.87
As	-0.97	-0.96	-0.98	-0.93	-1.00	-0.95	-0.98	-0.97	-0.97	-0.99	-0.96	-0.98	-0.98
B	-0.83	-0.70	-0.87	-0.85	-0.72	-0.78	-0.85	-0.69	-0.45	-0.74	-0.88	-0.85	-0.85
Ba	-0.98	-0.98	-0.95	-0.97	-0.85	-0.96	-0.98	-0.97	-0.98	-0.96	-0.92	-0.97	-0.97
Cd	-0.98	-0.98	-0.97	-0.96	-0.97	-0.97	-1.00	-0.99	-0.99	-0.98	-0.98	-0.99	-0.99
Cr	-0.88	-0.89	-0.94	-0.94	-0.93	-0.85	-0.94	-0.94	-0.88	-0.79	-0.90	-0.84	-0.84
Cu	-1.00	-1.00	-1.00	-1.00	-1.00	-1.00	-1.00	-1.00	-1.00	-1.00	-0.99	-1.00	-1.00
Fe	-0.85	-0.61	-0.85	-0.91	2.70	0.14	-0.88	-0.86	-0.77	-0.84	-0.66	-0.93	-0.93
Mn	-1.00	-0.43	-0.94	-0.67	1.43	-0.98	-0.97	-0.98	-0.85	-0.97	-0.99	-0.98	-0.98
Mo	-0.92	-0.84	-0.92	-0.96	-0.97	-0.95	-0.86	-0.92	-0.90	-0.93	-0.97	-0.97	-0.97
Ni	-0.96	-0.91	-0.96	-0.96	-0.82	-0.95	-0.97	-0.91	-0.96	-0.96	-0.96	-0.97	-0.97
Pb	-0.96	-0.96	-0.93	-0.90	-0.91	-0.92	-0.96	-0.95	-0.93	-0.90	-0.83	-0.97	-0.97
Sb	-0.99	-1.00	-0.99	-0.99	-0.99	-0.99	-0.99	-1.00	-0.99	-1.00	-1.00	-1.00	-1.00
Se	-0.96	-1.00	-0.99	-0.99	-1.00	-0.99	-0.99	-0.97	-0.96	-0.99	-0.99	-0.99	-0.99
U	-0.70	-0.69	-0.92	-0.80	-0.44	-0.59	-0.61	-0.42	-0.85	-0.47	-0.61	-0.37	-0.37
Zn	-1.00	-0.95	-1.00	-1.00	-0.99	-0.99	-1.00	-1.00	-0.99	-0.99	-0.99	-0.99	-0.99
Cd	< 1	< 1	< 1	< 1	4.13	0.50	< 1	< 1	< 1	< 1	< 1	< 1	< 1

Table 5. Single pollution weight (*Ci* / *Si*), Nemerow Pollution Index(NI) and Heavy metal evaluation index (HEI) of the studied samples

Heavy metals	Sample No.												
	1M	2M	3M	4M	5M	6M	7M	8M	9M	10M	11M	12M	13M
Al	0.255	0.182	0.241	0.170	0.304	1.358	0.175	0.200	0.223	0.208	0.480	0.132	0.132
As	0.034	0.038	0.018	0.072	0.004	0.050	0.017	0.026	0.028	0.015	0.045	0.017	0.017
B	0.174	0.300	0.126	0.152	0.279	0.215	0.150	0.306	0.548	0.257	0.116	0.150	0.150
Ba	0.021	0.021	0.053	0.035	0.155	0.042	0.024	0.025	0.017	0.042	0.084	0.032	0.032
Cd	0.016	0.016	0.025	0.039	0.027	0.027	0.002	0.015	0.012	0.022	0.023	0.005	0.005
Cr	0.119	0.106	0.061	0.056	0.074	0.146	0.062	0.062	0.117	0.213	0.098	0.160	0.160
Cu	0.004	0.004	0.005	0.004	0.005	0.005	0.004	0.004	0.004	0.005	0.005	0.004	0.004
Fe	0.147	0.385	0.148	0.090	3.697	1.139	0.116	0.142	0.231	0.160	0.338	0.068	0.068
Mn	0.002	0.568	0.055	0.328	2.430	0.018	0.033	0.017	0.154	0.027	0.009	0.016	0.016
Mo	0.082	0.155	0.076	0.035	0.031	0.047	0.145	0.075	0.098	0.075	0.028	0.026	0.026
Ni	0.042	0.087	0.038	0.042	0.182	0.050	0.034	0.094	0.040	0.038	0.042	0.027	0.027
Pb	0.042	0.036	0.071	0.101	0.092	0.078	0.037	0.048	0.065	0.100	0.166	0.033	0.033
Sb	0.007	0.005	0.007	0.007	0.009	0.005	0.006	0.004	0.006	0.004	0.004	0.004	0.004
Se	0.040	0.005	0.012	0.011	0.004	0.013	0.006	0.026	0.037	0.010	0.009	0.015	0.015
U	0.301	0.310	0.083	0.198	0.561	0.413	0.387	0.582	0.148	0.532	0.394	0.632	0.632
Zn	0.003	0.049	0.004	0.003	0.015	0.005	0.003	0.004	0.008	0.010	0.006	0.005	0.005
HEI	1.287	2.266	1.023	1.343	7.869	3.611	1.200	1.632	1.737	1.717	1.848	1.327	1.327
NI	0.22	0.41	0.18	0.24	2.64	0.97	0.28	0.42	0.39	0.38	0.35	0.11	0.45

3.2 Statistical analysis and trace element sources

3.2.1 Factor analysis

Factor analysis was performed on the trace elements data using the principal component analysis approach and based on the normalized varimax rotated matrix. The analysis revealed six major factors with eigenvalues >1 influencing the trace elements concentration as shown by the scree plot (Figure 4). These factors together constitute more than 88% of the variance (Table 6).

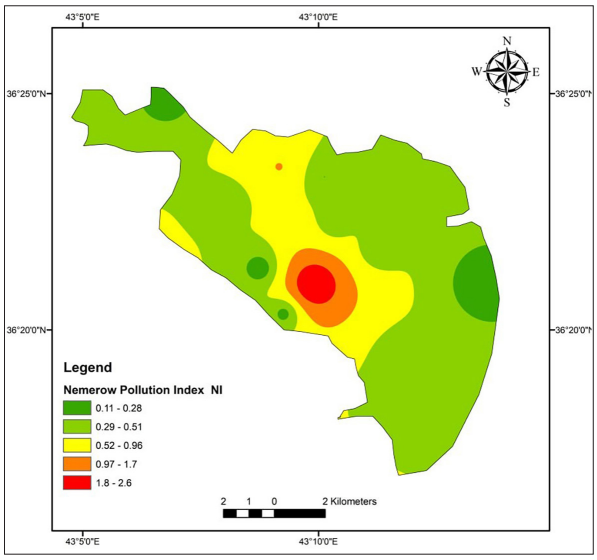

Figure 3. Spatial Distribution of the Nemerow Pollution Index in Groundwater on the Left Bank of Mosul

The first factor accounts for 28.5% of the total variance represented by the positive loadings of Fe, Mn, Co, Ni, Ba, Sn, Zn, and Sb. This factor is naturally related to redox processes that control Fe and Mn phases in the groundwater (Brown et al., 1999; Suada Luzati et al., 2016). It suggests that Fe and Mn oxy-hydroxides regulate the concentration of Co, Ni, Ba, Sn, Zn, and Sb, as these colloids can reduce the dissolved concentrations of heavy metals by adsorption (Mary Ugwu & Anthony Igbokwe, 2019; Wołowiec et al., 2019). With 19.4% of the total variance, the second factor high loaded with Br, B, Li, Se, and EC. The variables loaded on this factor suggest a geogenic source, particularly evaporite rocks commonly found in the study area (Khattab et al., 2023). This is further supported by the fact that the elements with the highest loadings on this factor are highly soluble in water (Kabata-Pendias & Pendias, 2001), along with the positive loading of electrical conductivity (EC) on this factor. The third and fifth factors, which account for 17.7% and 7.8% of the total variance, respectively, show positive loadings on elements such as Cr, Si, U, Al, Ti, V, and Y. These factors also indicate a geogenic origin. However, unlike the elements loaded on the second factor, the elements associated with the third and fifth factors are among the least soluble. Their source is silicate minerals found in sand and sandstone (Kabata-Pendias & Pendias, 2001; Mahmood, 2021). The fourth and sixth factors account for 10.3% and 5% of the variance, respectively, and are represented by the positive loading of the following elements (Cd, Pb, and As on the fourth factor and Cu, Zn on the sixth factor). The trace elements loaded ontp the last two factors are typically influenced by both natural and anthropogenic sources from groundwater of urban areas (Huang et al., 2020; Mohammed et al., 2024; Ou et al., 2024; Rivera-Rivera et al., 2020; Souza et al., 2016). These two factors are therefore likely to reflect the combined effect of natural and anthropogenic sources within the city on the concentrations of these elements, particularly since they are widely used in the various fields of industry, agriculture, and transport. Given Mosul's history as a conflict zone, it is plausible that military activities, including the use of explosives and ammunition during the conflict with ISIS, could have contributed to the contamination of groundwater. Elements such as lead, cadmium, and copper, potentially from explosive residues or the destruction of infrastructure, might have leached into the environment (Hantoush & Hassen, 2023). While the statistical results point to a combination of natural and anthropogenic sources, the potential impact of military operations remains an important consideration when interpreting these findings.

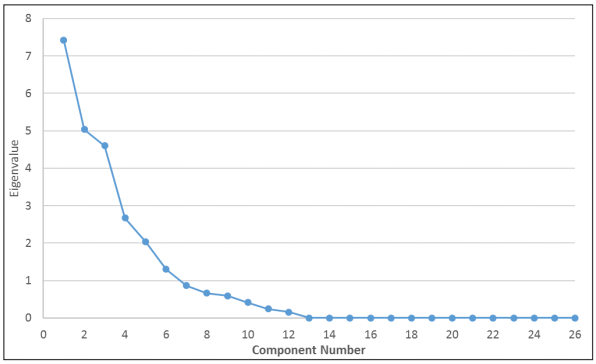

Figure 4. Scree plot showing that the data has six major factors with eigenvalues>1

3.2.2 Cluster analysis

The Hierarchical Cluster Analysis (HCA) results were presented as a dendrogram (Figure 5), revealing four distinct groups. Variables within a given group (cluster) are likely to be derived from the same source, exhibit a similar geochemical behavior, or are influenced by particular factors unrelated to the element's geochemical behavior (Chen et al., 2007b; Danielsson et al., 1999; Dhannoun & Mahmood, 2019)

The HCA results broadly match the FA results, as the clustering of trace elements in the four groups is largely compatible with the factor analysis findings, as seen below:

Cluster 1 consists of Fe, Mn, Co, Ni, Ba, Sn, and Sb. It appears that the elements of this group were aggregated in the same group by the impact of the natural factor represented by the Redox reactions and their effect on the iron and manganese phases and the rest of the group elements. It suggests that Fe and Mn oxy-hydroxides regulate the concentrations of Co, Ni, Ba, Sn, and Sb, as these colloids can reduce the dissolved concentrations of heavy metals through adsorption (Mary Ugwu & Anthony Igbokwe, 2019; Wołowiec et al., 2019).

Cluster 2 consists of B, Br, Li, Se, Mo, Sr, and EC. This cluster contains a group of trace elements that are distinguished by a high ability to move in dissolved form in the aquatic environment, as evidenced by the presence of EC in this group. Such elements are usually present at substantial concentrations in evaporites and carbonate rocks that are highly abundant in the study area (Kabata-Pendias and Pendias, 2001; Khattab et al., 2023).

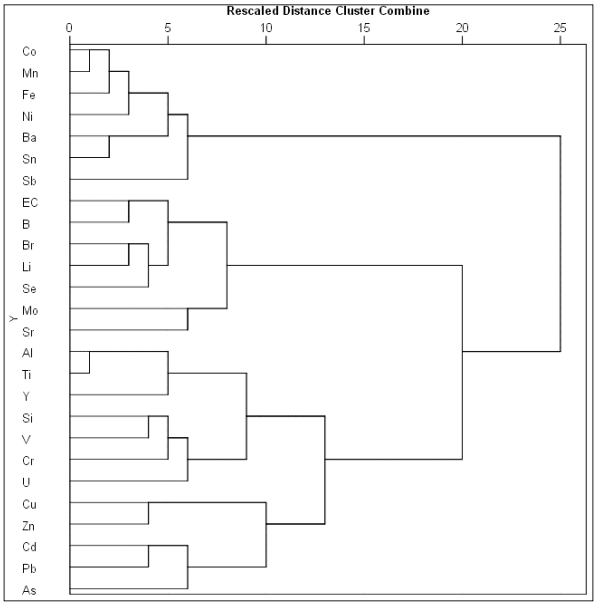

Figure 5. Dendrogram using ward's linkage showing results of hierarchical clustering

Cluster 3 consists of Al, Ti, Y, Si, V, Cr, and U. It seems that the grouping of the elements in this group is the consequence of the influence of similar geochemical behavior and common sources. this group includes several lithophilic trace elements, which are characterized by low mobility in the aquatic environment (White, 2013). These elements are found in igneous and metamorphic silicate minerals such as feldspar, mica, and amphiboles, which are commonly present in sand and sandstone in the study area (Mahmood, 2021).

Cluster 4 consists of Cu, Zn, Cd, Pb, and As. These heavy metals are commonly associated with urban and agricultural activities and often originate from both geogenic and anthropogenic sources (Boateng et al., 2015, 2019; Galitskaya et al., 2017; Leung & Jiao, 2006). The clustering of these elements suggests that contamination from various anthropogenic activities, including urban waste, emissions from auto repair workshops and power generators, and the use of fertilizers and pesticides in agricultural practices, alongside the impacts of military operations during the city›s liberation from terrorist groups, contribute to the observed concentrations in the studied groundwater.

Table 6. Varimax rotated principal component analysis for the groundwater samples

Variables	PC1	PC2	PC3	PC4	PC5	PC6	Communalities
EC	0.269	0.856	-0.193	-0.167	-0.100	-0.237	0.926
Al	0.088	-0.019	0.956	0.190	0.049	-0.041	0.965
As	-0.417	-0.070	0.308	0.521	-0.357	-0.215	0.728
B	0.200	0.855	-0.007	-0.119	0.052	-0.079	0.818
Ba	0.853	-0.235	0.002	0.294	0.027	0.307	0.975
Br	-0.208	0.937	0.112	-0.038	-0.012	-0.023	0.935
Cd	0.305	-0.100	0.180	0.800	-0.212	-0.302	0.921
Co	0.980	0.018	-0.109	0.056	-0.102	0.036	0.987
Cr	-0.128	0.181	0.151	0.106	0.773	-0.062	0.689
Cu	-0.087	-0.163	0.056	0.012	-0.280	0.924	0.984
Fe	0.974	0.016	0.164	0.047	-0.020	0.079	0.937
Li	-0.010	0.796	0.263	-0.340	0.335	0.056	0.981
Mn	0.969	0.000	-0.156	0.026	-0.107	-0.006	0.711
Mo	-0.208	0.085	-0.054	-0.701	-0.199	-0.325	0.895
Ni	0.908	0.082	-0.023	-0.019	0.018	-0.181	0.798
Pb	0.191	-0.147	0.183	0.804	0.154	0.174	0.844
Sb	0.593	0.111	-0.127	0.169	-0.627	-0.239	0.808
Se	-0.386	0.785	-0.080	-0.018	-0.131	0.090	0.960
Si	-0.379	-0.025	0.453	0.122	0.688	-0.341	0.923
Sn	0.882	-0.052	0.184	0.304	0.063	0.108	0.831
Sr	0.055	0.489	-0.132	-0.662	0.206	0.289	0.944
Ti	-0.028	-0.007	0.959	0.121	0.083	-0.042	0.829
U	0.356	-0.086	0.050	-0.121	0.822	-0.110	0.943
V	-0.301	-0.068	0.776	0.105	0.427	0.209	0.963
Y	0.423	0.524	0.694	0.132	0.105	-0.016	0.832
Zn	0.602	0.085	-0.092	0.018	0.116	0.723	
Eigen values	7.418	5.035	4.602	2.67	2.03	1.298	
Variance(%)	28.531	19.366	17.702	10.268	7.808	4.994	
Cumulative(%)	28.531	47.896	65.598	75.866	83.674	88.667	

4. Conclusions

Groundwater was analyzed and assessed in terms of trace element content and heavy metal pollution status in the left bank of Mosul city. Of all the trace elements analyzed and evaluated, Fe, Mn, and Al had a concentration above the acceptable limits at two locations for Fe and one of the two locations for each of Mn and Al. The results of the pollution indices showed that the groundwater under investigation, excluding one sample (M5), is not polluted by heavy elements. For the M5 sample, the findings of the pollution indices varied as they were highly polluted, non-polluting, and moderately polluted according to the Contamination index, Heavy metal evaluation index and Nemerow Pollution Index, respectively. Among the three indices used, the Nemerow Pollution Index was the most sensitive and representative of the water quality status in the current study, as its findings were in complete agreement with any exceedance of WHO guideline values.

Statistical techniques (factor analysis and cluster analysis) have shown that the main source of trace elements originates from geogenic sources, with a secondary influence of the city activities on the concentrations of certain heavy elements represented by copper, zinc, cadmium, lead and arsenic. After it became obvious that there is evidence of the city›s influence on the concentrations of certain heavy metals in groundwater, it is advised that both residents and the government take preventive measures to reduce heavy metal emissions and their impact on the urban environment, as well as an urbanization plan.

Declarations

• The authors declare that no funds, grants, or other support were received during the preparation of this manuscript.

• The authors have no relevant financial or non-financial interests to disclose.

• Both authors contributed to the conception, design, and writing of the manuscript. Both authors read and approved the final manuscript.

• This research includes water hydrochemistry analysis. This study does not include any animal experiments or analyses.

• The data used in this research are data analyzed by the authors, and they have the full right to publish.

References

Adamo, N., Al-Ansari, N., Sissakian, V. K., Laue, J., & Knutsson, S. (2018). The Future of the Tigris and Euphrates Water Resources in view of Climate Change. Journal of Earth Sciences and Geotechnical Engineering, 8(3), 1792–9660.

Al-Ansari, N., Adamo, N., Sissakian, V., Knutsson, S., & Laue, J. (2018). Geopolitics of the Tigris and Euphrates Basins : Geopolitics of the Tigris and Euphrates Basins. Journal of Earth Sciences and Geotechnical Engineering, 8(3), 187–222. http://urn.kb.se/resolve?urn=urn:nbn:se:ltu:diva-68451

Al-Jiburi, H. K., & Al-Basrawi, N. H. (2015). Hydrogeological Map of Iraq, Scale 1: 1000 000, 2nd Edition, 2013. Iraqi Bulletin of Geology and Mining, 11(1), 17 − 26.

Al-Naqib, S. ., Al-Youzbakey, K. T., & Suleman, A. M. (2018). Hydrochemistry and groundwater level fluctuations (2009-2011) in selected wells at the Eastrern part of Mosul City, Northern Iraq. The 9th Periodical Scientific Conference, 19–34.

Al-Nuaimi, H. J., & Al-Sayegh, A.-H. Y. (2004). The Use of Chemostratigraphy in Determining The Boundary Between Al-Fat`ha Fn. (Middle Miocene) and Injana Fn. Iraqi National Journal of Earth Science, 4(1), 1.0-14.0. https://doi.org/10.33899/EARTH.2004.37772

Alaarajy, G. G., Mahmood, H. J., & Abdulqader, O. N. (2023). Groundwater Hydrochemistry and Aquifer Identification at Wana Area, Northwest of Mosul, Iraq. Iraqi Geological Journal, 56(2), 85–101. https://doi.org/10.46717/igj.56.2A.7ms-2023-7-16

Alobaidy, A. H. M. J., Abid, H. S., & Maulood, B. K. (2010). Application of Water Quality Index for Assessment of Dokan Lake Ecosystem, Kurdistan Region, Iraq. Journal of Water Resource and Protection, 02(09), 792–798. https://doi.org/10.4236/jwarp.2010.29093

AtlasWorld. (2019). Where Is Mosul, Iraq?

Backman, B., Bodiš, D., Lahermo, P., Rapant, S., & Tarvainen, T. (1998). Application of a groundwater contamination index in Finland and Slovakia. Environmental Geology, 36(1–2), 55–64. https://doi.org/10.1007/s002540050320

Belkhiri, L., Tiri, A., & Mouni, L. (2018). Assessment of Heavy Metals Contamination in Groundwater: A Case Study of the South of Setif Area, East Algeria. Achievements and Challenges of Integrated River Basin Management. https://doi.org/10.5772/intechopen.75734

Bhuiyan, M. A. H., Islam, M. A., Dampare, S. B., Parvez, L., & Suzuki, S. (2010). Evaluation of hazardous metal pollution in irrigation and drinking water systems in the vicinity of a coal mine area of northwestern Bangladesh. Journal of Hazardous Materials, 179(1–3), 1065–1077. https://doi.org/10.1016/j.jhazmat.2010.03.114

Boateng, T. K., Opoku, F., Acquaah, S. O., & Akoto, O. (2015). Pollution evaluation, sources and risk assessment of heavy metals in hand-dug wells from Ejisu-Juaben Municipality, Ghana. Environmental Systems Research. https://doi.org/10.1186/s40068-015-0045-y

Boateng, T. K., Opoku, F., & Akoto, O. (2019). Heavy metal contamination assessment of groundwater quality: a case study of Oti landfill site, Kumasi. Applied Water Science. https://doi.org/10.1007/s13201-019-0915-y

Bodrud-Doza, M., Islam, A. R. M. T., Ahmed, F., Das, S., Saha, N., & Rahman, M. S. (2016). Characterization of groundwater quality using water evaluation indices, multivariate statistics and geostatistics in central Bangladesh. Water Science, 30(1), 19–40. https://doi.org/10.1016/j.wsj.2016.05.001

Brown, C. J., Coates, J. D., & Schoonen, M. A. A. (1999). Localized sulfate-reducing zones in a coastal plain aquifer. Ground Water. https://doi.org/10.1111/j.1745-6584.1999.tb01136.x

Chen, K., Jiao, J. J., Huang, J., & Huang, R. (2007a). Multivariate statistical evaluation of trace elements in groundwater in a coastal area in Shenzhen, China. Environmental Pollution, 147(3), 771–780. https://doi.org/10.1016/j.envpol.2006.09.002

Chen, K., Jiao, J. J., Huang, J., & Huang, R. (2007b). Multivariate statistical evaluation of trace elements in groundwater in a Multivariate statistical evaluation of trace elements in groundwater in a coastal area in Shenzhen , China. Environmental Pollution, 147, 771–780. https://doi.org/10.1016/j.envpol.2006.09.002

Danielsson, Å., Cato, I., Carman, R., & Rahm, L. (1999). Spatial clustering of metals in the sediments of the Skagerrak/Kattegat. Applied Geochemistry, 14(6), 689–706. https://doi.org/10.1016/S0883-2927(99)00003-7

Dhannoun, H. Y., & Mahmood, H. J. (2019). The Use of Factor Analysis in Defining Factors Responsible for the Variation of

the Concentrations of Dissolved Major Ions in Tigris River Water from Fishkabur to Baghdad. Iraqi National Journal of Earth Sciences, 19(1), 1–18.

Dmitrijeva, M., Cook, N. J., Ehrig, K., Ciobanu, C. L., Metcalfe, A. V., Kamenetsky, M., Kamenetsky, V. S., & Gilbert, S. (2020). Multivariate statistical analysis of trace elements in pyrite: Prediction, bias and artefacts in defining mineral signatures. Minerals, 10(1). https://doi.org/10.3390/min10010061

Edet, A. E., & Offiong, O. E. (2002). Evaluation of water quality pollution indices for heavy metal contamination monitoring. A study case from Akpabuyo-Odukpani area, Lower Cross River Basin (southeastern Nigeria). GeoJournal. https://doi.org/10.1023/B:GEJO.0000007250.92458.de

Galitskaya, I. V., Mohan, K. R., Krishna, A. K., Batrak, G. I., Eremina, O. N., Putilina, V. S., & Yuganova, T. I. (2017). Assessment of soil and Groundwater Contamination by Heavy Metals and Metalloids in Russian and Indian Megacities. Procedia Earth and Planetary Science. https://doi.org/10.1016/j.proeps.2016.12.180

Hantoush, R. A. K. A., & Hassen, P. D. S. I. Al. (2023). An Environmental Study of Heavy Metals selected from Soils contaminated by Mines & Remnants of War in Basrah Governorate. Basra Studies Journal, 1607–634. https://bsj.uobasrah.edu.iq/index.php/bsj/article/view/182

Huang, L., Rad, S., Xu, L., Gui, L., Song, X., Li, Y., Wu, Z., & Chen, Z. (2020). Heavy metals distribution, sources, and ecological risk assessment in Huixian Wetland, South China. Water (Switzerland). https://doi.org/10.3390/w12020431

Jones, C., Sultan, M., Yan, E., Milewski, A., Hussein, M., Al-Dousari, A., Al-Kaisy, S., & Becker, R. (2008). Hydrologic impacts of engineering projects on the Tigris-Euphrates system and its marshlands. Journal of Hydrology, 353(1–2), 59–75. https://doi.org/10.1016/j.jhydrol.2008.01.029

Kabata-Pendias, A., & Pendias, H. (2001). Trace Elements in Soils and Plants, Third Edition (Vol. 3nd, Issue 2). http://www.scopus.com/inward/record.url?eid=2-s2.0-2942666004&partnerID=tZOtx3y1

Khattab, Mohammed F. Mahmood, H. J., & Al-Sarraj, E. S. (2023). Spatial Modeling of Groundwater Quality Parameters on Mosul's Left Bank. The Iraqi Geological Journal, 56(1), 58–66. https://doi.org/10.46717/IGJ.56.1D.5MS-2023-4-14

Khattab, M. F. O., Al-Sarraj, E. S., Mahmood, H. J., & Wiche, O. (2021). Water Quality Investigation of Recent Wells Which Were Randomly Dug at the Left Side of Mosul City. Advances in Science, Technology and Innovation, 297–306. https://doi.org/10.1007/978-3-030-67028-3_25

Lead IG. (2017). Operation Inherent Resolve. In Report to the U.S. Congress.

Leung, C. M., & Jiao, J. J. (2006). Heavy metal and trace element distributions in groundwater in natural slopes and highly urbanized spaces in Mid-Levels area, Hong Kong. Water Research. https://doi.org/10.1016/j.watres.2005.12.016

Li, S., & Zhang, Q. (2010). Spatial characterization of dissolved trace elements and heavy metals in the upper Han River (China) using multivariate statistical techniques. Journal of Hazardous Materials. https://doi.org/10.1016/j.jhazmat.2009.11.069

Liu, W. X., Li, X. D., Shen, Z. G., Wang, D. C., Wai, O. W. H., & Li, Y. S. (2003). Multivariate statistical study of heavy metal enrichment in sediments of the Pearl River Estuary. Environmental Pollution. https://doi.org/10.1016/S0269-7491(02)00234-8

M. J. Trondalen. (2009). Climate Changes, Water Security and Possible Remedies for the Middle East. Scientific Paper from Potential Conflict to Co-Operation Potential (UNESCO-PCCP).

Mahder-Bashi, T. D., & Khattab, M. F. O. (2009). The Use of Hydrograph Analysis to Evaluate the Groundwater Contribution to Tigris River Flow at Mosul City. Iraqi Journal of Earth Sciences, 9(1), 73– 84.

Mahmood, H. J. (2021). The influential factors on the geochemistry of chemical elements in recent sediments of the Tigris River, Iraq. Research Journal of Chemistry and Environment, 25(5), 151–159.

Mary Ugwu, I., & Anthony Igbokwe, O. (2019). Sorption of Heavy Metals on Clay Minerals and Oxides: A Review. In Advanced Sorption Process Applications. https://doi.org/10.5772/intechopen.80989

Mohammed, A. A., Falih, A. H., Al-Paruany, K., Al Maliki, A., & Jasim, A. A. (2024). Study of the Water Quality in the Tigris River Using Isotopic and Hydrochemical Techniques in South-Eastern Iraq. Jordan Journal of Earth and Environmental Sciences.

Ou, L., Jiang, C., Li, Y., Zuo, Y., Huang, K., Liu, P., & Tang, J. (2024). Spatial characteristics and driving factors of groundwater hydrochemistry and heavy metals in peri-urban agricultural areas of in Southwest China. Environmental Earth Sciences, 83(10), 1–12. https://doi.org/10.1007/S12665-024-11646-7/METRICS

Prasad Ahirvar, B., Das, P., Srivastava, V., & Kumar, M. (2023). Perspectives of heavy metal pollution indices for soil, sediment, and water pollution evaluation: An insight. Total Environment Research Themes, 6, 100039. https://doi.org/10.1016/J.TOTERT.2023.100039

Rahi, K. A., & Halihan, T. (2010). Changes in the salinity of the Euphrates River system in Iraq. Regional Environmental Change, 10(1), 27–35. https://doi.org/10.1007/s10113-009-0083-y

Rivera-Rivera, D. M., Escobedo-Urías, D. C., Jonathan, M. P., Sujitha, S. B., & Chidambaram, S. (2020). Evidence of natural and anthropogenic impacts on rainwater trace metal geochemistry in central Mexico: A statistical approach. Water (Switzerland). https://doi.org/10.3390/w12010192

Singh Brraich, O., & Jangu, S. (2015). Evaluation of water quality pollution indices for heavy metal contamination monitoring in the water of Harike Wetland (Ramsar Site), India. International Journal of Scientific and Research Publications, 5(2), 1–4. www.ijsrp.org

Sissakian, V. K., Hagopian, D. H., & Hasan, E. A. (1995). The geology of Al-Mosul quadrangle sheet NJ-38-3 (GM 4) scale 1:250 000.

Smith, M., Cross, K., Paden, M., & Laban, P. (2016). Spring - Managing groundwater. In Icun.

Souza, A. M., Salviano, A. M., Melo, J. F. B., Felix, W. P., Belém, C. S., & Ramos, P. N. (2016). Seasonal study of concentration of heavy metals in waters from lower São Francisco River basin, Brazil. Brazilian Journal of Biology. https://doi.org/10.1590/1519-6984.05215

Suada Luzati, Arjan Beqiraj, Enkeleida Beqiraj Goga, & Olgert Jaupaj. (2016). Iron and Manganese in Groundwater of Rrogozhina Aquifer, Western Albania. Journal of Environmental Science and Engineering B. https://doi.org/10.17265/2162-5263/2016.06.002

UN-Habitat. (2016). CITY PROFILE OF MOSUL, IRAQ. Multi-sector assessment of a city under siege.

White, W. M. (2013). Geochemistry (1st ed.). Wiley-Blackwell.

WHO. (2011). Guidelines for Drinking-water Quality World Health Organization, Geneva. In WHO press.

Wołowiec, M., Komorowska-kaufman, M., Pruss, A., Rzepa, G., & Bajda, T. (2019). Removal of Heavy Metals and Metalloids from Water Using Drinking Water Treatment Wołowiec, M.,

Komorowska-Kaufman, M., Pruss, A., Rzepa, G., & Bajda, T. (2019). Minerals, 9(Table 1), 1–17.

Xu, N., Peng, M., Li, Q., & Xu, C. (2020). Towards Consistent Interpretations of Coal Geochemistry Data on Whole-Coal versus Ash Bases through Machine Learning. Minerals, 10(4), 328. https://doi.org/10.3390/min10040328

Zhong, S., Geng, H., Zhang, F., Liu, Z., Wang, T., & Song, B. (2015). Risk Assessment and Prediction of Heavy Metal Pollution in Groundwater and River Sediment: A Case Study of a Typical Agricultural Irrigation Area in Northeast China. International Journal of Analytical Chemistry, 2015. https://doi.org/10.1155/2015/921539

JJEES

JJEES (2026) 17 (1): 26-36
ISSN 1995-6681

Jordan Journal of Earth and Environmental Sciences

Ecological Risks of Toxic Metals in Contaminated Marine Sediments: A Case Study of Elechi Creek, Rivers State

Davies Ibienebo Chris[1, 2], Parashuram Kallem[3], Khang Wen Goh[1,4,5], Fathurrahman Lananan[6], Zulhisyam Abdul Kari[7], Nova Amalia Sakina[8**], Mohamad Nor Azra[9,10], Davies Imachrist Ibienebo[11]

[1]*Department of Fisheries, University of Port Harcourt, Port Harcourt, East-West Road, Choba, Rivers State, P.M.B. 5323, Nigeria; davies.*
[2]*Faculty of Data Science and Information Technology, INTI International University, Nilai, Malaysia; khangwen.*
[3]*Department of Environmental and Public Health, College of Health Sciences, Abu Dhabi University, Abu Dhabi, 59911, United Arab Emirates*
[4]*Faculty of Engineering, Shinawatra University, Samkhok, Pathum Thani, 12160, Thailand*
[5]*Faculty of Mathematics and Natural Sciences, Universitas Negeri Padang, Padang, 25131, Indonesia*
[6]*School of Animal Sciences, Aquatic and Environment, Faculty of Bioresources and Food Industry, Universiti Sultan Zainal Abidin, Besut Campus, 22200 Besut, Terengganu, Malaysia*
[7]*Department of Agricultural Science, Faculty of Agro-Based Industry, Universiti Malaysia Kelantan, 17600 Jeli, Kelantan, Malaysia;*
[8]*School of Environmental Science, Universitas Indonesia, Jakarta 10430, Indonesia*
[9]*Higher Institution Centre of Excellence, Institute of Climate Adaptation and Marine Biotechnology (ICAMB), Universiti Malaysia Terengganu, 21030, Kuala Nerus, Terengganu, Malaysia*
[10]*Research Center for Marine and Land Bioindustry, Earth Sciences and Maritime Organization, National Research and Innovation Agency (BRIN), Lombok 83352, Indonesia*
[11]*Department of Animal and Environmental Biology, Faculty of Science, University of Port Harcourt, P.M.B 5323, Choba, Rivers State, Nigeria*

Received on 16 December 2024; Accepted on 16 July 2025

Abstract

Industrial activities and inadequate waste management in the Niger Delta have led to the accumulation of toxic metals in sediments, posing persistent ecological threats. This study assessed contamination and ecological risks at three sites in the region, focusing on six metals: cadmium (Cd), lead (Pb), zinc (Zn), iron (Fe), arsenic (As), and copper (Cu). Contamination was evaluated using several indices including the Contamination Factors (CF), Pollution Load Index (PLI), Geo-accumulation Index (Igeo), Enrichment Factor (EF), and Contamination Quantification (QoC). Among the sites, Site 3 exhibited the highest contamination levels, particularly for Cd, with a CF of 2.8, a PLI of 1.393, and a QoC of 46.43%. At this site, Cd also showed an Igeo of 0.562, indicating moderate pollution, and an EF of 6.36. At Site 2, Pb and Zn exhibited lower contamination levels, with CF values of 0.01476 and 0.01269, respectively, and a QoC of 35.48%. The Cd posed the most significant ecological risk at Site 3, with a potential Ecological Risk Index (PERI) of 16.18. These findings highlight industrial discharges as a major source of contamination. Immediate pollution control measures and improved waste management practices are essential to protect the sediment quality and maintain ecosystem health of the Niger Delta.

Keywords: *Metal contamination, Niger Delta, Sediment, Ecological risk, Pollution*

1. Introduction

Anthropogenic marine pollution and toxic metal poisoning have become major global environmental problems that continue to endanger ecosystems and public health. The persistence of these pollutants in the environment, their bioaccumulation in organisms, and their amplification through the food chain ultimately cause harmful effects across ecological and human systems, making them especially problematic (Sonone et al., 2020). These problems are exacerbated in coastal areas such as Nigeria's Niger Delta by heavy industry, poor waste disposal, and rapid urbanization, all of which increase the levels of Potentially Toxic Elements (PTEs) in sediments. In addition to disrupting the equilibrium of aquatic ecosystems, these hazardous metals pose serious risks to local populations, especially in areas with high pollution levels (Reckermann et al., 2022; Chris et al., 2024b). The results of this study align with those of related investigations conducted in the Niger Delta and other developed areas. Research in the Niger Delta has consistently shown that heavy metals, including Zn, Cd, and As, can persist and accumulate in aquatic systems, posing serious threats to the environment and human health (Chris et al., 2023a).

Furthermore, similar results have been found in research carried out in nations other than Nigeria, like China and India, indicating that industrial activities have elevated heavy metal in sediments, increasing the risk of cancer for the local population. These similarities show how widespread heavy metal contamination is, and they emphasize the need for concerted international action to combat it. The Hazard Index (HI) and Carcinogenic Risk Assessments (CRA) show that Elechi Creek's existing metal pollution levels, especially at Site 3, represent serious health hazards. The increased risks, linked to both non-cancerous and cancerous results, demand quick action to lessen these risks.

* Corresponding author e-mail: nova.amalia01@ui.ac.id; novaamaliasakina@gmail.com

Elechi Creek, situated in Rivers State, Nigeria, is a prime example of a region where toxic metal contamination and anthropogenic marine pollution present formidable environmental challenges. Fish and other aquatic life that are crucial to the local economy and way of life depend on the creek, a vital waterway that supports many biological processes and provide local inhabitants with the necessary supplies. However, the increasing industrial discharges and human encroachments into the creek have resulted in increased concentrations of metals in its sediments, raising significant concerns about the long-term ecological and health effects of these contaminants are in progress (Chris et al., 2024a; Seiyaboh and Izah, 2017).

Toxic metals are frequently associated with industrial and anthropogenic activities. For example, a study conducted by Sakina and et al. (2023) in Indonesia, stated that heavy metals are found in hospital wastewater, such as Cr (10 µg/L), Pb (9 µg/L), and Cd (0.8 µg/L). A study by Quist et al. (2022) found that there is an exposure of Mn, a predominantly heavy metals related to oil drilling site, in 29 pregnant women who live near the hydraulic fracturing. A study, conducted in Balqa, Jordan, found that Cr (CF= 11.82) and Ni (CF = 11.59) were the predominant contaminants in the soil (Tarawneh et al. 2021). Although these metals naturally occur in the environment, human activity may greatly increase their concentrations, resulting in pollution that seriously affects human health and aquatic environments. For example, the lead in human blood can increase the risk of blood pressure which is an increase in diastolic (0.013 mmHg) and systolic blood pressure (0.014 mmHg) with 1 µg/dL increase in blood lead levels (Bayat et al., 2016). Sakina (2021) stated that the blood lead levels in pregnant woman are 9 times higher (46.24 µg/L) than the threshold value (5 µg/L). In marine ecosystems, the heavy metals are accumulated in sediments and can lead to bioaccumulation in aquatic organisms, which, in turn, can be biomagnified through the food chain, disrupting ecological balance and causing harmful hazards to people and species eating polluted seafood (Vareda et al., 2019; Chris et al., 2023a; Ekperusi and Asiwa, 2024). For example, a study conducted in the Xiangshan Bay found that As found in seasnail, bivalve, oyster, crab, shrimp and other fish which exceeds the target hazard quotient (Liu et al., 2019). In Europe, Cd was found generally high in squid with close to the maximum residue level. Not only Cd, Hg is also found in tuna and mackerel.

The toxic effects of these metals include disruptions to reproductive and developmental processes, immune system impairments, and increased mortality rates in affected populations. Moreover, the persistence of these metals in the environment means that their impacts can be felt long after the initial contamination event, making them particularly insidious pollutants (Afzaal et al., 2022). Therefore, the evaluation of the potential negative consequences of toxic metal pollution on the environment depends critically on ecological risk assessments, which also consider their toxicity, bioavailability, and potential bioaccumulation. Understanding the severity of toxic metal contamination and anthropogenic marine pollution in Elechi Creek are particularly important, given the region's history of industrial activity and environmental degradation. The Niger Delta, where Elechi Creek is located, has long been recognized as a pollution hotspot, with numerous studies documenting the high levels of toxic metals and other contaminants in the region's water bodies (Kpee et al., 2014; Oritsemuelebi et al., 2021). These studies highlight the urgent need for comprehensive environmental assessments in key areas like Elechi Creek, where industrial activities and human encroachment continue to pose significant threats to the ecological health of the waterway. This study systematically evaluates the ecological risks posed by toxic metals in Elechi Creek's marine sediments, employing geochemical analysis and pollution indices to quantify their spatial distribution and threat to benthic ecosystems. The results identify severe contamination hotspots for metals, like Pb, Cd, Cu, Zn, As, and Fe, linked to anthropogenic sources, such as industrial effluents and urban runoff. The risk assessment underscores their potential to disrupt aquatic food webs, through bioaccumulation in benthic organisms and endanger human populations reliant on the creek for fisheries and water resources.

Given the global nature of toxic metal contamination and the specific challenges faced by regions like the Niger Delta, this study also aims to contribute to the broader understanding of how industrial and urban activities affect aquatic environments. The results from Elechi Creek can be compared with similar studies in other regions, providing a basis for developing more effective environmental policies and remediation strategies. In doing so, this research not only addresses local environmental issues in Rivers State but also contributes to the global discourse on managing and mitigating the impacts of toxic metal pollution on the marine coast.

The contamination of Elechi Creek with toxic metals from anthropogenic activities poses a significant environmental health challenge. This study's focus on sediment analysis and ecological risk assessment offers a comprehensive approach to understanding the scale and impact of this contamination. By highlighting the need for ongoing monitoring, stronger environmental regulations, and targeted public health interventions, this research underscores the importance of integrating scientific findings into policy and management practices aimed at preserving the environment and the communities that depend on it.

2. Materials and Methods

2.1 Study Stations

The research focuses on Elechi Creek in Port Harcourt, which contains both freshwater and saltwater due to tidal influences (Figure 1). The creek borders Eagle Island and reaches the Illoabuchi Street Riverbank. The creek's width varies, with some areas wider and others narrower. Station one (N04°47.15' and E006°58.96'), also known as Eagle Island, is a sand-fill area with hanging latrines, sharp sand, and vegetation dominated by Nipa palm and scattered white and red mangroves. Elephant grass surrounds the mangrove vegetation. Station two (N04°47.2' and E006°59.3'), the

Sawmill area, is downstream and features Nipa palm as the main vegetation, along with smaller numbers of white and red mangroves. Elephant grass is also present around the mangrove vegetation. Station three (Appa area, located at latitude N04°47.05' and longitude E006°59.36'), has Nipa palm vegetation with fewer white and red mangroves. Unfortunately, some Nipa palm trees have been cut down, and hanging latrines have been constructed along the waterway (Vincent-Akpu and Babatunde, 2013; Meregini-Ikechukwu et al., 2020).

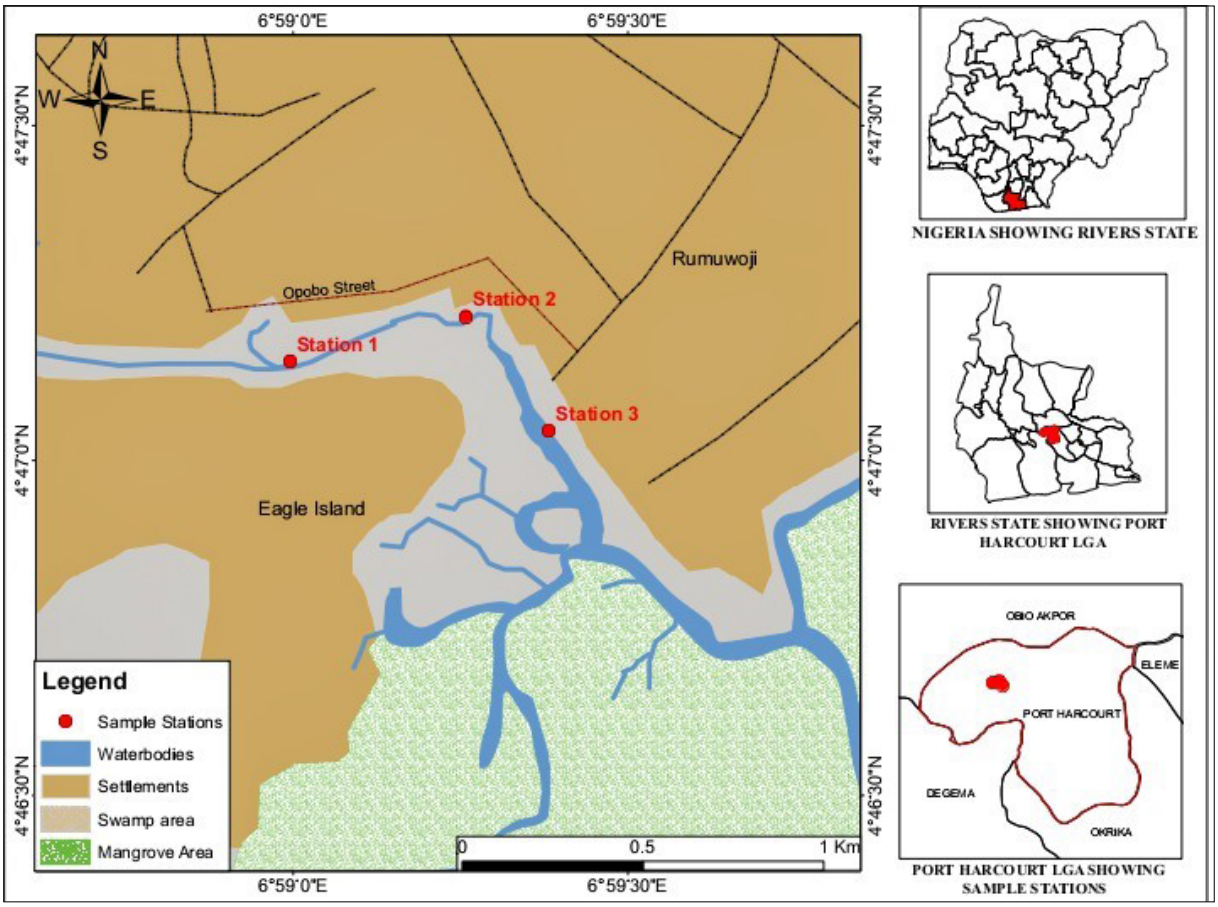

Figure 1. The map of the study area

2.2. Sample collection and preparation

Sediments of approximately 250 g each were collected in triplicate, monthly from three specified sites from January 2023 to July 2023. This sampling was consistently carried out during the first week of each designated month, with sample collection at 3 stations. The selection of the sampling distance from the bank was deliberate, ensuring that the collected sediment samples precisely represented the specific areas within the research site that experienced significant pollution impact. Sediment was collected from three different locations in the creek on a monthly basis for six months, utilizing an 'Ekman grab' sampler. A total of 54 samples, 9 per month and 3 at each station, were collected from the study sites (Moslen et al., 2018). After submersion in 10% nitric acid for 24 hours, the sediments were stored in plastic containers and, subsequently, washed with deionized water. The choice of sampling distance from the bank ensured that the sediment samples accurately represented the observable pollution hotspots within the research area. The frozen samples were then transported to the laboratory, where a UNICAM Solar 969 atomic absorption spectrometer (AAS) with model number API-RP 45 was employed to analyze them (Davies et al., 2024). The samples were maintained at 20°C in the laboratory.

2.3 Quality assurance and control

A calibration curve was generated, using atomic absorption for multiple heavy metals. The reagent blanks were performed after every 10 sample analyses to mitigate the effects of equipment drift. Using the Buck Scientific Model 210 VGP, an atomic absorption spectrophotometer, a range of recovery rates from 82% to 110% was observed for metal amounts in sediment samples.

2.4. Digestion and analysis of the sample

Following accepted procedures, acid digestion was carried out using the technique by Yi et al. (2011) and Chris and Anyanwu (2022), utilizing sediment samples. After four hours at 105°C, the samples were pulverized finely using an agate mortar and pestle. The 0.5 grams of powdered sediment samples were kept in a borosilicate beaker and then mixed with the Aqua regia concoction of HCl and HNO3. After two hours at 80°C, the samples were heated intermittently, adding 1% v/v HNO3 to stop drying. After cooling, the samples were filtered through Whatman 41 filter papers; the final volume was changed to 50 ml. Every stage of preparation used deionized water.

2.5. Analytical method

Sediment samples were analyzed for Pb, Cd, Cu, Zn, As, and Fe using an AAS (GBC Scientific Equipment, Sens AA-Pty Ltd, Australia) fitted with an air- acetylene flame (APHA, 2017). The device was calibrated using AAS standard solutions containing hazardous elements (Pb, Cd, Cu, Zn, As, and Fe) at a concentration of 1,000 mg/L. These solutions were appropriately diluted to generate calibration curves, from which the amounts of the metals were determined. For background reasons, the wavelength calibration was performed using a deuterium lamp. The preparation of standard and blank solutions involved the use of a 1 % (v/v) HNO3 solution. Three distinct concentrations were generated by combining an appropriate volume of a stock standard solution (1,000 mg/L) with a graduated flask of 100.0 mL capacity and subsequently filling it to the brim with deionized water.

2.6. The degree of contamination [Cd]

The degree of contamination (C_d) represents the cumulative effect of several pollutants and serves as an indicator of the environmental hazards related to the presence of multiple toxic metals in sediment. The creation of the afore-mentioned tool was attributed to Hakanson (1980), while its subsequent utilization has been observed in the studies by Guan et al. (2014). Equation 1 presents a mathematical expression. Hakanson (1980) classified C_d as low, moderate, significant, or extremely high (C_d as < 6; 6 ≤ C_d < 12; 12 ≤ C_d < 24 = significant contamination, and C_d ≥ 24), with CF1 denoting the metal contamination factor.

$$C_d = \sum_{i=1}^{n} CF_1 \quad \text{..... (1)}$$

2.7. Contamination Factor (CF)

The concentration factor (CF) is defined by Hakanson (1980), as a ratio of THE metal content to the background value for each metal (Equation 2) where C_{metal} is the sample of mean metal content, while $C_{background}$ is the metal's mean natural value. The study categorizes emtal pollution into four grades: low, moderate, significant, and extremely high (CF > 1, 1 < CF < 3, 3 < CF < 6, CF > 6), using C_{metal} and $C_{background}$ values.

$$CF = \frac{C_{metal}}{C_{background}} \quad \text{..... (2)}$$

2.8. Metals Pollution Load Index (MPLI)

The PLI was assessed using the mathematical expression shown in Equation 3, as suggested by Chris and Anyanwu (2023b).

$$MPLI = (CF1 \times CF2 \times CF3 \ldots \times CFn)\frac{1}{n} \quad \text{..... (3)}$$

The variable n denotes the number of metals under evaluation. In contrast, the contamination factor, denoted as CF, represents the degree of contamination. An MPLI value greater than 1 indicates the presence of pollution, whereas a value less than 1 indicates the absence of pollution (Barakat et al., 2020). While n denotes the numerical value assigned to heavy metals in the specific context.

2.9 Potential Ecological Risk Index (PERI)

Hakanson introduced The Potential Ecological Risk Index (PERI) in 1980, and the Equation 4 is used to calculate it. In this context, n represents the number of heavy metals analyzed, and Er refers to the ecological risk index. According to Mwakisunga et al. (2021), the PERI is used to categorize the level of ecological risk linked to heavy metal contamination. The risk levels are defined as follows: a PERI value below 150 indicates low ecological risk, between 150 and 300 suggests moderate ecological risk, between 300 and 600 signifies high ecological risk, and a PERI value of 600 or more represents significantly high ecological risk. These categories help evaluate the severity of contamination and its potential impact on environmental health and ecosystem stability.

$$PERI = \sum_{i=1}^{N} E_r^i \quad \text{..... (4)}$$

2.10 Geo-accumulation index (Igeo)

The geo-accumulation index is a method for assessing the heavy metal content of sediment by comparing the current levels of contaminants with the historical levels (Qingjie et al., 2008). This approach has been implemented extensively in the evaluation of sediment contamination (Ahirvar et al., 2023; Islam et al., 2014). Müller's (1969) is employed to determine the Igeo (Equation 5).

$$Igeo = log_2 \frac{c_n}{1.5 \times B_n} \quad \text{..... (5)}$$

The average content of toxic metals (C_n) in sediment samples is used to calculate the Igeo, with the reference background value (B_n) provided by Guan et al. (2014). In order to accommodate fluctuations in the baseline value, a 1.5-fold factor is implemented. The Igeo indices are classified into seven categories, as per Abdullah et al. (2020).

2.11 Ecological risk assessment

One or more contaminant or metals polluting the sediment are both evaluated in terms of their potential ecological danger using the risk factors evaluation (Er and PERI). The ecological risk factor (Er) is computed statistically using Equation 6.

$$Er = Tr \times C_f \quad \text{..... (6)}$$

The contamination factor (Cf) is employed in conjunction with the toxic-response factor (Tr) for each metal, including Cd, Pb, Zn, Ni, and Cu, to evaluate ecological risks according to how Mugoša et al. (2016) categorize the ecological risk factor (Er). Er signifies the single index used to quantify the ecological risk factor.

2.12 Enrichment Factor (EF)

The Enrichment Factor (EF) serves as a universal index, providing a straightforward and convenient approach to assessing enrichment and facilitating comparisons of contamination across various environmental media, as outlined by Nowrouzi and Pourkhabbaz (2014). Furthermore, it helps confirm whether heavy metal contamination originates from anthropogenic sources, as suggested by Jahan and Strezov (2018). The calculation for this index is specified in Equation 7.

$$EF = \frac{Cn\,/\,Crefsample}{Bn/Bref} \quad \text{..... (7)}$$

The EF is a measure of metal enrichment in samples, comparing the concentration of the analyzed metal to reference material (Bref) and background levels (B_n). EF

values can be classified into five ranges: less than 2 indicates mineral enrichment, 2 to less than 5 indicates moderate enrichment, 5 to less than 20 signifies significant enrichment, 20 to less than 40 indicates very high enrichment, and greater than 40 indicates extremely high enrichment. Enrichment factors, close to or less than 1, indicate heavy metals from natural sources. In contrast, those factors greater than 1 indicate potential anthropogenic sources.

2.13 Quantification of contamination (QoC)

The Quantification of contamination (QoC) index, a tool used to assess the main sources of metals, was assessed using Equation 8 in a study by Zarei et al. (2014). The mean metal content in sediment samples is *Ci*, with negative values indicating natural sources and positive values indicating anthropogenic sources, as per Guan et al. (2014) and Malvandi (2021).

$$\text{QoC}\ (\%) = \left[\frac{(Ci - Cin)}{Ci}\right] \times 100 \quad \text{..... (8)}$$

2.14 Statistical analysis

The mean and standard deviation of all measured parameters across stations were calculated using descriptive statistics and months to summarize the data. Pearson correlation coefficients were used to assess relationships between the parameters. Furthermore, ANOVA was performed to test for statistical significance in differences between stations and months, applying a 95% confidence level with a significance level at $p < 0.05$.

3. Results and Discussion

In Table 1, the mean concentrations of six toxic metals (Cd, Pb, As, Cu, Zn, and Fe) were measured across three different stations in the surface sediment of Elechi Creek. However, the mean concentrations of toxic metals in surface sediments among the three stations were not significantly different ($p < 0.05$). These values are compared with the World Health Organization (WHO) and the Nigerian Standard for Drinking Water Quality (NSDWQ), which serve as reference points for assessing the severity of sediment contamination. The Cd concentrations at all stations significantly exceed the WHO and NSDWQ guideline values of 0.003 mg/kg, indicating substantial anthropogenic input, likely from industrial discharges and urban runoff. The high toxicity and persistence of Cd in the environment are concerning, as it can bioaccumulate in aquatic organisms, posing long-term health risks to both wildlife and humans (Abugu et al., 2023; Zhang et al., 2024).

Pb concentrations exceeded the WHO and NSDWQ guideline values of 0.01 mg/kg, indicating significant contamination, likely originating from sources such as leaded gasoline, industrial emissions, and improper waste disposal. Similarly, As levels also surpassed the WHO guideline of 0.01 mg/kg, with the highest concentration recorded at Station 3 (0.18 mg/kg) and the lowest at Station 2 (0.16 mg/kg). As is a potent carcinogen, and even at low concentrations, its presence in sediments poses substantial health risks due to potential bioaccumulation within the food chain, thereby necessitating continuous monitoring and possible remediation efforts (Ogbeide and Henry, 2024; Jiang et al., 2023; Okon et al., 2023; Shentu et al., 2023). Cu concentrations are well above the WHO and NSDWQ guideline of 0.02 mg/kg, with the highest levels at Station 2 (0.79 mg/kg) and the lowest at Station 3 (0.74 mg/kg). The variability in Cu levels suggests localized sources of contamination, likely related to industrial and agricultural activities in the region (Bhuyan et al., 2023; Chen et al., 2021).

The Zn level, although below the WHO and NSDWQ guideline of 3 mg/kg, indicates ongoing contamination with the highest concentration at Station 3 (0.83 mg/kg) and the lowest at Station 1 (0.72 mg/kg). High Fe concentrations in these sediments suggest substantial anthropogenic contributions (Ali et al., 2022; Li et al., 2023a; 2023b), likely from industrial discharges, impacting sediment chemistry and nutrient cycling, with potential downstream effects on aquatic life (Chris and Anyanwu, 2023b; Liu et al., 2023).

Table 1. Mean data for toxic metals in surface sediment

Sites	Cd	Pb	As	Cu	Zn	Fe
1	0.24±0.02[a]	0.29±0.01[a]	0.17±0.00[a]	0.78±0.02[a]	0.72±0.14[a]	6.21±0.27[a]
2	0.23±0.02[a]	0.31±0.02[a]	0.16±0.01[a]	0.79±0.03[a]	0.80±0.15[a]	5.75±0.38[a]
3	0.28±0.0[a]	0.29±0.02[a]	0.18±0.00[a]	0.74±0.04[a]	0.83±0.15[a]	6.00±0.24[a]
WHO	0.003	0.01	0.01	0.5	3.0	0.3
NSDWQ	0.003	0.01	0.05	0.02	3	0.3

Mean values with the same alphabet superscript are not significantly different ($p < 0.05$)
Mean values with different alphabet superscripts are significantly different ($p > 0.05$)

These findings in Table 2 align with similar studies in the Niger Delta, where elevated levels of toxic metals, particularly Cd and Pb, have been consistently reported due to industrial activities and oil exploration (Idowu, 2022; Ogbeide and Henry, 2024). Bwatanglang et al. (2021) found that Cd is the most abundant heavy metals in surface soils and sorrel plants, indicating moderate-to-considerable ecological risks ($40 < Er < 86$) in Adamawa State, Nigeria. Studies in industrialized regions, such as China's Yangtze River Delta, show high levels of heavy metals, such as Cd and Pb in sediments (Liu et al., 2023). Elechi Creek's surface sediment shows elevated levels of toxic metal, primarily due to human activities. These high concentrations of Cd, Pb, and As are of concern due to their toxicity and potential bioaccumulation, which could have severe consequences for aquatic ecosystems and human health. If these trends continue unchecked, there is a risk of long-term environmental degradation and public health crises.

The CF values indicate that the highest Cd contamination occurs at Site 3 (2.8), suggesting a relatively higher

anthropogenic impact at this location. Cd also shows the lowest CF at Site 2 (2.3), suggesting slightly less pollution than at other sites. For Pb, the CF values are very low across all sites, with the highest being at Site 2 (0.01476). This finding aligns with a study by Khudhur et al. (2018), which found Pb in soil (CF = 4.79) in the Sahdawa, Shamamal, and Sardasht areas of Erbil City. Zn shows a similar pattern, with the highest CF at Site 3 (0.01269). Fe, which typically indicates natural background levels, shows minimal variation across sites, with the highest value at Site 1 (0.00161). As has the highest CF at Site 3 (0.01385), and Cu is most concentrated at Site 2 (0.03511).

Similar studies in the Niger Delta have shown elevated CF for Cd, especially in areas near industrial activities and oil spill sites (Idowu, 2022). Pb contamination has also been reported, though generally at lower levels, similar to the findings in this study (Shentu et al., 2023). In other industrialized regions, like the Yangtze River in China, have reported comparable CF values for Cd and Pb, indicating similar contamination sources and industrial activities (Liu et al., 2023).

The higher Cd contamination factor at Site 3 suggests that this site is particularly vulnerable to industrial pollution, which could have long-term health implications for local populations. The consistent PLI values across the sites indicate a moderate pollution load, with Site 3 being the most polluted, warranting focused remediation efforts. The PLI is highest at Site 3 (1.393), indicating that this site experiences the most significant overall pollution. The PLI at Site 1 (1.219) and Site 2 (1.222) are lower, suggesting at these sites are less impacted by contamination but are still affected.

Table 2. Contamination Factor and Pollution Load Index

Metal	Studied Sites		
	1	2	3
Cd	2.4	2.3	2.8
Pb	0.01381	0.01476	0.01381
Zn	0.01101	0.01223	0.01269
Fe	0.00161	0.00149	0.00156
As	0.01308	0.01231	0.01385
Cu	0.03467	0.03511	0.03289
PLI	1.219	1.222	1.393

In Table 3, Cd exhibits the highest ecological risk at Site 3, with a value of 8.40. In contrast, the lowest risk is recorded at Site 2, with a value of 6.90. Pb, Zn, Ar, and Cu present their highest ecological risks at Site 2 and Site 3, albeit they appear with relatively minor differences. In Table 3, the PERI reaches its peak at Site 3, registering a value of 16.18, underscoring the heightened potential for ecological harm at this location. This site-specific increase in ecological risk aligns with findings from other studies in the Niger Delta, where industrial activities and oil exploration have significantly contaminated the environment (Iwegbue et al., 2018; Osayande and Nwokedi, 2019).

Similar patterns have been reported in the Niger Delta, where Cd is a significant contributor to ecological risk, particularly in areas impacted by oil spills and industrial discharges (Osayande and Nwokedi, 2019). In heavily industrialized regions such as India, elevated PERI values for Cd and lead are common, mirroring the results observed in this study (Kumar et al., 2020). The elevated PERI at Site 3, with a value of 16.18, indicates that this site is especially vulnerable, potentially leading to adverse effects on local biodiversity. While the consistent toxic response values for other metals suggest some level of ecological risk, Cd remains the most concerning pollutant in this context.

Table 3. Ecological risk factor and Potential Ecological Risk Index (PERI)

Metal	Studied Sites		
	1	2	3
Cd	7.20	6.90	8.40
Pb	1.45	1.55	1.45
Zn	0.72	0.80	0.83
As	1.70	1.60	1.80
Cu	3.90	3.95	3.70
PERI	14.97	14.80	16.18

In Figure 2, the degree of contamination (DC) is an aggregate measure of contamination across all metals. Site 1 has the highest DC (8.41), slightly higher than Site 3 (8.32), and Site 2 shows the lowest DC (8.04). These values indicate that all sites are experiencing a significant contamination, with Site 1 being the most affected. The high DC at these sites reflects the ongoing anthropogenic pressures in the Niger Delta, including oil spills and industrial waste discharge (Katz, 2012).

Site 1 has the highest contamination level (8.41), followed closely by Site 3 (8.32). Site 2 has the lowest DC (8.04), though still indicative of significant contamination. Similar DC values have been reported in studies from other parts of the Niger Delta, especially in areas with high industrial activity and oil exploration (Ugochukwu et al., 2022).

Globally, regions with similar industrial profiles, such as parts of South America, have reported DC values comparable to those observed here, indicating that the contamination levels observed here are not unique to Nigeria (Sangeetha et al., 2021; Romero-Murillo et al., 2023). The high DC values across all sites underscore the need for comprehensive remediation strategies to reduce cumulative contamination. Site 1, particularly high DC, suggests nearby industrial activities may more heavily impact it.

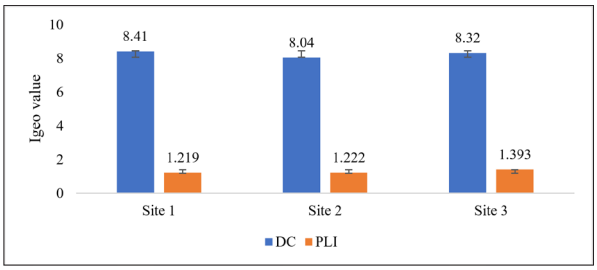

Figure 2. Degree of Contamination (DC)

The Igeo is highest for Cd at Site 3 (0.562), indicating moderate pollution levels. The Igeo values for Cu, Zn, Pb, As, and Fe are very low across the sites, reflecting minimal to no pollution from these metals. These findings align with previous studies in the Niger Delta that have identified Cd as a significant sediment pollutant from industrial and agricultural runoff (Attah et al., 2021). Igeo values for Cd have been reported as moderately high in other studies conducted in the Niger Delta, particularly near oil production sites (Iwegbue et al., 2018). The low Igeo values for other metals align with findings in less impacted areas. In industrial regions, such as southeast asia, similar Igeo trends have been observed, with Cd showing higher Igeo values than other metals, reflecting its widespread use and persistence (Banerjee, 2022).

In Table 4, the moderate Igeo for Cd at Site 3 emphasizes the need for targeted pollution control measures to prevent further environmental degradation. The low Igeo values for other metals suggest that natural background levels are more influential in these cases, reducing the urgency for immediate intervention for these specific contaminants.

Table 4. Geo-accumulation index (Igeo) for the three sites

Metal	Studied Sites		
	1	2	3
Cd	0.482	0.462	0.562
Pb	0.003	0.003	0.003
Zn	0.002	0.002	0.003
Fe	0.000	0.000	0.000
As	0.003	0.002	0.003
Cu	0.007	0.007	0.007

In Table 5, the EF indicates the degree of anthropogenic influence on sediment metal concentrations. Cd shows significant enrichment at Site 3 (6.36), which is categorized as moderate to a considerable enrichment according to Al-Jaberi et al. (2020). The other metals, including Pb, Zn, As, and Cu, exhibit very low EF values across all sites, suggesting that these metals are primarily of natural origin. Similar findings have been reported in studies focusing on areas affected by industrial waste and oil spills, consistent with the elevated Cd enrichment at Site 3 (Nriagu et al., 2016). Low enrichment factors for other metals are consistent with less impacted sites in the region. This pattern has also been observed in European rivers, where Cd is often enriched by industrial discharges. At the same time, other metals tend to reflect natural background levels (Schulte et al., 2024). The significant enrichment of Cd at Site 3 indicates a strong anthropogenic influence, which could have serious ecological and health implications if not addressed. The low enrichment of other metals indicates that they are less likely to be of immediate concern, though continued monitoring is recommended.

Table 5. Enrichment factor for toxic metals in sediment

Metal	Studied Sites		
	1	2	3
Cd	5.45	5.22	6.36
Pb	0.03	0.03	0.03
Zn	0.02	0.03	0.03
As	0.03	0.03	0.03
Cu	0.08	0.08	0.07

In Figure 3, the QoC shows that Cd shows the highest contamination level at Site 3 (46.43%). In comparison, Site 2 shows the highest QoC for Pb (35.48%) and Cu (36.71%). These results highlight the variability in metal contamination across the sites, with different metals being more prominent in various areas. The high QoC for Cd at Site 3 is particularly concerning, as Cd is known to have toxic effects even at low concentrations (Ogbeide and Henry, 2024).

High QoC values for Cd and Pb are consistent with findings in other contaminated sites in the Niger Delta, where industrial and urban runoff are major contributors (Iwegbue et al., 2018). Similar patterns have been observed in other studies of highly industrialized areas. Globally, areas with heavy industrialization and poor waste management, such as in some parts of India, report similar QoC values, highlighting the widespread nature of this issue (Gupta and Gupta, 2023). The high QoC for Cd and Pb, particularly at Sites 2 and 3, suggests an urgent need for intervention to prevent further contamination and mitigate potential health risks. These results emphasize the importance of implementing stricter pollution controls and remediation efforts.

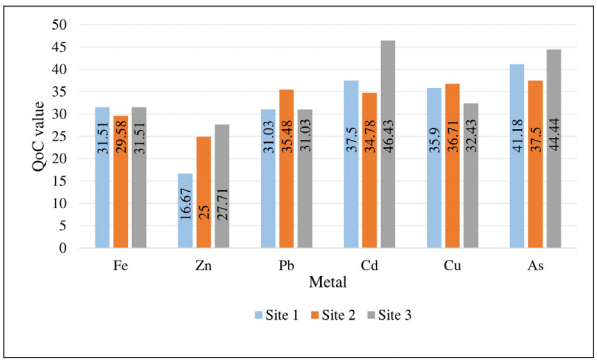

Figure 3. Quantification of contamination (QoC) in Sites 1, 2, and 3

The study reveals that Site 3 in the Niger Delta is experiencing the highest levels of contamination, particularly for Cd, indicating a high ecological risk and enrichment factor. This finding is concerning due to the toxic nature of Cd and its potential to cause adverse health effects in wildlife and humans (Osayande and Nwokedi, 2019). The elevated PLI and PERI at Site 3 underscore the need for urgent remediation. Similar patterns of heavy metal contamination have been observed in the Niger Delta, particularly concerning Cd and Pb, often linked to oil spills and industrial activities (Iwegbue et al., 2018). International studies, such as those in China and India, also report significant ecological risks associated with Cd and Pb contamination (Kumar et al., 2020; Liu et al., 2023). The study highlights the need for targeted environmental management strategies to mitigate

further pollution and protect the ecological integrity of the Niger Delta.

The correlation in Table 6 shows the associations between heavy metals (Cd, Pb, As, Cu, Zn, Fe) in sediment samples. The table shows Pearson's r values and their significance ($p < 0.05$). The matrix analysis, presented in Table 6, revealed significant relationships among heavy metals in the sediment samples. Cd and Pb showed a strong positive correlation ($r = 0.96$), suggesting a common anthropogenic source, such as oil spills or industrial effluents, which have been documented in similarly polluted deltaic regions (Onyena et al., 2024). As and Cu also exhibited a strong positive correlation ($r = 0.95$), consistent with findings in agricultural and mining- impacted sediments where these metals co-occur due to pesticide use and ore processing (Ratnakar et al., 2018). Cu and Zn were positively correlated ($r = 0.91$), a pattern frequently observed in urbanized coastal areas where corroded infrastructure and stormwater runoff contribute to metal deposition (Onyena, A. P. and Nwaogbe, 2024).

Notably, strong negative correlations were observed between Cd and As ($r = –0.94$), Cd and Cu ($r = –0.99$), and Pb and As ($r = –0.99$). The inverse relationships observed among certain metals likely result from competition for binding sites in the sediment. This phenomenon has been well documented in estuarine environments, where similar competitive interactions between metals have been observed (Zhang et al., 2022). Interestingly, iron showed almost no correlation with the other metals studied. This makes sense because the iron in these sediments likely comes mostly from naturalrock weathering rather than human activities, as other researchers working in the Niger Delta have found (Ogbeide et al., 2024).

The close connection between Cd and Pb is particularly concerning because both metals are toxic and often originate from the same pollution sources, such as oil spills and factory waste. Recent studies have confirmed that these metals pose serious threats to both ecosystems and human health in contaminated areas (Afolabi et al., 2024). The strong link between Cu and Zn points to urban runoff as a major contributor, something coastal cities need to address through better stormwater management (Adimalla and Taloor, 2020).

What's really interesting is how some metals seem to "push each other out" of the sediment. This behavior, especially between Cd, Cu, and As, shows a need to pay close attention to sediment chemistry-factors like acidity and organic content can dramatically affect how these metals move through the environment (Bao et al., 2024). Our results add to growing evidence from around the world that industrialized river deltas need comprehensive pollution control plans that address both cleanup and prevention (Akpa et al., 2025).

Table 6. Pearson Correlation Matrix for Heavy Metals

Metals	Cd	Pb	As	Cu	Zn	Fe
Cd	1.00					
Pb	0.96*	1.00				
As	−0.94*	−0.99*	1.00			
Cu	−0.99*	−0.94*	0.95*	1.00		
Zn	−0.87	−0.80	0.82	0.91*	1.00	
Fe	0.12	0.08	−0.10	−0.15	−0.33	1.00

Bold = Strong correlation.
** = Significant ($p < 0.05$).*
Negative values = Inverse relationships.

4. Conclusion

The study reveals significant contamination across all sites, with Site 3 exhibiting the highest levels, particularly for Cd, which poses the most substantial ecological risk. The CF and PLI highlight the greater anthropogenic impact at Site 3, where Cd contamination is notably higher than at other sites. The ecological risk factor and PERI indicate that Site 3 has the highest potential for ecological harm. The DC indicates widespread contamination, with Site 1 showing the highest cumulative contamination due to industrial proximity. Igeo indicates moderate Cd pollution levels, indicating the need for pollution control measures. The enrichment factor analysis confirms significant anthropogenic influence, particularly for Cd, aligning with similar findings in the Niger Delta and other industrialized regions globally. The quantification of contamination indicates that Cd and Pb are the most concerning contaminants, particularly at Sites 2 and 3. Immediate action is required to reduce industrial discharges and implement sustainable waste management practices to safeguard both the environment and public health in the region.

Competing Interests and Funding

There is no conflict of interest to declare, and no funding for the proposed project.

Ethical Approval

No specific ethical approval was required for this study.

Data Availability Statement

All relevant data supporting the study are in the article, and the raw data are also available upon request from readers.

References

Abdullah, M.I.C., Sah, A.S.R.M., Haris, H. (2020).

Geoaccumulation Index and Enrichment Factor of Arsenic in Surface Sediment of Bukit Merah Reservoir, Malaysia. Tropical Life Science Research 31:109-125.

Abugu, H.O., Ezugwu, A.L., Ihedioha, J.N. (2023). Assessment of Polycyclic Aromatic Hydrocarbon Contamination of Fruits, Leaves, and Soil Within Automobile Repair Workshops in Nsukka Metropolis. Polycyclic Aromatic Compounds 43: 8333-8355.

Adimalla, N., Taloor, A.K. (2020). Hydrogeochemical investigation of groundwater quality in the hard rock terrain of South India using Geographic Information System (GIS) and groundwater quality index (GWQI) techniques. Groundwater for Sustainable Development 10: 100288.

Afolabi, O.O., Ugwu, M.O., Fubara, A.I., Ugwuechendu, T.T., Okoye, O.N., Jackson, S.O., Wokocha, A.O. (2024). Human health risk exposure from suspected BTEX and HMs contamination of Manihot spp. from nearby remediated oil spill field in Niger Delta, Nigeria. Environmental Chemistry and Ecotoxicology 6: 347-353.

Afzaal, M., Hameed, S., Liaqat, I., Ali Khan, A. A., Abdul Manan, H., Shahid, R., and Altaf, M. (2022). Heavy Metals Contamination in Water, Sediments and Fish of Freshwater Ecosystems in Pakistan. Water Practice and Technology 17: 1253-1272.

Ahirvar, B.P., Das, P., Srivastava, V., Kumar, M. (2023). Perspectives of Heavy Metal Pollution Indices for Soil, Sediment, and Water Pollution Evaluation: An Insight. Total Environment Research Themes 6: 1-16

Akpa, C., Nworie, C.D., Obasi, P.N., Omoruyi, N., Ugbor, C.C. (2025). Assessment of the heavy metal induced environmental pollution in Abakaliki mining district using geochemical analysis of soils and stream sediments. International Journal of River Basin Management 1-21.

Ali, M.M., Ali, M.L., Rakib, M.R.J., Islam, M.S., Habib, A., Hossen, S., Ibrahim, K.A., Idris, A.M., Phoungthong, K. (2022). Contamination and Ecological Risk Assessment of Heavy Metals in Water and Sediment from Hubs of Fish Resource River in A Developing Country. Toxin Reviews 41:1253-1268.

Al-Jaberi, M. H., Sedkhan, M. T., Hussain, G. A., Jasim, A. A. (2020). Assessment of Heavy Metals and Ecological Risk in the Sediments of Thi Qar and Basrah Governorates-Southern Iraq. In IOP Conference Series: Materials Science and Engineering 928. p. 022012).

APHA (2017). Standard Methods for the Examination of Water and Wastewater, 23rd ed. American Public Health Association, Washington, DC.

Attah, U.E., Chinwendu, O.C., Chieze, C.P., Obiahu, O.H., Yan, Z. (2021). Evaluating The Spatial Distribution of Soil Physicochemical Characteristics and Heavy Metal Toxicity Potential in Sediments of Nworie River Micro-Watershed, Imo State, Southeastern Nigeria. Environmental Chemistry and Ecotoxicology 3:261-268.

Banerjee, S. (2022). Ecotoxicological Consequences of the Invasive Apple Snail Pomacea Maculata in Louisiana Wetlands, M.Sc. Thesis, University of Louisiana at Lafayette.

Barakat, A., Ennaji, W., Krimissa, S. Bouzaid, M. (2020). Heavy Metal Contamination and Ecological-Health Risk Evaluation in Peri-Urban Wastewater-Irrigated Soils of Beni-Mellal City (Morocco). International Journal Environmental Health Research 30:372-387.

Bao, T., Wang, P., Hu, B., Jin, Q., Zheng, T., Li, D. (2024).

Adsorption and distribution of heavy metals in aquatic environments: The role of colloids and effects of environmental factors. Journal of Hazardous Materials 474: 134725.

Bayat, F., Akbari, S.A.A., Dabirioskoei, A., Nasiri, M., Mellati,

A. (2016). The Relationship Between Blood Lead Level and Preeclampsia. Electron Physician 12:3450-3455.

Bhuyan, M. S., Haider, S. M. B., Meraj, G., Bakar, M. A., Islam,

M. T., Kunda, M., Siddiquw, M.A.B., Ali, M.M., Mustary, S., Mojumder, I.A., Bhat, M.A. (2023). Assessment of Heavy Metal Contamination in Beach Sediments of Eastern St. Martin's Island, Bangladesh: Implications for Environmental and Human Health Risks. Water 15: 2494.

Bwatanglang, I., Yonnana, E., Ibrahim, L., Medugu, A., & Bitrus, E. (2021). Assessment of environmental pollution on the soil, plants, and water chemistry of insurgency-inflicted communities of Madagali, Adamawa State, Nigeria. Jordan Journal of Earth and Environmental Sciences, 12(1), 62–71.

Chen, Q., Huang, F., Cai, A. (2021). Spatiotemporal Trends, Sources and Ecological Risks of Heavy Metals in the Surface Sediments of Weitou Bay, China. International Journal of Environmental Research and Public Health 18: 1-15.

Chris, D. I., and Anyanwu, B.O. (2022). Pollution and Potential Ecological Risk Evaluation Associated with Toxic Metals in an Impacted Mangrove Swamp in the Niger Delta, Nigeria. Toxics 11:1-6.

Chris, D.I., Amaewhule, E.G., Onyena, A.P. (2024a). Estimation of Potential Health Risks on Metals and Metalloids Contaminants in Black Goby (Gobius niger) Consumption in Selected Niger Delta Coast, Nigeria. Journal of Trace Elements and Minerals8:1-8.

Chris, D.I., Juliana, N.O., Wokeh, O.K., Nor, A.M., Lananan, F., Wei, L.S. (2024b). Comparative Ecotoxicological Study on the Current Status of Artisanal Crude Oil Contaminated Mangrove Swamps in Rivers State, Southern Nigeria. Heliyon 10:1-16.

Chris, D.I., Onyena, A.P., Sam, K. (2023). Evaluation of Human Health and Ecological Risk of Heavy Metals in Water, Sediment and Shellfishes in Typical Artisanal Oil Mining Areas of Nigeria. Environmental Science and Pollution Research 30: 80055-80069.

Chris, D.I. and Anyanwu, B.O. (2023). Pollution and Potential Ecological Risk Evaluation Associated with Toxic Metals in an Impacted Mangrove Swamp in Niger Delta, Nigeria. Toxics 11:1-166.

Davies, I.C., Ibienebo, D.I., Yusuf, S. (2024). Environmental Impact Assessment of Trace Metals Contaminated Water, Fish, and Sediments from Riparian Communities in the Niger Delta Region, Nigeria. International Journal of Research in Environmental Science.13:1-9.

Ekperusi, A.O., and Asiwa, D.O. (2024). Trophodynamics and Health Risk Assessment of Heavy Metals in Seafood from a Tropical Estuary in the Gulf of Guinea. Environmental Research 252: 1-10.

Guan, Y., Shao, C., Ju, M. (2014). Heavy Metal Contamination Assessment and Partition for Industrial and Mining Gathering Areas. International Journal of Environmental Research and Public Health 11: 7286-7303.

Gupta, S., and Gupta, S.K. (2023). Application of Monte Carlo Simulation for Carcinogenic and Non-Carcinogenic Risks Assessment Through Multi-Exposure Pathways of Heavy Metals of River Water and Sediment, India. Environmental Geochemistry and Health 45: 3465-3486.

Hakanson, L. (1980). An Ecological Risk Index for Aquatic Pollution Control. A Sedimentological Approach. Water Research 14: 975-1001.

Idowu, G.A. (2022). Heavy Metals Research in Nigeria: A Review of Studies and Prioritization of Research Needs. Environmental Science and Pollution Research, 29: 65940-65961.

Islam, M.S., Han, S., Ahmed, M.K., Masunaga, S. (2014). Assessment of Trace Metal Contamination in Water and Sediment of Some Rivers in Bangladesh. Journal of Water and Environment Technology 12: 109-121.

Iwegbue, C.M.A., Beecroft, O.V., Ogala, J.E., Egobueze, F.E., Tesi, G.O., Nwajei, G.E., Martincigh, B.S. (2018). Concentrations and Ecological Risks of Metals in Surface Sediments of Some Coastal Creeks in the Niger Delta, Nigeria. African Journal of Aquatic Science 43:241-253.

Jahan, S., and Strezov, V. (2018). Comparison of Pollution Indices for the Assessment of Heavy Metals in the Sediments of Seaports of NSW, Australia. Marine Pollution Bulletin 128: 295-306.

Jiang, Y., Hu, B., Shi, H., Yi, L., Chen, S., Zhou, Y., Cheng, J., Huang, M., Yu, W., Shi, Z. (2023). Pollution and Risk Assessment of Potentially Toxic Elements in Soils from Industrial and Mining Sites Across China. Journal of

Environmental Management336:1-13.

Katz, R.S. (2012). Environmental Pollution: Corporate Crime and Cancer Mortality. Contemporary Justice Review 15: 97-125.

Khudhur, N.S., Khudhur, S.M., Ahmad, I.N. (2018). An Assessment of Heavy Metal Soil Contamination in a Steel Factory and the Surrounding Area in Erbil City. Jordan Journal of Earth and Environmental Sciences 9: 1-11.

Kpee, F., and Nwadinigwe, C.A. (2014). Pollution Status of Heavy Metals in Sediments, Water and Biota of Kalabari Creeks, Rivers State, Nigeria. Academic Research International 5: 69-80.

Kumar, A., Cabral-Pinto, M., Kumar, A., Kumar, M., and Dinis, P.A. (2020). Estimation of Risk to the Eco-Environment and Human Health of Using Heavy Metals in the Uttarakhand Himalaya, India. Applied Sciences 10: 1-18.

Liu, X., Sheng, Y., Liu, Q., and Li, Z. (2023). Ecological and Environmental Risks of Heavy Metals in Sediments in Dingzi Bay, South Yellow Sea. Marine Pollution Bulletin 188: 1-10.

Liu, Q., Xu, X., Zeng, J., Shi, X., Liao, Y., Du, P., Tang, Y., Huang, W., Chen Q., Shou, L. (2019). Heavy Metals Concentrations in Commercial Marine Organisms from Xiangshan Bay, China, and the potential health risks. Marine Pollution Bulletin 141:215-226.

Malvandi, H. (2021). An Assessment of Metal Contamination Risk in Sediments of the Mohammad Abad River, Northern Iran. Journal of Biomedical Research and Environmental Sciences 2: 696-704.

Meregini-Ikechukwu, P.C., Ogbonna, D.N., Akani, N.P. (2020). Water quality assessment of Elechi creek receiving effluent discharges from industrial activities in Port Harcourt, Nigeria. Journal of Advances in Microbiology 20: 21-30.

Moslen, M., Ekweozor, I.K., Nwoka, N.D. (2018). Assessment of heavy metals pollution in surface sediments of a tidal creek in the Niger Delta, Nigeria. Archives of Agriculture and Environmental Science 31: 81-85.

Mugoša, B., Đurović, D., Nedović-Vuković, M., Barjaktarović-Labović, S., and Vrvić, M. (2016). Assessment of Ecological Risk of Heavy Metal Contamination in Coastal Municipalities of Montenegro. International Journal of Environmental Research and Public Health 13:1-15.

Mwakisunga, B., Pratap, H. B., Machiwa, J. F., and Stephano,

F. (2021). Heavy Metal Contamination and Potential Ecological Risks in Surface Sediments Along Dar Es Salaam Harbour Channel. Tanzania Journal of Science 47: 1606-1621

Nowrouzi, M., and Pourkhabbaz, A. (2014). Application of Geoaccumulation Index and Enrichment Factor for Assessing Metal Contamination in the Sediments of Hara Biosphere Reserve, Iran. Chemical Speciation and Bioavailability 26: 99-105.

Nriagu, J., Udofia, E. A., Ekong, I., Ebuk, G. (2016). Health Risks Associated with Oil Pollution in the Niger Delta, Nigeria. International Journal of Environmental Research and Public Health13: 1-23.

Ogbeide, O., and Henry, B. (2024). Addressing Heavy Metal Pollution in Nigeria: Evaluating Policies, Assessing Impacts, and Enhancing Remediation Strategies. Journal of Applied Sciences and Environmental Management 28:1007-1051.

Okon, A. O., Ebong, G. A., Tombere, V. P., Anweting, I. B., Etuk, H. S., Ambrose, I. (2023). Toxicity Profile of Metals in Water, Sediments and Liza Grandisquamis from Iko River, South-South of Nigeria. International Journal of Frontier Research in Science 2:001-016.

Onyena, A.P., Folorunso, O.M., Nwanganga, N., Udom, G.J., Ekhator, O.C., Frazzoli, C., ... Orisakwe, O.E. (2024). Engaging one health in heavy metal pollution in some selected Nigerian Niger delta cities. A Systematic review of pervasiveness, bioaccumulation and subduing environmental health challenges. Biological Trace Element Research 202: 1356-1389.

Onyena, A.P., Nwaogbe, O.R. (2024). Assessment of water quality and heavy metal contamination in ballast water: Implications for marine ecosystems and human health. Maritime Technology and Research 6(4): 270227

Oritsemuelebi, B., Frazzoli, C., Eze, E. C., Ilo, C. E., Nwaogazie,

I. L., Orisakwe, O. E. (2021). Levels of Toxic and Essential Metals in Maternal Cord Blood and Anthropometry at Birth: A Pilot Study. Journal of Global Health Reports 5:1-15.

Osayande, A. D., and Nwokedi, A. V. (2019). Assessment of Some Heavy Metals and Physico-Chemical Properties of Soils Within the Vicinity of University of Port Harcourt Teaching Hospital Medical Dumpsite, Port Harcourt, Rivers State, Nigeria. Scientia Africana 18: 61-74.

Qingjie, G., Jun, D., Yunchuan, X., Qingfei, W., Liqiang, Y. (2008). Calculating Pollution Indices by Heavy Metals in Ecological Geochemistry Assessment and a Case Study in Parks of Beijing. Journal of China University of Geoscience 19: 230-241.

Quist, A.J.L., Horne, Y.O.V., Farzan, S.F., Johnston, J.E. (2022). Metal Exposure in Residents Living Near an Urban Oil Drilling Site in Los Angeles, California. Environmental Science and Technology 56: 16981-15989.

Ratnakar, A. (2018). Assessment of co-contamination in soil samples from agricultural areas in and around Lucknow city, Uttar Pradesh, India. Current Science 115: 2267-2274.

Reckermann, M., Omstedt, A., Soomere, T., Aigars, J., Akhtar, N., Bełdowska, M., Beldowski, J., Cronin, T., Czub, M., Eero, M., Hyytiainen, K.P., Jalkanen, J., Kiessling, A., Kjellstrom, E., Kulinski, K., Larsen, Z.G., McCrackin, M., Meier, H.E.M., Oberbeckmann, S., Parnell, K., de Brauwer, C.P., Poska, A., Saarinen, J., Szymczycha, B., Undeman, E., Worman, A., Zorita, E. (2022). Human Impacts and Their Interactions in the Baltic Sea Region. Earth System Dynamics 13: 1-80.

Romero-Murillo, P., Gallego, J.L., Leignel, V. (2023). Marine Pollution and Advances in Biomonitoring in Cartagena Bay in the Colombian Caribbean. Toxics 11: 1-24., 631.

Sakina, N.A., Sodri, A., Kusnoputranto, H. (2023). Heavy Metals of Hospital Wastewater during Covid-19 pandemic. International Journal of Public Health Science 12:187-195.

Sangeetha, S., Vimalkumar, K., Loganathan, B. G. (2021). Environmental Contamination and Human Exposure to Select Endocrine-Disrupting Chemicals: A Review. Sustainable Chemistry, 2: 343-380.

Schulte, P., Weber, A., Keßels, J., Lehmkuhl, F., Schüttrumpf, H., Esser, V., Wolf, S. (2024). Morphodynamics and Heavy Metal Accumulation in an Artificially Built Near-Natural River (Inde, Germany). Journal of Sedimentary Environments 9:117-133.

Seiyaboh, E. I., and Izah, S. C. (2017). Review of Impact of Anthropogenic Activities in Surface Water Resources in the Niger Delta Region of Nigeria: A Case of Bayelsa State. International Journal of Ecotoxicology and Ecobiology 2: 61-73.

Shentu, J., Fang, Y., Wang, Y., Cui, Y., Zhu, M. (2023). Bioaccessibility and Reliable Human Health Risk Assessment of Heavy Metals in Typical Abandoned Industrial Sites of Southeastern China. Ecotoxicology and Environmental Safety 256: 1-11.

Sonone, S. S., Jadhav, S., Sankhla, M. S., Kumar, R. (2020). Water Contamination by Heavy Metals and Their Toxic Effect on Aquaculture and Human Health Through Food Chain. Letters in Applied NanoBioScience 10: 2148-2166.

Tarawneh, K., Eleyan, I., Alalwan, R., Sallam, S., Hammad,

S. (2021). Assessment of heavy metals contamination levels in surfaces soil in Baqa's area, Jordan. Jordan Journal of Earth

and Environmental Sciences 12: 285-294.

Ugochukwu, U. C., Agu, C., Jidere, C., Kurumeh, L., Ewoh,

J. C., Alika, H. (2022). Effect of Petroleum Products Depot on Nwaenebo-Emene River Sediments, Enugu, Nigeria: Contamination by PAHs and Associated Exposure Risks to Both Humans and Aquatic Biota. International Journal of Environmental Analytical Chemistry, 104: 4993-5011.

Vareda, J.P., Valente, A.J., Durães, L. (2019). Assessment of Heavy Metal Pollution from Anthropogenic Activities and Remediation Strategies: A Review. Journal of Environmental Management 246: 101-118.

Vincent-Akpu, I.F., Babatunde, B.B. (2013). Trace metals in water, fish and sediments from Elechi creek, Port Harcourt, Rivers state, Nigeria. Tropical Freshwater Biology 22: 13-21.

Yi, Y., Yang, Z., Zhang, S. (2011). Ecological Risk Assessment of Heavy Metals in Sediment and Human Health Risk Assessment of Heavy Metals in Fishes in the Middle and Lower Reaches of the Yangtze River Basin. Environmental Pollution 159:2575-2585.

Zarei, I., Pourkhabbaz, A., Khuzestani, R. B. (2014). An Assessment of Metal Contamination Risk in Sediments of Hara Biosphere Reserve, Southern Iran with a Focus on Application of Pollution Indicators. Environmental Monitoring and Assessment 186: 6047-6060.

Zhang, Y., Gong, X., Li, R., Gao, W., Hu, D., Yi, X., Liu, Y.,

Fang, J., Shao, J., Ma, Y., Jin, L. (2024). Exposure to Cadmium and Lead is Associated with Diabetic Kidney Disease in Diabetic Patients. Environmental Health 23:1-9.

Zhang, Y.M., Lin, C.Y., Li, B.Z., Cheng, Y.X., Xu, W.B., Xiao,

Y., ...Shu, M.A. (2022). The health risk for consumers under heavy metal scenarios: Reduce bioaccumulation of Cd in estuary mud crab (Scylla paramamosain) through the antagonism of Se. Science of The Total Environment 844: 157149.

JJEES

JJEES (2026) 17 (1): 37-42
ISSN 1995-6681

Jordan Journal of Earth and Environmental Sciences

Prediction Relationships between Dynamic and Some Static Properties of Sedimentary Rocks in Kirkuk, Northern Iraq

Mahmood A. Al-Mufarji[1], Dhahir K. Ali[2*]

[1] Department of Food Sciences ,College of Medicinal and Industrial Plants, University of Kirkuk, Kirkuk, Iraq
[2] Department of Soil Sciences and Water Resources, College of Agriculture, University of Kirkuk, Kirkuk, Iraq

Received on 16 May 2025; Accepted on 16 July 2025

Abstract

The dynamic and static properties of rocks are essential demand for different types of engineering projects. In many situations there are difficulties in obtaining an adequate number of rock samples for laboratory tests in to determine the geotechnical properties of these samples. Therefore, to define the variety of static property parameters of certain rocks derived from the non-destructive geophysical refraction seismic technique, which is conducted in the field, could be achieved by solving problems in measuring the compression and shear wave velocities. Other procedures are the laboratory core sample, the Ultrasonic pulse test and the density measurement. Fifteen sedimentary rock samples composed of silty sandstones, Claystone, and clayey siltstone were prepared in the laboratory to measure compression and shear wave velocities then to calculate dynamic properties such as shear, Young's bulk, and Poisson's ratios.. The static properties, uniaxial compressive strength, material index, internal friction angle, and Young's modulus was determined by certain equations. The goal of this research is to derive empirical equations relating the dynamic parameters to the static parameter of the study rocks. The studied samples were classified as very strong competent and dense rocks.

Keywords: *Empirical relation, dynamic modulus, static modulus, Kirkuk, Iraq*

1. Introduction

Knowledge of geotechnical properties of rocks is necessary for conducting various engineering projects, such as tunnels, quarries, roads, underground storage dams, buildings and drilling operations for groundwater, and fossil oil explorations. There are two methods for obtaining both static and non-static properties of the rocks. The first is a destruction method where the stress-strain relation is drawn to know the deformation behavior of the rocks, under conditions where the measurements of geotechnical properties could not be achieved easily to get and prepare intact rocks especially where the subsurface bed rocks are not outcropped to the surface. The second one is a non-destructive method used to determine dynamic moduli. The Ultrasonic pulse test for the compression and shear wave elastic velocities is applied to calculate the rock elastic dynamic properties. By constructing empirical relationships between the static and dynamic properties, the amount of the static property for a certain rock could be estimated from knowing its dynamic one. Many researchers studied the correlation between the static and dynamic properties of different rocks in many locations around the world. Altindag (2012) analyzed the data on sedimentary rocks from previous studies to correlate compression velocity with some mechanical properties; he constructed some empirical equations with high correlation coefficients. Hammam and Eliwa (2013) investigated the dynamic and static properties of soil in Saudi Arabia. They used cross-hole seismic and pressure meter methods to establish a good comparison between Young's and shear moduli and the standard penetration test. Najibi et al. (2015) correlated static uniaxial compressive strength and dynamic properties of limestone rocks in Iran and suggested equations that compared their relations with previous studies. Broton et al. (2016) studied the relationship between static and dynamicmodulus of different igneous metamorphic, and sedimentary rocks and proposed new relationships for those parameters. Majstorovic et al. (2019) measured the compressive strength and compression with shear wave velocities and dynamic modulus for different rocks to find relationships between those parameters. Using the least-squares method, they developed new empirical correlation equations. Garia et al. (2020) provided an overview of the correlation between variation in mineralogy and porosity with saturation condition and sedimentary rock compression wave velocity. The yielded analysis showed an increase in quartz content in the sandstone that led to a decrease in young modulus and compression velocity. Mehammod et al. (2020) carried out a refraction seismic survey at a site in Egypt to delineate subsurface characteristics by measuring compression and shear wave velocities. They determined the material index coefficient for the subsurface rocks and soils, categorized them into three different competent materials. Al-Awsi et al. (2021) investigated the ability of the geophysical Ultrasonic method to estimation geotechnical parameters for engineering applications. They classified the studied rock samples into incompetent and fairly competent materials, and they are suitable as foundations for engineering projects. Panchal et al. (2024) studied the correlation between the static

* Corresponding author e-mail: dhahirgeo@uokirkuk.edu.iq

modulus determined by the uniaxial compression test and the dynamic elastic modulus determined by the Ultrasonic pulse velocity test for different sedimentary, metamorphic and Igneous rocks. They proposed a correlation equation using the linear regression statistical method.

The determination of static uniaxial compression strength and static Young modulus are two necessary parameters for any engineering project in design and construction. Therefore, this paper aims to establish empirical relationships between elastic compression, shear wave velocities and dynamic modulus with the material index, internal friction angle, Young's static modulus and uniaxial compressive strength of sedimentary rock samples taken from outcrops of the lower Bakhtiari Formation in the northeastern area of Kirkuk city.

2- Materials and methods

The uniaxial Compression Strength (UCS), static Young modulus (Es), material index coefficient (MI) and internal friction angle(Φ) amount for the rock samples in this study were determined using the empirical equations derived from many studies had been applied on the rock samples are situated in the countries nearby Iraq, as a result it might yield convinced finding.

Fifteen samples were taken from outcrop of sedimentary bedrocks of lower Bakhtiari Formation in northeastern of Kirkuk anticline near Shawan town locate about 20 km northeastern of Kirkuk city (35o 44' 51.04" N) (44o 35' 17.62"E) (Figure1), as (Compton,1962) the samples were classified into brown silty sand stones, brown claystone and brown clayey siltstone rock types.

Figure 1. Location of the study site from a satellite image (red square).

The rock samples were prepared in the to cut as cylinder shapes to determined its density(P), by Ultrasonic pulse test to determine compression(Vp) and shear(Vs) wave velocities using (Matest Ultrasonic Tester C372 N) by applying the two probes terminate form the tool upon the two end faces of the rock sample, then the dynamic shear(μ) modulus, Young(Ed) modulus, bulk (K) modulus and Possion s' ratio(σ) were calculated according to (Goodman,1989) using the following equations;

$\mu = P\,(Vs)2$ $E = 2\,\mu\,(1+\sigma)$

$K = E/\,3(1-2\sigma)$

$\sigma = (\,Vp)2 - 2\,(Vs)2\,)\,/2\,[(Vp)2 - (Vs)2\,]$

The uniaxial compressive strength(UCS), Young static modulus(Es), material index

(MI) and internal friction angle (Φ) are determined as follows:

$UCS = 7.1912Vp + 26.258$ (Tercan et al ,2005)

UCS (Uniaxial Compression Strength) Vp (compression wave velocity)

$Es = 0.74Ed - 0.82$ (Essa & Kazi ,1988)

Es (static Young modulus) Ed (dynamic Young modulus)

$MI = 3-(Vp - Vs)2 / (Vp - Vs)2-1$ (Abd-El Rahman ,1989)

(MI material index) (VP & Vs compression and shear velocity)

$Sin\Phi = 1-[(Vp - Vs)2 -2 / (Vp - Vs)2]$ (Abd-El Rahman ,1989)

The results data include dynamic parameters and some static coefficients which are subjected to statistical processes and rely on simple regression analysis to derive empirical relationships and related equations.

3- Results and discussion

Table1 shows the calculated physico-mechanical measured properties of the studied rocks, including density, compression and shear wave velocities, dynamic shear, dynamic Young, and dynamic bulk moduli, in addition to Poisson's ratio . The Vp/Vs ratio range (1.48- 1.59), the

compression velocity range (1558-2109) m/s, and the shear velocity range (847-1345) m/s.The rock's density range (2.1-2.48) g/cc and the Poisson's ratio range (0.21-0.44).The shear modulus range (1578- 5140) MPa, dynamic Young modulus range (6471-12458) MPa, and dynamic baulk modulus range (5475-29661) MPa.

Table 1. physical and dynamic properties of the study rocks.

Sample no	Vp (m/s)	Vs (m/s)	P (g/cc)	μ MPa	σ	Ed MPa	K MPa	Vp/Vs	description
1	1849	1223	2.4	3589	0.28	9187	6959	1.51	Br claystone
2	1934	1239	2.3	3530	0.38	9744	13533	1.57	Br claystone
3	2109	1345	2.35	4251	0.41	11987	22198	1.56	Br. Claystone
4	1948	1236	2.48	3788	0.42	10757	22410	1.57	Br. Claystone
5	1759	1169	2.29	3129	0.26	7885	5475	1.5	Br. silty Claystone
6	1321	847	2.2	1578	0.36	4292	5109	1.55	Br. silty Claystone
7	1734	1094	2.1	2513	0.44	7238	20105	1.58	Br. silty Claystone
8	2321	1495	2.3	5140	0.37	14083	18055	1.55	Br. silty Claystone
9	1663	1069	2.35	2685	0.38	7411	10293	1.55	Br. silty sandstone
10	1762	1172	2.3	3217	0.26	8106	5629	1.5	Br. silty sandstone
11	1898	1231	2.4	3636	0.35	9819	10910	1.54	Br. silty sandstone
12	2083	1320	2.5	4356	0.43	12458	29661	1.57	Br. silty sandstone
13	1568	985	2.3	2231	0.45	6471	21570	1.59	Br. clayey siltstone
14	1932	1302	2.3	3898	0.21	9435	5421	1.48	Br. clayey siltstone
15	1753	1104	2.25	2742	0.44	7896	21933	1.58	Br. clayey siltstone

Table 2 shows the material index (MI), internal friction angle (Φ), static Young modulus (Es), and uniaxial compressive strength (UCS). The material index values range (0.33 – 0.68), the internal friction angle range (52-65) degree, the static young modulus range (2037-6805) MPa, and the uniaxial compressive strength range (11302-16717) MPa.

Table 2. Static properties of the study rocks.

Sample no	MI	Es MPa	Φ degree	UCS MPa	description
1	0.56	4372	60	13322	Br. Claystone
2	0.36	4451	54	13934	Br. Claystone
3	0 .39	6805	55	15192	Br. Claystone
4	0.36	4816	54	14034	Br claystone
5	0.6	3291	62	12675	Br. silty Claystone
6	0.42	2037	56	9525	Br. silty Claystone
7	0.33	3089	53	12495	Br. silty Claystone
8	0.42	6697	56	16717	Br. silty Claystone
9	0.42	3390	56	11985	Br. silty sandstone
10	0.6	3828	62	12697	Br. silty sandstone
11	0.45	4354	57	13675	Br. silty sandstone
12	0.36	4878	57	15005	Br. silty sandstone
13	0.30	2077	52	11302	Br. clayey siltstone
14	0.68	4595	65	13919	Br. clayey siltstone
15	0.33	3624	53	12632	Br. clayey siltstone

The Figures (2–7), which were constructed to determine the relationships between the physico-mechanical and dynamic properties of the studied rock samples, are expressed by linear regression equations; most of them have strong correlation coefficients. Figure 2a ies the relationship between the compression and shear elastic wave velocities of the silty sandstones claystone, and clayey siltstone rocks; it shows a strong correlation coefficient and a clear linear regression curve, indicating that they have confidence values to derive dynamic moduli. Figure 2 b is a dynamic Young modulus versus static Young modulus relationship with a high correlation coefficient; the static Young modulus can be estimated accordingly, which is the most needed property for rock deformation.

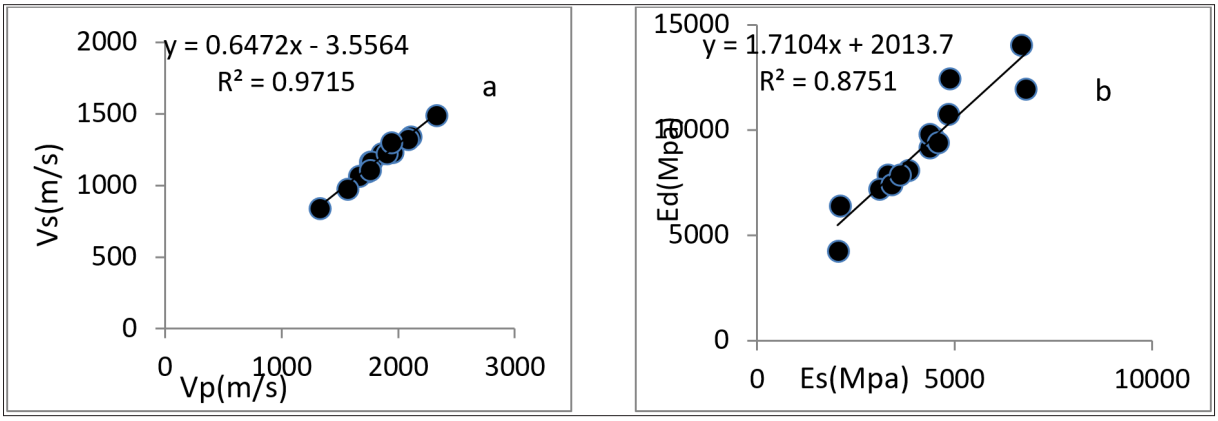

Figure 2. Relationship between: **a.** compression and shear wave velocities, **b.** dynamic and static young modulus.

The plots (Figure3a) and (Figure3b) show that the Poisson's ratio has a powerful reciprocal relationship with each material index and internal friction angle of the rocks, where the Poisson s' ratio decreases with increasing both properties. According to Sheriff and Geldart (1995), Tatham (1982), and Birch (1966), most of the studied rock material indices are classified as moderately competent to highly competent materials (Table 3). According to(Meyerhof, 1956) the studied rocks are classified as very dense materials based on their internal friction angle.

Table 3. Description of soil according to Poisson s' ratio and Material index.

Soil description parameter	Incompetent to slightly competent	Fairly to moderately competent	Competent material	Very high-quality material
Poisson's- ratio	0.41-0.49	0.35-0.27	0.25-0.16	0.12-0.03
Material index	-1 -- -0.5	-0.5 — 0.0	0.0— 0.5	0.5

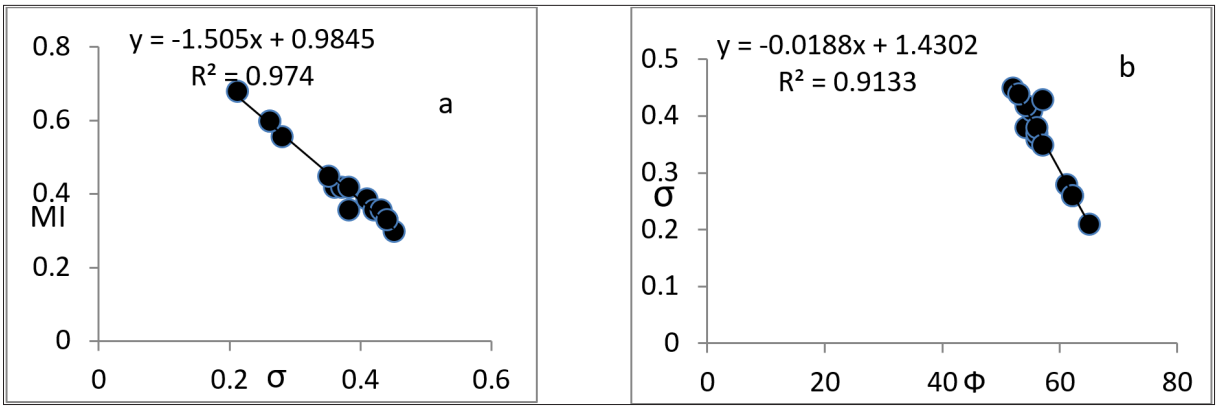

Figure 3. a. Material index versus Poisson's ratio plot, **b.** Poisson's ratio versus internal friction angle plot.

The relation between the material index and internal friction angle, as shown in(Figur4a) has a high correlation coefficient; the friction angle, which reflects the brittleness (Zhou et al,2018) of the soil and rocks, can be estimated by this relationship, which was gained by dynamic calculations. Figure 4b reveals a powerful relationship between the elastic compression wave velocity and uniaxial compressive strength. According to Bieniawsky (1989), the studied rocks are classified as very high-strength rocks.

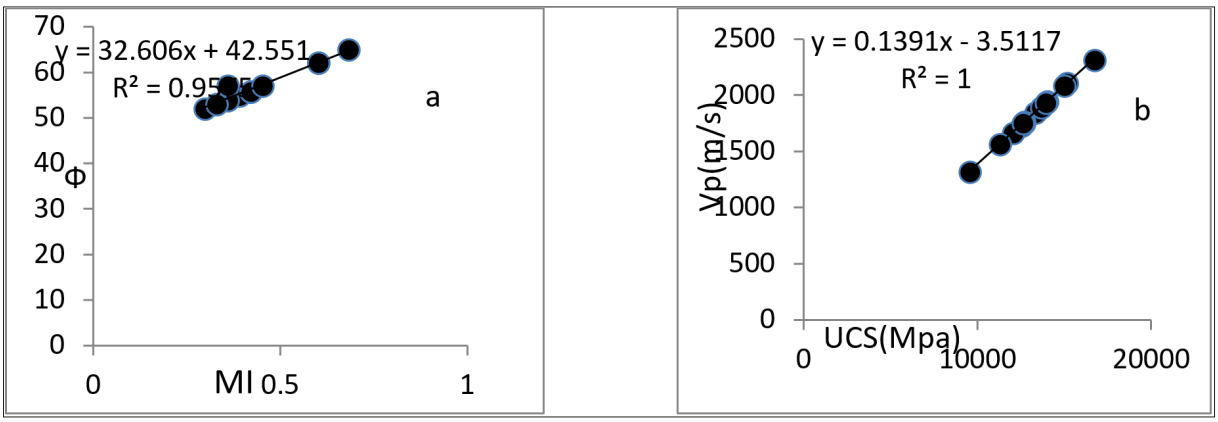

Figure 4. Relationship between **a.** internal friction angle and material index, **b.** compression wave velocity and uniaxial compressive strength.

Dynamic Young modulus in (Figure 5a) shows a strong correlation with the uniaxial compressive strength of the studied rocks; it is clear that an increase in Young dynamic modulus corresponds to an increase in the compressive strength of the rocks. This empirical relationship is confirmed by the relation between static Young modulus and uniaxial compressive strength (Figure 5 b).

Table 5. Correlation between: **a.** uniaxial compressive strength and Young's dynamic modulus, **b.** Young's static modulus and uniaxial compressive strength

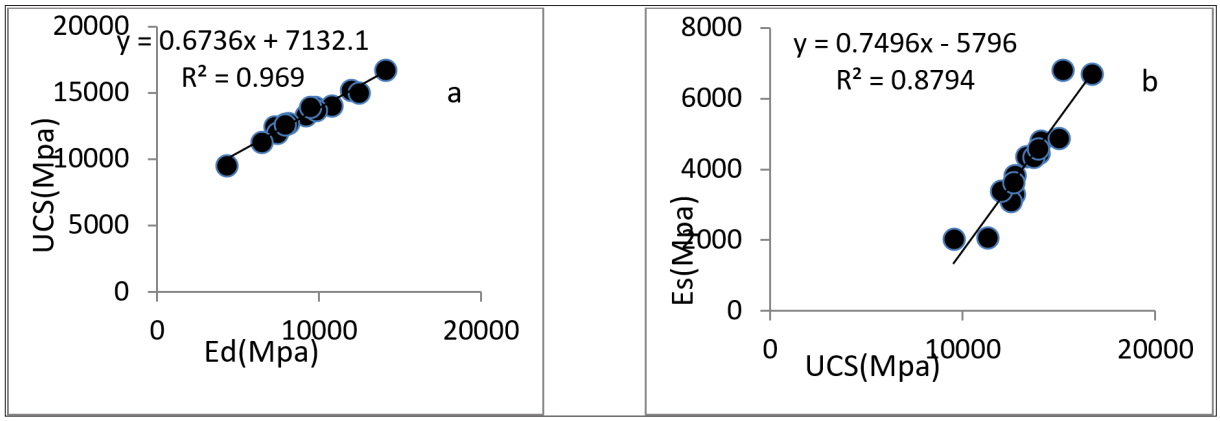

Figure 5. a. Material index versus Poisson's ratio plot, **b.** Poisson's ratio versus internal friction angle plot.

Figure 6a presents a reciprocal relationship between the dynamic bulk modulus (compressibility) and the material index with a moderate correlation coefficient. It is helpful to give information about the degree of competency in studied rocks by the dynamic property(k) indicator. Still, it has a direct relationship with the Poisson's ratio of the investigated rocks as shown in Figure 6 b.

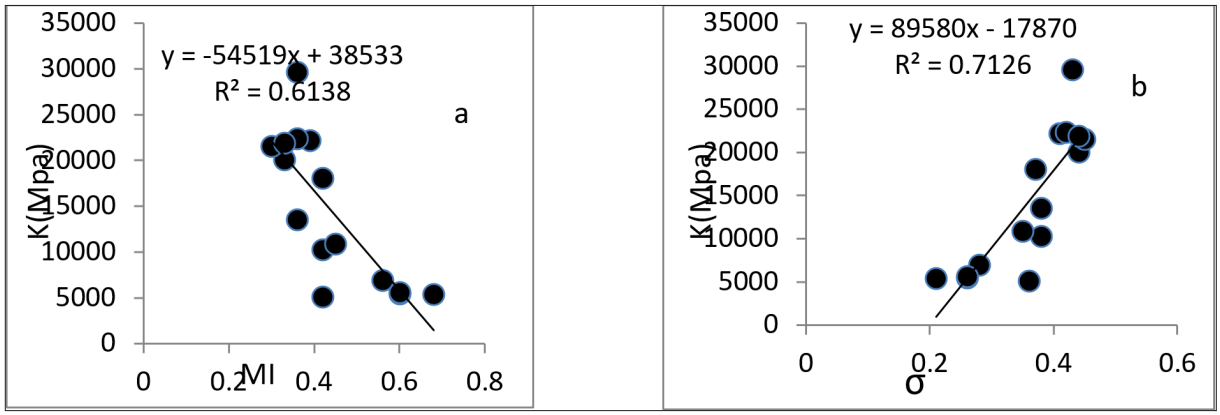

Figure 6. a. Bulk dynamic modulus versus material index plot**, b.** Bulk dynamic modulus versus Poisson's ratio plot

There is a good relationship between the compression wave velocity and the static Young modulus (Figure 7a). They have a high correlation coefficient; as a consequence, the engineer can obtain knowledge of that property from the seismic method procedure. Similarly, the relationship between the dynamic shear modulus and uniaxial compressive strength is shown in Figure 7 b.

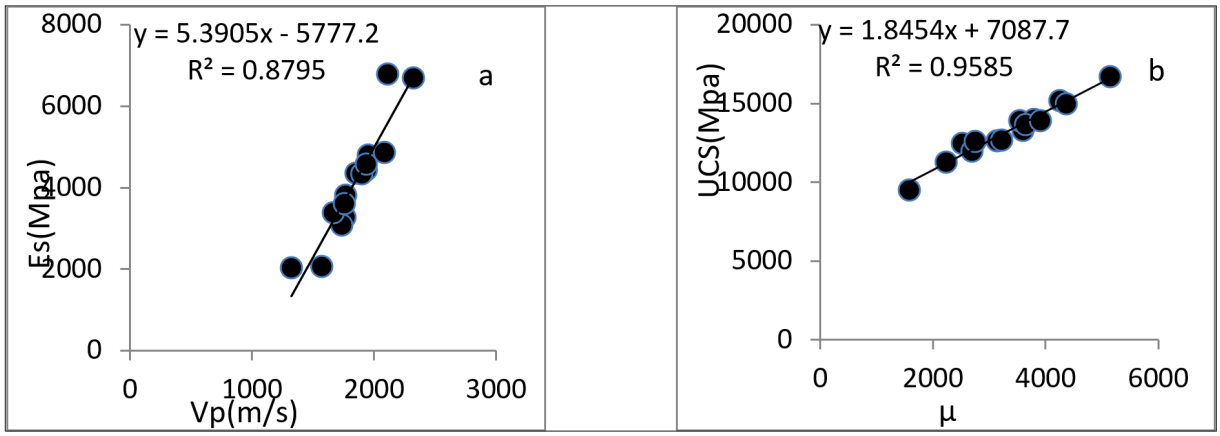

Figure 7. Relationship between: **a.**Young static modulus and compression wave velocity, **b.** uniaxial compressive strength and shear dynamic modulus.

4- Conclusions

Fifteen sedimentary rock samples have been chosen of silty sandstones, claystone and clayey siltstone compositions to determine the compression velocity, shear wave velocity, dynamic Young modulus with dynamic bulk modulus, and in static situation, material index, internal friction angle, uniaxial compressive strength and Young modulus were derived by application many available equations to construct empirical correlation equation between the dynamic and physical-mechanical properties. The highest correlation coefficient was in the high to very high range; accordingly, we could classify the studied rock into powerful rocks, moderately competent to highly competent materials, and very dense materials. Engineers might use this outcome to apply to future planned projects.

References

Al-Awsi, M.D., Khorshid, S.Z., Ahmed, M.T.(2021).Ultrasonic Method as a Tool for Geotechnical Parameters Estimation at Proposed Engineering Site/Western Iraq, Journal of Physics: Conference Series, 1818 (1), 012010

Abd El-Rahman, M.(1989). Evaluation of the kinetic elastic moduli of the surface materials and application to engineering geologic maps at Maba-Risabah area (Dhamar Province), Northern Yemen. Egyptian Journal of Geology,33: 229–250.

Altindag, R.(2012).Correlation between P-wave velocity and some mechanical properties for sedimentary rocks. Journal of The Southern Africa Institute of Mining and Metallurgy. Volume 112: 229-237.

Birch, F.(1966). Handbook of physical constants. Geol. Soc. Am. Mem. 97: 97–174.

Bieniawski, Z.T.(1989). Engineering rock mass classifications. New York: Wiley.

Brotons, V, Tomás, R., Ivorra, S, Grediaga, A., Martínez-Martínez, J., Benavente, D. and Gómez-Heras. M.(2016). Improved correlation between the static and dynamic elastic modulus of different types of rocks. Material and Structure ,49(8): 3021-3037.

Compton, R. R. (1962). Manual of field geology. Soil Science, 93(4), 295.

Eissa ,E. and kazi, A.(1988). Relation between static and dynamic Youngs moduli of Rocks. International Journal of Mock Mechanics Mining and Geomechanic Abstracts, Vol. 25, No. 6: 479-482.

Garia, S., Pal, K.A., Nair, A. M., and Ravi, K.(2020). Elastic wave velocities as indicators of lithology-based geomechanical behavior of sedimentary rocks: an overview. SN Applied Sciences (2020) 2:1521.

Goodman, R.E.(1989). Introduction to rock mechanics. (Vol. 2) : Wiley New York.

Hammam, A.H. and Eliwa, M. (2013). Comparison between results of dynamic & static moduli of soil determined by different methods. Housing and Building National Research Center journal, 9:144-149.

Majstorović, j., Gligorić, M., Lutovac, S. , Negovanović, M., and Crnogorac, L.(2019). Correlation of Uniaxial Compressive Strength with the Dynamic Elastic Modulus P – Wave Velocity and S – Wave Velocity of Different Rock Types. Underground Mining Engineering, 34 : 11-25.

Meyerhof, G. (1956). Penetration tests and bearing capacity of cohesionless soils. Journal of Soils Mechanic and Foundation Division ASCE, 82(SM1).

Mohammed ,M. A., Abudeif, A .M., and Abd el-aal, A .K. (2020). Engineering geotechnical evaluation of soil for foundation purposes using shallow seismic refraction and MASW in 15th Mayo, Egypt. Journal of African Earth Sciences 162 (2020) 103721.

Najibi, A. R., Ghafoori, M., Lashkaripour, G.R. and Asef, M. R.(2015). Empirical relations between strength and static and dynamic elastic properties of Asmari and Sarvak limestones two main oil reservoirs in Iran. Journal of Petroleum Science and Engineering 126: 78–82

Panchal, S., Ronghe, S .S. and Lokhande, R. D.(2024). Correlation between Static and Dynamic ‘ ‘Young’s Modulus of Elasticity of Different Types of Rocks. International Journal of Geology and Earth Sciences, Vol. 10, No. 1, 2024.

Sheriff, R.E., Geldart, L.P.(1995). Exploration Seismology. Cambridge university press, Cambridge.

Tatham, R.H.(1982). V p/V s and lithology. Geophysics 47 (3), 336–344.

Tercan, A. E., Unver, B., Tiryakil, B., and Ozbilgin, B.,2005. A study of relationships among mechanical, index and petrographic properties of some sandstones using canonical correlation analysis , (in Turkish). Madencilik ,vol.44,2005:3-14.

Zhou, H. , Chen, J. , Lu, J., Jiang, Y. and Meng, F.(2018).A New Rock Brittleness Evaluation Index Based on the Internal Friction Angle and Class I Stress–Strain Curve. Rock Mechanics and Rock Engineering. https://doi.org/10.1007/s00603-018-1487-0 (jun. 19, 2025)

JJEES

JJEES (2026) 17 (1): 43-55
ISSN 1995-6681

Jordan Journal of Earth and Environmental Sciences

Evaluation of Economic Valuation of Air Quality Improvement: A Systematic Review

Manirul Islam[1], Moududa Khatun[2*], Muniyandi Balasubramanian[3], Walter Leal Filho[4]

[1]Senior Research Fellow, Department of Geography, Aliah University, Kolkata, West Bengal, India
[2]Assistant Professor, Department of Geography, Aliah University, Kolkata, West Bengal, India
[3]Assistant Professor, Centre for Ecological Economics and Natural Resources, Institute for Social and Economic Change Bangalore, Bangalore 560072, India
[4] Professor, Department of Natural Science, Manchester Metropolitan University, Chester Street, Manchester M15 5GD, UK, and European School of Sustainability Science and Research, Hamburg University of Applied Sciences, Ulmenliet 20, 21033 Hamburg, Germany

Received on 24 January 2025; Accepted on 14 August 2025

Abstract

Air quality improvement (AQI) can reduce health costs and improve socio-economic and human well-being. AQI is one of the regulating ecosystem services that maintain air pollution and improve environmental quality. The study aimed to identify and analyze studies on the economic valuation of AQI and its application in cities worldwide. This study identified 97 documents across three phases that addressed economic or monetary valuation, using a list of keywords in accordance with the PRISMA 2020 statement. The result shows that among 18 methods, the contingent valuation method is used the most. Spatially, China is the dominant contributor, and most studies are done in cities in the global South. This study will further guide planners, policymakers, and potential users of these methods. It will also help identify the gap between studies conducted in the global north and south cities. Additionally, improving urban settlements, making them safe for residents, and inclusive and sustainable management are the 11th goals of the Sustainable Development Goals.

Keywords: *Air Quality Improvement; Contingent Valuation Method; Economic Valuation; Ecosystem Service; Global Cities; Regulating Ecosystem Service*

1. Introduction

In 2022, the world's population is 7.924 billion and will reach around 8.5 billion by 2030 (United Nations, 2022). This increasing population triggers more demands for basic needs and economic growth, enhancing air pollution (Malla et al., 2011). Air pollution is one of a major global problem that negatively impacts the environment and human health. It contributes to life-threatening diseases such as chronic obstructive pulmonary disease, lung cancer, acute lower respiratory illness, non-fatal diseases, lung disorders, and acute asthma (Lelieveld et al., 2015; Giannadaki et al., 2017; Nowak et al., 2018). Moreover, Johnson et al. (2021) found that $PM_{2.5}$ and PM_{10} pollution concentrations are highest in less developing countries, higher in developing countries, and the most minor in developed countries. Air pollution-related mitigation costs can be one approach to assess the the burden of the economic costs of Air Quality Improvement (AQI) in the country and the cost of enhancing human health (Giannadaki et al., 2017). This burden is higher in cities with larger populations and diverse economic activities, which generate higher emissions. The emergence of global consciousness and initiatives to protect the environment virtually divided the world into global South and North countries where financial and technological transfer remains the central theme of global environmental politics (Jaiswal, 2015). Low-income or vulnerable communities have been adversely affected by air pollution. For example, due to health damages, air pollution impacts their income and employment (Clougherty & Kubzankdy, 2009; Forastiere et al., 2007). Air pollution also increases sickness and reduces working productivity. Thus, labor supply and the country's economy are shortened (Ostro, 1983; Hansen & Selte, 2000; Hanna & Oliva, 2011). Likewise, air pollution harms stock returns by altering human mood (Li & Peng, 2016; Demir & Ersan, 2016). Moreover, exposure to air pollution is associated with crime, homicide, and aggressive and offending behavior (Nevin, 2000; Stretesky & Lynch, 2001). The studies also found a strong negative relationship between air pollution and happiness, which has been seen worldwide (Ambrey et al., 2014; Barrington-Leigh & Behzadnejad, 2017). However, this problem can be reduced by delivering its corresponding Ecosystem Service (ES), such as AQI or Air Quality Regulation (AQR). Ecosystem Service is "the benefits people obtain from the properties and processes of ecosystems" (de Groot et al., 2002). Regulating Ecosystem Services (RES) is crucial for mitigating negative impacts and providing regulatory services such as environmental protection and human safety (Mengist et al., 2020). AQI is one of the regulating ecosystem services that can mitigate and improve environmental quality (TEEB, 2011; Gómez-Baggethun & Barton, 2013). The study of AQI is very significant for increasing people's happiness and improving working productivity and efficiency. Estimating air contaminants, comprehending their health impacts, and anticipating air quality are essential to safeguarding public health from dangerous air pollutants (Mathew et al., 2024). Along with public health benefits, improving air quality also

* Corresponding author e-mail: moududa.mrr@gmail.com

yields social, economic, and environmental benefits (Wang et al., 2024). Remarkably, the economic valuation of ecosystem services can help decision-makers assess ES holistically by integrating them into environmental management. It can explain the effects of artificial policies on the quality of life and ecological structures (Farber et al., 2006). Moreover, there are few global studies on the economic value of regulating ecosystem services. For example, Balasubramanian (2019) estimated the value of regulating ecosystem services at 29.08 US$ trillion based on various economic valuation methods. Mengist et al. (2020) argued that the value of regulating ecosystem services should be integrated into environmental management policies, rules, and regulations. Moreover, the value of air quality regulations/improvements can improve environmental quality and sustainable development goals at the local level (Koudouri et al., 2023). Therefore, it is crucial to investigate the studies on AQI using an economic valuation approach and its application in cities across the rich and poor countries of the globe.

The literature has identified different types of ecosystem services, such as air filtration or gas regulation, microclimate regulation, noise reduction, etc. (MA, 2003; TEEB, 2011; Gómez-Baggethun & Barton, 2013). AQR and environmental improvement of the can be understood through valuation approaches (TEEB, 2011; MA, 2005; Haines-Young & Potschin, 2018). Though studies of ES valuation have been conducted since the 1960s, they have increased tremendously since the 1990s (de Groot et al.,2002). The concept of value was first introduced by Ehrlich & Ehrlich in 1992 to evaluate biodiversity (Torres et al., 2021). The valuation of ES has increased tremendously worldwide after the monumental work 'The Value of the World's Ecosystem Services and Natural Capital' by Costanza et al.,1997. ES valuation can be classified mainly into three types: ecological value, economic value, and socio-cultural value dimensions based on axiology, ontology, and epistemology aspects (Groot et al., 2002; Gómez-Baggethun & Barton, 2013). Moreover, there are many studies on different methods of ES valuation, which focus on ecological values (Bagstad et al., 2013; Neugarten et al., 2018; Rötzer et al., 2020; Agudelo et al., 2020; Meraj et al., 2022; Zaman-Ul-haq et al., 2022; Yu et al., 2023; Liu et al., 2023), and socio-cultural values (Neugarten et al., 2018; Scholte et al., 2015; Castro et al., 2011). Furthermore, economic valuation of environmental amenities (Adamowicz, 1991), ecosystem management (Farber et al., 2006), mangrove ecosystem services (Vo Quoc et al., 2012), and land degradation and restoration (Turner et al., 2016) has already been done. Zhao et al. (2022) showed that air pollution has increased in the global South due to increased fossil fuel use.

After extensive studies, the following research gaps have been identified: Firstly, the valuation methods for ecosystem services have been widely studied to understand ecological and socio-cultural values. However, economic valuation needs to be studied to understand the monetary significance of ecosystem services, such as regulating ecosystem services. Secondly, studies focusing on the economic valuation of regulating ecosystem services, such as AQI, are not summarized in review work, which needs to be assessed. Thirdly, the financial division of world countries, such as those in the Global South and North countries, needs more attention to examine the application patterns of the economic value of air quality improvement (EVAQI) and to determine the scope of further studies. Air pollution is a global phenomenon than a local one. However, globally, most deaths occur in low-nd middle-income countries (World Health Organization, 2021). Considering these, it is essential to identify studies on the EVAQI, particularly in cities in the global north and south.

Therefore, the main objectives of this study are (1) to identify and analyze methodological approaches of existing studies on the EVAQI and (2) their application in the global south and north cities. The study has been organized into two sections. The first includes the methodological approaches to the EVAQI, which incorporates the study's approaches, identified methods, variables used, and temporal analysis. The second part discusses their geographical application, including their application in the global south and north cities, and the spatial scale of studies. The study will be a significant addition to the field of research, i.e., ecosystem services. It will further guide planners, policymakers, and potential users of these methods. It will also help identify the gap between the studies executed in the global north and south cities. Additionally, improving urban settlements, making them safe for residents, and inclusive and sustainable management are the 11th goals of the Sustainable Development Goals, where air pollution-free urban centers are one of the main missions of SDGs (United Nations, 2015).

2. Materials and Methods

Search strategy: In the present study, an extensive literature survey was conducted from January 1992, the year of the first publication on the value of the ecosystem (Torres et al., 2021), to December 2022. The process of data collection, search strategy, screening, and analysis is based on the guidelines of the Preferred Reporting Items for Systematic reviews and Meta Analyses or PRISMA 2020 statement for systematic review (Page et al., 2021). The checklist for the abstract and for the whole study has also been included (Appendix Tables 1 and 2). The search was conducted across digital repositories, including Google Scholar, Web of Science, Scopus, and ScienceDirect. It includes peer-reviewed articles, review papers, conference papers, reports, dissertations/theses, and grey literature in English. Particular keywords are used for data search on digital repositories (Table 1).

Literature selection, inclusion, and exclusion criteria: Based on these keywords, the literature review was conducted in three phases (Figure 1). At the primary stage, 17000, 2952, 5780, and 5935 results were retrieved from Google Scholar, Web of Science, Scopus, and ScienceDirect, respectively; thus, 31667 studies were identified. However, 29122 duplicate documents have been removed after using the first set of keywords. In the second phase, a new set of keywords was used to further refine the results. This search string returned 2152, 134, 195, and 109 results in Google Scholar, Web of Science, Scopus, and ScienceDirect, respectively.

Table 1. List of keywords used for document search

Search Order	Keywords	Yielded Results	Total
First-order search string	a. "Ecosystem services" AND "Economic valuation" OR "Monetary valuation"	17000	31667
	b. (Economic Valuation OR Monetary Valuation) AND Ecosystem services	2952	
	c. {Economic valuation} AND {Ecosystem service} & {Monetary valuation} AND {Ecosystem service}	5780	
	d. ("Economic valuation OR Monetary valuation") AND Ecosystem service	5935	
Second-order search string	a. "Economic valuation" OR "Monetary valuation" AND "Air quality regulation", "Economic valuation" OR "Monetary valuation" AND "Air quality Improvement" & "Economic valuation" OR "Monetary valuation" AND "Air quality purification"	2152	2590
	b. (Economic valuation OR Monetary valuation) AND Air quality regulation, (Economic valuation OR Monetary valuation) AND Air quality Improvement and (Economic valuation OR Monetary valuation) AND Air quality purification	134	
	c. {Economic valuation} AND {Air quality regulation}, {Economic valuation} AND {Air quality improvement} and {Economic valuation} AND {Air quality purification}	195	
	d. ("Air quality regulation" OR "air quality improvement" OR "air quality purification") AND economic valuation OR monetary valuation with keywords (Air quality regulation OR air quality improvement AND economic valuation OR monetary valuation)	109	
Third order search string	The following must be used explicitly in title and abstract: 1. keyword either economic valuation or monetary valuation 2. One keyword among air quality regulation, air quality improvement and air quality purification	274	
Final selection	97 documents included for systematic review out of 274		

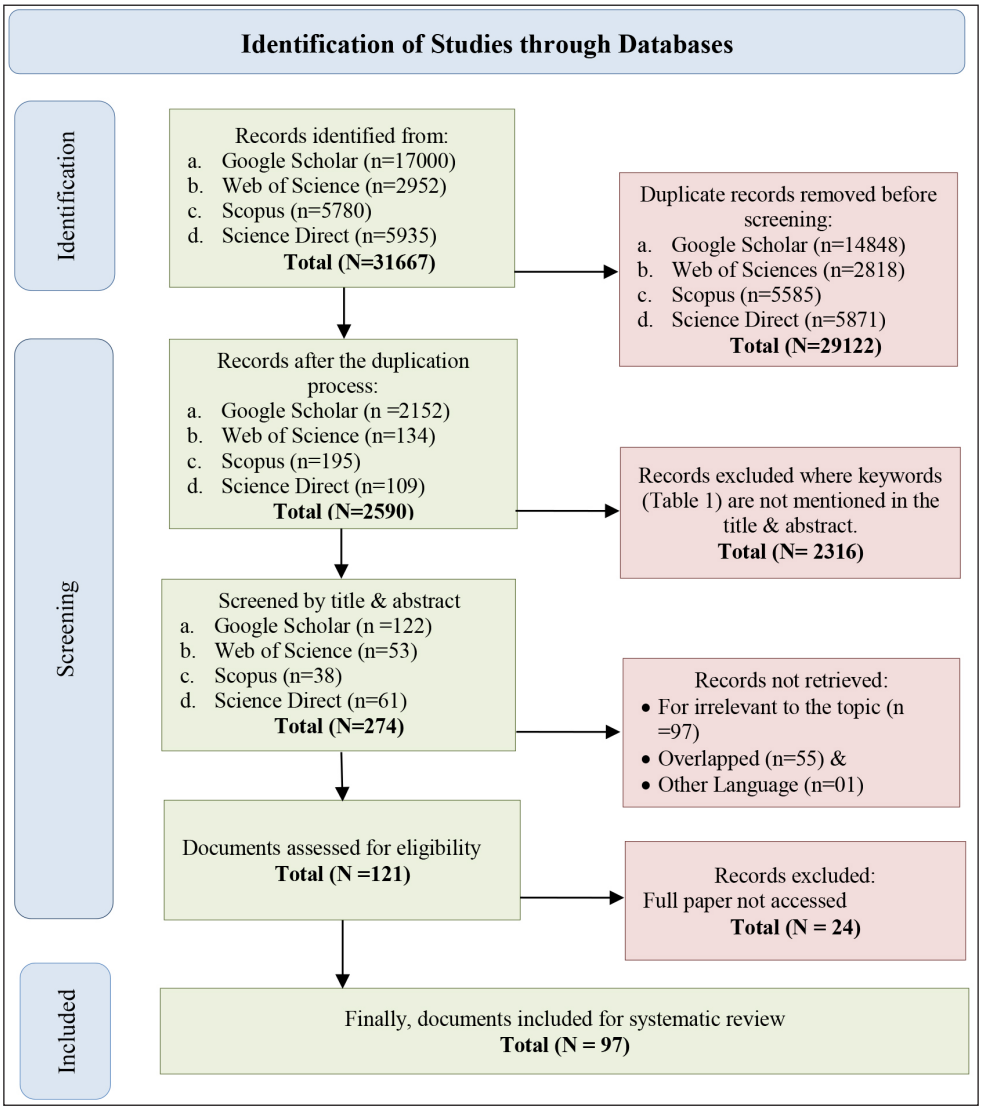

Figure 1. Flow chart for the reviewed study based on PRISMA 2020 statement

Consist of keywords searched in databases i.e. a. Google Scholar b. Web of Science c. Scopus d. Science Direct Of 2590 documents, 2316 records without selected keywords in the title and abstract were excluded. Then, 122, 53, 38, and 61 documents were refined at the third search string based on two criteria, i.e., (i) any documents that incorporate either economic valuation or monetary valuation and (ii) one keyword among 'air quality regulation,' 'air quality improvement' and 'air quality purification' must be used explicitly in title and abstract. Out of 274 searched documents, 153 have been excluded due to overlap across the databases, irrelevance, use of another language, or inaccessibility. Finally, in the last phase, 121 documents were refined manually to get more relevant, specific, and accurate results. After excluding 24 inaccessible documents, 97 documents were included in this study. These consist of review papers (n=03), dissertations/theses (n=05), working papers (n=02), a conference paper (n=01), and research articles (n=86).

3. Results

3.1 Methodological Approaches

Selected 97 pieces of literature have been further analyzed based on the methodological background. Thus, the study's approaches, identified methods, variables used, and temporal analysis have been executed.

Valuation Approaches and Methods: Four main approaches and eighteen valuation methods have been identified. The approaches are the Revealed-preference approach (RPA), the Stated-preference approach (SPA), the Cost-based approach (CBA), and the Subjective well-being approach (SWA) (Table 2).

Table 2. Identified methods used for economic valuation of air quality improvement

Method	About the Methods	Approach
Hedonic Price Method (HPM)	It is a method in which the valuation of goods is determined based on external characteristics of the premises or environment (Pagiola et al., 2004; Turner et al., 2010).	Revealed-preference approach (RPA)
Dose-Response method /Dose-Response Function (DRM)	It is based on the effects of changes in particular elements or pollutants on economic activity or a consumer's utility. For example, levels of air pollution affect the growth of various plant species differentially (Turner et al., 2010).	
Cost of Illness Method (CIM)	It is also known as the burden of disease, defined as the impact of diseases on human health and their effect on individuals, regions, or countries (Jo, 2014).	
Compensating Surplus Value (CSV)	CSV is a method in which people are willing to pay to reduce the number of air pollution days (Liu et al., 2022).	Stated-preference approach (SPA)
Contingent Valuation Method (CVM)	People are directly asked about their WTP or are compensated for a change in ecological services (e.g., WTP for cleaner air) (Pagiola et al., 2004; Turner et al., 2010).	
choice modeling/choice experiment (CEM)	People are asked to choose or rank based on service scenarios or ecological conditions(Pagiola et al., 2004; Turner et al., 2010).	
Theory of Planned Behavior Method (TPB)	It is based on behavior, attitudes, and subjective norms to predict behavioral intention, which helps individuals pay for improvements (Fu et al., 2018).	
Median Externality Value (MEV)	It is a method for each pollutant based on the pollutants' price applied in the USA. (i-Tree, 2021)	Cost-based approach (CBA)
Replacement Cost Method (RCM)	The loss of a natural system service is evaluated by the cost of replacing it with a man-made system (Turner et al., 2010).	
Shadow Project Price (SPP)	Shadow project price is the allotment of cost on something without services or goods (Xie et al., 2019).	
Cost of Emission Control (CEC)	It is determined by the government's prevention cost to control air pollution (Jim & Chen, 2008).	
Avoided Cost Method/ Damage cost (ACM)	The method considers the costs people incur to avoid damage from the loss of ecosystem services or from air quality regulations (Farber et al., 2006). (Example- cost for clean water reduces costly incidents of diarrhea)	
Cost saving method	In this method, the cost applied for treating pollutants in a region or country is considered for valuation (Xi, 2009).	
Demand Function Approach (DFA)	The demand function method is based on market demand for goods, which affects the value of the benefits of those goods (Okuyama, 2018).	
Value Transfer Method (VTM)	In this method, the economic valuation of ecosystem services is based on previously estimated values (Turner et al., 2010).	Stated-preference & Revealed-preference approach
Value of Statistical Life (VSL)	The VSL is defined as the amount an individual is willing to pay to reduce mortality risk (Hammitt, 2000).	
BenMap Program (BMP)	BenMap (Environmental Benefits Mapping and Analysis) is a computer program that estimates the economic value of air pollution-related costs using air quality and demographic data, along with concentration-response relationships (US EPA, 2016).	
Life Satisfaction Method (LSM)	This method is based on the experience of utility and emphasizes the subjective opinions of the individual(Frey et al., 2009).	The subjective well-being approach (SWA)

Source: Prepared by the researchers

Among these identified methods, the contingent valuation method (CVM) accounted for the largest share, i.e., 45.91 percent of the total. However, the choice modeling/ choice experiment (CEM), median externality value (MEV), Avoided cost method/ Damage cost (ACM), and the value transfer method (VTM) are used at 9.18 %, 8.16%, 5.10 %, and 5.10%, respectively. Moreover, the hedonic price method (HPM), dose-response method/dose-response function (DRM), value of statistical life (VSL), BenMap program (BMP), and life satisfaction methods (LSM) are used at 3.06 percent each. Methods like the replacement cost method (RCM), cost of emission control (CEC), and cost-saving method (CSM) are used at only 2.04 percent each. Besides, some methods, such as the cost of illness method (CIM), compensating surplus value (CSV), theory of planned behavior (TPB), shadow project price (SPP), and demand function approach (DFA), are used only once.

Variables used for valuation: Many variables were used in the selected studies (Appendix Table 3). They can be summarized into five broad dimensions, i.e., Air quality (directly), Environmental, Infrastructure, Human, and Technology (Appendix Table 4). The study reveals that the majority of studies select variables for valuation under the air quality dimension (54.29 percent), followed by Human (21.90 percent), environmental (13.33 percent), infrastructure (8.57 percent), and technology (1.90 percent). Moreover, the decade-wise use of valuation variables in the selected documents reveals that the variable 'clean air/improved air' has been widely used throughout the decades (Figure 2). Apart from that, the variable human health is widely used in the literature.

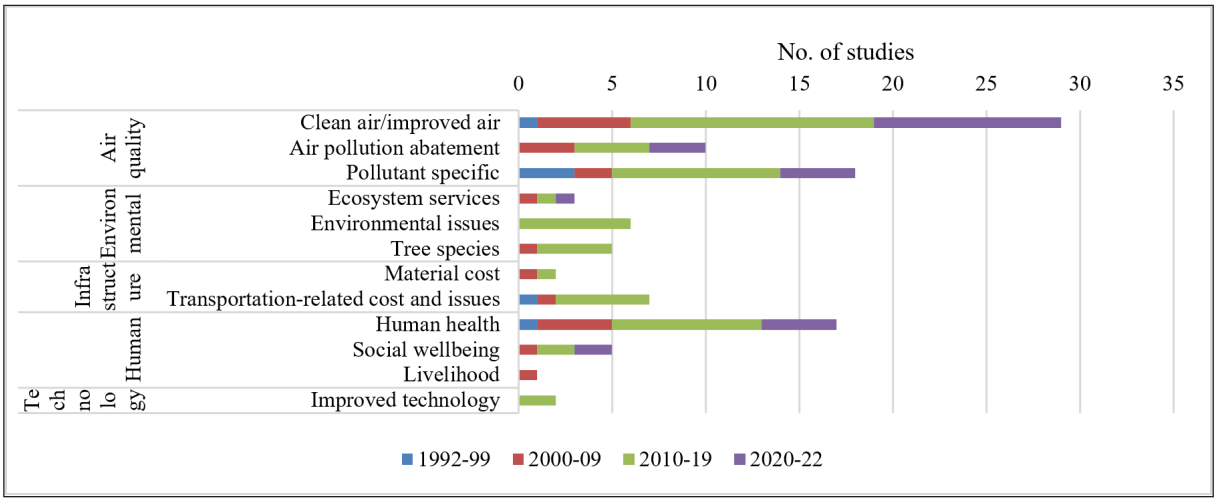

Figure 2. Decade-wise use of variables used for valuation in the selected documents

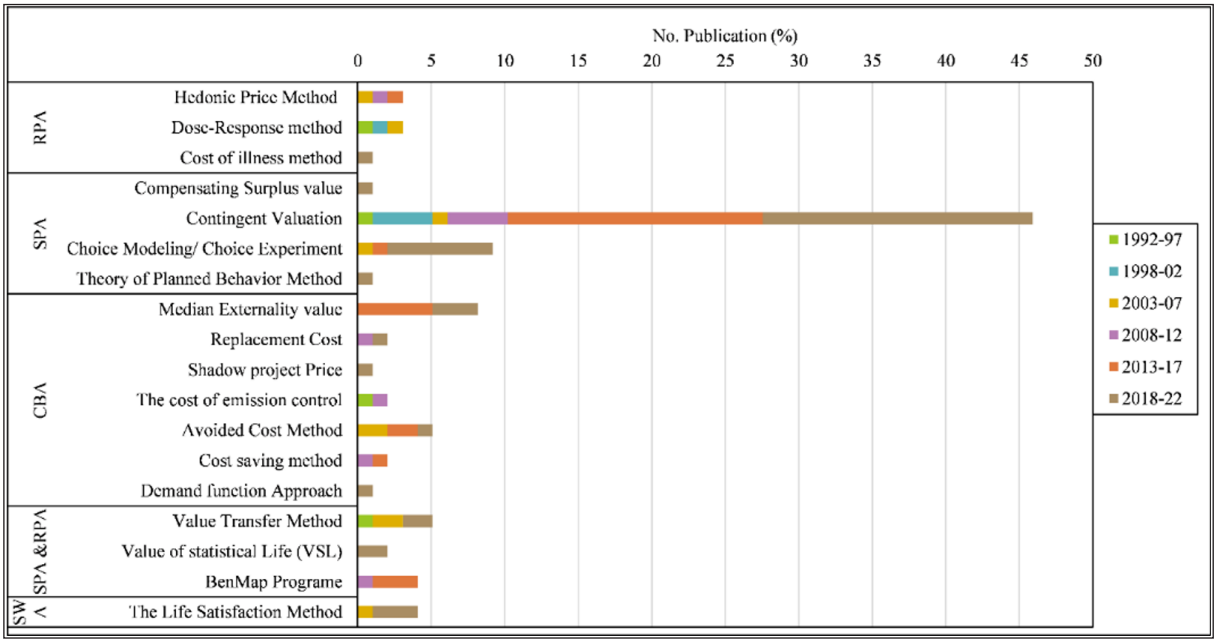

Figure 3. Identified methods used from 1992 to 2022

Publication year-wise methods: Publication year-wise use of the identified methods has been presented with a five-year gap (i.e., for periods 1992-97, 1998-2002, 2003-07, 2008-12, 2013-17, and 2018-22) and is interesting (Figure 3). Among these methods, CVM is the most consistently used in all the periods. CIM, CSV, TPB, VSL, and LSM are relatively recent methods. After the first use of CEC in 1994, it was used once during 2008-12.

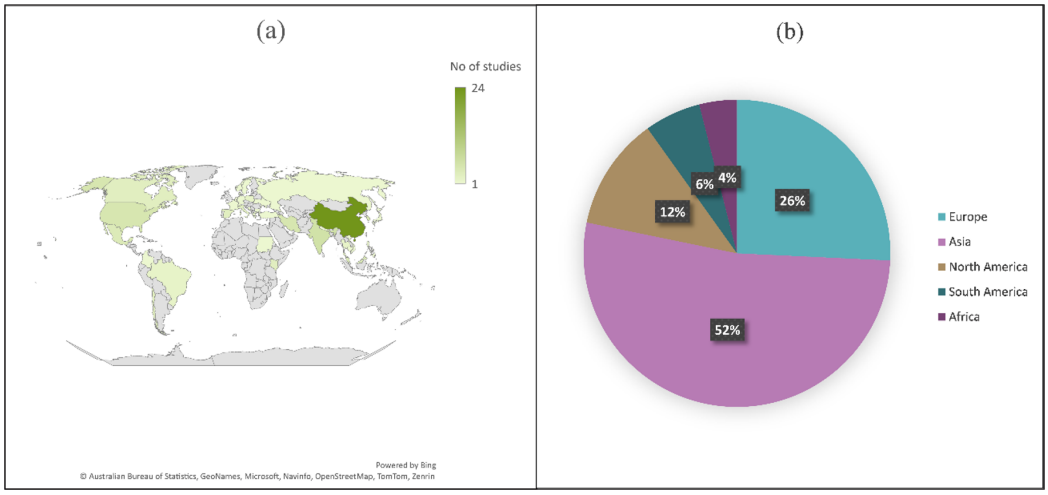

Figure 4. Worldwide spatial distribution of reviewed studies (a) Country-wise (b) Continent wise

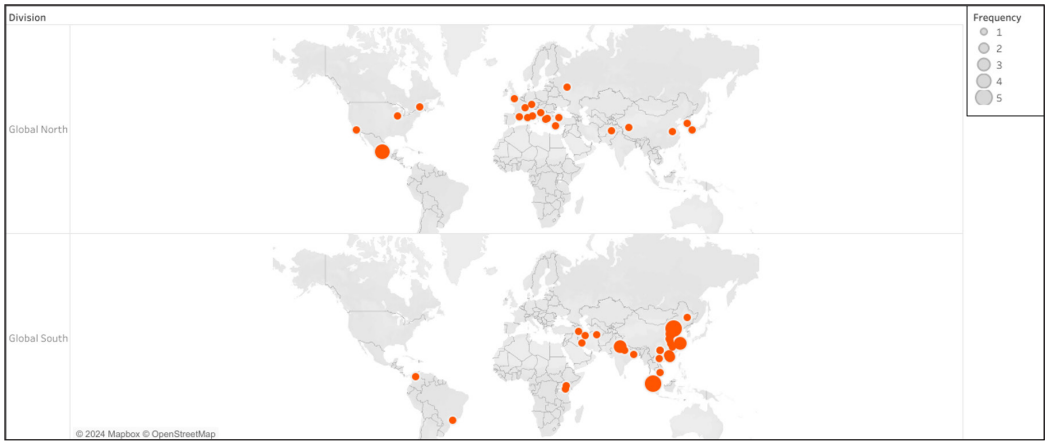

Figure 5. Publication in world megacities

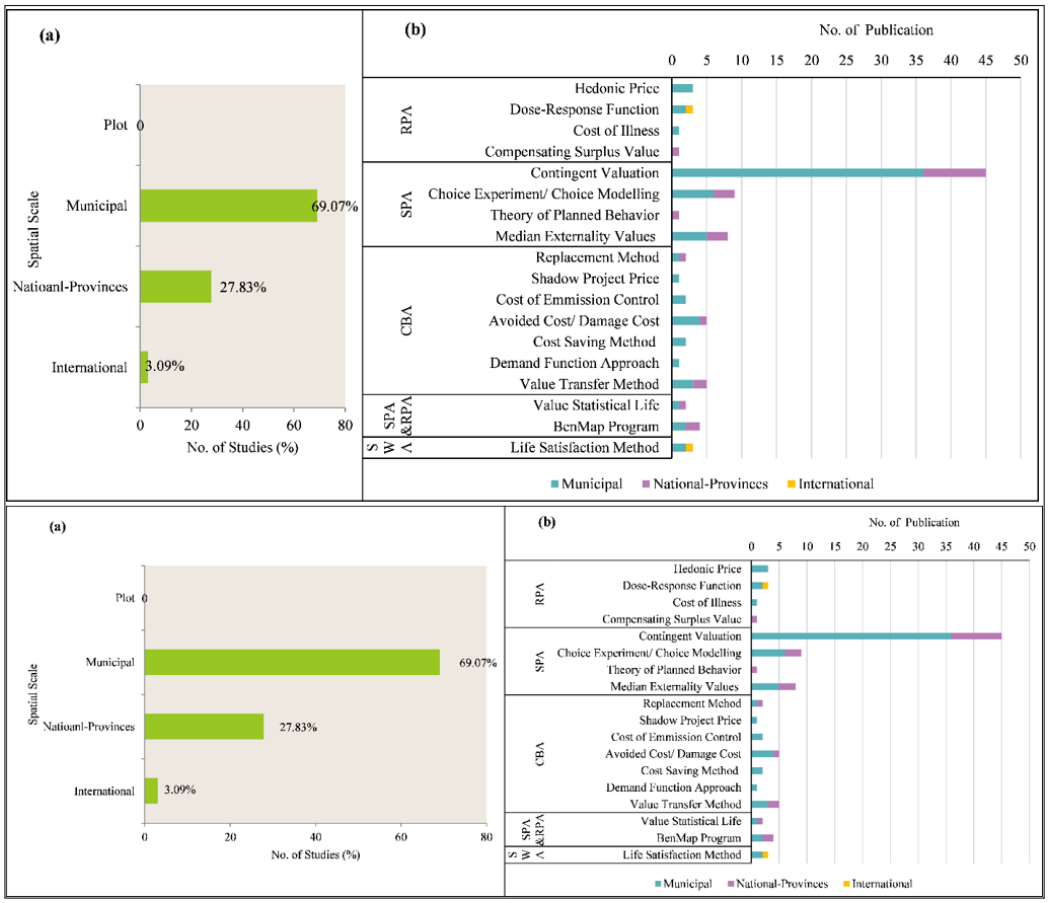

Figure 6. Reviewed studies at (a) Percentage of studies based on spatial scale (b) Method-wise spatial scale

3.2 Geographical application of the methods

Identified methods are used worldwide for EVAQI. Countries in Asia and Europe contribute more than those in North America, South America, and Africa (Figure 4). Asia is the leading continent (with 52.48 percent), and along with Europe (25.74 percent), it accounts for more than 75 percent (Appendix Table 5). Furthermore, China is the leading country in terms of the number of studies on EVAQI.

Publication in global cities: To understand the publication in cities across the globe, the city-level study has been segregated from the non-city-level study (Appendix Table 3). The city-level studies were further classified into global North and South cities to examine publication patterns from a global economic division perspective (Figure 5). Publications in the global south cities have been found to be higher than in the global north cities. Although the number of publications is higher in the southern world, it is repeatedly studied in a few cities. Most of them were carried out in Beijing City and Klang Valley (05 each), followed by Delhi and Shanghai (03 each), and Hong Kong and Guangzhou (02 each). There are 30 more cities that were studied once. On the other hand, studies in the global north mainly were carried out in different cities, 20 cities were studied once. Only Mexico City was studied 4 times.

Spatial scale: Four types of spatial scales have been considered for the analysis based on their size (Figure 6a and 6b). These are (i) plot (< 1 sq. km), (ii) municipal (1-10,000 sq. km), (iii) national provinces (10,000-1,000,000 sq. km), and (iv) international or global (>1,000,000) based on both ecological and institutional dimensions (Groot et al., 2010; Hein et al., 2006). At the municipal level, both urban and non-urban areas are included as physical dimensions to demarcate boundaries (Appendix Table 3). The non-urban regions are delineated at a municipal level based on the studies of Kumar & Rao (2001), Masahina et al. (2012), Srisawasdi et al. (2021), and Ribeiro et al. (2022). The results show that most studies are conducted at the municipal (69.07 percent) level, followed by provincial (27.83 percent) and international/global (3.09 percent) levels. Interestingly, no study was executed at the plot level (Figure 6a). Likewise, the CVM method has been applied extensively at the municipal level, with only a few studies conducted at the national level (Figure 6b).

4. Discussion

The study tries to identify and analyze the methods used for EVAQI through a systematic review of the selected literature. The methods identified for EVAQI have been categorized based on different approaches to the study.

4.1 Methods based on Revealed-Preference Approach

HPM, DRM, and CIM consider the actual behavior of consumers i.e. RPA. It estimates the expenditures made on ES-related market goods (Hawkins, 2003). This approach entails valuing recreation, environmental impacts on residential property, and human health (Bateman et al., 2011). Using the HPM, Komarova (2009) evaluated the value of air quality levels based on house prices and showed that house prices decrease with increasing levels of air pollutants. Although it is based on actual rather than hypothetical prices, this method has ignored other local factors such as, crime levels, noise levels, and transportation factors that might influence the considered prices. Bhat et al. (2022) considered treatment and hospital admission costs and estimated the value of human health and productivity influenced by air pollution. However, the value of mortality estimates is limited to people affected by air pollution-related diseases, not to other morbid or non-morbid conditions. Practically, air pollution affects both groups of residents.

4.2 Methods based on the Stated-Preference Approach

SPA is based on a hypothetical market in which respondents are asked hypothetical questions about whether they are willing to pay for ES that are not tradable in the market. This approach has been used to estimate the valuation of water quality, species conservation, flood prevention, air quality, and recreation (Turner et al., 2010; Bateman et al., 2011). Here, CSV, CVM, CEM, and TPB methods are based on the respondent's behavior lying on a hypothetical market of AQI, which is the SPA-based approach.

Compensating surplus can be defined in terms of any other good an individual is willing to substitute for it being valued (Freeman, 2003). Liu et al. (2022) used the CSV in national provinces in China to examine a relationship between air pollution and satisfaction, but it could not predict a cause-and-effect relationship between them. Moreover, CVM became the most popular method to assess the value of non-market goods and services following the landmark support from the National Oceanic and Atmospheric Administration (Arrow et al., 1993). In this method, data collection is easy and straightforward, withrespondents asked to pay or accept compensation based on their maximum willingness to improve air pollution, and it is widely used across disciplines such as ecology, economics, environmental science, and other social sciences. The use of the technique is increasing rapidly in developing countries (Alam, 2005). However, there are three limitations of the method. These are (i) hypothetical biases (which overestimate the value), (ii) there are significant differences between WTP and willingness to accept, and (iii) persistent disparities appear in surveys (Hausman, 2012). Besides, it creates inconsistency in sample size (Iqbal, 2020). Sarabdeen et al. (2019) found that the mean WTP in CVM is higher than that in CEM, though the statistical difference is almost the same. Thus, the CEM method can overcome the weakness of CVM, as identified during the survey, i.e., data collection inefficiency. In this method, residents rank different attribute alternatives of ES based on environmental conditions. The TPB method emphasizes characteristics of psychological behavior that influence people's intention to pay for something. Here, this method considers five factors, i.e., behavior, attitude, subjective norms, perceived behavior control, and behavior intention. It indicates that subjective norms and behavioral attitudes substantially influence people's WTP. However, there are some uncertainties of real value, such as whether the resident's intention is reflected in their income level.

4.3 Methods based on the cost-based approach

CBA is one of the most comprehensive economic valuation methods, which places monetary value on both costs and benefits. This approach has been widely used to estimate the economic value of the world's ecosystem services (Costanza et al.,1997; Wegner & Pascual, 2011). Here, MEV, RCM, SPP, CEC, ACM, CSM, and DFA consider the monetary value of both cost and benefit.

The reviewed paper by Rabl et al. (2007) identified the methods of CBA and proposed incorporating the life quality index into monetary valuation, as it might overcome the uncertainties in the economic valuation of mortality. Notably, MEV is applied during i-Tree model application in these studies. It also does not involve people in the decision-making process for valuation using secondary data (i-tree 2021), which is the method's main drawback. The technique emphasizes the costs of man-made items rather than the AQR service. However, these man-made items can hardly maintain air quality in large outdoor environments, even after significant investment. For example, the tallest air purification tower is installed in Chandigarh, which has a 1 km radius of capacity to purify the air ("Country's Tallest Air Purification Tower to Be Inaugurated Today," 2021). Whereas SPP is used to assess ES values of urban parks in AQI in Wuhan City, China, the denitrification treatment cost for vehicles is considered the value of air pollutant removal (Xie et al., 2019). Here, people without a vehicle are not included in the EVAQI process. Moreover, the ACM estimates the value of the ecosystem based on the costs required to avoid damage from the loss of a service. It has two perspectives: it estimates potential property damage due to service loss and calculates the cost of protecting property from potential injuries. This avoidance expenditure would be an estimated value of the service. It can be a helpful method for estimating property damage due to environmental factors, but it might yield uncertain results if multiple services are provided (Economic Valuation: Damage Avoided, Replacement, and Substitute Cost Methods, n.d.). Then, the CSM is used at the municipal level in China (Xi, 2009) and Cambodia (Kibria et al., 2017), where governments determine the cost of pollutant treatment. DFA is used at the municipal level in Japan based on market-related demand data for goods (such as facemasks and air purifiers), which are used as a defense to estimate AQI values (Okuyama, 2018).

4.4 Methods based on both Stated-preference and Revealed-preference approachs

Interestingly, methods like VTM, VSL, and BMP are derived from both SPA and RPA, in which the actual behavior of consumers is assessed based on a hypothetical market. The VTM is a critical method usually used where primary data are unavailable (Baró et al., 2014). Thus, the process may not always provide actual information on the study area. In the case of VSL, the method estimates the value of the risk fatality based on an individual's preferences, which can be elicited from SPA and RPA. The monetary value of mortality risk mainly depends on the level of wealth (i.e., income) and age. Thus, it may vary individually based on their circumstances. However, this technique helps assess the risk of death (Hammitt, 2000; Andersson, 2020). Based on the Geographical Information System, BMP calculates the economic value of changed health due to air pollution (US EPA, 2016). Here, four studies that used the BenMap program have been identified. Among them, two studies were carried out in the USA; one is at the municipal level (covering ten cities such as Atlanta, Baltimore, Boston, Chicago, Los Angeles, Minneapolis, New York, Philadelphia, San Francisco & Syracuse) and another study is at national-provinces level (Nowak et al.,2013; Nowak et al.,2014). The remaining two studies are taken at the municipal level in China (Ding et al.,2016) and South Korea (Chae & Park, 2011). These studies include the CIM, the cost of health care, WTP, and the cost of decreasing productivity of individuals. However, Ding et al. (2016) suggested that value emission control, transportation, industrial pollutant control, etc., should be considered for long-term AQI.

4.5 Methods based on the subjective well-being approach

Moreover, the SWA is based on the individual's pleasure in life that comes from the individual's experiences or situations related to services or goods. Based on that experience, individuals would be willing to pay for those services (Frey et al., 2009). Thus, the LSM is considered a type of SWA. LSM is based on the individual's judgment about their own welfare and the judgmental aspect of people, which can reveal their self-assessment of a good life. This approach depends on goods or services, income level, and subjective well-being factors (Frey et al., 2009). With higher income and greater life satisfaction, people are more willing to pay for reducing air pollution. Thus, there is a decreasing trend in air pollution with increasing income levels. Moreover, the technique evaluated the value of air quality reduction based on the individual's experience utility rather than preference utility. However, the output of WTP using this technique is very similar to HPM (as it is based on experienced utility) (Mendoza et al., 2019). Moreover, it is found that one of the review papers is conducted at the international level (Kougea & Koundouri, 2011), and the other two are at the provincial level in Canada (Rabl et al., 2007) and China (Jim & Chen, 2008).

The selected variables used to value the AQI can be categorized as either direct or indirect valuations. The variables related to Air Quality and Environment primarily contribute to the direct valuation of AQI and are thoroughly covered in the EVAQI framework. In contrast, the variables categorized under the Infrastructure, Human, and Technology dimensions are utilized for indirect valuation of the AQI. Human health is a particularly significant variable that is frequently employed in EVAQI assessments. Research into the health impacts of atmospheric pollution has shown a strong correlation between pollutant concentrations and conditions such as respiratory disorders, cardiovascular diseases, and lung cancer mortality (Cesaroni et al., 2013; Silveira et al., 2016; Srisawasdi et al., 2021; Chattopadhyay, 2021). As a result, studies assessing EVAQI through a human healthare becoming increasingly popular.

David J Nowak first introduced the economic valuation of air pollution using the CEC method in the USA in the report on Chicago's urban forest ecosystem (McPherson et al., 1994). After this, publications on EVAQI increased

worldwide almost every year. Air quality concerns are a global issue rather than a local one, which may be the reason for the lack of plot-level studies. On the other hand, air quality concerns are primarily associated with urban areas, where air pollution is prevalent due to increasing population concentration, transportation, and industrialization in and around cities. Thus, the maximum studies are found at the municipal level.

The EVAQI was initiated in a developed country, and studies were conducted in various cities across the global north. In contrast, developing cities face significant challenges, including high population density, increased transportation demand, and greater pollution. Many of these cities are in or near the tropics, where pollution processes more quickly than at higher latitudes (Parrish et al., 2016). Consequently, cities in the Global South are often more advanced in their application to EVAQI than those in the Global North. The research indicates that China is the leading contributor to EVAQI efforts in Asia and worldwide, with studies conducted at municipal, national, and provincial levels. Following Asia, many studies have also been conducted in various cities across Europe. Notable Global South cities involved in these studies include Beijing, Klang Valley, Mexico City, Delhi, Shanghai, Hong Kong, and Guangzhou. Zhang et al. (2019) identify air pollution as a significant concern in China. Addressing this issue has become a top priority, requiring substantial efforts in policy design, social investment, and technological innovation (Liu et al., 2023). China has more economic benefits from air quality improvement studies The reasons are: 1) a large number of population has been affected due to poor air pollution, 2) China is willing to invest more in the better air quality as well as balancing economic growth and ecological conservation, 3) an effective policy intervention at the local, regional and national level, 4) Clean air access and achieving SDGs 5) reduce more health expenditure in the present and future. Consequently, China has incorporated environmental valuation methods into its policy decisions. The country initiated the Payment for Ecosystem Services (PES) program in 1999 to promote the sustainable management of ecosystem services (Zhang et al., 2000). Through the PES scheme, China has improved its ecological situation with increased forest cover (Liu et al., 2008) while also generating higher incomes for rural communities (Song et al., 2014). Additionally, two programs were launched: the Conversion of Cropland to Forest Land (also known as the Grain for Green program) in 1999 and the Ecological Welfare Forest Program (a forest resource management initiative) in 2001 (Wang et al., 2020). Furthermore, studies on the valuation of ecosystem services in India are growing, focusing primarily on forest ecosystem services and wetlands (Chora et al., 2022). Thus, economic policy initiatives with local people's participation will be effective in mitigating air pollution.

5. Conclusion and Implications

An in-depth review of the selected research articles, government reports, and theses on the EVAQI service as an ES provides significant outcomes. Among evaluation methods, the most common is CBA. It is followed by SPA, where CVM is the dominant method. The method considers an individual's contribution to the monetary valuation of air quality. This study also revealed that CEM is more effective than CVM for economic valuation of AQI, as CEM can overcome data-collection inefficiencies during the survey. However, COI and BNM techniques showed that government policies related to transportation, industry, and other factors that affect air quality should be included in the methods along with the cost of health care and resources for long-term AQI. EVAQI has been widely used to assess human health. Thus, integrating the costs of health effects and policies into processes will provide more inclusive outputs to environmental decision-makers. Besides, the WTP is the most frequently used term in the selected literature. WTP is much more effective when the subjective and behavioral approach is used in the TPB and LSM. The Damage cost method and the life of statistical life are better methods for valuing damages and the risk of property or resources due to air pollution, which are not traded in the market. Moreover, no study has been conducted at the plot level, whereas most studies are conducted at the municipal level. It may be to consider the space required for monitoring AQI, as well as urban challenges in managing air quality. Interestingly, studies have been found only at the continental level in Europe, and this pattern has arisen due to the concentration of most urbanized countries there. However, most studies are conducted in global South cities rather than global North cities. The studies are primarily concentrated in a few cities in countries of the global south, given their state. Finally, except for China, most studies in developing countries are replications of developed countries. The emergence of ES valuation in the developed world is a significant reason behind this trend. China has applied a new method for evaluating AQI, such as the TPB. The study will be helpful to potential users of EVAQI for assessment and further research, especially in global North and South cities.

Acknowledgments:

We would like to thank the Central librarian of Aliah University, Park Circus Campus, Kolkata, and the University of Calcutta, Rajabazar Science College Campus, Kolkata, for the collection of e-resources through the scientific databases. Moreover, we would like to express our gratitude to Dr. Mir Islam, Assistant Professor, SLL, Nalanda University, and Mr. Kamble Dhammapal, Teaching Associate, SLL, Nalanda University, for their efforts to improve the text.

References

Agudelo, C. A. R., Bustos, S. L. H., & Moreno, C. A. P. (2020). Modeling interactions among multiple ecosystem services. A critical review. Ecological Modelling, 429(March), 109103. https://doi.org/10.1016/j.ecolmodel.2020.109103

Amini Parsa, V., Salehi, E., Yavari, A. R., & Van Bodegom, P. M. (2019). Analyzing temporal changes in urban forest structure and the effect on air quality improvement. Sustainable Cities and Society, 48, 101548. https://doi.org/10.1016/j.scs.2019.101548

Alam, K. (2005). Valuing the environment in developing countries: Problems and potentials.1–14.Coffs Harbour, NWS, Australia. http://www.aares.org.au/

Alam, M., Olivier, A., Paquette, A., Dupras, J., Revéret, J.-P., &

Messier, C. (2014). A general framework for the quantification and valuation of ecosystem services of tree-based intercropping systems. Agroforestry Systems, 88(4), 679–691. https://doi.org/10.1007/s10457-014-9681-x

Ambrey, C. L., Fleming, C. M., & Chan, A. Y.-C. (2014). Estimating the cost of air pollution in South East Queensland: An application of the life satisfaction non-market valuation approach. Ecological Economics, 97, 172–181. https://doi.org/10.1016/j.ecolecon.2013.11.007

Adamowicz, W. L. (1991). Valuation of Environmental Amenities. In Staff paper, Departmernt of Rural Economy ,University of Alberta ,E. https://doi.org/10.4324/9780429325212-11

Andersson, H. (2020). The value of a statistical life. In Advances in Transport Policy and Planning (Vol. 6, pp. 75–99). Elsevier.

Arrow, K., Solow, R., Portney, P. R., Leamer, E. E., Radner, R., & Schuman, H. (1993). Report of the NOAA Panel on Contingent Valuation. Federal Register, 58(10), 4601–4614.

Balasubramanian, M., (2019). Economic value of regulating ecosystem services: a comprehensive at the global level review. Environmental monitoring and assessment, 191(10), p.616.

Bagstad, K. J., Semmens, D. J., Waage, S., & Winthrop, R. (2013). A comparative assessment of decision-support tools for ecosystem services quantification and valuation. Ecosystem Services, 5, 27–39. https://doi.org/10.1016/j.ecoser.2013.07.004

Barrington-Leigh, C., & Behzadnejad, F. (2017). Evaluating the short-term cost of low-level local air pollution: A life satisfaction approach. Environmental Economics and Policy Studies, 19(2), 269–298. https://doi.org/10.1007/s10018-016-0152-7

Baró, F., Chaparro, L., Gómez-Baggethun, E., Langemeyer, J., Nowak, D. J., & Terradas, J. (2014). Contribution of Ecosystem Services to Air Quality and Climate Change Mitigation Policies: The Case of Urban Forests in Barcelona, Spain. AMBIO, 43(4), 466–479. https://doi.org/10.1007/s13280-014-0507-x

Bateman, I. J., Mace, G. M., Fezzi, C., Atkinson, G., & Turner, K. (2011). Economic Analysis for Ecosystem Service Assessments. Environmental and Resource Economics, 48(2), 177–218. https://doi.org/10.1007/s10640-010-9418-x

Bhat, T. H., Farzaneh, H., & Toosty, N. T. (2022). Co-Benefit Assessment of Active Transportation in Delhi, Estimating the Willingness to Use Nonmotorized Mode and Near-Roadway-Avoided PM2.5 Exposure. International Journal of Environmental Research and Public Health, 19(22), 14974. https://doi.org/10.3390/ijerph192214974

Castro, A. J., Martín-López, B., García-LLorente, M., Aguilera, P. A., López, E., & Cabello, J. (2011). Social preferences regarding the delivery of ecosystem services in a semiarid Mediterranean region. Journal of Arid Environments, 75(11), 1201–1208. https://doi.org/10.1016/j.jaridenv.2011.05.013

Castro, A., Künzli, N., & Götschi, T. (2017). Health benefits of a reduction of PM10 and NO2 exposure after implementing a clean air plan in the Agglomeration Lausanne-Morges. International Journal of Hygiene and Environmental Health, 220(5), 829–839. https://doi.org/10.1016/j.ijheh.2017.03.012

Cesar, H., Olsthoorn, X., Borja -Aburto, V. H., Rosales-Castillo, A., Cicero-Fernandez, P., Montes de Oca, G. S., & Dorland, K. (2002). Improving Air Quality in Metropolitan Mexico City: An Economic Valuation, pp. 1–56 [Health Risks of Atmospheric Pollution]. Comision Ambiental Metropolitana (CAM) and the World Bank. https://doi.org/10.1596/1813-9450-2785

Cesaroni, G.; Badaloni, C.; Gariazzo, C.; Stafoggia, M.; Sozzi, R.; Davoli, M.; Forastiere, F. (2013). Long-Term Exposure to Urban Air Pollution and Mortality in a Cohort of More than a Million Adults in Rome. Environ. Health Perspect, 121, 324–331. https://doi.org/10.1289/ehp.1205862

Chae, Y., & Park, J. (2011). Quantifying costs and benefits of integrated environmental strategies of air quality management and greenhouse gas reduction in the Seoul Metropolitan Area. Energy Policy, 39(9), 5296–5308. https://doi.org/10.1016/j.enpol.2011.05.034

Chattopadhyay, M. (2021). Economics of clean air: Valuation of reduced health risks from Household Air Pollution—A study of rural Indian households. WINPEC, No.E2119.

Chora, B., Khuman, Y. S. C., & Dhyalini, S. (2022). Advances in Ecosystem Services Valuation Studies in India: Learnings from a Systematic Review | SpringerLink. Anthropocene Science (, 1(3), 342–357. https://doi.org/10.1007/s44177-022-00034-0

Clougherty J. E., Kubzansky L. D. (2009). A framework for examining social stress and susceptibility to air pollution in respiratory health. Environ Health Perspect, 117:1351–8. 10.1289/ehp.0900612

Costanza, R., D'Arge, R., De Groot, R., Farber, S., Grasso, M., Hannon, B., Limburg, K., Naeem, S., O'Neill, R. V., Paruelo, J., Raskin, R. G., Sutton, P., & Van Den Belt, M. (1997). The value of the world's ecosystem services and natural capital. Nature, 387(6630), 253–260. https://doi.org/10.1038/387253a0

Country's tallest air purification tower to be inaugurated today. (2021, September 7). The Indian Express. https://indianexpress.com/article/cities/chandigarh/countrys-tallest-air-purification-tower-to-be-inaugurated-today-7493214/

Demir, E., & Ersan, O. (2016). When Stock Market Investors Breathe Polluted Air. In M. H. Bilgin & H. Danis (Eds.), Entrepreneurship, Business and Economics—Vol. 2 (Vol. 2, pp. 705–715). Springer International Publishing. https://doi.org/10.1007/978-3-319-27573-4_14

Dey, M. (2013). A Contingent Valuation Approach to Estimate the Maximum Willingness-to-pay for Improved Air Quality in Asansol, Industrial Area of West Bengal. International Journal of Trends in Economics, Management and Technology, II(IV). https://www.ijtemt.org

Ding, D., Zhu, Y., Jang, C., Lin, C.-J., Wang, S., Fu, J., Gao, J., Deng, S., Xie, J., & Qiu, X. (2016). Evaluation of health benefit using BenMAP-CE with an integrated scheme of model and monitor data during Guangzhou Asian Games. Journal of Environmental Sciences, 42, 9–18. https://doi.org/10.1016/j.jes.2015.06.003

Economic Valuation: Damage Avoided, Replacement, and Substitute Cost Methods. (n.d.). https://www.ecosystemvaluation.org/cost_avoided.htm

Edwards, P. J., & Abivardi, C. (1998). The value of biodiversity: Where ecology and economy blend. Biological Conservation, 83(3), 239–246. https://doi.org/10.1016/S0006-3207(97)00141-9

Farber, S., Costanza, R., Childers, D. L., Erickson, J., Gross, K., Grove, M., Hopkinson, C. S., Kahn, J., Pincetl, S., Troy, A., Warren, P., & Wilson, M. (2006). Linking ecology and economics for ecosystem management. BioScience, 56(2), 121–133. https://doi.org/10.1641/0006-3568(2006)056[0121:LEAEFE]2.0.CO;2

Forastiere F., Stafoggia M., Tasco C., Picciotto S., Agabiti N., Cesaroni G., et al. (2007). Socio-economic status, particulate air pollution, and daily mortality: differential exposure or differential susceptibility. Am J Ind Med; 50:208–16. 10.1002/ajim.20368.

Francisco, J. P. S. (2015). Willingness to pay for air quality improvements from using electric jeepneys in metro manila. The Singapore Economic Review, 60(04), 1550073. https://doi.org/10.1142/S0217590815500733

Freeman, A. M. (2003). Economic Valuation: What and Why. In P. A. Champ, K. J. Boyle, & T. C. Brown (Eds.), A Primer on

Nonmarket Valuation (Vol. 3, pp. 1–25). Springer Netherlands. https://doi.org/10.1007/978-94-007-0826-6_1

Frey, B. S., Luechinger, S., & Stutzer, A. (2009). The life satisfaction approach to environmental valuation. CESifo Working Paper, No. 2836. http://hdl.handle.net/10419/30462

Fu, B., Kurisu, K., Hanaki, K., & Che, Y. (2018). Influential factors of public intention to improve the air quality in China. Journal of Cleaner Production, 2018, 595–607. https://doi.org/10.1016/j.jclepro.2018.10.192

Giannadaki, D., Lelieveld, J., & Pozzer, A. (2017). The Impact of Fine Particulate Outdoor Air Pollution to Premature Mortality. In T. Karacostas, A. Bais, & P. T. Nastos (Eds.), Perspectives on Atmospheric Sciences (pp. 1021–1026). Springer International Publishing. https://doi.org/10.1007/978-3-319-35095-0_146

Gómez-Baggethun, E., & Barton, D. N. (2013). Classifying and valuing ecosystem services for urban planning. Ecological Economics; Elsevier B.V. https://doi.org/10.1016/j.ecolecon.2012.08.019

Goulder, L., & Kennedy, D. (1997). Valuing ecosystem services: Philosophical bases and empirical methods. In Naturis Services societal dependance on Natural Ecosystem (pp. 23–49).

Groot, R. S. D., Alkemade, R., Braat, L., Hein, L., & Willemen, L. (2010). Challenges in integrating the concept of ecosystem services and values in landscape planning, management and decision making. Ecological Complexity, 7(3), 260–272. https://doi.org/10.1016/j.ecocom.2009.10.006

Groot, R. S. D., Wilson, M. A., & Boumans, R. M. J. (2002). A typology for the classification, description and valuation of ecosystem functions, goods and services. Ecological Economics, 41(3), 393–408. https://doi.org/10.1016/S0921-8009(02)00089-7

Haines-Young, R., & Potschin, M. (2018b). Common International Classification of Ecosystem Services (CICES) V5.1 and Guidance on the Application of the Revised Structure.

Hammitt, J. K. (2000). Valuing Mortality Risk: Theory and Practice. Environmental Science & Technology, 34(8), 1396–1400. https://doi.org/10.1021/es990733n

Hanna, R., & Oliva, P. (2011). THE EFFECT OF POLLUTION ON LABOR SUPPLY: EVIDENCE FROM A NATURAL EXPERIMENT IN MEXICO CITY. NATIONAL BUREAU OF ECONOMIC RESEARCH, Working Paper 17302. http://www.nber.org/papers/w17302

Hansen, A. C., & Selte, H. K. (2000). Air Pollution and Sick-leaves. Environmental and Resource Economics, 16(31–50).

Hausman, J. (2012). Contingent valuation: From dubious to hopeless. Journal of Economic Perspectives, 26(4), 43–56. https://doi.org/10.1257/jep.26.4.43

Hawkins, K. (2003). Economic Valuation of Ecosystem Services (Issue October).

Hein, L., Van Koppen, K., De Groot, R. S., & Van Ierland, E. C. (2006). Spatial scales, stakeholders and the valuation of ecosystem services. Ecological Economics, 57(2), 209–228. https://doi.org/10.1016/j.ecolecon.2005.04.005

Iqbal, H. M. (2020). Valuing ecosystem services of Sundarbans Mangrove forest: Approach of choice experiment. Global Environmental Change, 24(e01273). https://doi.org/10.1016/j.gecco.2020.e01273

i-Tree. (2021). I-Tree Eco User's Manual-Department of Agriculture or the Forest Service, U.S.

Jaiswal, A. (2015). Global Environmental Politics and the North-South Divide. The Indian Journal of Political Science, 76(4), 816–820. https://www.jstor.org/stable/26575609

Jim, C. Y., & Chen, W. Y. (2008). Assessing the ecosystem service of air pollutant removal by urban trees in Guangzhou (China). Journal of Environmental Management, 88(4), 665–676. https://doi.org/10.1016/j.jenvman.2007.03.035

Jo, C. (2014). Cost-of-illness studies: Concepts, scopes, and methods. Clinical and Molecular Hepatology, 20(4), 327. https://doi.org/10.3350/cmh.2014.20.4.327

Johnson, R., Rieuwerts, J. & Comber, S.D.W. (2021). How does a country's developmental status affect ambient air quality with respect to particulate matter?. Int. J. Environ. Sci. Technol. 18, 3395–3406. https://doi.org/10.1007/s13762-020-03072-6

Kibria, A. S. M. G., Behie, A., Costanza, R., Groves, C., & Farrell, T. (2017). The value of ecosystem services obtained from the protected forest of Cambodia: The case of Veun Sai-Siem Pang National Park. Ecosystem Services, 26, 27–36. https://doi.org/10.1016/j.ecoser.2017.05.008

Komarova, V. (2009b). Valuing Environmental Impact of Air Pollution in Moscow with Hedonic Prices. World Academy of Science, Engineering and Technology International Journal of Environmental and Ecological Engineering, 57(1), 319–326.

Koundouri, P., Halkos, G., Landis, C., Dellis, K., Stratopoulou, A., Plataniotis, A. and Chioatto, E. (2023). Valuation of marine ecosystems and Sustainable Development Goals. Frontiers in Environmental Economics, 2, p.1160118.

Kougea, E., & Koundouri, P. (2011). Air Quality Degradation: Can Economics Help in Measuring its Welfare Effects? A Review of Economic Valuation Studies. In Indoor and Outdoor Air Pollution (pp. 106–126). InTech. https://doi.org/10.5772/16794

Kumar, S., & Rao, D. N. (2001). Valuing The Beneficts of Air Pollution Abatement Using a Health Production Function A Case Study of Panipat Thermal Power Station, India. Environmental and Resource Economics, 20, 91–102. https://doi.org/10.1023/A:1012635627808

Lelieveld, J., Evans, J. S., Fnais, M., Giannadaki, D., & Pozzer, A. (2015). The contribution of outdoor air pollution sources to premature mortality on a global scale. Nature, 525(7569), 367–371. https://doi.org/10.1038/nature15371

Li, Q., & Peng, C. H. (2016). The stock market effect of air pollution: Evidence from China. Applied Economics, 48(36), 3442–3461. https://doi.org/10.1080/00036846.2016.1139679

Liu, H., Wang, R., Sun, H., Cao, W., Song, J., Zhang, X., Wen, L., Zhuo, Y., Wang, L., & Liu, T. (2023). Spatiotemporal evolution and driving forces of ecosystem service value and ecological risk in the Ulan Buh Desert. Frontiers in Environmental Science, 10, 1053797. https://doi.org/10.3389/FENVS.2022.1053797/BIBTEX

Liu, Q., Dong, G., Zhang, W., & Li, J. (2022). The Influence of Air Pollution on Happiness and Willingness to Pay for Clean Air in the Bohai Rim Area of China. International Journal of Environmental Research and Public Health, 19(9), 5534. https://doi.org/10.3390/ijerph19095534

Liu, J., Li, S., Ouyang, Z., Tam, C., & Chen, X. (2008). Ecological and socio-economic effects of China's policies for ecosystem services. Proceedings of the National Academy of Sciences, 105(28), 9477–9482. https://doi.org/10.1073/pnas.0706436105

Liu, X., Guo, C., Wu, Y., Huang, C., Lu, K., Zhang, Y., Duan, L., Cheng, M., Chai, F., Mei, F., & Dai, H. (2022). Evaluating cost and benefit of air pollution control policies in China: A systematic review. Journal of Environmental Sciences, 123, 140-155. https://doi.org/10.1016/j.jes.2022.02.043

MA. (2003). Millennium Ecosystem Assessment:Ecosystems and Human Well-being -A Framework for Assessment. Island Press.

MA. (2005). Millennium Ecosystem Assessment,Ecosystems and human well-being. https://doi.org/10.1016/B978-0-12-

809665-9.09206-5

Malla, M. B., Bruce, N., Bates, E., & Rehfuess, E. (2011). Applying global cost-benefit analysis methods to indoor air pollution mitigation interventions in Nepal, Kenya and Sudan: Insights and challenges. Energy Policy, 39(12), 7518–7529. https://doi.org/10.1016/j.enpol.2011.06.031

Masahina, S., Afroz, R., Duasa, J., & Mohamed, N. (2012). A framework to estimate the willingness to pay of household for air quality improvement: A case study in Klang Valley, Malaysia. International Journal of Sustainable Development, 04(09), 11–16.

Mathew, A., Shekar, P. R., Nair, A. T., Mallick, J., Rathod, C., Bindajam, A. A., Alharbi, M. M., & Abdo, H. G. (2024). Unveiling urban air quality dynamics during COVID-19: A Sentinel-5P TROPOMI hotspot analysis. Scientific Reports, 14(1), 1-20. https://doi.org/10.1038/s41598-024-72276-4

McPherson, G. E., Nowak, D. J., & Rowntree, R. A. (1994). Chicago's urban forest ecosystem: Results of the Chicago Urban Forest Climate Project (NE-GTR-186; p. NE-GTR-186). U.S. Department of Agriculture, Forest Service, Northeastern Forest Experimental Station. https://doi.org/10.2737/NE-GTR-186

Mendoza, Y., Loyola, R., Aguilar, A., & Escalante, R. (2019). Valuation of Air Quality in Chile: The Life Satisfaction Approach. Social Indicators Research, 145(1), 367–387. https://doi.org/10.1007/s11205-019-02103-1

Mengist, W., Soromessa, T. & Feyisa, G.L. (2020). A global view of regulatory ecosystem services: existed knowledge, trends, and research gaps. Ecological Process, 9(40), https://doi.org/10.1186/s13717-020-00241-w

Meraj, G., Singh, S. K., Kanga, S., & Islam, Md. N. (2022). Modeling on comparison of ecosystem services concepts, tools, methods and their ecological-economic implications: A review. Modeling Earth Systems and Environment, 8(1), 15–34. https://doi.org/10.1007/s40808-021-01131-6

Montazar-Hojat, A. H., Mansouri, B., Zoufan, P., & Saeid, H. (2018). Economic Valuation of Air and Noise Pollutions Abatement Performance. Journal of Environmental Studies, 44(1), 113–129. https://doi.org/10.22059/jes.2018.237694.1007469

Ndambiri, H., Mungatana, E., & Brouwer, R. (2015). Stated preferences for improved air quality management in the city of Nairobi, Kenya. The European Journal of Applied Economics, 12(2), 16–26. https://doi.org/10.5937/ejae12-9058

Neugarten, R. A., Langhammer, P. F., Osipova, E., Bagstad, K. J., Bhagabati, N., Butchart, S. H. M., Dudley, N., Elliott, V., Gerber, L. R., Gutierrez Arrellano, C., Ivanić, K.-Z., Kettunen, M., Mandle, L., Merriman, J. C., Mulligan, M., Peh, K. S.-H., Raudsepp-Hearne, C., Semmens, D. J., Stolton, S., & Willcock, S. (2018). Tools for measuring, modelling, and valuing ecosystem services: Guidance for Key Biodiversity Areas, natural World Heritage sites, and protected areas. IUCN. https://doi.org/10.2305/iucn.ch.2018.pag.28.en

Nevin, R. (2000). How Lead Exposure Relates to Temporal Changes in IQ, Violent Crime, and Unwed Pregnancy. Environmental Research, 83(1), 1–22. https://doi.org/10.1006/enrs.1999.4045

Nowak, D. J., Hirabayashi, S., Bodine, A., & Greenfield, E. (2014). Tree and forest effects on air quality and human health in the United States. Environmental Pollution, 193, 119–129. https://doi.org/10.1016/j.envpol.2014.05.028

Nowak, D. J., Hirabayashi, S., Bodine, A., & Hoehn, R. (2013). Modeled PM2.5 removal by trees in ten U.S. cities and associated health effects. Environmental Pollution, 178, 395–402. https://doi.org/10.1016/j.envpol.2013.03.050

Nowak, D. J., Hirabayashi, S., Doyle, M., McGovern, M., & Pasher, J. (2018). Air pollution removal by urban forests in Canada and its effect on air quality and human health. Urban Forestry & Urban Greening, 29, 40–48. https://doi.org/10.1016/j.ufug.2017.10.019

Okuyama, T. (2018). Economic valuation of reducing air pollutants for precautionary air conservation policies. Journal of Environmental Economics and Policy, 7(3), 287–302. https://doi.org/10.1080/21606544.2018.1426500

Ostro, B. D. (1983). The effects of air pollution on work loss and morbidity. Journal of Environmental Economics and Management, 10(4), 371–382. https://doi.org/10.1016/0095-0696(83)90006-2

Page, M. J., McKenzie, J. E., Bossuyt, P. M., Boutron, I., Hoffmann, T. C., Mulrow, C. D., Shamseer, L., Tetzlaff, J. M., Akl, E. A., Brennan, S. E., Chou, R., Glanville, J., Grimshaw, J. M., Hróbjartsson, A., Lalu, M. M., Li, T., Loder, E. W., Mayo-Wilson, E., McDonald, S., … Moher, D. (2021b). The PRISMA 2020 statement: An updated guideline for reporting systematic reviews. International Journal of Surgery, 88, 105906. https://doi.org/10.1016/j.ijsu.2021.105906

Pagiola, S., Von Ritter, K., & Bishop, J. (2004). Assessing the Economic Value of Ecosystem Conservation (The World Bank).pdf. 101.

Parrish, D.D., Xu, J., Croes, B., Shao M. (2016). Air quality improvement in Los Angeles—perspectives for developing cities. Frontiers of Environmental Science & Engineering 10, 11. https://doi.org/10.1007/s11783-016-0859-5

Rabl, A., Nathwani, J., Pandey, M., & Hurley, F. (2007). Improving Policy Responses to the Risk of Air Pollution. Journal of Toxicology and Environmental Health, Part A 70(3–4), 316–331. https://doi.org/10.1080/15287390600884966

Ribeiro, A. N., Pavani, B. F., Ribeiro, A. C. G., Sosa, P. R. B., Sinisgalli, P. A. D. A., & Sousa Júnior, W. C. D. (2022). Valuation of the air quality regulation ecosystem service: Impacts from a Brazilian Northeast industrial complex. Ambiente & Sociedade, 25, e01501. https://doi.org/10.1590/1809-4422asoc2021150r1vu2022l4oa

Rötzer, T., Moser-Reischl, A., Rahman, M. A., Grote, R., Pauleit, S., & Pretzsch, H. (2020). Modelling Urban Tree Growth and Ecosystem Services: Review and Perspectives. In F. M. Cánovas, U. Lüttge, M.-C. Risueño, & H. Pretzsch (Eds.), Progress in Botany Vol. 82 , pp. 405–464. Springer International Publishing. https://doi.org/10.1007/124_2020_46

Sarabdeen, M., Afroz, R., Kijas, A. C. M., & Sheikh, S. (2019). Consumer Surplus for Air Quality Improvement in the Transport Sector in Klang Valley, Malaysia: Contingent Valuation Method and Choice Experimental Approach. International Journal of Supply Chain Management, 8(6), 118–132.

Scholte, S. S. K., Van Teeffelen, A. J. A., & Verburg, P. H. (2015). Integrating socio-cultural perspectives into ecosystem service valuation: A review of concepts and methods. Ecological Economics, 114, 67–78. https://doi.org/10.1016/j.ecolecon.2015.03.007

Silveira, C., Roebeling, P., Lopes, M., Ferreira, J., Costa, S., Teixeira, J. P., Borrego, C., & Miranda, A. I. (2016). Assessment of health benefits related to air quality improvement strategies in urban areas: An Impact Pathway Approach. Journal of Environmental Management, 183, 694–702. https://doi.org/10.1016/j.jenvman.2016.08.079

Song, C., Zhang, Y., Mei, Y., Liu, H., Zhang, Z., Zhang, Q., Zha, T., Zhang, K., Huang, C., Xu, X., Jagger, P., Chen, X., & Bilsborrow, R. (2014). Sustainability of Forests Created by China's Sloping Land Conversion Program: A comparison among three sites in Anhui, Hubei, and Shanxi. Forest Policy and Economics, 38, 161–167. https://doi.org/10.1016/j.forpol.2013.08.012

Srisawasdi, W., Tsusaka, T. W., Winijkul, E., & Sasaki, N. (2021).

Valuation of Local Demand for Improved Air Quality: The Case of the Mae Moh Coal Mine Site in Thailand. Atmosphere, 12(9), 1132. https://doi.org/10.3390/atmos12091132

Stretesky, P. B., & Lynch, M. J. (2001). The Relationship Between Lead Exposure and Homicide. ARCH PEDIATR ADOLESC MED, 155.

TEEB ,The Economics of Ecosystems and Biodiversity. (2011). In TEEB Manual for Cities: Ecosystem services in urban Managements.

Torres, A. V., Tiwari, C., & Atkinson, S. F. (2021). Progress in ecosystem services research: A guide for scholars and practitioners—ScienceDirect. Ecosysytem Services, 49(101267). https://doi.org/10.1016/j.ecoser.2021.101267

Turner, K. G., Anderson, S., Gonzales-Chang, M., Costanza, R., Courville, S., Dalgaard, T., Dominati, E., Kubiszewski, I., Ogilvy, S., Porfirio, L., Ratna, N., Sandhu, H., Sutton, P. C., Svenning, J.-C., Turner, G. M., Varennes, Y.-D., Voinov, A., & Wratten, S. (2016). A review of methods, data, and models to assess changes in the value of ecosystem services from land degradation and restoration. Ecological Modelling, 319, 190–207. https://doi.org/10.1016/j.ecolmodel.2015.07.017

Turner, R. K., Morse-Jones, S., & Fisher, B. (2010). Ecosystem valuation: A sequential decision support system and quality assessment issues. Annals of the New York Academy of Sciences, 1185(1), 79–101. https://doi.org/10.1111/j.1749-6632.2009.05280.x

United Nation. (2015). Sustainable Development: The 17 Goals. United Nations | Department of Economic and Social Affairs-Sustainable Development. https://sdgs.un.org/goals

United Nations. (2022). United Nations Deparment for Economic and Social Affairs, Population Division.World Population Prospects 2022: Summary of results: Vol. UN DESA/POP/2022/TR/NO. 3.

US EPA. (2016, November 16). US Environmental Protection Agency (US EPA) [Collections and Lists]. https://www.epa.gov/environmental-topics/air-topics

Vo Quoc, T., Kuenzer, C., Vo, Q. M., Moder, F., & Oppelt, N. (2012). Review of valuation methods for mangrove ecosystem services. Ecological Indicators, 23, 431–446. https://doi.org/10.1016/j.ecolind.2012.04.022

Wang, H., He, J., & Huang, D. (2020). Public distrust and valuation biases: Identification and calibration with contingent valuation studies of two air quality improvement programs in China. China Economic Review, 61, 101424. https://doi.org/10.1016/j.chieco.2020.101424

Wang, S., Song, R., Xu, Z., Chen, M., Di Tanna, G. L., Downey, L., Jan, S., & Si, L. (2024). The costs, health and economic impact of air pollution control strategies: a systematic review. Global health research and policy, 9(1), 30. https://doi.org/10.1186/s41256-024-00373-y

Wang, Y., Zhang, Q., Bilsborrow, R., Tao, S., Chen, X., Sullivan-Wiley, K., Huang, Q., Li, J., & Song, C. (2020). Effects of payments for ecosystem services programs in China on rural household labor allocation and land use: Identifying complex pathways. Land Use Policy, 99, 105024. https://doi.org/10.1016/j.landusepol.2020.105024

Wegner, G., & Pascual, U. (2011). Cost-benefit analysis in the context of ecosystem services for human well-being: A multidisciplinary critique. Global Environmental Change, 21(2), 492–504. https://doi.org/10.1016/j.gloenvcha.2010.12.008

World Health Organization. (2021, September 22). New WHO Global Air Quality Guidelines aim to save millions of lives from air pollution. Retrieved from https://www.who.int/news/item/22-09-2021-new-who-global-air-quality-guidelines-aim-to-save-millions-of-lives-from-air-pollution

Xi, J. (2009). Valuation of Ecosystem Services in Xishuangbanna Biodiversity Conservation Corridors Initiative Pilot Site, China (pp. 1–52). Greater Mekong Subregion Core Environment Program (ADB TA6289).

Xiao, F., Brajer, V., & Mead, R. W. (2006). Blowing in the wind: The impact of China's Pearl River Delta on Hong Kong's air quality. Science of The Total Environment, 367(1), 96–111. https://doi.org/10.1016/j.scitotenv.2006.01.010

Xie, Q., Yue, Y., Sun, Q., Chen, S., Lee, S.-B., & Kim, S. W. (2019). Assessment of Ecosystem Service Values of Urban Parks in Improving Air Quality: A Case Study of Wuhan, China. Sustainability, 11(22), 6519. https://doi.org/10.3390/su11226519

Yu, H., Chen, C., & Shao, C. F. (2023). Spatial and temporal changes in ecosystem service driven by ecological compensation in the Xin'an River Basin, China. Ecological Indicators, 146, 109798. https://doi.org/10.1016/J.ECOLIND.2022.109798

Zaman-Ul-haq, M., Saqib, Z., Kanwal, A., Naseer, S., Shafiq, M., Akhtar, N., Bokhari, S. A., Irshad, A., & Hamam, H. (2022). The Trajectories, Trends, and Opportunities for Assessing Urban Ecosystem Services: A Systematic Review of Geospatial Methods. Sustainability (Switzerland), 14(3). https://doi.org/10.3390/su14031471

Zhang, L., Fukuda, H., & Liu, Z. (2019). Public willingness to pay for sand and dust weather mitigation: A case study in Beijing, China. Journal of Cleaner Production, 217, 639–645. https://doi.org/10.1016/j.jclepro.2019.01.234

Zhang, P., Shao, G., Zhao, G., Le Master, D. C., Parker, G. R., Dunning, J. B., & Li, Q. (2000). China's Forest Policy for the 21st Century. Science, 288(5474), 2135–2136. https://doi.org/10.1126/science.288.5474.213

Zhang, X., Jin, Y., Dai, H., Xie, Y., & Zhang, S. (2019). Health and economic benefits of cleaner residential heating in the Beijing–Tianjin–Hebei region in China. Energy Policy, 127, 165-178. https://doi.org/10.1016/j.enpol.2018.12.008

Zhao, A., Stevenson, D., Heal, M., & Bollasina, M. (2022). The North-South divide in global air pollution: drivers and impacts. 10.21203/rs.3.rs-1188431/v1

JJEES

JJEES (2026) 17 (1): 56-62
ISSN 1995-6681

Jordan Journal of Earth and Environmental Sciences

"Soil Evolution Response Using Geochemical Weathering Indicators in Different Climates" (a Scientific review)

Omar Alsalam[1*], Abdul Baqi D.S. Almaamouri[1], Mahmood Ahmed L. Al-Bayati[2]

[1] Department of Soil Sciences and Water Resources, College of Agricultural Engineering Sciences, University of Baghdad, Baghdad, Iraq.
[2] Department of Soil Sciences and Water Resources, College of Agriculture, University of Tikrit, Tikrit, Iraq.

Received on 30 December 2024; Accepted on 16 August 2025

Abstract

Rates of weathering and renewable soil production are significantly influenced by climate. To assess the level of soil development, geochemical weathering indices are frequentlyutilized. Infinite varieties of soils with different characteristics could be created by accounting for the climatic variability of the variables and processes. The impacts of weathering are reflected in the concentrations of elements in soils. Yet, the effects of pedogenic losses, transformations, gains, and translocations, as well as chemical weathering are prominently reflected in the mineralogical and chemical composition of more mature soils. The impact of climatic contrast on soil properties has been demonstrated by studies in humid regions with declining temperatures and rising rainfall. Generally speaking, tropical climates produce deeply weathered soils made up of stable secondary minerals. The soils, on the other hand, are typically weakly to moderately developed in areas with drier climates, such as arid or semi-arid environments. Climate is accountable for the emergence of weakly to moderately developed soils. To predict how climate will affect weathering rates, soil- formating processes, and soil evolutionary stages, research on the diversity of soils grown under opposing climate conditions might be useful in this regard.

Keywords: *Climate, Indices weathering, Soil development, Soil formation, Geochemical weathering, Soil pedogenesis.*

1. Introduction

Information on the factors that influence weathering rates due to climatic change can be found in the evolution of soil. Thus, weathering rates are regarded as a function of climate, and there are variable climatic factors like evapotranspiration, weathering, precipitation amount, and water percolation, among other properties that change with climate (Moshtaha et al., 2025; Al Shamary et al., 2022; Al-Shamare and Essa, 2020). Climate is a significant soil-forming factor that affects the genesis, characteristics, and classification of soils. One crucial element that regulates chemical weathering processes is the availability of water (Merkli et al., 2009; Lybrand et al., 2011; Moazallahi and Farpoor, 2012; Fayyadh and Ismail, 2021; Saleh et al., 2023; Jimoh et al., 2023). Precipitation driven by climate change might influence the dynamics of soil water availability. The rates and types of biological, chemical, and physical processes are influenced by temperature and precipitation, which have a special impact on soil properties. The effect of climatic variations on plant groups and soil types has been previously studied. The primary mechanisms guiding soil development might alter when pedogenesis processes alter the geochemical characteristics of the soil.

Through changing the rate and type of chemical processes and the consequent chemical characteristics, climate change could have a considerable effect on geochemical weathering. Changes in soil organic matter, acidity, clay content, and exchangeable ions were prevalent trends in previous investigations of how climate affects weathering and soil (Egli et al., 2006; Lawrence et al., 2015; Fattah and Karim, 2021; Razvanchy and Fayyadh, 2023; Ilevbare and Adeleye, 2023). The process by which weathering modifies the constituents of the parent deposit by removing more mobile (i.e., soluble) elements and simultaneously enriching less mobile elements, as well as by altering and forming new secondary minerals and accumulating organic matter, is known as pedogenesis. The lithology of the parent material, climatic conditions, topography, time, existence of organisms within the strata, vegetation, and time all have a significant impact on the rate of pedogenesis. In both non-crystalline and crystalline phases, geochemical weathering begins with the loss of non-hydrolyzing cations (such as magnesium, calcium, and sodium) and the concomitant enrichment of aluminum, silicon, and iron ions. Geochemical weathering indices, based on the chemistry of surface soils, are frequently used to quantify and compare the relative intensity and extent of soil pedogenesis. As a result, the climate regime has a significant influence on the link between chemical weathering and the extent of the response to soil evolution. Although their respective roles are still hotly contested, climate variability has been considered the principal controlling influence on weathering up to this point. Gathering as various chemical weathering indicators as possible while knowing how to use and apply them to the evolution of soil profiles and their properties which were examined across various ecosystems is the primary goal of this work.

* Corresponding author e-mail: omar.t@coagri.uobaghdad.edu.iq

2. References Review

2.1. Chemical weathering indices

The most significant geochemical proxies frequently employed to show soil weathering processes are chemical weathering indices (Zhou et al., 2015). (Lybrand etal., 2011; Moazallahi and Farpoor, 2012; Egli etal., 2003; Osat et al., 2016) They could be utilized to illustrate how climate affects soil weathering. The primary function of chemical weathering indices is to predict the sources of mobile nutrients and changes in metal concentrations, evaluate soil fertility, determine the amount of yield of mobile components throughout weathering, and improve kinetic element mobility in weathering (Dönmez, 2023). The mechanisms and intensity of chemical weathering are described by chemical indices derived from soil chemical investigations. Mineral breakdown causes element breakdown and redistribution during weathering. Since various weathering processes have varying effects on particular elements, element redistribution can follow contrasting patterns (Alsalam et al., 2025). A common method for estimating the extent of weathering and the behavior of elements throughout weathering is the redistribution and mobility of elements within the secondary environment (Beyala et al., 2009; El-Hafez et al., 2019; Issa, 2022). As they are freed from host minerals and leached from the parent rock, the more geochemically mobile total elements (MgO, Na_2O, CaO, and K_2O) will generally decrease with weathering grade. There will be fewer immobile and mobile oxides, including SiO_2, P_2O_5, Al_2O_3, Fe_2O_3, MnO, and TiO_2 (Baumann et al., 2014). Four crucial factors must be considered for the effective use of chemical weathering indices (Haskins, 2006):

1. It is best to use just those elements that exhibit consistent geochemical behavior throughout weathering.
2. The indices ought to be unaffected by the weathered material's level of oxidation.
3. It is best to use just those chemical elements that are frequently reported in studies.
4. Chemical indices have to be rather simple to use and apply.

The type and redistribution of weathered products cause the behavior of many chemical elements to be complex, and it was determined that chemical weathering indices must be chosen based on site-specific behavior (Haskins, 2006).

2.2. Calculation of weathering indices

Weathering indices is a technique for digitizing weathering. Conventionally, many formulas based on the molecular ratios of major-element oxides are used to calculate weathering indices. The index values show the chiometric variation of the key element oxides throughout weathering. The weight percentages of the individual oxides make it simple to determine the molecular ratios of each oxide (Al-Momani and Alqudah, 2020). For the purpose of describing weathering in soils, numerous indices were proposed (Harnois, 1988; Nesbit and Young, 1989). All indices share a common general premise:the calculation of various ratios between basic cations (Mg, Ca, Na, and K) and cations such as Si and Al. Some of the most popular indices are shown in the examples below.

Chemical weathering index	Formula	References
Weathering potential index (WPI)	$WPI = \frac{(K_2O+Na_2O+CaO-H_2O)*100}{SiO_2+AL_2O_3+Fe_2O_3+FeO+TiO_2+CaO+MgO+K_2O+Na_2O}$	Ruxton, 1968
Product index (PI)	$PI = \frac{(SiO_2)*100}{SiO_2+AL_2O_3+Fe_2O_3+FeO+TiO_2}$	Ruxton, 1968
Ruxton ratio (R)	$R = \frac{SiO_2}{AL_2O_3}$	Ruxton, 1968
Parker index (P)	$P = \left[\left(\frac{2Na_2O}{0.35}\right)+\left(\frac{MgO}{0.9}\right)+\left(\frac{2K_2O}{0.25}\right)+\left(\frac{CaO}{0.7}\right)\right]X100$	Parker, 1970
Vogt ratio (V)	$V = \frac{(K_2O+AL_2O_3)*100}{CaO+MgO+Na_2O}$	Vogt, 1927; Roaldest, 1972
Modified weathering potential index (MWPI)	$MWPI = \frac{(K_2O+Na_2O+CaO+MgO)*100}{SiO_2+AL_2O_3+Fe_2O_3+CaO+MgO+K_2O+Na_2O}$	Vogel, 1973
Lixiviation index (ß)	$ß = \frac{\left(\frac{K_2O+Na_2O}{AL_2O_3}\right)Weathered}{\left(\frac{K_2O+Na_2O}{AL_2O_3}\right)Fresh+\left(\frac{CaO}{MgO}\right)}$	Rocha-Filho et al., 1985
Loss on ignition (LOI)	LOI = H_2O^+ content (in weight) of specimen heated to 900-1000ºC	Sueoka et al., 1985
Alumina to potassium-sodium oxide ratio (ALK)	$ALK = (\frac{K_2O}{K_2O+Na_2O})X100$	Harnois & Moore, 1988

Alumina to calcium-sodium oxide ratio (ACN)	$CAN = (\frac{AL_2O_3}{AL_2O_3+CaO+Na_2O})X100$	Harnois, 1988
Chemical index alteration (CIA)	$CIA = \frac{AL_2O_3}{AL_2O_3+CaO+K_2O+Na_2O}X100$	Nesbitt & Young, 1982
Chemical index of weathering (CIW)	$CIW = \frac{AL_2O_3+K_2O}{AL_2O_3+CaO+Na_2O}X100$	Harnios, 1988
Plagioclase index of alteration (PIA)	$PIA = \frac{AL_2O_3-K_2O}{AL_2O_3+CaO+Na_2O-K_2O}X100$	Fedo *etal*., 1995
Silica-Titania index (STI)	$STI = \frac{\left(\frac{SiO_2}{TiO_2}\right)}{\left(\frac{SiO_2}{TiO_2}+\frac{SiO_2}{AL_2O_3}\right)+\left(\frac{AL_2O_3}{TiO_2}\right)}\ X\ 100$	De Jayawardena & Lzawa, 1994
Index of compositional variability (ICV)	$ICV = \frac{Fe_2O_3+TiO_2+CaO+MgO+K_2O+Na_2O+MnO}{AL_2O_3}$	Cox et al., 1995
Mobiles index (I_{mob})	$I_{mob} = \frac{(CaO+Na_2O+K_2O)fresh-(CaO+Na_2O+K_2O)\ weathered}{(CaO+Na_2O+K_2O)\ fresh}$	Irfan, 1996
Sesquioxide content (SOC)	$SOC = AL_2O_3 + Fe_2O_3$	Irfan, 1996
Mineralogical index of alteration (MIA)	MIA = 2*(CIA-50)	Voicu *etal*., 1996
Weathering index on carbonate-rich sediments (FENG)	$FENG = \frac{AL_2O_3+Fe_2O_3}{P_2O_5+CaO+MgO+K_2O+Na_2O}$	Feng, 1997
S/SAF	$\frac{SiO_2}{SiO_2 + AL_2\ O_3 + Fe_2O_3}$	Hill *etal*., 2000
Chemical proxy of alteration (CPA)	$CPA = \frac{AL_2O_3}{AL_2O_3+Na_2O}X100$	Buggle et al., 2011

The majority of mobile cations are among the elements removed during soil weathering, as measured by the weathering potential index (WPI). This index could be more dependable compared to a simple index that only depends on one or two chemical components, because it incorporates a large number of them—the intensity regarding leaching and weathering increases with decreasing measured WPI value. Stated differently, a declining Product Index (PI) indicates a declining silica content, which happens with the commencement of weathering, and a falling WIP index declines with greater weathering intensity as well as soil development (Ng et al., 2001). Ruxton (1968) developed the Silica-Alumina Ratio, which measures total element loss as a ratio of alumina content (assuming silica loss to be equivalent to total element loss). He believed that the SiO2/Al2O3 ratio could be used to determine the extent of weathering in humid climates on freely draining acidic rocks with an acidic weathering environment. The proportions of the main alkaline metals and their strength of binding with oxygen serve as weighting factors for the Parker Index (p), developed by Parker (1970). According to Gupta and Rao (2001), this index can be used for basic, intermediate, and acidic rocks, in which hydrolysis is the primary silicate weathering process. Vogt Ratio (V), developed by Vogt (1927) and promoted by Roaldset (1972), assumed that potassium remained stable within the soil weathering system while attempting to ascertain the ratio of immobile to mobile cations. In his evaluation of the weathering regarding acid metavolcanics, Vogel (1973) modified Ruxton's WPI by removing the H_2O^+ and iron oxidation state from the original WPI equation to create the Modified Weathering Potential Index (MWPI). Loss on ignition (LOI) has been suggested by Sueoka et al. (1985) as a reliable measure of the extent of chemical weathering. Just H_2O^+-content (in weight) of a specimen heated to 900 ˚C–1000 ˚C is referred to here as LOI, and it rises as weathering progresses due to hydration and clay formation. This signal, which is the sum of H_2O^- and H_2O^+, will be referenced frequently in the following.

Given that feldspars are the most prevalent reactive minerals in the earth's upper crust, Nesbitt and Young (1982) discovered that aggressive soil solutions typically remove

sodium, calcium, and potassium from the feldspars during weathering. They suggested that the aluminaratio-toalkalis ratio might normally increase in the weathered product as weathering progressed and that the Chemical Index of Alteration (CIA) may provide a reliable indicator of the extent of weathering. Although they were leached throughout weathering, Harnois, (1988) proposed that potassium cations could be adsorbed onto other clays in the weathered profile through ion exchange, potentially disrupting K+ geochemical trends. As an alternative to WPI, p,V, MWPI, and CIA, he suggested the Chemical Index of Weathering (CIW), which excludes K2O, as a more accurate indicator of weathering. Since plagioclase is common in silicate rocks and dissolves rather quickly, PIA could be used as an alternative to the CIW index in cases where just plagioclase weathering needs to be studied (Fedo et al., 1995). As soil changes and weathering intensity increase, so do the indicators. Since potassium has a high exchange capacity and can be adsorbed onto other clays in the weathering profile, obscuring its mobility, Harnois, (1988) argued that using K2O as a mobile component in WPI, CIA, and MWPI restricts their application to soils where potassium has leached. In contrast to evidence that potassium is frequently leached, the Vogt Ratio treats K2O as an immobile component.

CaO should be limited to that obtained from silicate minerals (CaO*) in such indices. The carbonates Ca have been subtracted from total Ca to estimate CaO*. Depending on the supposition that feldspar and mica are the most prevalent minerals in the soil, CIW, CIA, and PIA are regarded as indicators of the degree of feldspar and mica conversion to clay (Baumann et al., 2014; Osat et al., 2016). All such authors agree that knowledge of the geochemical composition, processes, and trends of specific material of interest is necessary for the successful application of any weathering index for chemical weathering indices to be effective. Through their investigations of metamorphic rocks in Sri Lanka, De Jayawardena and Izawa (1994) suggested the silica-titania index for chemical weathering and concluded that there may be correlations between SiO2, Al2O3, and TiO2. There has long been disagreement over whether the different weathering indices apply to other materials and weathering conditions. It is possible to ascertain the mineralogy (primary or secondary minerals) of soils by their chemical composition. The degree of chemical weathering is estimated by the index of compositional variability (Cox et al. 1995). The ratio of major cations to Al2O3 is higher in primary minerals than in pedogenic clay minerals. As a result, primary minerals have a higher ICV. ICV values greater than one are therefore indicative of young, immature soils that contain a significant proportion of primary silicate minerals. Conversely, ICV values below 1 should be observed in highly weathered soils that contain primarily secondary clay minerals formed under intense weathering (Cox et al. 1995).

The degree of decomposition regarding rocks containing feldspar is indicated by the mobiles index (Imob) (Aristizabal et al., 2005). Since it incorporates information from both the weathering products and their fresh parent materials, the index provides useful insights and evaluates the variation in the concentrations of mobile cations (Na2O, K2O, and CaO). Thus, it shows how soil composition varies as a result of weathering. The more intense the weathering, the greater the difference in the number of mobile cations in fresh and weathered soils (Ng et al., 2001). The insoluble oxides Al2O3 and Fe2O3 are represented by the sesquioxide content (SOC) of a sample. According to Ng et al. (2001), a higher SOC suggests either a intensity of leaching or oxidation driven by the enrichment of ferric iron from the oxidation of ferrous iron. The degree of mineralogical weathering is assessed using the mineralogical index of alteration (MIA). Incipient (0–20%), moderate (40–60%), weak (20–40%), and intense to extreme (60–100%) weathering are all indicated by the MIA value. A value of 100% indicates complete weathering of parent rock as well as the formation of a primary mineral into its corresponding weathered product. To overcome the carbonate biases mentioned above, Feng (1997) factored out Ca and added Mg and P as crucial factors. Throughout the weathering and soil development processes, this index rises. Since Al and Na are the best elements to reflect weathering intensity, CPA seeks to avoid the biases of carbonate Ca and K-fixation that have been previously addressed (Buggle et al., 2011). Because K phases, like the K-feldspar and clay minerals, have a higher susceptibility to weathering, the overall K release is less than the Na release. This analysis suggests that K has a negligible impact in cold climates, which makes this WI a useful substitute for our study.

2.3. Soil development response using chemical weathering

The stages of soil development are associated with characteristic soil features, namely typical geochemical properties, which were researched in the South China Sea, including Hainan Island, which experiences a tropical monsoon climate. The study found that whereas Mg, Ca, Na, K, and Si all significantly vanished throughout rock weathering and soil formation, Al and Fe were comparatively enriched. The degree of sequential weathering over successive time periods was not adequately reflected in indicators based on soil microelements, such as the silicon-aluminum ratio of the alteration, the chemical index of alteration (CIA), and the chemical index of weathering (CIW). As a measure of soil formation, the weathering index (WI) shows a strong correlation with soil formation stages (Zhang et al., 2007). The concept of geochemical weathering indices is introduced in Southeast and Eastern Europe. It stands for the records of Late and Middle Pleistocene climate shifts in the area. The best index for silicate weathering is the Chemical Proxy of Alteration (CPA). The CIA, CIW, and PIA were examined under regularly used climatic conditions. At the same time, biases brought on by K-fixation or uncertainties in distinguishing carbonate-Ca from silicate-Ca might affect (PIA, CIA, CIW). Against such impacts, the CPA is insensitive. It also offers the same advantages as other Na-type indices (Buggle et al., 2011). Understanding the relationships between climate, chemical weathering, and pedogenic processes in a variety of semi-arid ecosystems in southern Arizona. The data show that climate and chemical weathering have a significant

interactive effect on soil development rates (Lybrand et al., 2011). The intensity of chemical weathering in certain weathering profiles is assessed using Parker's WIP and CIA. To anticipate chemical weathering in China, which is affected by the humid subtropical climate, the concentrations of key oxides were investigated and gathered. The steady rise in CIA, the decline in WIP values, and the drop in altitude all point to an increase in weathering intensity. In China, the main determinants of chemical weathering are surface runoff and precipitation. This work illustrates that suitable geochemical proxies can be used to quantify the carefully applied concentration of integrated chemical weathering (Shao et al., 2012). The main soils formed on igneous rocks in the semi-arid northwest of Iran were evaluated for weathering intensity. The soil profiles formed on volcanic rocks are more weathered than those on plutonic igneous rocks, according to the research area's weathering indicator data (Yousefifard et al., 2012). Pedogenic oxide ratios (POR) and Weathering indexes (WI) were employed in China to characterize patterns of soil development and climate weathering intensity, especially during the climatic period along gradients of elevation that are most impacted by the varied influences of the Asia-India Monsoon. Although specific soil moisture (SM) conditions result from certain climatic factors, topography and climate are always linked to them. They discovered that WI might vividly show weathering tendencies under climatic variations. The most suitable is the CIA (Baumann et al., 2014). Surface soil samples have been -collected from a range of profiles (2000–3600 m) in a humid zone in northwest Ethiopia. The chemical weathering of the soils was investigated. Principal component analysis (PCA) was used to determine the mineral alteration assemblage and the formation throughout pedogenesis, and several chemical weathering indices were used to assess the degree of change in CIA and CIW. CIW and CIA could be more readily identified when comparing weathering indices computed in this work, and they could provide information regarding the formation of the initial rock composition. Furthermore, the degree of pedogenesis is known to be influenced by weathering factors, such as precipitation, which are linked to the CIA index. Information from traditional chemical weathering indices can be supported by the CIA index, which could help us better understand the processes that occur throughout weathering (Le Blond et al., 2015). To demonstrate the relationship between soil development indices and soil taxonomic classes, this work was carried out in a hilly area of northern Iran. To assess soil development, geochemical weathering indices are commonly used. Those indices indicated reduced weathering intensity in more developed soils, even though there were substantial relationships between mostgeochemical weathering indices and the Soil Taxonomic Classes; the Vogt index had the greatest coefficient of correlation. The reason for these connections was that low-gradient slopes, where weathering products from upper slopes accumulate and their parent materials are carbonatic, tended to have better-developed soils (Osat et al., 2016). Assess the sequential effects of climate on soil pedogenesis and weathering rates. Geochemical signals were directly linked to notable variations in the soils' morphological, chemical, and physical characteristics. Higher soil development in moist places was to be a significant factor in defining the soil properties in the study area, notwithstanding the influence of climate on weathering. Over successive climates, the intensity of weathering transformations has changed dramatically. The soil profiles in the moist region had the highest weathering densities (Silva et al., 2016). The reliability of various mineralogical and geochemical weathering proxies as climatic indicators is tested, and the relationships between provenance and climatic controls on soil composition are examined using complementary geochemical datasets on soil collected along the Atlantic margin of subequatorial southwestern Africa. These proxies are more accurate climate estimators in the geological context of SW Africa than traditional weathering indices, such as WIP or CIA (Dinis et al., 2017). Used geochemical data, specifically the CIA, CIW, Base/R2O3 Ratio, WIP, and PIA, to assess the extent of soil weathering in semi-arid and arid climatic zones in Turkey. The findings unequivocally demonstrated that gradual progressive weathering is the cause of soil development at the Altınova State Farm in Konya, Turkey's Central Anatolia region. The primary signs in this instance are weak structural development and secondary calcium carbonate illuviation, with a weathering ratio of silicon to aluminum larger than two in every profile (Tunçay et al., 2019). This investigation was carried out in Turkey's mountainous, humid regions. Four representative profiles were dug at various heights for this purpose. Four soils were transected between elevations of 1139 and 1809 meters, and soil samples were collected for geochemical analysis from each horizon. Pedogenic processes for climate across various elevations are compared using the Mineral Alteration Index (MIA), WIP, PIA, and CIA. Soil Taxonomic Classes were strongly impacted by climosequene characteristics. The findings indicate that as elevation increases, the rate of chemical weathering of the CIA, PIA, CIW, and MIA indicators decreases. On the other hand, the WIP value increased at higher altitudes. Thus, the region's elevation-dependent climatic factors were sufficiently effective to affect soil formation, and the elevation difference between the profiles has increased precipitation, leading to intense weathering and leaching. The main factors influencing weathering intensity are the availability and flux of water through the soil, which are also decisive factors and sufficient to distinguish the profiles. According to this research, climatic conditions had a considerable impact on soil qualities and processes (Alsalam et al., 2020).

3. Conclusions

This study has shown how different types of chemical weathering indices can be used to evaluate soil evolution as a function of climate according to their degree of weathering. Previous studies clearly indicate that climatic conditions are an essential factor in weathering since climate determines the weathering products of soil horizons. Water availability is a critical factor that controls chemical weathering processes. The speed of chemical reactions increases with increasing water availability. In other words, increased precipitation is linked to leaching processes and thus affects chemical

weathering indicators.

According to previous results, the rate of chemical weathering of CIA, CIW, PIA, CPA and MIA indicators went up with ncreased rainfall leaching, leading to the formation of more developed soils. In contrast, WIP value increased in climates with less leaching and therefore less developed soils formed. The availability and flux of water through the soil are the prime factors in chemical weathering intensity, and they have a decisive role in profile differentiation and the formation of different types of soils. This study indicated that soil properties and processes were strongly related to water availability, which determines the leaching regime and chemical weathering rates. This shift in climate produced appreciable changes in different types of soils.

References

AlMomani, T., & Alqudah, M. (2020). Mineralogical and geochemical characterization of Jarash kaolinitic clay, northern Jordan. Jordan Journal of Earth & Environmental Sciences, 11(4), 272–281.

Al Shamary, S. H. K., Al Maamouri, D. S., Hassan, A. B., & Dwenee, S. J. (2022). Effects of climatic variation on weathering intensity for the mineral composition in some Iraqi soils. Caspian Journal of Environmental Sciences, 5, 991–1001.

AlShamare, A. H. D., & Essa, S. K. (2020). The effect of sedimentation sources on the exchange properties of the clay particles of some soils in Wasit and Maysan governorates. Plant Archives, 20(2), 566–573.

Alsalam, O., Isa, H. A., Al-Bayati, M. A. L. and Alserae, H. (2025). Topographic effect on the total oxides distribution of calcareous soils in northern Iraq. PJOAR 38: 162-74. doi:10.17582/journal.pjar/2025/38.2.162.174.

Alsalam, O., Şeker, C., & Dedeoğlu, M. (2020). Quantifying the role of chemical weathering rates on soil developed along an altitudinal transect in mountainous environments, Turkey. Eurasian Journal of Soil Science, 2, 140–150.

Aristizabal, E., Roser, B., & Yokota, S. (2005). Tropical chemical weathering of hillslope deposits and bedrock source in the Aburrá Valley, northern Colombian Andes. Engineering Geology, 81, 389–406.

Baumann, F., Schmidt, K., Dörfer, C., He, J.S., Scholten, T., & Kühn, P. (2014). Pedogenesis, permafrost, substrate and topography: Plot and landscape scale interrelations of weathering processes on the centraleastern Tibetan Plateau. Geoderma, 226, 300–316. https://doi.org/10.1016/j.geoderma.2014.02.016

Beyala, V. K. K., Onana, V. L., Priso, E. N. E., Parisot, J. C., & Ekodeck, G. E. (2009). Behaviour of rare earth elements and mass balance calculations in a lateritic profile over chlorite schist in South Cameroon. Chemie der Erde, 69, 61–73.

Buggle, B., Glaser, B., Hambach, U., Gerasimenko, N., & Marković, S. (2011). An evaluation of geochemical weathering indices in loess–paleosol studies. Quaternary International, 2, 12–21.

Cox, R., Lowe, D. R., & Cullers, R. L. (1995). The influence of sediment recycling and basement composition on evolution of mudrock chemistry in the southwestern United States. Geochimica et Cosmochimica Acta, 59, 2919–2940. https://doi.org/10.1016/00167037(95)001694

De Jayawardena, U., & Izawa, E. D. S. (1994). Application of present indices of chemical weathering for Precambrian metamorphic rocks in Sri Lanka. Bulletin of the International Association of Engineering Geology, 49, 55–61.

Dinis, P., Garzanti, E., Vermeesch, P., & Huvi, J. (2017). Climatic zonation and weathering control on sediment composition (Angola). Chemical Geology, 7, 110–121.

Dönmez, H. (2023). Applications of soil geochemistry in mineral exploration. ISERDAR, 1(1), 12–18. https://doi.org/10.5281/zenodo.10436738

Egli, M., Mirabella, A., Sartori, G., & Fitze, P. (2003). Weathering rates as a function of climate: results from a climosequence of the Val Genova (Trentino, Italian Alps). Geoderma, 111, 99–121.

Egli, M., Mirabella, A., Sartori, G., Zanelli, R., & Bischof, S. (2006). Effect of north and south exposure on weathering rates and clay mineral formation in Alpine soils. Catena, 67, 155–174.

ElHafez, N. A., Mousa, A., ElHariri, T., ElMoghny, M. A., & Sharaka, H. (2019). Mineralogical and geochemical studies on some early Miocene sediments of southwestern Sinai, Egypt. Jordan Journal of Earth & Environmental Sciences, 10(2), 64–74.

Fattah, M. A., & Karim, K. H. (2021). Performance of linear models in predicting cation exchange capacity of calcareous soils. Iraqi Journal of Agricultural Sciences, 52(6), 1489–1497.

Fayyadh, M. A., & Ismail, H. K. (2021). Genesis, development, and classification for some selected soils at Kurdistan region, north of Iraq. Iraqi Journal of Agricultural Sciences, 52(6), 1498–1507.

Fedo, C. M., Nesbitt, H. W., & Young, G. M. (1995). Unraveling the effects of potassium metasomatism in sedimentary rocks and paleosols, with implications for paleoweathering conditions and provenance. Geology, 23, 921–924. https://doi.org/10.1130/0091 7613(1995)023<0921:UTEOKM>2.3.CO;2

Gupta, A. S., & Rao, K. S. (2001). Weathering indices and their applicability for crystalline rocks. Bulletin of Engineering Geology and the Environment, 60, 201–221. https://doi.org/10.1007/s100640100100

Harnois, L. (1988). The CIW index: A new chemical index of weathering. Sedimentary Geology, 55, 319–322.

Harnois, L., & Moore, J. M. (1988). Geochemistry and origin of ore chemistry formation, a transported paleoregolith in the Grenville Province of southern Ontario, Canada. Chemical Geology, 69, 267–289.

Haskins, D. A. V. I. D. (2006). Chemical and mineralogical weathering indices as applied to a granite saprolite in South Africa. In The 10th IAEG International Congress, Nottingham, United Kingdom: Cosmogenic Nuclides, Geology, 7, 597–600.

Hill, I., Worden, R., & Meighan, I. (2000). Yttrium: The immobilitymobility transition during basaltic weathering. Geology, 28, 923–926.

Ilevbare, M., & Adeleye, R. A. (2023). Geochemical discriminant for provenance, source area weathering and paleoredox of some shale deposits in Edo State, Nigeria. Jordan Journal of Earth & Environmental Sciences, 14(4), 258–267.

Irfan, T. (1996). Mineralogy, fabric properties and classification of weathered granites in Hong Kong. Quarterly Journal of Engineering Geology and Hydrogeology, 1, 5–35.

Issa, S. K. (2022). Soil minerals. Ministry of Higher Education and Scientific Research, University House for Printing and Publishing.

Jimoh, R. O., Olatunji, A. S., Ajadi, J., & Afolabi, A. O. (2023). Mineralogy and geochemistry of berylbearing pegmatite dykes from Gbayo, southwestern Nigeria. Jordan Journal of Earth & Environmental Sciences, 14(2), 91–102.

Lawrence, C. R., Harden, J. W., Xu, X., Schulz, M. S., & Trumbore, S. E. (2015). Longterm controls on soil organic carbon with depth and time: a case study from the Cowlitz River Chronosequence, WA, USA. Geoderma, 247–248, 73–87. https://doi.org/10.1016/j.geoderma.2015.02.005 U.S. Geological Survey

Le Blond, J. S., Cuadros, J., Molla, Y. B., Berhanu, T., Umer, M., Baxter, P. J., & Davey, G. (2015). Weathering of the Ethiopian volcanic province: A new weathering index to characterize and compare soils. American Mineralogist, 100(11–12), 2518–2532. ResearchGate

Lybrand, R., Rasmussen, C., Jardine, A., Troch, P., & Chorover, J. (2011). The effects of climate and landscape

position on chemical denudation and mineral transformation in the Santa Catalina Mountain Critical Zone Observatory. Applied Geochemistry, 26(Supplement), S80–S84. https://doi.org/10.1016/j.apgeochem.2011.03.036

Merkli, C., Sartori, G., Mirabella, A., Egli, M., Mancabell, A., & Plotze, M. (2009). The soils in the Brenta region: Chemical and mineralogical characteristics and their relation to landscape evolution. Studi Trentini di Scienze Naturali, 85, 7–22.

Moazallahi, M., & Farpoor, M. H. (2012). Soil genesis and clay mineralogy along the xericaridic climotoposequence in southcentral Iran. Journal of Agricultural Science & Technology, 14, 683–696. SDIOPR

Moshtaha, R., Romer, R. L., & Jarrar, G. H. (2025). Age, geochemistry, and petrogenetic constraints on Ediacaran granitoids, southwest Jordan. Jordan Journal of Earth & Environmental Sciences, 16(2), 117–135. Jordan Journal+1

Nesbitt, H. W., & Young, G. (1982). Early Proterozoic climates and plate motions inferred from major element chemistry of lutites. Nature, 299(5885), 715–717. Eurasian Journal of Soil Science

Nesbitt, H. W., & Young, G. M. (1989). Formation and diagenesis of weathering profiles. Journal of Geology, 97(2), 129–147. Eurasian Journal of Soil Science

Ng, C. W. W., Guan, P., & Shang, Y. J. (2001). Weathering mechanisms and indices of igneous rocks of Hong Kong. Quarterly Journal of Engineering Geology and Hydrogeology, 34(2), 133–151. Eurasian Journal of Soil Science

Osat, M., Heidari, A., Eghbal, M. K., & Mahmoodi, S. (2016). Impacts of topographic attributes on soil taxonomic classes and weathering indices in a hilly landscape in northern Iran. Geoderma, 281, 90–101.

Parker, A. (1970). An index of weathering for silicate rocks. Geological Magazine, 107(6), 501–504.

Razvanchy, H. A. S., & Fayyadh, M. A. (2023). Study of development and classification in Erbil province, Kurdistan, Iraq using mathematical indices. Iraqi Journal of Agricultural Sciences, 54(6), 1802–1813.

Roaldset, E. (1972). Mineralogy and geochemistry of Quaternary clays in the Numedal area, southern Norway. Norsk Geologisk Tidsskrift, 52, 335–369.

RochaFilho, P., Antunes, F. S., & Falco, M. F. G. (1985). Quantitative influence of the degree of weathering upon the mechanical properties of a young gneiss residual soil. In Proceedings of the First International Conference on Geomechanics in Tropical Lateritic and Saprolitic Soils, Brasília, 1, 281–294.

Ruxton, B. P. (1968). Measures of the degree of chemical weathering of rocks. Journal of Geology, 76, 518–527.

Saleh, A. M., Khudhair, M. F., & Ahmed, F. W. (2023). Identification of top soils with discriminant analysis in AlMaimouna project, Maysan, Iraq. International Journal of Agricultural and Statistical Sciences, 19(2), 657–668.

Shao, J., Yang, S., & Li, C. (2012). Chemical indices (CIA and WIP) as proxies for integrated chemical weathering in China: Inferences from analysis of fluvial sediments. Sedimentary Geology, 265, 110–120.

Silva, Y. J. A. B., Do Nascimento, C. W. A., Biondi, C. M., Van Straaten, P., de Souza Jr, V. S., & Ferreira, T. O. (2016). Weathering rates and carbon storage along a climosequence of soils developed from contrasting granites in northeast Brazil. Geoderma, 284, 1–12.

Sueoka, T., Lee, I. K., Huramatsu, M., & Imamura, S. (1985). Geomechanical properties and engineering classification for decomposed granite soils in Kaduna district, Nigeria. In First International Conference of Geomechanics in Tropical Lateritic and Saprolitic Soils, Brasília, 1, 175–186.

Tunçay, T., Dengiz, O., Bayramin, I., Kilic, S., & Baskan, O. (2019). Chemical weathering indices applied to soils developed on old lake sediments in a semiarid region of Turkey. Eurasian Journal of Soil Science, 1, 60–72.

Vogel, D. E. (1973). Precambrian weathering in acid metavolcanic rocks from the Superior Province, Villebon Township, southcentral Quebec. Canadian Journal of Earth Sciences, 12, 2080–2085.

Vogt, T. (1927). Sulitjelmefeltets geologi og petrografi. Norges Geologiske Undersøkelse, 121, 1–560.

Voicu, G., Bardoux, M., Jébrak, M., & Voicu, D. (1996). Normative mineralogical calculations for tropical weathering profiles. Winnipeg' '96, GAC/MAC Annual Meeting, Winnipeg, Canada, 27 May.

Yousefifard, M., Ayoubi, S., & Jalalian, A. (2012). Mass balance of major elements in relation to weathering in soils developed on igneous rocks in a semi-arid region, northwestern Iran. Agricultural Science, 9, 41–58.

Zhang, G. L., Pan, J. H., Huang, C. M., & Gong, Z. T. (2007). Geochemical features of a soil chronosequence developed on basalt in Hainan Island, China. Revista Mexicana de Ciencias Geológicas, 24(2), 261–269.

Zhou, X., Li, A., Jiang, F., & Lu, J. (2015). Effects of grain size distribution on mineralogical and chemical compositions: A case study from sizefractional sediments of the Huanghe (Yellow River) and Changjiang (Yangtze River). Geological Journal, 50(4), 414–433.

JJEES

JJEES (2026) 17 (1): 63-72
ISSN 1995-6681

Jordan Journal of Earth and Environmental Sciences

Empirical Orthogonal Transformation and Trend Analysis of Aerosols in West Africa

Sharafa S. B.[1*], Aliyu R.[2], Ibrahim B. B.[3], Akpootu D. O.[4], Tijjani B. I.[5], Darma T. H.[5], Saidu I. G.[4], Alaiyemola S. R.[4] and Ayedun F.[6]

[1]Department of Physics, University of Ilorin, Ilorin, Nigeria.
[2]Department of Physics, Kano State University of Science and Technology, Wudil, Kano, Nigeria.
[3]Physics/Electronics Unit, Kwara State Polytechnic, Ilorin, Nigeria.
[4]Department of Physics, Usmanu Danfodiyo University Sokoto, Sokoto, Nigeria.
[5]Department of Physics, Bayero University Kano, Kano, Nigeria.
[6]Department of Pure and Applied Science, National Open University of Nigeria.

Received on 19 October 2024; Accepted on 23 August 2025

Abstract

Properties of aerosols in Cinzana and Ilorin in Western Africa were studied using data on aerosol properties for a period of 16 years (2000–2015). Moderate Resolution Imaging Spectroradiometer (MODIS) is the data source. There has been an inadequate report on the aerosol loading patterns between these two West African Nations. The trend analysis and Empirical Orthogonal Transformation (EOT) evaluation were analyzed. Statistical Package for the Social Sciences (SPSS) software was used for the EOT analysis. Monthly averaged measurements of aerosol optical depth at 550 nm (AOD550), Angstrom exponent estimated for the wavelength pair of 470 and 660 nm (AE470-660), cloud fraction (Ncloud), fine mode fraction (FMF), and single scattering albedo (ωo) over the two nations were analysed using EOT, while the trend of AE and AE were analyzed. The trend suggests higher aerosol loading at the Ilorin station and possibly more aerosol types at the Cinzana station. Aerosol loading in Cinzana is lower during the dry season than during the rainy season. The EOT analysis shows that the two stations were characterised by four (4) seasons. The rainy and dry seasons were both characterized by two phases each.

Keywords: *EOT, Aerosols, Cinzana, Ilorin, Trend.*

1. Introduction

Aerosols in the atmosphere are created by both human activities and natural processes, and are moved directly (or formed in places) due to the physicochemical variations of the released gas-phase in the atmosphere. They are essential in modulating the Earth's radiation budget. Their negative impact on health, plants, and solar radiation applications has been widely researched (Havemann, 2006; Ramachandran & Rupakheti, 2020; Nisa et al., 2022). They have been found to perform key roles in climate change by affecting the radiative equilibrium of the Earth's surface (Wang et al., 2020). This process is known as aerosol radiative forcing (ARF). Aerosols also affect the macro- and microphysical characteristics of clouds by acting as cloud condensation nuclei (CCN) and ice nuclei (IN), thereby indirectly affecting the Earth's radiation budget (Wang et al., 2020). Because of these overwhelming aerosol effects, there are complex nonlinear mechanisms that lead to aerosols affecting Radiative Forcing (RF), specifically aerosol–cloud interaction, which remains one of the largest concerns in global climate projections. The RF idea has found usefulness in the guiding principle framework as a precursor to global warming potential, paralleling ozone layer depletion potentials (Ramaswamy et al., 2019) formulation, quantification, application, and utilization of "radiative forcing" (RF.

Mineral dust pollution is a big issue in West Africa. Around 40% of the yearly aerosols released to the troposphere are mineral dust emitted from arid regions. The region is also disturbed by biomass-burning aerosol episodes, too (Aliyu et al., 2019). Most researchers working on properties of aerosol and their impacts focused on aerosols from biomass burning and dust (Tanré et al., 2003; Sharafa et al., 2019; Rezaei et al., 2019)Iran, is an interesting location for aerosol studies because it is affected by anthropogenic pollution and desert dust aerosols. The aim of this study was to discriminate the aerosol types using satellite data over the city. Method: The study was performed using Level-2 daily Aerosol Optical Depth (AOD. Empirical Orthogonal Transformation (EOT) has been used to evaluate the MODIS C006 Level 2 aerosol optical depth (AOD) and Angstrom exponent (AE) products and to compare the data with AERONET AOD and AE readings (Aliyu et al., 2019). It has also been used to find the link between aerosols and rainfall in Ilorin (Sharafa et al., 2018). Gianelli et al. (2007) reported significant information on both the physical processes in the atmosphere above the instrument and the instrument's performance; this information can be obtained by conducting an EOT

* Corresponding author e-mail: sb69010@gmail.com, sharafa.sb@unilorin.edu.ng

analysis of AOD data. Li et al. (2013) used an EOT method to investigate the spatial and temporal unpredictability in multisensor aerosol retrievals and to examine the uniformity and changes across data sets.

In spite of all the advancement made in comprehending atmospheric aerosols and their impacts on climate, aerosol studies are still characterized with lots of uncertainties (Fawole et al., 2019;Aliyu et al., 2019;Ramachandran & Rupakheti, 2020). This is, partly because of the deficiency in the available information on aerosols' spatio-temporal changes and their associated characteristics (Tanré et al., 2003; Sharafa et al., 2018). For these reasons, various measurement methods (Knapp, 2002; Alam et al., 2011; Cheng et al., 2012; Granados-Muñoz et al., 2016) have been developed to measure aerosols across diverse regions of the world. Ground-based remote sensing networks, such as Aerosol Robotic Network (AERONET; (Holben et al., 1998)) and other remote sensing networks, offer nonstop datasets at several wavelengths to describe aerosol optical, microphysical and radiative properties. Studies using this type of network have been emerged in different parts of the globe (Holben et al., 1998; Cheng et al., 2012; Boiyo et al., 2017;Sharafa et al., 2018; Aliyu et al., 2019). Earlier studies over Africa (Adesina et al., 2014; Tan et al., 2015"ISBN" :"1537552015","ISSN":"16807324","abstract":"Obtaining continuous aerosol-optical-depth (AOD;.Sharafa et al., 2023) showthe presence of fine-and coarse-mode aerosols from a variety of natural and man-made sources giving rise to changes in concentration at diverse spatio-temporal scales.

Given the significant importance of aerosols locally and regionally, this study aims to examine the EOT of aerosol optical and microphysical characteristics, as well as trends in Cinzana and Ilorin, two sites in West Africa. The analysis used Level 2.0 (high quality cloud-screened and quality assured) data of some aerosol characteristics extracted from MODIS satellite for 15 years (February 2000 to July, 2015) to study (i) the latent characteristics of the two sites and (ii) the trend.

1.1 Empirical Orthogonal Transformation (EOT)

Empirical orthogonal transformation (EOT) is adaptable and has been used to reduce dimensionality and extract features. This technique allows scientists to conduct exploratory probes of underlying variables, shrink data in large datasets, and also test individual models. The procedure is mathematical and it changes a quantity of (possibly) correlated variables into fewer uncorrelated variables known as principal components (Chan & Mozurkewich, 2007). The EOT technique aims to decompose the data matrix into a set of independent, orthogonal eigenvectors, with the initial eigenvector representing the most variance, the second eigenvector amplifying the most of the outstanding variance, etc. (Landau & Everitt, 2004; Leech, Barrett, & Morgan, 2005). EOT has been applied to climate variables such as SST to examine climate modes (Monahan et al., 2009)EOFmodes are interpreted individually, independent of other modes. In fact, it can be shown that no such attribution can generally be made. This review demonstrates that in general individual EOF modes (i. Li et al. (2013) used an EOT approach to analyze the spatial and temporal variability in multisensor aerosol retrievals and examine the consistency and differences between the data sets. The eigenvectors (factors) are rotated to attain simple structure (Brown, 2009b). This process can be done in a number of ways, depending on whether the factors are thought to be correlated (oblique) or uncorrelated (orthogonal). The orthogonal (rotated through 90°) rotations are Equamax, Quartimax, and Varimax while the oblique (no rotation) is Direct Oblimin and Promax. Quartimax minimizes the number of factors required to provide details for each variable. Varimax reduces the number of variables with elevated loadings on each factor and makes small loadings even smaller. Oblique rotation is more complex. Also, oblique rotation gives a pattern matrix that includes the factor and factor correlation matrix that comprises the correlations among the factors (Yong & Pearce, 2013). To decide between using orthogonal and oblique rotation, a request must be made for direct oblimin rotation with the chosen number of factors (Brown, 2009a) and look at the correlations among factors. Check the factor correlation matrix for correlations around 0.32 and beyond. If correlations is more than 0.32, then a possibility of overlap in variance among factors exist, enough variance to use oblique rotation.

If the value of the determinant of each dataset is less than 0.00001, EOT cannot be conducted. The Kaiser-Meyer-OIkin (KMO) measure is adequate if its value is greater than 0.50. The Bartlett test should yield a p-value less than 0.05; this result indicates that the variables are sufficiently correlated to provide a realistic basis for the use of EOT.

The table of the rotated component Matrix, t, is necessary for interpreting the analysis results. Typically, component correlations are less than are deemed low while that of or more are typically considered acceptable.

The tendency of empirical modes to inadequately capture typical communality across subdomains of large datasets can be addressed by categorizing the variance using a rotation technique.

Generally, a rotation is a linear change of the modes that attempts to discover a new location for the coordinate axes, such that forecasts of the variables onto those axes make the spatial or temporal structure of the modes easier to interpret.

The rotated component matrix and component transformation matrix are shown for orthogonal rotations. For oblique rotations, the pattern, structure, and component correlation matrices are revealed. Also, both have the component score coefficient matrix (Eigen vectors) displayed.

2. Materials and Methods

2.1. Collection of Data

West Africa has been reported to have a clear seasonal cycle. Dry season starts in November and s in February, while the rainy season begins in March and ends in October (Sultan & Janicot, 2003).

Multisensor Aerosol Products Sampling System (MAPSS) (http://giovanni.gsfc.nasa.gov/mapss/) provides collocated data of AERONET and MODIS that was used for this analysis (Petrenko et al., 2012).

Measurements of MODIS AOD, AE, cloud fraction (N_{cloud}), fine mode fraction (FMF), and single scattering albedo (ωo) from 2000 to 2015 was used in this study. Trend analysis and EOT evaluation were carried out for two stations in West Africa. The AERONET stations covered are Cinzana and Ilorin. Some useful information about the stations is shown in Table 1 and Figure 1.

Table 1. Information about Cinzana and Ilorin

S/ No	Country	Aeronet station	Station Abbreviation	Longitude	Latitude
1.	Mali	Cinzana	CIN	5°W	13°N
2.	Nigeria	Ilorin	ILO	4°E	8°N

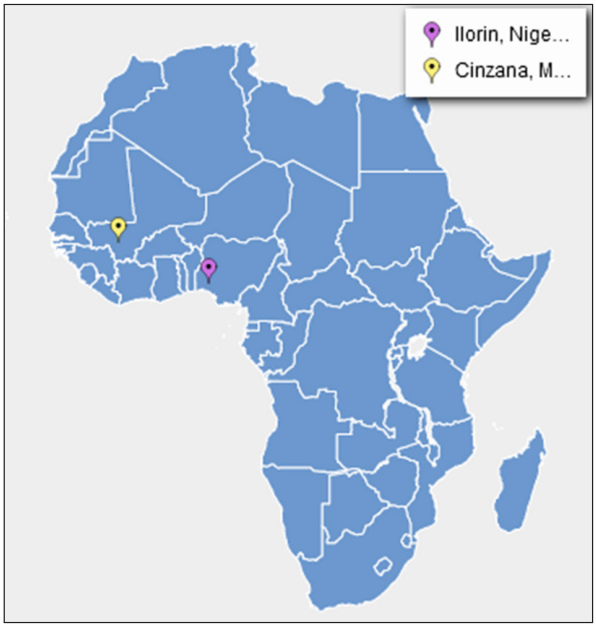

Figure 1. Map of Africa showing the location of Cinzana and Ilorin (West Africa)

Figure 1 shows the positions of Cinzana and Ilorin on a map of Africa.

2.2 Analysis

The data used for this study are daily. The data were converted to mean monthly and mean seasonal data for the study period. The datasets were separated into two parts: rainy and dry seasons.

Time-series graphs of the data were used to determine the overall and seasonal trends in the variation of the AE and AOD data series at the two stations. Values of the average, standard deviation, Coefficient of Variation (CV), and Seasonal Fraction (SF) of the AE and AOD data were calculated. The SF (Soni et al., 2015) of AOD signifies the mean seasonal contribution (percentage) to the sum of annual AOD and is defined as the ratio of the sum of AOD in each season to the total AOD in all seasons during a year, that is:

$$SF(\%)_{For\ AOD} = \frac{AOD_s}{AOD_y} x\ 100\% \quad \text{..... (1)}$$

where AODs is the sum of AOD in a particular season, and AODy is the sum of AOD in all months of a year.

Similarly, the seasonal fraction of AE represents the mean seasonal contribution (percentage) to the total annual AE and is defined as the ratio of the sum of AE in each season to the total AE in all seasons during a year, that is:

$$SF(\%)_{For\ AE} = \frac{AE_s}{AE_y} x\ 100\% \quad \text{..... (2)}$$

CV in (%) is used to analyze the temporal variability of AOD and AE. It is the ratio of standard deviation to the mean of the dataset (Soni et al., 2015) and is defined as:

$$CV(\%) = \frac{Standard\ deviation}{mean} x\ 100\% \quad \text{..... (3)}$$

Empirical orthogonal transformation (EOT) is used to analyze latent modes (i.e., patterns) of variability and how they change with time. The technique is an explanatory means, which permits a time display and a space display of the space-time field that can be valuable to atmospheric scientists.

EOT is useful in analyzing aerosol data mainly because of two reasons: (1) the composition of aerosols is complex, and diverse aerosol types have diverse methods of generation, transformation, and deposition. The EOT technique may aid in separating different aerosol sources or processes like conveyance and elimination; (2) the aerosol data are relatively noisy, due to complexities of surface reflectance, cloud screening, instrument calibration, and assumptions during retrievals. Normally, a considerable amount of the noise should be arbitrarily shared, and EOT analysis will sieve the noise into different modes, while sieving signals in the leading modes.

Precisely, let us assume A is the data matrix of size V×W, where V is the number of parameters and W is the number of observations at each station. Then the EOTs can be deduced by evaluating the eigenvectors of the covariance matrix C, which is

$$C = \frac{1}{W-1} AA^T \quad \text{..... (4)}$$

C is a V×V real, positive semidefinite matrix, and this can be rewritten as

$$C = E\Lambda E^T \quad \text{..... (5)}$$

Λ is a diagonal matrix whose elements are the V eigenvalues of C, and E is an orthogonal matrix whose columns are the V orthogonal eigenvectors, i.e., EOTs. Individual EOT has a matching time series, the Principal Components (PCs), and can be calculated from

$$P = A^T E \quad \text{..... (6)}$$

P is a V×W matrix whose columns are the V PCs. So P and E satisfy

$$A = EP^T \quad \text{..... (7)}$$

Combining Eqns. (1), (2), and (4), we have

$$\Lambda = \frac{1}{W-1} P^T P \quad \text{..... (8)}$$

Since Λ is diagonal, the principal components are mutually orthogonal, and their eigenvalues are the same as their variances.

EOT using direct Oblimin rotation was conducted on the monthly-averaged aerosol data from each station to determine if oblique or orthogonal rotation is the best for each station (Brown, 2009b). The Rotated Component Matrix table is key to understanding the analysis results. The content of the items with high weights for each factor was examined to see whether they fit together conceptually and can be named.

$$\tau_{ext}(\lambda) = \beta\lambda^{-\alpha_{ext}} \quad \text{..... (9)}$$

where τ_{ext} is the AOD at a chosen wavelength λ while β is the Angstrom turbidity coefficient, and α is the AE.

3. Results and Discussion

3.1 Analysis of the trends

The trend analysis of AOD and AE in the selected AERONET stations is presented here.

3.1.1 Trends of Aerosol Optical Depth (AOD)

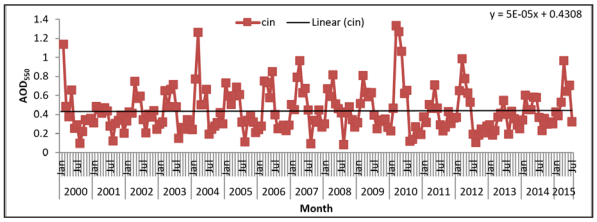

Figure 2. AOD trend in Cinzana (Mali) for periods between 2000 and 2015

Figure 2 shows the equation and trend of AOD550 in CIN. Though this station is close to the desert, only five of the average AOD have values exceed 1.0. The average AOD trend during the dry season is -0.001 month-1, and it is 0.0006 month-1 in the rainy season. The mean AOD in the dry season is 0.4333, while it is 0.4375 during the rainy season. Rainfall and wind speed affects aerosols negatively while temperature enhances them (Masoudi & Gerami, 2018). They are also affected by temporal and local scale perturbations (Banankhah, Nejadkoorki, & Sodaeezadeh, 2014).

The overall period has an average value of 0.4357 and a trend of 0.00005 month-1. Zhang et al., (2024) also reported an increasing AOD trend in Africa. A decreasing trend is observed in the dry-season data over the years, indicating a reduction in aerosol loading during this period. During the rainy season, the washout of atmospheric aerosols could not cause a reduction in the loading. This means that biomass burning, exhaust from automobiles and farming activities, etc., could be the reason for the observed increment. It could also be due to the delayed onset of the rainy season. The highest variance (54.11%) at this station occurred in the dry season; the overall data (51.82%) had the second-highest, and the rainy season (50.42%) had the least. In a 40-year study period of global AOD spanning 1980 to 2018, analysis of seasonal and monthly changes in AOD showed that its maximum value was recorded in the south part of the Sahara Desert. The Sahara Desert also accounts for about 80 % of the dust emissions (Zhao et al., 2025).

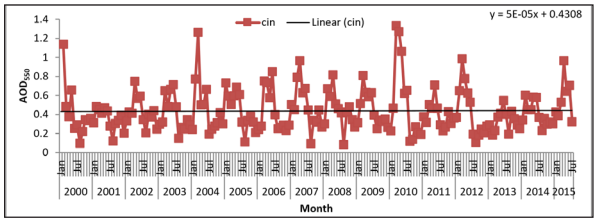

Figure 3. AOD trend in Ilorin (Nigeria) for periods between 2002 and 2015

Figure 3 shows the equation and trend of AOD550 in ILO. This station is farther from the desert than Cinzana station. The observed aerosol loading indicates that there are more dust episodes in Ilorin. This can only be linked to the Intertropical Convergence Zone (ITCZ). The average AOD trend during the dry season was 0.0008 month-1, and the mean in the rainy season was 0.0004 month-1. This plot displays a steady decrease in aerosol loading during the dry season and a gradual increase during the rainy season. These observations could be due to the early onset of rain and/or the increase in anthropogenic aerosols entering the environment. The mean AOD in the dry season was 0.8081 and 0.5659 in the rainy season. The overall period had an average value of 0.6870 and also an increasing trend of 0.0002 month-1. The overall data had the highest variance (43.56%), followed by the dry season (39.68%) and then the rainy season (38.69%).

3.1.2 Angstrom Exponent (AE) Trends

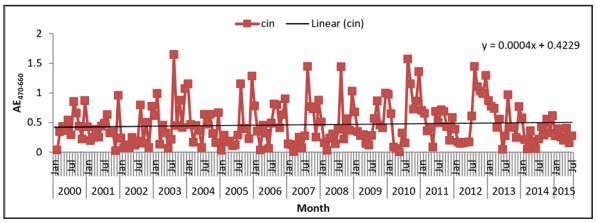

Figure 4. $AE_{470\text{-}660}$ trend in Cinzana (Mali) for periods between 2000 and 2015

Figure 4 shows the equation and trend of A 470-660 in CIN. The average α trend during the dry season was 0.00217 month-1, and during the rainy season, it was 0.000248 month-1. The mean AE was 0.479 in the dry season and 0.455 in the rainy season. The overall period has an average value of 0.465 and with a trend of 0.000447 month-1. An increasing trend is observed at the station over the years, with a gradual increase in fine-mode aerosol loading. The rainy season at this station also had the highest variance (76.26%), trailed by the overall data (75.48%) and the rainy season (74.95%).

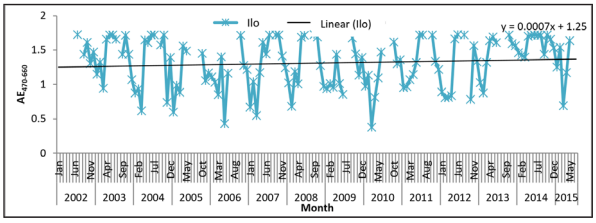

Figure 5. AE470-660 trend in Ilorin (Nigeria) for periods between 2002 and 2015

Figure 5 shows the equation and trend of AE470-660 in ILO. The AE trend during the dry season was 0.00429 month-1, and during the rainy season, it was -0.000582 month-1. The mean AE was 0.747 in the dry season and 1.085

in the rainy season. The overall period has an average value of 0.921 and also an increasing trend of 0.000557 month-1. The AE trend at this station shows a consistent increase in coarse-mode aerosols over the years during the rainy seasons. The highest variance (51.25%) was observed in the rainy season, trailed by the overall data (46.58%), while the least is the dry season (39.22%).

Table 2. Mean, trends and coefficient of variation (CV) of AOD_{550} and $AE_{470-660}$ in Cinzana and Ilorin

Description	Mean	trend (month-1)	CV (%)	Summary of findings
Cinzana				
AOD	0.4357	0.00005	51.82	High aerosol loading but with a slowly increasing variability
$AE_{470-660}$	0.4652	0.00040	75.47	Coarse mode aerosols, slowly increasing fine mode but high variability
Ilorin				
AOD	0.6870	0.00020	43.56	High aerosol loading but with an slowly increasing variability
$AE_{470-660}$	1.3115	0.00070	26.93	Dominated by fine mode aerosols, slowly increasing fine mode variability

Table 2 shows the mean, trend and CV of AOD_{550} and $AE_{470-660}$ in Cinzana and Ilorin. The mean AOD show that there is greater aerosol loading in Ilorin than in Cinzana during the period under consideration. Also, the mean values of AE show that coarse-mode aerosols dominate in Cinzana, while fine-mode aerosols dominate in Ilorin. The CV values show the level of dispersion of the data around the mean. The AOD data in Cinzana are more dispersed (51.82 %) around the mean than those in Ilorin (43.56 %). Similarly, the AE data in Cinzana (75.47 %) is more dispersed around the mean value than that of Ilorin (26.93 %). These observations suggest that there is high aerosol loading in both stations, but that of Ilorin is higher. The observations for the AE components are not similar, either. The mean AE for Ilorin shows that fine-mode aerosols dominate the atmosphere, whereas coarse-mode aerosols dominate in Cinzana. The CV values for AE indicate that more aerosol types may be present in Cinzana, while fewer (singular) types may be present in Ilorin.

Table 3. Seasonal mean values, trends, and coefficient of variation (CV) of AOD_{550} and $AE_{470-660}$ in Cinzana and Ilorin

Description	Dry season			Rainy season		
	mean	trend (month-1)	CV(%)	mean	trend (month-1)	CV(%)
Cinzana						
AOD	0.4333	-0.0010	54.11	0.4375	0.0006	54.42
Summary	High loading but decreasing. High variability			High loading, and increasing. High variability		
$AE_{470-660}$	0.4789	0.0022	74.92	0.4554	0.0002	76.16
Summary	Coarse mode aerosols, slowly increasing fine mode. High variability.			Coarse mode aerosols, slightly increasing fine mode. High variability		
Ilorin						
AOD	0.8081	0.0008	39.68	0.5659	0.0004	38.69
Summary	High loading and increasing. Low variability			High loading and increasing. Low variability		
$AE_{470-660}$	1.1139	0.0043	25.86	1.5091	-0.0004	19.77
Summary	Fine mode aerosols, slowly increasing fine mode. Low variability.			Fine mode aerosols, decreasing fine mode. Low variability		

Table 3 displays the values of the seasonal averages, trend and the CV of AOD550 and AE470-660 observed at the two stations.

During the dry season, the mean AOD values show higher aerosol loading in Ilorin than in Cinzana during the period under consideration. Also, the mean values of AE show that coarse-mode aerosols dominate in Cinzana, while fine-mode aerosols dominate in Ilorin. The CV values show that the AOD data in Cinzana are more dispersed (54.11 %) around the mean than those in Ilorin (39.68 %). Similarly, the AE data in Cinzana (74.92 %) are more dispersed around the mean than those in Ilorin (25.86 %). These observations suggest that the AOD loading in Cinzana and Ilorin is similar, while the AE components are not. More aerosol types may be present in Cinzana while fewer (singular) types may be present in Ilorin. The decreasing trend in AOD during the dry season in Cinzana is highly unusual, as the dry season is typically characterized by increasing AOD loading.

During the rainy season, the mean AOD values show higher aerosol loading in Ilorin (0.5659) than in Cinzana (0.4375). This is similar to what was obtained in the dry season. Also, the averaged values of AE show that coarse-mode aerosols (AE < 1.0) dominate in Cinzana, while fine-mode aerosols (AE > 1.0) dominate in Ilorin. The CV values show that the AOD data in Cinzana is greatly dispersed (54.42 %) around the mean value than that of Ilorin (38.69 %). Similarly, the AE data in Cinzana (76.16 %) is more dispersed around the mean value than that of Ilorin (19.77 %).

These observations suggest that the AOD loading in Cinzana and Ilorin is similar, while the AE component shows that the aerosol types are not similar. More aerosol types may be present in Cinzana, while fewer types may be present in Ilorin. The increasing trend of AOD during rainy season in Cinzana is also highly unusual because the rainy season is always characterized by decreasing AOD loading

Table 4. The value of Seasonal fractions (SF) of AOD and AE in Cinzana and Ilorin

AOD_{550}		$AE_{470-660}$	
Dry season SF (%)	Rainy season SF (%)	Dry season SF (%)	Rainy season SF (%)
CIN			
41.16	58.84	42.62	57.38
ILO			
58.81	41.19	42.47	57.53

Table 4 depicts the value of the SF of both AOD_{550} and $AE_{470-660}$ in Cinzana and Ilorin.

In the dry season, the seasonal contribution of AOD in Cinzana and Ilorin was 41.16 % and 58.81% respectively. The values became 58.84 % and 41.19% during the rainy season. These results corroborate the observation in Table 3 where aerosol loading was low during dry season and high during rainy season in Cinzana. This may suggest that there is an overlap between rainy season and dry season in the station.

In the dry season, the seasonal contribution of AE in Cinzana and Ilorin is 42.62 % and 42.47 %, respectively. The values become 57.38 % and 57.53 % in the rainy season. These results show that the trend of the contribution of aerosol types is similar in both stations.

3.2 EOT results and interpretation

3.2.1 Cinzana (Mali)

Table 5. Component Correlation Matrix for Cinzana station (Mali) using Direct Oblimin rotation

Component	1	2	3	4
1	1.000	0.140	0.167	0.283
2	0.140	1.000	0.040	0.166
3	0.167	0.040	1.000	0.059
4	0.283	0.166	0.059	1.000

From the results of the direct oblimin analysis of aerosol data from Cinzana in Table 5, it can be seen that all off-diagonal correlations are less than 0.32, indicating that the best rotation for this dataset is an orthogonal rotation.

The value of the determinant in this station is 0.428. Therefore, an EOT analysis can be performed on data from this station. The data are also adequate, as the KMO value is 0.558. Also, the data is highly correlated enough for this type of analysis, as indicated by the statistical significance. Quartimax rotation provides the best description of this station, as it minimizes the number of factors needed to describe each variable.

Table 6. The explained total variance and Rotated Component Matrix of data for Cinzana station using Quartimax rotation

Parameters	Component				
	1	2	3	4	
$AE_{470-660}$	0.929				
AOD_{550}	-0.898				
FMF		0.992			
ω_o			0.992	0.976	
N_{cloud}					
Eigenvalues	1.992	0.985	0.938	0.805	Before rotation
% of Variance	39.849	19.706	18.767	16.099	
Cumulative %	39.849	59.555	78.322	94.420	
Eigenvalues	1.651	1.039	1.018	1.012	After rotation
% of Variance	33.029	20.790	20.366	20.236	
Cumulative %	33.029	53.819	74.185	94.420	
Months (%)	5.15 months of rainy period	2.64 months of dry period	1.97 months of dry period	1.57 months of rainy period	

Table 6 shows the explained total variance and the rotated component matrix for Cinzana station (Mali) using Quartimax rotation.

The four principal components extracted for this station, after rotation, are shown in the columns of Table 6. Before rotation, Component 1 explained 39.849 % of the variance, Component 2 explained 19.706 % of the variance, Component 3 explained 18.767 %, and Component 4 explained 16.099 % of the variance. This means that 94.420 % of the variance can be explained by this method of analysis. The remaining 5.580 % is the noise signal. The values for the individual variances explained changed after the Qartimax rotation. Component 1 now explained 33.029 % of the variance, Component 2 now explained 20.790 % of the variance, Component 3 now explained 20.366 %, and Component 4 now explained 20.236 % of the variance. The total percentage of the variance explained, and the noise signal remain unchanged.

The Table also illustrates the aerosol parameters and the correlation coefficients of the rotated components in Cinzana, after suppressing all other coefficients below 0.4.

The first component in Table 6 is most strongly extracted from AOD and AE, with their regression coefficients shown in the first column. This indicates a rainy season because of the negative (inverse) correlation of τ550 (reduction in the atmosphere) with component 1.

The second component is extracted from FMF, with the correlation coefficient in column 2. This indicates a dry and warm season because FMF is synonymous with the absorption of electromagnetic radiation, thereby warming the Earth.

The third component had only ωo with a correlation coefficient in the third column. This indicates a dry and cold dry season (it has values above 0.92 in this station (Sharafa et al., 2023)) because it is synonymous with scattering of electromagnetic radiation into space, thereby reducing the amount reaching the Earth.

The fourth component had only Ncloud with a correlation coefficient in the fourth column. This also indicates a rainy season because an increase in cloud cover always brings about more precipitation.

The latent characteristics of this station is that there are well pronounced rainy and dry seasons. As expected, the rainy season is characterized by a reduction in aerosol load (negative sign for AOD). Two phases characterize the dry season; (1) hot dry season and (2) cold dry season (harmattan). The total rotated eigenvalues for the rainy and dry seasons are 2.663 (53.265 % of variance) and 2.057 (41.156 % of variance), respectively. This variance translates to 6.72 months of rainy season and 4.61 months of dry season. The remaining 0.68 months could not be classified. The unclassified period in Cinzana may be a result of a brief pause during the rainy season or a little precipitation during the dry season.

3.2.2 Ilorin

Table 7. Component Correlation Matrix for Ilorin station (Nigeria) using Direct Oblimin rotation

Component	1	2	3	4
1	1.000	0.055	-0.187	-0.233
2	0.055	1.000	-0.220	-0.309
3	-0.187	-0.220	1.000	0.018
4	-0.233	-0.309	0.018	1.000

From the results of the direct oblimin analysis of aerosol data from Cinzana in Table 7, it can also be seen that all off-diagonal correlations are less than 0.32 (similar to the Cinzana analysis), indicating that the best rotation for this dataset is an orthogonal rotation.

The value of the determinant at Ilorin station is 0.569. Therefore, an EOT analysis can be performed on data from this station. The data is also adequate, as the value of the KMO measure is 0.545. Also, the data is highly correlated enough for this type of analysis because it is statistically significant. Quartimax rotation was adopted for this station as well.

Table 8. The explained total variance and Rotated Component Matrix for Ilorin station using Quartimax rotation

Parameters	Component				
	1	2	3	4	
N_{cloud}	0.918				
AOD_{550}	-0.653	-0.446			
$AE_{470-660}$		0.969			
ω_o			0.959		
FMF				0.980	
Eigenvalues	1.818	1.111	1.008	0.585	Before rotation
% of Variance	36.354	22.227	20.154	11.706	
Cumulative %	36.354	58.581	78.734	90.441	
Eigenvalues	1.257	1.167	1.088	1.011	After rotation
% of Variance	25.134	23.332	21.753	20.222	
Cumulative %	25.134	48.466	70.219	90.441	
Months (%)	3.02 months of rainy period	2.80 months of rainy period	2.61 months of dry period	2.43 months of dry period	

Table 8 shows the explained total variance and the rotated component matrix for Ilorin station (Nigeria) using Quartimax rotation.

From Table 8, four principal components were also extracted. Before the Quartimax rotation, component 1 explained 36.354 % of the total variance, component 2 explained 22.227 % of the total variance, component 3 explained 20.154 % of the total variance, while component 4 explained 11.706 % of the total variance. This means that 90.441 % of the variance can be explained by this method of analysis. The remaining 9.559 % constitutes the noise signal. After the Quartimax rotation, component 1 explained 25.134 % of the total variance, component 2 explained 23.332 % of the total variance, component 3 explained 21.753 % of the total variance, while component 4 explained 20.222 % of the total variance. The total percentage of variance that can be explained using this method of analysis and the noise signal remains unchanged.

The Table also depicts the parameters and the extracted components' correlation coefficients for the rotated components in Ilorin, after suppressing coefficients below 0.4.

The first component is extracted most strongly from Ncloud and AOD, with their correlation coefficients shown in the first column. These indicate a rainy season because of the inverse correlation between the component and AOD. This correlation also shows that there is a significant reduction in atmospheric aerosol content (as cloud condensation nuclei (CCN)) as Ncloud increases during this season.

The second component consisted of AOD and AE with their correlation coefficients in column 2. This correlation also indicates the rainy season. The negative correlation of AOD at this station also supports the inverse power-law relationship between the two parameters.

The third component had only ωo (it has values above 0.98 in this station (Sharafa et al., 2023)) with a positive correlation coefficient in the third column. This indicates a cold and dry (harmattan) season because of the increased scattering of electromagnetic radiation in the station.

The fourth component had FMF with a correlation coefficient in column 4. This indicates a hot and dry season because of the capacity of FMF to absorb electromagnetic radiation. AOD has a complex correlation coefficient i.e., it is correlated in both components 1 and 2.

This indicates that this station has two types of rainy seasons and dry seasons, just like Cinzana. The difference between the two stations is that the warmth in Cinzana is more pronounced than that of Ilorin. The total rotated eigenvalues for the rainy and dry seasons are 2.434 (48.446 % of variance) and 2.099 (41.975 % of variance), respectively. This translates to 5.82 months of rainy season and 5.04 months of dry season. The remaining 1.14 months could not be classified. This unclassified period in Ilorin may be due to a brief pause during the rainy season or a brief period of precipitation during the dry season.

3.3 Visual summary of key results

Analysis/Station	Cinzana	Implication	Ilorin	Implication
Trend of AOD	0.00005 month^{-1}	Increasing trend for the period under review	0.00020 month^{-1}	Increasing trend for the period under review
Seasonal trend of AOD	-0.0010 month^{-1} Dry season 0.0006 month^{-1} Rainy season	Decreasing trend Increasing trend	0.0008 month^{-1} Dry season 0.0004 month^{-1} Rainy season	Increasing trend Increasing trend
Trend of AE	0.00040 month^{-1}	Increasing trend	0.00020 month^{-1}	Increasing trend
Seasonal trend of AE	0.0022 month^{-1} Dry season 0.0002 month^{-1} Rainy season	Increasing trend Increasing trend	0.0043 month^{-1} Dry season -0.0004 month^{-1} Rainy season	Increasing trend Decreasing trend
CV of AOD	54.11 % Dry season 54.42 % Rainy season	medium data variability Medium data variability	39.68 % Dry season 38.69 % Rainy season	Low variability of data Low variability of data
CV of AE	74.92 % Dry season 76.16 % Rainy season	Very high variability of data Very high data variability	25.86 % Dry season 19.77 % Rainy season	Very low data variability Very low data variability
Seasonal fraction of AOD	41.16 % Dry season 58.84 % Rainy season	Less aerosol loading during the dry months. More aerosol loading during the rainy months	58.81 % Dry season 41.19 % Rainy season	More aerosol loading during the dry months. Less aerosol loading during the rainy months
Seasonal fraction of AE	42.62 % Dry season 57.38 % Rainy season	Less aerosol types during the dry months. More aerosol types during the rainy months	42.47 % Dry season 57.53 % Rainy season	Less aerosol types during the dry months. More aerosol types during the rainy months
EOT	Two types of dry season accounting for 4.61 months. Two types of rainy season accounting for 6.72 months. 0.68 Months of unclassified season	Evidence of two types of dry and rainy seasons.	Two types of dry season accounting for 5.04 months. Two types of rainy season accounting for 5.82 months 1.14 Months of unclassified season	Evidence of two types of dry and rainy seasons.

4. Conclusions

Research on trend and EOT assessment of aerosol parameters in the Western part of Africa is scarce. We leveraged the availability of AERONET stations in these countries to account for the trends and fundamental modes of these parameters in this part of the continent. This research

aims to establish a link between the trend and EOT of aerosol parameter values in these countries.

The distribution of aerosols in western Africa has been studied using their optical and physical parameters. It was discovered that the aerosol loading in Cinzana does not follow the traditional pattern of having more aerosols in the atmosphere during the expected dry season (October to March). It can also be observed that there is a higher amount of aerosols in the atmosphere of Ilorin than in Cinzana. This result can only be linked to the ITCZ. Also, there are indications that more aerosol types may be present in Cinzana, as higher aerosol loading was detected during the rainy season. Coarse-mode aerosol episodes are much more frequent in Cinzana than in Ilorin during the period under review.

In general, both AOD and AE show increasing trends at the two stations, but seasonal differences were observed. Only the AOD in Cinzana during the dry season and the AE in Ilorin during the rainy season showed a decreasing trend; the others showed an increasing trend.

The seasonal fraction shows that AE makes a similar contribution at both stations during the rainy season, but has a dissimilar impact during the dry season.

The EOT analysis, with a Quartimax rotation, indicates that the aerosol parameters obtained from the Cinzana and Ilorin stations are similar in character but not identical. Both have four underlying characteristics because of the four principal components extracted. The extracted components translated into four seasons, which are two types of rainy and dry seasons, i.e., (1) a cloudy rainy season, (2) a warm rainy season, (3) a warm and dry season, and (4) a cold (harmattan) dry season.

Field experiments can be carried out in the future to provide additional insight into activities that may have led to the outcomes of the analysis of aerosol parameter trends and the EOT evaluation.

Acknowledgements

Our appreciation goes to the Principal Investigators (PIs) and support staff of AERONET sites for creating and keeping these sites in good condition. Furthermore, we appreciate the Giovanni team for producing and presenting the MAPSS database and the Web MAPSS user interface.

References

Adesina, A. J., Kumar, K. R., Sivakumar, V., & Griffith, D. (2014). Direct radiative forcing of urban aerosols over Pretoria (25.75°S, 28.28°E) using AERONET Sunphotometer data: First scientific results and environmental impact. Journal of Environmental Sciences (China), 26(12). https://doi.org/10.1016/j.jes.2014.04.006

Alam, K., Qureshi, S., & Blaschke, T. (2011). Monitoring spatio-temporal aerosol patterns over Pakistan based on MODIS, TOMS and MISR satellite data and a HYSPLIT model. Atmospheric Environment, 45(27), 4641–4651. https://doi.org/10.1016/j.atmosenv.2011.05.055

Aliyu, R., Tijjani, B. I., & Sharafa, S. B. (2019). Assesment and comparison of modis AOD and AE product over Ilorin Aeronet station using the statistical analysis of empirical orthogonal function (EOF). Bayero Journal of Pure and Applied Sciences, 11(1), 223. https://doi.org/10.4314/bajopas.v11i1.37s

Banankhah, A. S., Nejadkoorki, F., & Sodaeezadeh, H. (2014). Shiraz Air Pollution : Dependency on Meteorology and Temporal Variability. Jordan Journal of Earth and Environmental Sciences, 6(1), 21–28.

Boiyo, R., Kumar, K. R., Zhao, T., & Bao, Y. (2017). Climatological analysis of aerosol optical properties over East Africa observed from space-borne sensors during 2001–2015. Atmospheric Environment, 152. https://doi.org/10.1016/j.atmosenv.2016.12.050

Brown, J. D. (2009a). Statistics Corner Questions and answers about language testing statistics : Choosing the Right Number of Components or Factors in PCA and EFA. Shiken: JALT Testing & Evaluation SIG Newsletter, 13(May), 19–23.

Brown, J. D. (2009b). Statistics Corner Questions and answers about language testing statistics: Choosing the Right Type of Rotation in PCA and EFA. Shiken: JALT Testing & Evaluation SIG Newsletter, 13(November), 20–25.

Chan, T. W., & Mozurkewich, M. (2007). Simplified representation of atmospheric aerosol size distributions using absolute principal component analysis. Atmospheric Chemistry and Physics, 7(3), 875–886. https://doi.org/10.5194/acp-7-875-2007

Cheng, T., Chen, H., Gu, X., Yu, T., Guo, J., & Guo, H. (2012). The inter-comparison of MODIS, MISR and GOCART aerosol products against AERONET data over China. Journal of Quantitative Spectroscopy and Radiative Transfer, 113(16), 2135–2145. https://doi.org/10.1016/j.jqsrt.2012.06.016

Fawole, O. G., Cai, X., Pinker, R. T., & Mackenzie, A. R. (2019). Analysis of radiative properties and direct radiative forcing estimates of dominant aerosol clusters over an urban-desert region in West Africa. Aerosol and Air Quality Research, 19(1), 38–48. https://doi.org/10.4209/aaqr.2017.12.0600

Gianelli, S. M., Carlson, B. E., & Lacis, A. A. (2007). Using EOF analysis to qualitatively analyze, and identify inhomogeneities in, data from ground-based aerosol monitoring instruments. Journal of Geophysical Research Atmospheres, 112(20), 1–11. https://doi.org/10.1029/2006JD008300

Granados-muñoz, M. J., Navas-guzmán, F., Guerrero-rascado, J. L., Baldasano, J. M., Belegante, L., Chaikovsky, A., … Amico, G. D. (2016). Profiling of aerosol microphysical properties at several EARLINET / AERONET sites during the July 2012 ChArMEx / EMEP campaign. Atmos. Chem. Phys., 16(August 2015), 7043–7066. https://doi.org/10.5194/acp-16-7043-2016

Havemann, S. (2006). The development of a fast radiative transfer model based on an empirical orthogonal functions (EOF) technique. Proc. SPIE 6405, Multispectral, Hyperspectral, and Ultraspectral Remote Sensing Technology, Techniques, and Applications, 64050M (22 December 2006), (December 2006), 1–9. https://doi.org/10.1117/12.693995

Holben, B. N., Eck, T. F., Slutsker, I., Tanre´, D., Buis, J. P., Setzer, A., … Smirnov, A. (1998). AERONET — A Federated Instrument Network and Data Archive for Aerosol Characterization. Remote Sensing Environment, 66, 1–16.

Holben, B. N., Eck, T. F., Slutsker, I., Tanre, D., Buis, J. P., Setzer, A., … Smirnov, A. (1998). AERONET-A Federated Instrument Network and Data Archive for aerosol characterization. Remote Sensing of Environment, 66(October), 1–16. https://doi.org/10.1016/S0034-4257(98)00031-5

Knapp, K. R. (2002). Aerosol optical depth retrieval from GOES-8: Uncertainty study and retrieval validation over South America. Journal of Geophysical Research, 107(D7), 4055. https://doi.org/10.1029/2001JD000505

Landau, S., & Everitt, B. S. (2004). A Handbook of Statistical Analyses Using SPSS (p. 354). p. 354. https://doi.org/10.1002/sim.2134

Leech, N. L., Barrett, K. C., & Morgan, G. A. (2005). SPSS for

Intermediate Statistics: Use and Interpretation, Second Edition. In LAWRENCE ERLBAUM ASSOCIATES, PUBLISHERS London.

Li, J., Carlson, B. E., & Lacis, A. A. (2013). Application of spectral analysis techniques in the intercomparison of aerosol data: 1. An EOF approach to analyze the spatial-temporal variability of aerosol optical depth using multiple remote sensing data sets. Journal of Geophysical Research Atmospheres, 118(15), 8640–8648. https://doi.org/10.1002/jgrd.50686

Masoudi, M., & Gerami, S. (2018). Assessment of PM10 concentration and its prediction using meteorological parameters in the air of Isfahan, Iran. Jordan Journal of Earth and Environmental Sciences, 9(2), 75–80.

Monahan, A. H., Fyfe, J. C., Ambaum, M. H. P., Stephenson, D. B., & North, G. R. (2009). REVIEW Empirical Orthogonal Functions: The Medium is the Message. Journal of Climate, 22, 6501–6514. https://doi.org/10.1175/2009JCLI3062.1

Nisa, A., Chel, M., Ooi, G., Juneng, L., Isra, M. A., Hernandi, R., & Tangang, F. (2022). Spatio-temporal analysis of aerosol optical depth using rotated empirical orthogonal function over the Maritime Continent from 2001 to 2020. Atmospheric Environment, 290(February), 119356. https://doi.org/10.1016/j.atmosenv.2022.119356

Petrenko, M., Ichoku, C., & Leptoukh, G. (2012). Multisensor Aerosol Products Sampling System (MAPSS). Atmospheric Measurement Techniques, 5(5), 913–926. https://doi.org/10.5194/amt-5-913-2012

Ramachandran, S., & Rupakheti, M. (2020). Inter-annual and seasonal variations in columnar aerosol characteristics and radiative effects over the Pokhara Valley in the Himalayan foothills – Composition, radiative forcing, and atmospheric heating. Environmental Pollution, 264, 1–14. https://doi.org/10.1016/j.envpol.2020.114799

Ramaswamy, V., Collins, W., Haywood, J., Lean, J., Mahowald, N., Myhre, G., … Storelvmo, T. (2019). Radiative Forcing of Climate: The Historical Evolution of the Radiative Forcing Concept, the Forcing Agents and their Quantification, and Applications. Meteorological Monographs, 59, 14.1-14.101. https://doi.org/10.1175/amsmonographs-d-19-0001.1

Rezaei, M., Farajzadeh, M., Mielonen, T., & Ghavidel, Y. (2019). Discrimination of aerosol types over the Tehran city using 5 years (2011-2015) of MODIS collection 6 aerosol products. Journal of Environmental Health Science and Engineering, 17(1). https://doi.org/10.1007/s40201-018-00321-2

Sharafa, S. B., Aliyu, R., Ibrahim, B. B., Akpootu, D. O., Tijjani, B. I., Darma, T. H., … Sulu, H. T. (2023). Analysis of Aerosols in West Africa: Modelling and Radiative Forcing. Environmental Contaminants Reviews, 6(2), 105–115. https://doi.org/10.26480/ecr.02.2023.105.115

Sharafa, S. B., Tijjani, B. I., Aliyu, R., Darma, T. H., Sulu, H. T., & Bube, M. (2019). Discrimination of Aerosol Types over Nairobi, Skukuza and Ilorin Using AOD-AE Clusters. Jordan Journal of Physics, 12(3), 269–289.

Sharafa, S. B., Tijjani, B. I., Ibrahim, B. B., Sulu, H. T., Salawu, M. A., & Shehu, S. J. (2018). Seasonal variability of Aerosols and their radiative impacts on Sub-Saharan African climate during the period 2000-2015 using Modis data. Monograph of Atmospheric Research 2018, Edited by A. B. Rabiu and E. O. Abiye, Centre for Atmospheric Research, Anyigba, 57–64.

Sharafa, S B, Aliyu, R., Ibrahim, B. B., Akpootu, D. O., Tijjani, B. I., Darma, T. H., … Sulu, H. T. (2023). Analysis of aerosols in West Africa : Modelling and Radiative Forcing. Environmental Contaminants Reviews (ECR), 6(2), 80–90. https://doi.org/10.26480/ecr.02.2023.80.90

Sharafa, Salihu B, Tijjani, B. I., Ibrahim, B. B., Aliyu, R., Darma, T. H., Abdullahi, M. B., & Sani, M. (2018). An EOT Approach to Analyze the Temporal Variability of Rainfall Data and Some Aerosol Properties over Ilorin using MODIS Data. Journal of the Nigerian Geophysical Society, 1(1), 50–57.

Soni, K., Parmar, K. S., & Kapoor, S. (2015). Time series model prediction and trend variability of aerosol optical depth over coal mines in India. Environmental Science and Pollution Research, 22(5), 3652–3671. https://doi.org/10.1007/s11356-014-3561-9

Sultan, B., & Janicot, S. (2003). The West African Monsoon Dynamics. Part II: The “‘Preonset”’ and “‘Onset”’ of the Summer Monsoon. Journal of Climate, 16, 3407–3427.

Tan, F., Lim, H. S., Abdullah, K., Yoon, T. L., & Holben, B. (2015). Monsoonal variations in aerosol optical properties and estimation of aerosol optical depth using ground-based meteorological and air quality data in Peninsular Malaysia. Atmospheric Chemistry and Physics, 15(7). https://doi.org/10.5194/acp-15-3755-2015

Tanré, D., Haywood, J., Pelon, J., Léon, J. F., Chatenet, B., Formenti, P., … Myhre, G. (2003). Measurement and modeling of the Saharan dust radiative impact: Overview of the Saharan Dust Experiment (SHADE). J. Geophys. Res., 108(D18), 8574. https://doi.org/10.1029/2002JD003273

Wang, H., Dai, T., Zhao, M., Goto, D., Bao, Q., Takemura, T., … Shi, G. (2020). Aerosol effective radiative forcing in the online aerosol coupled cas-fgoals-f3-l climate model. Atmosphere, 11(10). https://doi.org/10.3390/atmos11101115

Yong, A. G., & Pearce, S. (2013). A Beginner ’ s Guide to Factor Analysis : Focusing on Exploratory Factor Analysis. Tutorials in Quantitative Methods for Psychology, 9(2), 79–94.

Zhang, L., Wang, X., Huang, G., & Zhang, S. (2024). Comprehensive Assessment and Analysis of the Current Global Aerosol Optical Depth Products. Remote Sensing, 16(1425), 1–19.

Zhao, H., Gui, K., Wang, Y., Wang, Y., Wang, H., Zheng, Y., … Zhang, X. (2025). Long-term distribution and evolution trends of absorption aerosol optical depth with different chemical components in global and typical regions. Atmospheric Research, 314(March), 1–10.

JJEES

JJEES (2026) 17 (1): 73-82
ISSN 1995-6681

Jordan Journal of Earth and Environmental Sciences

Contribution of GIS and Remote Sensing in Multicriteria Seismic Risk Assessment of Existing bridges in the Oran region of Algeria

Fatima-Zohra Baba-Hamed[1*], Farid Rahal[2], Farida Guenanou[3]

[1] Lecturer, Laboratory LM2SC. University of Sciences and Technology of Oran, Mohamed Boudiaf, Oran 31000, Algeria.
[2] Lecturer, Laboratory of Analysis and Application of Radiations, University of Sciences and Technology of Oran, Mohamed Boudiaf, Oran 31000, Algeria.
[3] Associate teacher, Laboratory LMST. University of Sciences and Technology of Oran, Mohamed Boudiaf, Oran 31000, Algeria.

Received on 30 December 2024; Accepted on 25 August 2025

Abstract

BRIDGES are an important aspect of transportation infrastructure and are crucial for keeping networks working during earthquakes. However, numerous past disasters have demonstrated that vigorous tectonic activity increases the likelihood of earthquake damage to these bridges. This paper presents a unified framework for evaluating the seismic risk of existing bridges by integrating the Analytic Hierarchy Process (AHP), Geographic Information Systems (GIS), and remote sensing techniques.

The method uses eight factors to assess both the risk of earthquakes and the weakness of structures. Four of these factors are related to seismic hazard: peak ground acceleration (PGA), closeness to active faults, topographic slope, and soil classification. The other four are related to structural vulnerability: seismic design, structural type, degradation state, and functional importance based on traffic.

The method was utilized in Algeria's Oran area. Risk maps were generated for two return periods: one for 100 years and one for 475 years. The mean scenario for the 100-year return period had a PGA of 0.068 g, and the worst-case scenario had a PGA of 0.095 g. The average case for a 475-year return period was PGA = 0.138g, and the worst case was PGA = 0.18g.

The data indicate that many bridges are at significant risk during the most severe earthquake conditions. This risk is significantly greater for older structures, those exhibiting deterioration, or those inadequately designed for seismic loads, particularly when located on soft soils, or in proximity to active faults.

The suggested integrated strategy makes it easier to decide which intervention measures to focus on first. It is also a valuable tool for strengthening transportation infrastructure against earthquakes.

Keywords: *Seismic Risk Assessment; Bridges; Geographic Information Systems (GIS); Remote Sensing (RS); Multicriteria Decision Analysis (MCDA); Analytical Hierarchy Process (AHP).*

1. Introduction

One of the most deadly natural catastrophes is an earthquake. It can harm people, the economy, and the environment significantly (Al-Dogom et al., 2021). They are especially dangerous in places with high seismic activity and weak infrastructure because they can erupt unexpectedly, are challenging to predict, and can trigger other problems.

Geographic Information Systems (GIS) provide a robust framework for the management and analysis of earthquake-related datasets (Erdik et al., 2010; Kim, 1993; Kiremidjian et al., 2007; Al-Dogom et al., 2021; Almasri et al., 2024; Singh et al., 2016; Cheddad et al., 2025), while Remote Sensing (RS) delivers accurate spatial data on topography and lithology, which are critical inputs for seismic hazard modeling. Several studies (Baillifard et al., 2003; Pitilakis, 2004; Theilen-Willige, 2010; Theilen-Willige and Burnett, 2011; Galy et al., 2013; Braganza et al., 2016; Farzam et al., 2018; Farzam et al., 2021) have demonstrated that satellite-derived products are effective for analyzing site effects, particularly in how local terrain and geological conditions can amplify ground motion.

In this context, Multi-Criteria Decision Analysis (MCDA), particularly the Analytical Hierarchy Process (AHP), provides a robust methodology for weighting various aspects (Almasri et al., 2024; Sinha et al., 2016). Its integration with GIS and RS enables the production of composite risk maps, transforming complex datasets into practical decision-making tools.

Past earthquakes have shown that transportation networks, especially bridges, are highly vulnerable to seismic disasters. The 1971 San Fernando earthquake, the 1989 Loma Prieta earthquake, and the 1994 Northridge earthquake in the United States; the 1995 Kobe earthquake in Japan; and other

* Corresponding author e-mail: fatimazohra.babahamed@univ-usto.dz

destructive events around the world, such as El Asnam 1980, Costa Rica 1990, Kocaeli 1999, Taiwan 1999, and Chile 2010 (Anderson et al., 1996; Mitchell et al., 1991; Mitchell et al., 1995; Mitchell et al., 2013; Yashinsky, 1998; Priestley et al., 1994; Priestley et al., 1996). These events caused significant damage or the collapse of multiple steel and reinforced concrete bridges, which indicates how readily they may be harmed by seismic loads.

Bridges should, in principle, be able to withstand earthquakes. A lot of the bridges that are still standing were built before modern seismic guidelines were implemented, making them exceptionally unstable.

Algeria is a very difficult place since the African and Eurasian plates intersect there, which makes the seismotectonic environment quite intricate. Over the years, the country has suffered many earthquakes that caused significant damage (CRAAG, 1994; Baba-Hamed et al., 2013). The 1716 Algiers earthquake (epicentral intensity X), the 1825 Blida earthquake (intensity IX), the 1790 Oran earthquake (intensity XI), and the 1889 Mascara earthquake (intensity IX) are some of these earthquakes. There have been more recent earthquakes that have caused significant damage to people and structures, such as El Asnam in 1980 (Ms 7.3), Tipasa in 1989 (Ms 6.0), and Boumerdès in 2003 (Ms 6.0).

Many of Algeria's still-used bridges were built before earthquake-resistant design rules were established. Their construction makes them particularly fragile, especially in Oran, which is a large city and industrial center.

In this context, this study develops a GIS-based seismic risk assessment system for 116 bridges in Oran, integrating seismic hazards with the vulnerability information set. The parameters are integrated and weighted using AHP within an MCDA framework.

The goal is to identify the bridges most at risk, prioritize retrofitting and maintenance, and present decision-makers with a data-based tool that reveals where bridges are and strengthens Algeria's transportation network.

2. Methods

2.1 Study area

Oran is considered the second-largest city in Algeria. It is located in the northwest of the country on the shores of the Mediterranean, as shown in Figure 1. The city of Oran has an area of 2,114 km². It is a veritable economic and industrial hub, rich in both history and architecture. It is home to an international airport, three major ports (Oran, Mers-El Kebir, and Arzew), and several universities and research centers with regional and national influence. All of these activities generate significant traffic on the roads (Rahal et al., 2018).

The Oran region is characterized by two distinct types of geological formations (Benabdellah, 2011). The area between the base of Djebel Murdjajo and Misserghin contains Miocene formations. These formations consist of limestones and marl-limestones. In the lower part of the series, there are layers of fine sandstone associated with beds of yellow marl and some layers of shell limestone. To the south, the facies changes, leading to an increasing prominence of marly and clayey deposits. Quaternary deposits are located in the region of Es-Sénia, Chteibo, and Daia Morsli. These deposits consist of layers of highly gypsiferous and saline tuffaceous limestones, which are cracked and feature numerous lenses of detrital clay, silt, and loess, along with lignite.

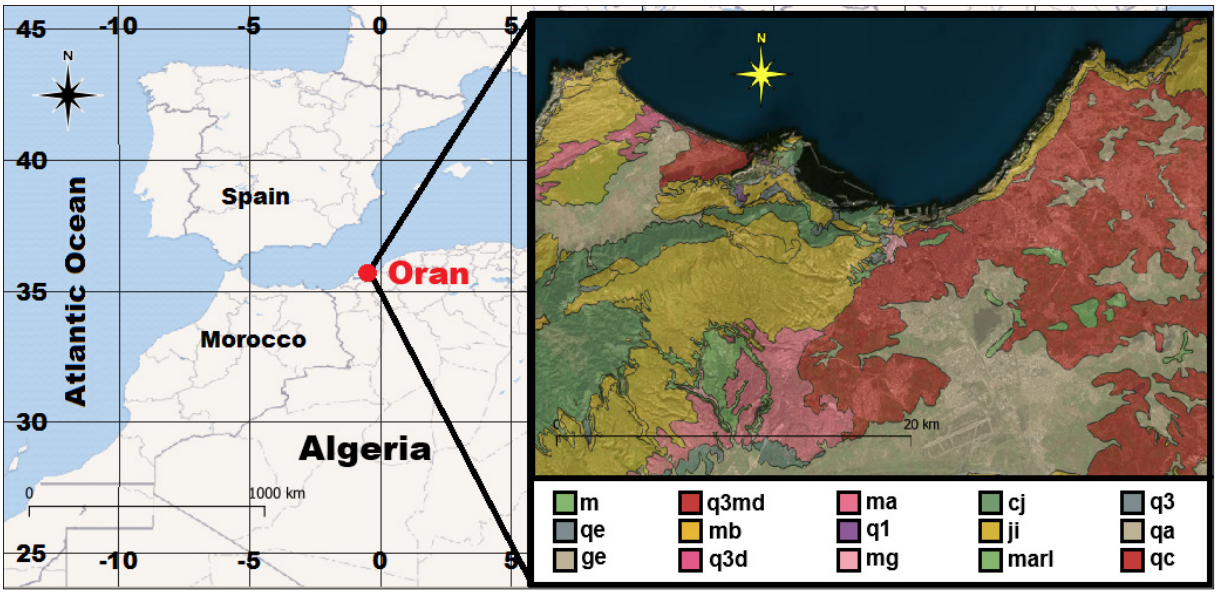

Figure 1. Geographical location of Oran city and its geological map

The altitude of Oran city increases beyond the port area as shown in Figure 2. The maximum altitude (936 m) is reached near Oued-Tlelat; the lowest, -6 m, is near the swamps of Mers-El-Hadjadj. This information appears in Figure 2, which presents the digital terrain model of Oran city.

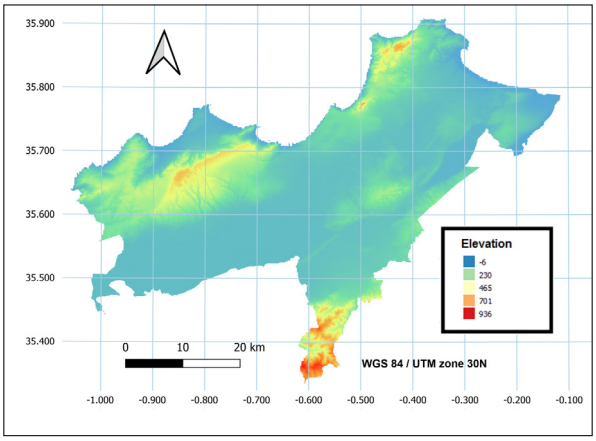

Figure 2. Elevation map of Oran city

Recent field investigations have led to the identification of two major active structures (Yelles-Chaouche et al., 2006) that can generate significant earthquakes: The Sebkha North fault spans approximately 15 km in a NE-SW direction. It delineates the Murdjadjo Mountains to the north and the vast plain of the Sebkha to the south, the Mléta basin.The Sebkha south fault extends along the Tessala Mountains for approximately 30 km in a NE–SW orientation. It intersects the piedmont surfaces represented by alluvial levels ranging from the Lower Pleistocene to the Holocene, which separate the large Sebkha of Oran (Mléta basin) to the north from the Tessala mountains to the south.

2.2 Methodology for assessing the seismic risk of bridges

This study proposes a novel framework for assessing the seismic risk of bridges in the Oran region, combining a systematic weighting method with geospatial tools, including GIS and remote sensing. The key objective is to construct a multicriteria seismic risk map that integrates both seismic hazard elements (e.g., peak ground acceleration, vicinity to active faults) and structural vulnerability characteristics (e.g., seismic design, structural condition).

In Algeria, the level of structural vulnerability is closely linked to how bridge building has changed over time, as shown in Figure 3. There are three distinct periods: before 1980, when most bridges were built with masonry, steel, or reinforced concrete without any thought to how they would hold up in an earthquake; from 1980 to 2008, when the 1980 El Asnam earthquake led to the gradual adoption of earthquake-resistant design and the implementation of the Algerian Seismic Code (RPA); and after 2008, when the introduction of a dedicated regulatory framework (RPOA) for the seismic design of engineering structures, including bridges, marked the end of the previous period.

Figure 3. Representative Bridge Structures in the Oran region

2.2.1 Decision Criteria

For a reliable seismic risk assessment, it is necessary to identify essential criteria and have access to accurate data. Eight critical criteria were selected for this study, as they were crucial for the seismic risk assessment of bridge infrastructure. These criteria are divided into two main groups: one concerns seismic hazard, the other concerns bridge vulnerability. The seismic hazard part indicates the probability and intensity of earthquakes in a given area. We selected the following factors because of their proven importance in previous studies and their availability in the studied area: Peak Ground Acceleration (PGA). We measured

PGA as the peak ground acceleration during an earthquake. It is an essential measure of seismic intensity. Regions with higher PGA values are more prone to experiencing firm ground shaking. In this study, PGA values were extracted from seismic hazard maps corresponding to return periods of 100 and 475 years, respectively, based on the maps provided by. (Peláez et al., 2003)

Distance to fault: The distance to active faults is an important factor in seismic hazard assessment, as structures located near faults are exposed to higher levels of ground shaking resulting from the sudden release of energy during fault rupture.

The fault map used in this study comes from the work of Bouhadad and Laouami (2002). Using this information, the fault proximity map is generated using QGIS software.

Slope: The steepness of a slope significantly affects the propagation and amplification of seismic waves due to topographic site effects. Slopes are classified into three groups (Borfecchia, 2016): flat surfaces, gentle slopes, or isolated reliefs with slopes less than 15° ($p < 15°$); slopes between 15° and 30° ($15° \leq p < 30°$); and steep to very steep slopes with slopes equal to or greater than 30° ($p \geq 30°$). Steeper slopes tend to accentuate ground motions in some areas, increasing the seismic threat. We used SRTM Digital Elevation Model (DEM) values to measure slope evolution over the studied area. Soil type: The lithological impacts of the site greatly influence the magnitude of ground motion amplification by local soil conditions. For example, soft soils tend to intensify seismic waves, while steep or rocky soils tend to weaken them. The Algerian Seismic Code for Works of Art (RPOA, 2008) stipulates that soil classification is generally based on parameters such as the average shear wave velocity to a depth of 30 m (Vs30) or the Standard Penetration Test (SPT) values. Table 1 summarizes these values. In this study, Vs30 values are estimated using the USGS Global Vs30 Map service, which bases its estimations on topographic slope analysis (Wald and Allen, 2007).

Table 1. Soil classification based on the Standard Penetration Test (SPT) and Average Shear Wave Velocity (Vs30)

Site Class	Soil Description	N SPT (SPT Test)	Vs(m /s) (Average Shear Wave Velocity)
S1	Rock	-	800
S2	Stiff soil	> 50	400~<800
S3	Soft soil	10~ 50	200~<400
S4	Very soft soil	<10	100~<200

Source: RPOA, 2008.

The vulnerability component denotes the intrinsic ability of a bridge to resist and dissipate seismic energy. The subsequent parameters were employed to evaluate the susceptibility of bridges:

Seismic Design: This criterion assesses if the bridge was engineered in compliance with seismic-resistant requirements.

Structural Type: This criterion pertains to the primary structural system of the bridge, encompassing the materials employed (reinforced concrete, steel, masonry) and the structural configuration (Continuous bridge, girder bridge, arch bridge, etc.). Each structure type demonstrates unique dynamic behavior and particular seismic susceptibility.

Degradation State: This parameter evaluates the current structural integrity of the bridge, based on visual inspections, technical assessments, or maintenance documentation. The degradation level is often categorized as good, fair, or poor, reflecting the extent of material deterioration or structural damage that could jeopardize the bridge's capacity to endure seismic stresses.

Functional importance: The functional importance is assessed using Average Annual Daily Traffic (AADT), an indicator of the bridge's significance in the transportation network. Bridges with elevated traffic loads are deemed operationally essential, as their failure could lead to substantial mobility disruptions and considerable socio-economic consequences.

This study utilized data from the official bridge inventory published by the Algerian Public Works Department, which offers comprehensive details on bridge location, structural type, physical condition, traffic volume, and year of construction.

2.2 .2 Analytical Hierarchy Process (AHP)

Once the criteria were identified and the spatial data collected, it became necessary to establish the relative importance of each factor in the decision-making process. For this purpose, the AHP, developed by Saaty (1980), was applied.

This method enables the transformation of expert judgments into numerical weights (Rahimi et al., 2024), taking into account both the qualitative and quantitative nature of the criteria.

The AHP approach involves three fundamental steps:

(i) The first step consists of structuring the decision problem into a multi-level hierarchical model. This study aimed to establish a hierarchy for identifying areas susceptible to seismic risk. This objective is supported by two main criteria: seismic hazard parameters and structural vulnerability parameters, each subdivided into specific sub-criteria. The hierarchisation and ranks assigned to selected factors are summarized in Table 4.

(ii) The second step involves the development of pairwise comparison matrices at each level of the hierarchy to evaluate the relative preference between factors. These comparisons were performed using a 9-point scale, where 9 indicates extreme importance, and 1 indicates an equal importance (Saaty, 1990). The matrices for the seismic hazard and vulnerability parameters are presented in Tables 2 and 3, respectively.

Table 2. Pairwise comparison matrix for seismic hazard parameters.

	Peak ground acceleration	Distance from active faults	Slope	Soil class
Peak ground acceleration	1	1	2	3
Distance from active faults	1	1	1.5	2.5
Slope percent	1/2	1/1.5	1	1.5
Soil class	1/3	1/2.5	1/1.5	1

Table 3. Pairwise comparison matrix for seismic vulnerability parameters

	Seismic Design	Structural Type	Degradation State	Functional importance
Seismic Design	1	1	1.5	3
Structural Type	1	1	1	2
Degradation State	1/1.5	1	1	2
Functional importance	1/3	0.5	0.5	1

(iii) The final step was to determine the significant eigenvalue and the related normalized eigenvector from the pairwise comparison matrices. This work was done to determine the relative weights of each parameter. To evaluate the consistency of expert judgments, the Consistency Index (CI), Random Index (RI), and Consistency Ratio (CR) were computed using the following standard formulas (Almasri et al., 2024; Sinha et al., 2016):

$$CI = \frac{\lambda_{max} - n}{n - 1} \quad \text{..... (1)}$$

$$CI = \frac{1.98(n-1)}{n} \quad \text{..... (2)}$$

$$CI = \frac{CI}{RI} \quad \text{..... (3)}$$

Where λ_{max} represents the major eigenvalue and n denotes the matrix order. A CR rating under 10% is usually considered a sign of good consistency. In this study, the calculated CR substantiates the reliability and consistency of the evaluations and the validity of the obtained weights. Table 4 shows the computed weights for the hazard and vulnerability parameters.

Table 4. Weights and ranks of the reviewed factors for hazards and vulnerability assessment

Hazard criterion			
	Class value	Rank	Weight
PGA	Inf 0.07g	1	0.36
	0.07 ≤ PGA < 0.11 g	3	
	0.11 g ≤ PGA < 0.16 g	5	
	0.16 g ≤ PGA < 0.3 g	7	
	≥0.3g	9	
Distance from active faults (Km)	<25	1	0.32
	25-50	3	
	50-75	5	
	75-100	7	
	100-125	9	
Soil class	Rock	1	0.194
	Stiff soil	3	
	Soft soil	6	
	Very soft soil	9	
Slope (degree)	<15	3	0.126
	15-30	6	
	>30	9	
CI = 0.0027	RI= 0.90	CR = 0.29%	
Vulnerability criterion			
	Class value	Rank	Weight
Seismic Design	RPOA 2008	1	0.342
	RPA	5	
	Static	9	
Structural Type	Portal frame bridge	1	0.279
	Continuous bridge	3	
	Independent Multi-Span Bridge	5	
	Composite Reinforced Concrete–Masonry Bridge	7	
	Masonry arch bridges	9	
Degradation State	Good	1	0.252
	Medium	5	
	Poor	9	
Functional importance (AADT: veh/day)	<6250	1	0.126
	6250-12500	3	
	12500-18750	5	
	18750-25000	7	
	>25000	9	
CI=0.0069	RI= 0.90	CR =0.76%	

2.2.3 Assessment of risk levels

The computed weights were incorporated into thematic raster layers within a GIS system (QGIS), with each spatial layer denoting a distinct criterion. A weighted overlay analysis was subsequently employed to create two composite indices: the Seismic Hazard Index, derived from the initial four thematic levels, and the Seismic Vulnerability Index, based on the final four layers.

The indices were computed using the corresponding derived weights. The hazard score map was classified into five levels: Negligible (0–0.2), Low (0.2–0.4), Moderate (0.4–0.6), High (0.6–0.8), and Very High (0.8–1). The hazard score map was subsequently classified into five levels: Negligible (0–0.2), Low (0.2–0.4), Moderate (0.4–0.6), High (0.6–0.8), and Very High (0.8–1). A vulnerability score map was also categorized using the same five-level scale.

The ultimate Seismic Risk Index (R) was derived as the product of the Seismic Hazard (H) and Structural Vulnerability (V) indices, as expressed in the following equation:

Risk Index = Hazard Index × Vulnerability Index .....(4)

The risk index is the hazard index multiplied by the vulnerability index. The matrix in Table 5 (CEREMA, 2016) illustrates the convergence of hazard and vulnerability levels, which establishes the seismic risk levels of bridges based on their likelihood of failure.

Table 5. Risk matrix combining hazard and vulnerability classifications

	V1	V2	V3	V4	V5
H1	R1	R1	R1	R2	R2
H2	R1	R1	R2	R3	R3
H3	R1	R2	R3	R4	R4
H4	R2	R3	R4	R5	R5
H5	R3	R4	R5	R5	R5

Where :

R1: Very- Low level risk

R2: Low-level risk

R3: Moderate-level risk

R4: High-level risk

R5: Very-High level risk

Seismic risk maps were subsequently created for several earthquake scenarios, accounting for both average and extreme Peak Ground Acceleration (PGA) values associated with return periods of 100 and 475 years.

3. Results and discussion

3.1 Evaluation of Seismic Hazard Levels

Figures 4 to 6 show the main seismic hazard parameters that are included in the GIS environment. The active fault map as shown by Figure 4, delineates bridges situated in proximity to possible rupture zones. The soil classification map (Figure 5) indicates a significant prevalence of bridges built on soft soils, hence increasing their susceptibility to seismic amplification. The slope gradient map (Figure 6) identifies slope terrains that increase ground motion.

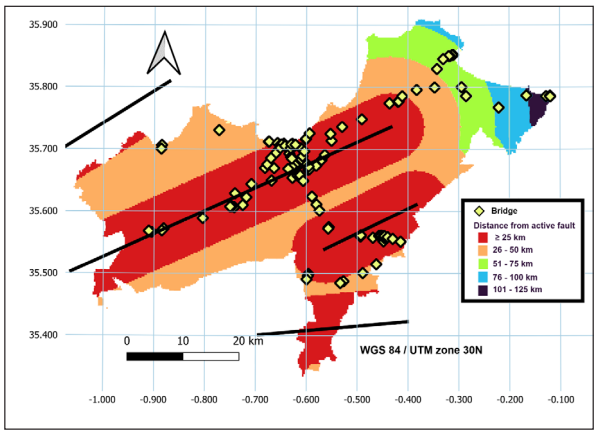

Figure 4. Distance for the active fault map in the Oran region

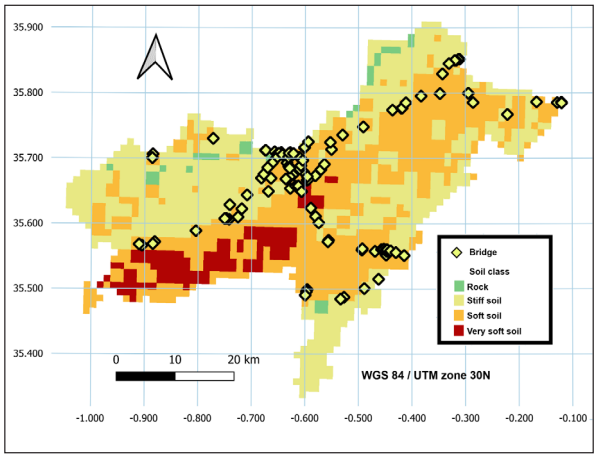

Figure 5. Soil classification map of the Oran region

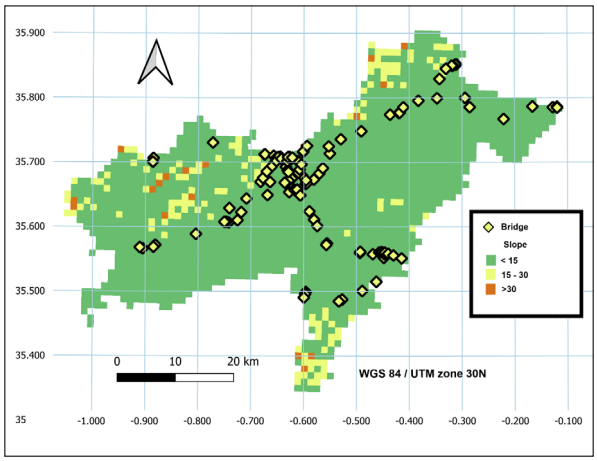

Figure 6. Slope gradient map of the Oran region

Applying the weighting strategy defined by the established method, these geographic layers were combined using a weighted overlay method within the GIS platform. The composite seismic hazard map illustrates the spatial distribution of seismic exposure, determined by active faults, terrain slope, and local soil characteristics.

Four seismic scenarios had been developed to provide a more complete evaluation of regional seismic exposure, each aligned with a specific return period and Peak Ground Acceleration (PGA) value.

• Scenario 1: Mean Peak Ground Acceleration for a 100-year Return Period (0.068 g)

• Scenario 2: Peak Ground Acceleration for a 100-year return period (0.095 g)

• Scenario 3: Average Peak Ground Acceleration for a 475-year return time (0.138 g)

• Scenario 4: Peak Ground Acceleration (PGA) for a 475-year return period (0.18 g)

Figures 7 and 8 illustrate the spatial distribution of seismic hazard levels for the analyzed bridges under four representative scenarios.

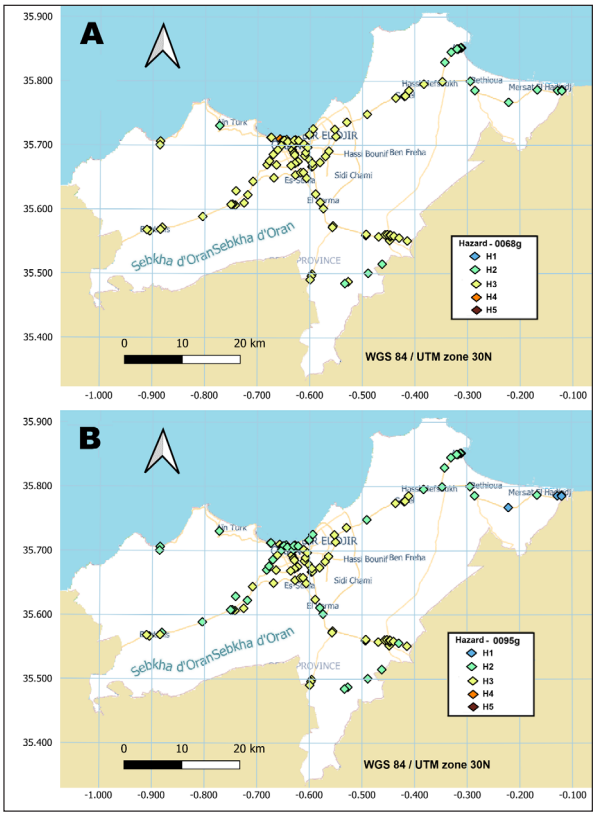

Figure 7. Mapping of seismic hazard levels of the analyzed bridges under average (PGA = 0.068g) and worst-case (PGA = 0.095g) scenarios for a 100-year return period

The comparative analysis of the four scenarios demonstrates a distinct progression in bridge exposure aligned with the increasing severity of seismic hazard.

Scenario 1 illustrates a basically secure context, with approximately 16% of bridges located in low hazard zones (H2) and 82% of bridges enduring moderate hazard levels (H3). Only 0.8% is situated in high hazard areas (H4), with no presence in the very high category (H5), signifying a limited seismic hazard.

In Scenario 2, a notable redistribution occurs: around 46% of bridges are now subjected to moderate hazard levels (H3), while an additional 50% are situated inside high hazard zones (H4). This transition indicates an increasing apprehension about structural safety.

Scenario 3 reveals an alarming situation, with over 83% of the bridge inventory in high hazard zones (H4) and the remaining 16.3% in moderate zones (H3). The lack of bridges in lower hazard categories indicates a significant rise in seismic risk.

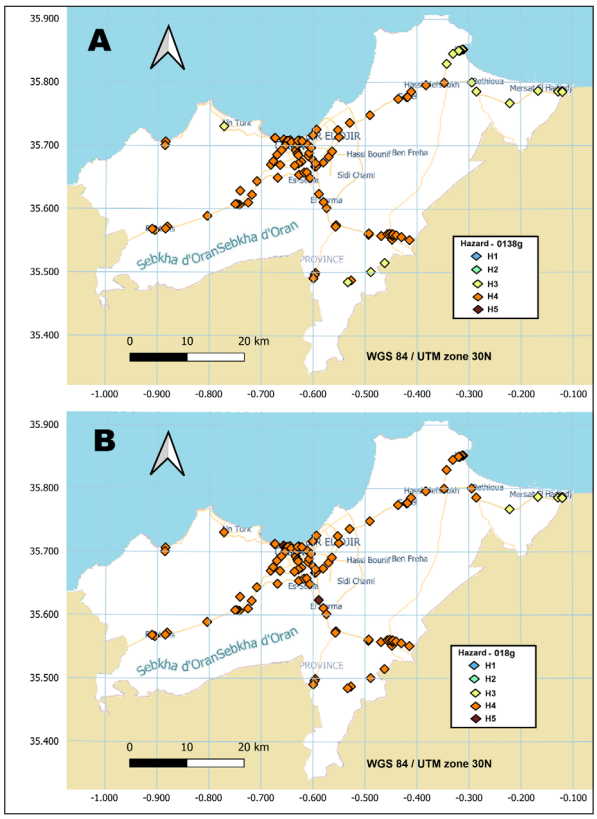

Figure 8. Mapping of seismic hazard levels of the analyzed bridges under average (PGA = 0.138 g) and worst-case (PGA = 0.18 g) scenarios for a 475-year return period

Scenario 4 represents the most critical scenario. Over 94% of bridges are located in high hazard zones (H4), while over 1.7% are in very high hazard zones (H5). Merely 4.3% persist in moderate zones (H3). This situation highlights an immediate necessity for their assessment of earthquake risk.

3.2 Seismic vulnerability Assessment of bridges

The seismic vulnerability evaluation of the bridge network was performed based on numerous critical factors outlined in the Methodology section. Figure 9 presents a visual synthesis of these criteria.

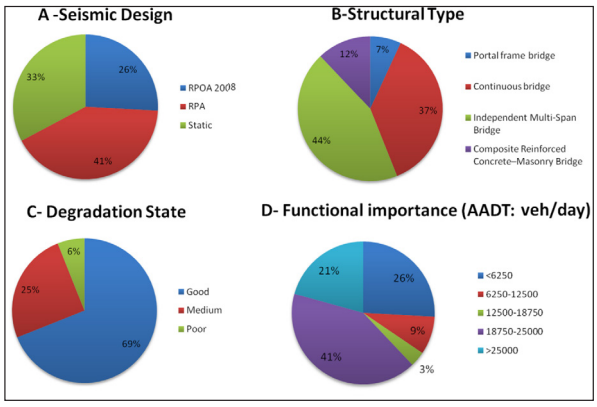

Figure 9. Graphical analysis of seismic vulnerability parameters

As illustrated in Figure 9A, significant portions, around 74%, of the bridges under study were constructed prior to the implementation of modern seismic design codes, thereby increasing their susceptibility to earthquake-induced forces.

Figure 9B indicates that the majority of the bridges studied are of conventional design, with approximately 44%

corresponding to independent multi-span bridges, which generally exhibit limited seismic performance due to their low energy dissipation capacity.

The state of degradation, shown in Figure 9C, was assessed through field inspections. The results indicate that approximately 69% of the bridges are in good condition, 25% in medium condition, and 6% in poor condition. Although the majority are in satisfactory condition, some bridges exhibit significant deterioration that negatively affects their dynamic response, meaning they require targeted maintenance and modernization.

Finally, the functional importance of each bridge, illustrated in Figure 9D, was assessed based on traffic volume and strategic role. Overall, 60% of bridges carry medium to high traffic, underscoring their key role in maintaining network connectivity.

As detailed in the Methodology section, these characteristics were weighted to reflect their relative contribution to structural vulnerability. The resultant weights were subsequently included in a GIS, facilitating a spatially referenced multicriteria analysis. This integration provided the allocation of vulnerability scores to each bridge, considering their geographic location and particular structural characteristics. Consequently, a seismic vulnerability map, illustrated in Figure 10, was produced, offering an extensive depiction of susceptibility levels over the whole bridge network.

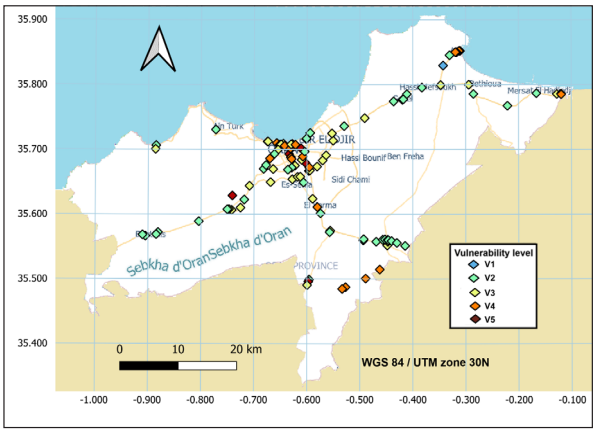

Figure 10. Map of the vulnerability levels of the inspected bridges

The analysis shows that about 38% of the bridges are in the very low to low vulnerability classifications (V1–V2), which means that their structural performance is generally satisfactory. About 33% are considered to have considerable vulnerability (V3), which means they need closer monitoringand may need to be protected. On the other hand, 29% of the bridges are in the V4–V5 range of high to very high vulnerability. They should be prioritized for intervention because their structural state is so unacceptable. The findings show that most bridges are in the moderate-to-high vulnerability classes. This result indicates the need for specific actions, such as strengthening the structure or conducting more thorough inspections, especially in areas with significant seismic hazards. Older bridges that are not reinforced for earthquakes, are built on soft soils, or exhibit structural damage are more likely to be vulnerable. In contrast, those with low vulnerabilities are generally newer constructions built in accordance with seismic design codes.

3.3 Risk Level Assessment

Seismic risk maps for each scenario were produced by integrating the hazard and vulnerability maps, as seen in Figures 11 and 12.

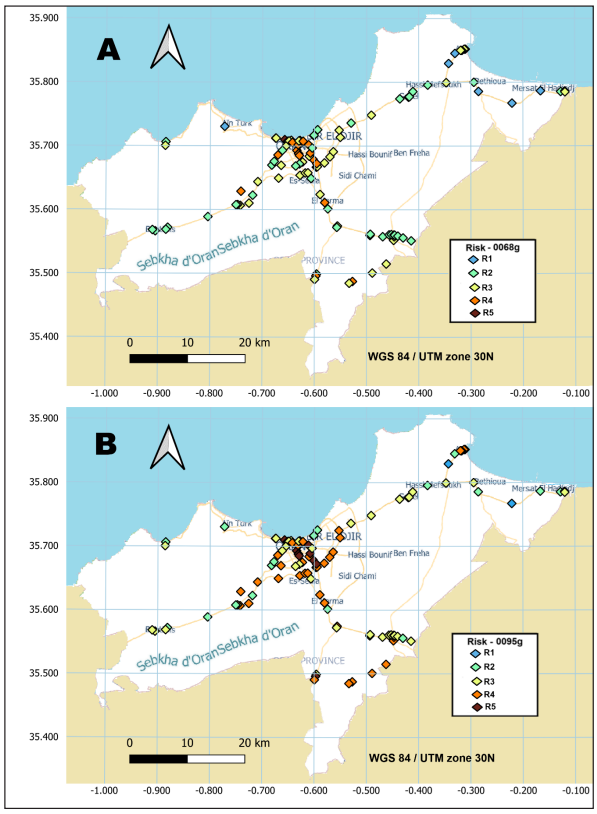

Figure 11. Mapping of seismic risk levels of the analyzed bridges under average (PGA = 0.068g) and worst-case (PGA = 0.095g) scenarios for a 100-year return period

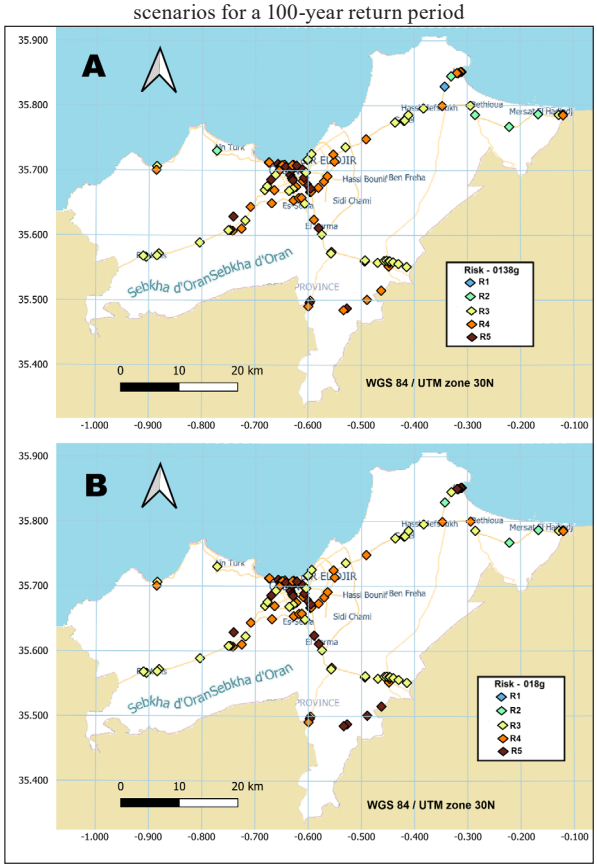

Figure 12. Mapping of seismic risk levels of the analyzed bridges under average (PGA = 0.138g) and worst-case (PGA = 0.18g) scenarios for a 475-year return period

The comparative examination of the four scenarios reveals a gradual increase in the seismic exposure of bridges as they progress from Scenario 1 to Scenario 4. In Scenario 1, most bridges are located in very low- to low-risk (40.51%) and moderate (38.80%) risk zones, with minimal presence in high (19.82%) and very high (0.86%) risk areas, reflecting a very even distribution. In Scenario 2, the distribution changes, exhibiting a substantial decline in the percentage of bridges located in lower-risk zones, with just 18.96% in very low- to low-risk and 17.24% in moderate-risk locations, while the number in high-risk (37%) and very high-risk (10.34%) zones escalates, indicating an increasing susceptibility. Scenario 3 maintains this trend, with a negligible presence in very low and low (5.17%) risk zones, a consistent proportion in moderate zones (35.34%), and a significant rise in high (38.79%) and very high (20.68%) risk categories, indicating a concerning transition into harmful areas. Finally, Scenario 4 indicates the most severe situation: no bridges exist in very low-risk places, with merely 2.58% located in low-risk zones, while 37% exist in intermediate areas. Significantly, 31% and 29.31% of the bridges are situated in high- and very-high-risk zones, respectively, highlighting the urgent necessity for immediate and extensive seismic risk assessment methods.

3.4 Discussion

The seismic risk evaluation indicates that a significant number of bridges are classified as high or very high risk. These structures are mostly located in regions with elevated seismic hazard levels and significant structural vulnerability. Such situations are commonly found near active fault lines, in areas with soft soils that amplify earthquake shaking, and near older bridges built without compliance with contemporary seismic design standards. These bridges are essential links in the infrastructure network, and their collapse following a significant earthquake could lead to severe human, economic, and logistical consequences. Extensive studies based on advanced numerical modeling (nonlinear analysis) and immediate measures, including retrofitting or replacement, are essential to improve their resilience. Bridges categorized as moderate risk necessitate meticulous monitoring. These structures are frequently exhibit moderate susceptibility and are located in areas with moderate seismic hazard. While they do not pose an immediate danger, they are vulnerable to operational degradation or service interruptions during significant earthquakes . A comprehensive evaluation grounded in state-of-the-art numerical modeling of preventive reinforcement strategies would mitigate future maintenance expenses and ensure service continuity. Bridges situated in low- and very-low risk zones are typically located in geologically stable regions and frequently have modern designs that adhere to present construction standards. However, regular evaluation and appropriate maintenance are crucial to guaranteeing their continued performance, especially given structural deterioration and altering environmental conditions. These results provide a solid basis for prioritizing intervention measures. Infrastructure managers may develop an effective and economically viable earthquake risk-reduction strategy by focusing on the most susceptible structures and by conducting continuous inspections of low-risk bridges.

4. Conclusion

The present study introduced a comprehensive technique for seismic risk assessment of bridges by integrating the AHP, GIS, and remote sensing data. The methodology used four hazard criteria (peak ground acceleration, fault proximity, topographic slope, and soil type) alongside four vulnerability criteria (seismic design, structural type, degradation state, and functional importance) to create a comprehensive, spatially explicit seismic risk map for a collection of engineering structures.

The results identified major intervention sites where bridges show structural vulnerabilities and significant hazard exposure. The established method is reproducible and adaptive, contributing as an essential decision-support tool for infrastructure managers, local authorities, and civil protection services. It simplifies resource allocation for maintenance and retrofitting while also improving emergency response strategies for potential earthquakes.

Nevertheless, specific constraints persist, especially the absence of dynamic data on bridge performance and the uncertainty surrounding the qualitative assessment of risk. The prospective combination of data from in situ sensor data with sophisticated numerical modeling (nonlinear analysis) may substantially enhance the precision of these analyses.

Conflict of Interest

The authors declare no conflict of interest.

Funding

The authors received no financial support for the research, authorship, and/or publication of this article.

References

Al-Dogom, D., Al-Ruzouq, R., Kalantar, B., Schuckman, K., Al-Mansoori, S., Mukherjee, S., & Ueda, N. (2021). Geospatial multicriteria analysis for earthquake risk assessment: Case study of Fujairah City, UAE. Journal of Sensors, 2021, Article 6638316. https://doi.org/10.1155/2021/6638316

Anderson, D. L., Mitchell, D., & Tinawi, R. G. (1996). Performance of concrete bridges during the Hyogo-ken Nanbu (Kobe) earthquake on January 17, 1995. Canadian Journal of Civil Engineering, 23, 714–726. https://doi.org/10.1139/l96-884

Baba Hamed, F. Z., Rahal, D. D., & Rahal, F. (2013). Seismic risk assessment of Algerian buildings in urban areas. Journal of Civil Engineering and Management, 19(3), 348–363. https://doi.org/10.3846/13923730.2012.744772

Baillifard, F., Jaboyedoff, M., & Sartori, M. (2003). Rockfall hazard mapping along a mountainous road in Switzerland using a GIS-based parameter rating approach. Natural Hazards and Earth System Sciences, 3, 435–442. https://doi.org/10.5194/nhess-3-435-2003

Benabdellah, M. (2011). Mise en évidence des phénomènes dynamiques contrôlant le littoral oranais (de la Calère à la Pointe de Canastel): Étape fondamentale pour une cartographie des risques géologiques (Doctoral dissertation). Université Mohamed Ben Ahmed d'Oran 2, Algeria.

Borfecchia, F., De Canio, G., De Cecco, L., Giocoli, A., Grauso, S., La Porta, L., & Zini, A. (2016). Mapping earthquake-induced landslide hazard around the main oil pipeline network of the Agri Valley (southern Italy) using GIS-based modeling approaches. Natural Hazards, 81, 759–777. https://doi.org/10.1007/s11069-015-2104-0

Bouhadad, Y., & Laouami, N. (2002). Earthquake hazard assessment in the Oran region (northwest Algeria). Natural Hazards, 26, 227–243. https://doi.org/10.1023/A:1015602815231

Braganza, S., Atkinson, G. M., Ghofrani, H., Hassani, B., Chouinard, L., Rosset, P., & Hunter, J. (2016). Modeling site amplification in eastern Canada on a regional scale. Seismological Research Letters, 87(4), 1008–1021. https://doi.org/10.1785/0220160009

CEREMA. (2016). Déclinaison régionale du cadre d'actions pour la prévention du risque sismique (CAPRiS) en région PACA (87 pp.). Centre d'Études et d'Expertise sur les Risques, l'Environnement, la Mobilité et l'Aménagement.

Cheddad, S., Haouchine, A., & Benmerabet, N. (2025). Surface runoff estimation using GIS data under HEC-HMS: Wadi Laussif sub-basin, Algeria. Jordan Journal of Earth & Environmental Sciences, 16, 220–226.

CRAAG. (1994). Les séismes en Algérie de 1365 à 1992. Centre de Recherche en Astronomie, Astrophysique et Géophysique, Algiers.

Davi, D., Kahan, M., Légeron, F., Marchand, P., Portier, B., Resplendino, J., Schmitt, P., Thibault, C., & Vivier, A. (2011). SISMOA: Évaluation préliminaire du risque sismique sur les ouvrages d'art existants (Technical report). SETRA.

Erdik, M., Sesetyan, K., Demircioglu, M., Hancilar, U., Zulfikar, C., Cakti, E., & Harmandar, E. (2010). Rapid earthquake hazard and loss assessment for the Euro-Mediterranean region. Acta Geophysica, 58, 855–892. https://doi.org/10.2478/s11600-010-0027-4

Farzam, A., Nollet, M. J., & Khaled, A. (2018). Susceptibility modeling of seismically induced effects integrated into rapid scoring procedures for bridges using GIS tools. Geomatics, Natural Hazards and Risk, 9, 589–607. https://doi.org/10.1080/19475705.2018.1466731

Farzam, A., Nollet, M. J., & Khaled, A. (2021). Integration of site condition information using GIS for seismic risk reduction of bridge networks. Georisk: Assessment and Management of Risk for Engineered Systems and Geohazards. https://doi.org/10.1080/17499518.2021.1952609

Galy, B., Khaled, A., & Nollet, M. J. (2013). Seismic vulnerability assessment of typical Quebec City bridges considering site-specific amplification. Canadian Journal of Civil Engineering, 40, 1–10. https://doi.org/10.1139/cjce-2011-0052

Kim, S. H. (1993). A GIS-based regional risk analysis approach for bridges against natural hazards (Doctoral dissertation). State University of New York at Buffalo.

Kiremidjian, A., Moore, J. E., Fan, Y., Yazlali, O., Basoz, N., & Williams, M. (2008). Seismic risk assessment of transportation network systems. Journal of Earthquake Engineering, 12(Supplement 1), 76–100.

Kibboua, A., Bechtoula, H., Mehani, Y., & Naili, M. (2014). Vulnerability assessment of reinforced concrete bridges in Algiers using scenario earthquakes. Bulletin of Earthquake Engineering, 12, 807–827. https://doi.org/10.1007/s10518-013-9523-7

Mitchell, D., Tinawi, R., & Sexsmith, R. G. (1991). Performance of bridges in the 1989 Loma Prieta earthquake—Lessons for Canadian designers. Canadian Journal of Civil Engineering, 18, 711–734. https://doi.org/10.1139/l91-085

Mitchell, D., Bruneau, M., Saatcioglu, M., Williams, M., Anderson, D., & Sexsmith, R. (1995). Performance of bridges in the 1994 Northridge earthquake. Canadian Journal of Civil Engineering, 22, 415–427. https://doi.org/10.1139/l95-050

Mitchell, D., Huffman, S., Tremblay, R., Saatcioglu, M., Palermo, D., Tinawi, R., & Lau, D. (2013). Damage to bridges due to the 27 February 2010 Chile earthquake. Canadian Journal of Civil Engineering, 40, 675–692. https://doi.org/10.1139/l2012-045

MTQ. (2013). Ouvrages d'art: Tome III—Classification des ouvrages d'art. Ministère des Transports du Québec.

OFROU. (2005). Seismic assessment of existing road bridges. Swiss Federal Roads Office.

Peláez, J. A., Hamdache, M., & Casado, C. L. (2006). Seismic hazard in terms of spectral accelerations and uniform hazard spectra in northern Algeria. Pure and Applied Geophysics, 163, 119–135. https://doi.org/10.1007/s00024-005-0011-0

Pitilakis, K. (2004). Site effects. In Recent advances in earthquake geotechnical engineering and microzonation (pp. 139–197). Springer. https://doi.org/10.1007/1-4020-2528-9_6

Priestley, M. J. N., Verma, R., & Xiao, Y. (1994). Seismic shear strength of reinforced concrete columns. Journal of Structural Engineering, 120, 2310–2329. https://doi.org/10.1061/(ASCE)0733-9445(1994)120:8(2310)

Priestley, M. J. N., Seible, F., & Calvi, G. M. (1996). Seismic design and retrofit of bridges. Wiley.

Rahal, F., Hadjou, Z., Blond, N., & Aguejdad, R. (2018). Urban growth, mobility, and air pollutant emissions in the Oran region, Algeria. Cybergeo: European Journal of Geography. https://doi.org/10.4000/cybergeo.29111

Rahimi, N., Kargaranbafghi, F., Shahid, M. R., & Afkhami, S. (2024). Using fuzzy logic and AHP for mineral potential mapping in the Janja exploration area, Iran. Jordan Journal of Earth & Environmental Sciences, 15, 275–286.

RPOA. (2008). Paraseismic rules applicable to civil engineering works. Ministry of Public Works, Algeria.

Saaty, T. L. (1980). The analytic hierarchy process. McGraw-Hill.

Saaty, T. L. (1990). How to make a decision: The analytic hierarchy process. European Journal of Operational Research, 48, 9–26. https://doi.org/10.1016/0377-2217(90)90057-I

Sinha, N., Nair, P., & Joshi, P. K. (2016). Using spatial multicriteria analysis (SMART) in earthquake risk assessment: Delhi region, India. Geomatics, Natural Hazards and Risk, 7, 680–701. https://doi.org/10.1080/19475705.2014.945100

Theilen-Willige, B. (2010). Detection of local site conditions influencing earthquake shaking using remote sensing and GIS methods in southwest Haiti. Natural Hazards and Earth System Sciences, 10, 1183–1196. https://doi.org/10.5194/nhess-10-1183-2010

Theilen-Willige, B., & Burnett, F. B. (2011). Detection of local site conditions influencing earthquake effects in the Valparaíso area, central Chile. Science of Tsunami Hazards, 30, 86–101.

Wald, D. J., & Allen, T. I. (2007). Topographic slope as a proxy for seismic site conditions. Bulletin of the Seismological Society of America, 97, 1379–1395. https://doi.org/10.1785/0120060267

Yashinsky, M. (1998). Performance of bridge seismic retrofits during the Northridge earthquake. Journal of Bridge Engineering, 3, 1–14. https://doi.org/10.1061/(ASCE)1084-0702(1998)3:1(1)

Yelles-Chaouche, A. K., Boudiaf, A., Djellit, H., & Bracene, R. (2006). Active tectonics in northern Algeria. Comptes Rendus Geoscience, 338, 126–139. https://doi.org/10.1016/j.crte.2005.11.002

JJEES

JJEES (2026) 17 (1): 83-96
ISSN 1995-6681

Jordan Journal of Earth and Environmental Sciences

Comparative Reliability Analysis of CHIRPS and Gauge-based Precipitation Measurements over the Zarqa River Basin

Michel Rahbeh [1*], Nisrein H. Alnizami [1], Mutaz M. Zoubi [2], Qusay Y. Abu-Afifeh [1,3], Tala A. Qutishat [4], Mutasem R. AlHalaigah [1], Heba F. Al-Jawaldeh [1,3], Saif Al-Omari [3,5], Bassam. Al Qarallah [6]

[1] Department of Land, Water and Environment, The University of Jordan, Amman 11942, Jordan
[2] Department of Chemistry, The University of Jordan, Amman 11942, Jordan
[3] Department of Civil Engineering, The University of Jordan, Amman 11942, Jordan
[4] Department of Geology, The University of Jordan, Amman 11942, Jordan
[5] Department of Water and Environmental Engineering, Scientific Sustainable Vision Company, Amman 11194, Jordan
[6] Department of Horticulture and Crop Science, The University of Jordan, Amman 11942, Jordan

Received on 6 June 2025; Accepted on 11 September 2025

Abstract

This study highlights the growing need for reliable and consistent precipitation data to support sustainable water resource management by evaluating the Climate Hazards Group Infrared Precipitation with Station dataset (CHIRPS) as a potential alternative to ground-based observations. The study objectives were to analyze the trends of precipitation indices using CHIRPS and observed data (station data) and to compare the correlations between station data and CHIRPS.

Trend analyses of extreme precipitation indices were conducted using observed data from 18 meteorological stations. A total of 12 annual climate indices were extracted from daily rainfall records (1985-2012) using the CLIMPACT software. Furthermore, a trend analysis was performed for the period 1998–2023 using CHIRPS data, and the results were compared with observations from five stations with available records for the same period. In addition, long-term trends spanning 1992–2023 were evaluated using CHIRPS data exclusively.

The CHIRPS data showed moderate agreement with station observations at the monthly and annual scales, with mean PCCs of 0.65 and 0.69, respectivelybut demonstrated clear limitations in capturing long-term trends. It identified only three significant trends (P< 0.05) at CDD, CWD, and R10mm, with values of 1, -0.05, and -0.132, respectively (20% of those detected by stations), none of which aligned with station records. For 1998–2023, CHIRPS detected three downward and four upward trends, the strongest trend shown in the PRCTOT indicator with values 1.92, 2.99, and 7.497 (28 % of those detected by stations), and the third part of the study, conducted over CHIRPS data (1998-2023) only, showed 3 downward trends and 11 upward trends. These results indicate that CHIRPS requires bias correction before reliable use and underscore the importance of expanding the rainfall monitoring network.

Keywords: *CHIRPS dataset; Climate variability; Data validation; Hydrological monitoring; Rainfall indices; Trend analysis.*

1. Introduction

Climate change remains one of the most pressing global challenges, affecting both environmental systems and socio-economic stability (Abu-Afifeh et al., 2023; Teweldebrihan and Dinka, 2024; Al-Afeshat et al., 2025; Hroub et al., 2025; Obeidat et al., 2025a, 2025b). Variability in precipitation and temperature—key indicators of climate change—has become a significant focus of hydrological studies (Suharyanto et al., 2023). These fluctuations have particularly severe consequences in arid and semi-arid regions, where fragile ecosystems are highly vulnerable to drought and water scarcity (Al-Addous et al., 2023; Dede et al., 2023). As global temperatures rise, evaporation rates increase, intensifying drought in some regions and amplifying rainfall in others. These dynamics complicate water management, especially in water-scarce areas (Kundzewicz et al., 2007). The Intergovernmental Panel on Climate Change (IPCC) highlights that changing rainfall patterns, rising temperatures, and more frequent extreme weather events are disrupting global water availability and distribution (Trenberth, 2011). For example, surface runoff in northwest China has increased due to altered rainfall patterns and glacier melt (Chen et al., 2020). In Africa, studies suggest that drought severity is projected to worsen (Masih et al., 2014; Justus Reymond and Sudalaimuthu, 2023). In the Middle East and North Africa (MENA), temperatures are expected to increase by up to 4 °C, accompanied by a decline in rainfall by the 'Century's end (Lelieveld et al., 2016). Regionally, Iraq has experienced declining spring and winter rainfall, with increasing summer rainfall and rising temperatures (Salman et al., 2017). Drought trends in the Gaza Strip between 1974 and 2016 varied spatially, with some areas severely affected during 1990, 2010, and 2014 (Ajjur and Riffi, 2020). Egypt recorded rising minimum temperatures and more hot days, though rainfall patterns remained relatively stable (Hamed et al., 2023).

* Corresponding author e-mail: m.rahbeh@ju.edu.jo

In Syria, rainfall slightly increased in autumn but declined significantly in winter between 1991 and 2009 (Zeleňáková et al., 2022). In Jordan, rainfall data from 58 stations (1970–2013) showed a decreasing trend at 38 stations at an average rate of 1.2 mm/year (Rahman et al., 2015). Droughts have become more frequent and severe (Al-Qinna et al., 2011). Alsalal et al. (2024) projected a 23 % decrease in precipitation in the Mujib Basin and a 1.4–6.4°C increase in temperature by the end of the Century. In the Zarqa River Basin (ZRB)—a key water source in Jordan—declining rainfall (Al-Houri, 2014) and shortened rainy seasons (Shatanawi et al., 2022) have been reported. Due to the limited distribution of meteorological stations in arid areas like the ZRB, alternative datasets such as the Climate Hazards Group Infrared Precipitation with Station (CHIRPS) are increasingly used to fill spatial gaps (Shen et al., 2020). However, CHIRPS must be evaluated before it is used in climate analysis. In Brazil, CHIRPS failed to capture rainfall trends in semi-arid zones, although its performance improved in wet seasons (Cavalcante et al., 2020; Hasibuan et al., 2025; Paredes-Trejo et al., 2017). In Colombia, CHIRPS performed better in highland areas (Ocampo-Marulanda et al., 2022). In Cyprus, rainfall was slightly overestimated but showed acceptable correlation (Katsanos et al., 2016). In India, CHIRPS reliably captured monthly rainfall variability (Prakash, 2019), and in Jordan, it has been deemed useful for filling data gaps (El-Mahroug et al., 2025; Alsalal et al., 2023). Furthermore, an investigation by Al Shamayleh et al. (2024) on rainfall in Mujib showed that a moderate correlation between CHIRPS and gauge data at the annual and monthly scale; however, an in-depth trend analysis for 11 extreme precipitation indices showed that CHIRPS captured the variability and produced the same trends as the observed data. The use of the mentioned indices significantly enhances the robustness of the climate trend analysis by providing a more detailed and comprehensive view of precipitation variability. This approach allows for the detection of subtle shifts in rainfall intensity and frequency, which are critical for understanding the impacts of climate change on water resources. Previous research indicated that there are still knowledge gaps in climate change research in Jordan, especially in major basins such as the ZRB, which still require trend analysis for major precipitation variables. Additionally, there is a need to validate alternative climatic data, such as CHRPS, to improve the spatial representation of precipitation in the ZRB, as well as to compensate for missing data. Thus, the study aims to analyze precipitation index trends using CHIRPS and observed (gauge station) data, and to compare correlations between the observed (gauge station) and CHIRPS data. This study was carried out at the ZRB, Jordan, during 2013-2023.

2. Materials and Methods

2.1 Study area description

The study area is located in the north-central part of Jordan (Fig. 1) and covers 3567 km². The Zarqa River Basin is the second major tributary to of the Jordan River and lies between longitudes 35° to 37° East and latitudes 31° to 33° North. The basin hosts parts of several major cities, Amman, Zarqa, and Jerash, and serves as a key area for urban expansion. It is considered one of the most vital basins in Jordan for agricultural, social, and economic importance (Al-Abed and Al-Sharif, 2007).

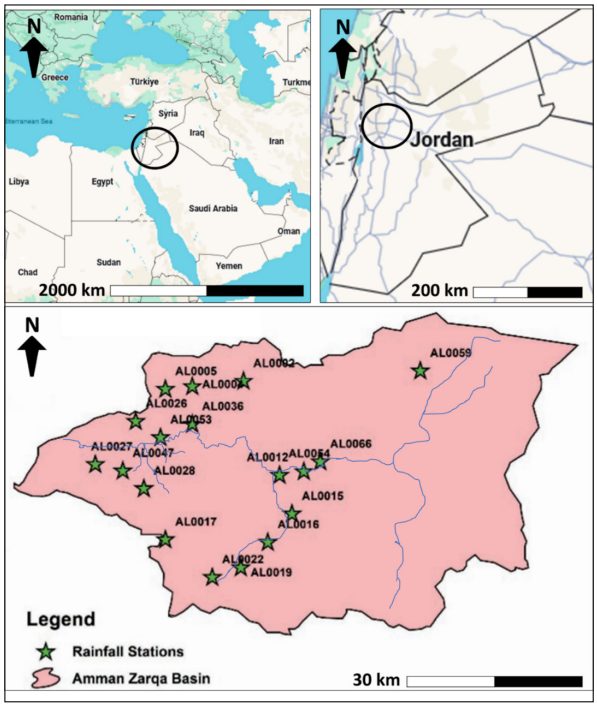

Figure 1. Geographical location of the study area along with rainfall stations in the Zarqa River Basin in Jordan

The ZRB is characterized by a semi-arid to arid Mediterranean climate. Summers are warm and dry, while winters are cool and wet, with occasional snowstorms and moderate frost events. The average summer temperature is 35°C, and the average winter temperature is 5 °C. Precipitation varies spatially, ranging from about 500 mm/y in the western half to 150 mm/y in the eastern half. Most of the rainfall occurs between November and April (MWI, 2020).

2.2 Methodological process overview

The research methodology flow of the study, illustrated in Fig. 2, comprised three main steps. First, observed meteorological data and CHIRPS satellite-based precipitation data were collected using the RStudio programming language (RStudio, 2024.08.0 Build 463©2009-2025 Posit Software, Public Benefit Corporation (PBC). Second, the CLIMPACT software was used to evaluate climate indices and analyze their trends for both observed and CHIRPS datasets. Finally, the results were analyzed, and the trends derived from both data sources were compared. Each step is briefly discussed in the following sections.

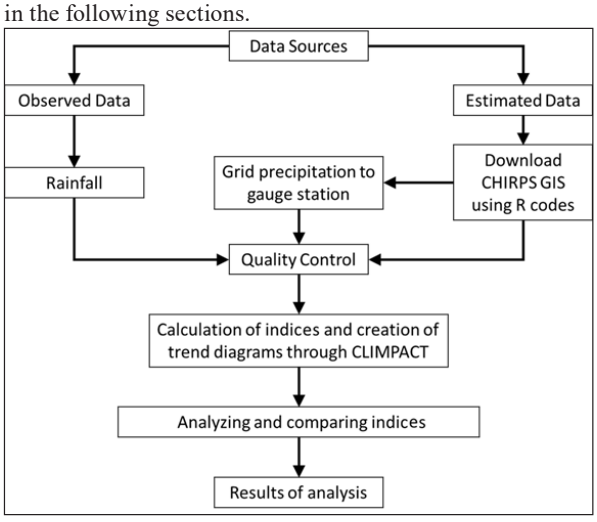

Figure 2. The study methodology flowchart

2.3 Data sources and quality control procedures

Observed daily precipitation data for 18 stations with different lengths of historical record were obtained from the Ministry of Water and Irrigation (MWI) (Table 1).

Table 1. Metadata for the selected meteorological stations used in Part One of the analysis. Stations annotated with an asterisk (*) were also used in Part Two of the analysis for the period 1998–2023.

Station		Location			Base year (start-end)	time period (years)
Name	Symbol	Latitude	Longitude	Altitude		
Amman Airport	AL0019*	31.97489	35.9878	790	1985-2012	28
King Talal Dam	AL0053*	32.19398	35.8316	218	1985-2012	28
Um El-Jumal	AL0059*	32.30221	36.3441	620	1985-2012	28
Burma	AL0026*	32.22127	35.7830	600	1985-2012	28
Rumimin	AL0028*	32.10847	35.7982	675	1985-2012	28
Kitta	AL0005	32.27509	35.8417	665	1985-2012	28
Sweilih	AL0017	32.32588	36.0916	1000	1985-2012	28
Amman Hussein College	AL0022	31.95899	35.9316	834	1985-2012	28
Subeihi	AL0027	32.14946	35.7031	500	1985-2012	28
Sihan	AL0047	32.13842	35.7570	495	1985-2012	28
Midwar	AL0002	32.28774	35.9957	760	1985-2012	28
Jarash	AL0004	32.27932	35.8948	585	1985-2012	28
Sukhna	AL0012	32.1294	36.0654	500	1985-2012	28
Zarqa	AL0015	32.06440	36.0891	610	1985-2012	28
Russifa	AL0016	32.34484	36.2087	655	1985-2012	28
Hashimiya	AL0054	32.13546	36.1131	550	1985-2012	28
Khirebit EsSamra	AL0066	32.12920	36.1925	540	1986-2012	27
Prince Feisal Nursery	AL0036	32.21620	35.8943	600	1985-2012	28

** only CHIRPS*

The study used version 2 of the open-source worldwide database CHIRPS 2.0, developed by the Climate Hazards Group at the University of California to provide precipitation data from 50° South to 50° North. CHIRPS data uses satellite- estimated precipitation blended with station data. Furthermore, the accuracy of the rainfall estimates is enhanced by using climatological models are used for bias correction. Overall, CHIRPS rainfall time series are produced at a high spatial resolution of the 0.05o (Funk et al., 2015). The data was downloaded using the library (CHIRPS) in RStudio. The longitude and latitude coordinates were entered in the R script for each station, then the daily CHIRPS data corresponding to the historical record of the selected stations (Table 1) was extracted from a spatial resolution of 0.05° using the point-to-pixel approach, which compares the observed rainfall to the grid-cell estimates that correspond to the coordinates of the selected stations. This is a widely used approach that eliminates the errors and uncertainties introduced by the interpolation process (Baez Villanueva et al., 2018; Wu et al., 2019). All selected stations are more than 5.5 meters apart, except for stations AL0047 and AL0028, so the same data extracted for both stations and thus CLIMPACT gave the same trend.

2.4 Trend and correlation analysis

CLIMPACT software, accessed online at CLIMPACT-sci.org, was used to analyse daily rainfall, maximum, and minimum temperature data, generating 71 climate indices relevant to the water and agriculture sectors. This study focused specifically on extreme precipitation indices (Table 2), which are critical for addressing climate risk, water scarcity, and food security (Alexander and Herold, 2013).

Table 2. Extreme precipitation indices

Indicator name and unit (Index)	Definition
Consecutive dry days (CDD)	Number of maximum consecutive days with rainfall record (RR) < 1 mm
Consecutive wet days (CWD)	Number of maximum consecutive days with RR > 1mm
Simple daily intensity index (SDII) millimeters per day (mm/day)	Annual Total RR divided by the number of wet days (when RR ≥ 1mm
Number of heavy precipitation days (R10mm)	Number of days when RR ≥ 10 mm
Number of very heavy precipitation days (R20mm)	Number of days when RR ≥ 20 mm
Very wet days (R95p) (mm)	Annual sum daily of RR > 95th %
Extremely wet days (R99p) (mm)	Annual sum daily of RR > 99th percentile
Contribution from very wet days (R95PTOT) (%)	Fraction of total wet-day rainfall that comes from very wet days
Contribution from extremely wet days (R99PTOT) (%)	Fraction of total wet-day rainfall that comes from extremely wet days
Max 1day precipitation amount (RX1day) (mm)	Maximum of total RR in 1 day
Max 5day precipitation amount (RX5day) (mm)	Maximum of total RR in 5 day
Annual total wet-day precipitation (PRCPTOT) (mm)	Annual total RR in wet days (when RR ≥ 1 mm)

The p-value criterion was applied to assess trend significance. A p-value less than 0.05 was considered statistically significant, while values above 0.05 were deemed non-significant (Mentaschi et al., 2013). For both observed station data and CHIRPS datasets, analyses were conducted at monthly and annual scales. In this study, the Pearson Correlation Coefficient (PCC) was used to assess the agreement between CHIRPS and station data, as it is a widely accepted and commonly applied metric in similar precipitation validation studies to evaluate the strength and direction of linear relationships. PCC values range from -1 to 1, where 1 indicates a perfect positive correlation, and -1 indicates a perfect negative correlation. The PCC was used to assess the reliability of CHIRPS in estimating monthly and yearly rainfall amounts and precipitation indices. The PCC is illustrated in Eq. 1 (Mentaschi et al., 2013):

$$PCC = \frac{\sum(P_{MWI} - \bar{P}_{MWI})(P_{CHIRPS} - \bar{P}_{CHIRPS})}{\sqrt{\sum(P_{MWI} - \bar{P}_{MWI})^2 \sum(P_{CHIRPS} - \bar{P}_{CHIRPS})^2}} \quad \text{..... (1)}$$

Where, P_{MWI} is the value of the precipitation according to the MWI, $\bar{P}_{MWI}$ is the mean of the values of the precipitation according to the MWI, P_{CHIRPS} is the value of the precipitation according to the CHIRPS and $\bar{P}_{CHIRPS}$ is the mean precipitation value according to CHIRPS.

The study was divided into three parts. The first part examined trends and compared station data with CHIRPS data for the period 1985–2012. The second part conducted the same comparison for a different period (1998–2023), focusing only on five stations identified in Table 1. The third part analyzed trends in CHIRPS data for the period 1992–2023.

3. Results and Discussion

3.1 Monthly and yearly precipitation assessment

The PCC for the annual precipitation between the station and CHIRPS datasets (Fig. 3) showed weak to moderate positive correlations (mean PCC = 0.70), although the PCC values were moderate to strong, with values greater than 0.5 (maximum PCC of 0.81), which were mainly observed in the eastern part of the basin. However, the PCC values for annual rainfall do not indicate a strong resemblance between the station and CHIRPS datasets, as evidenced by the low PCC values for all indices. Paredes-Trejo et al. (2017) and Du et al. (2024) noted that the sparse network of rainfall stations may contribute to weak correlation between CHIRPS and station data due to the lack of ground observations and CHIRPS's heavy reliance on satellite data. A study in Wadi Wala, Jordan found moderate correlation between annual station and CHIRPS data but performed poorly with extreme indices, indicating the need for further bias correction and validation of CHIRPS data in regions with limited station data (Al Shamayleh et al., 2024).

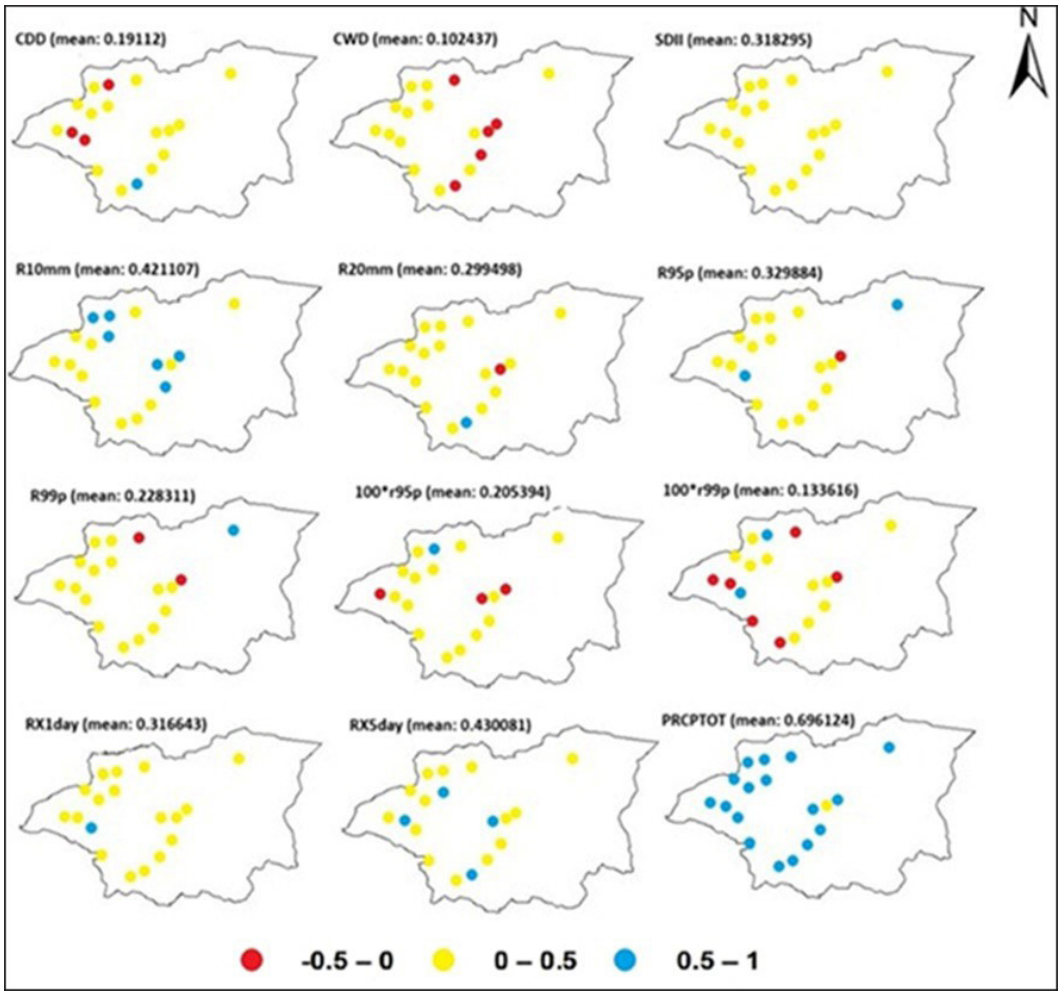

Figure 3. Spatial distribution of Pearson's linear yearly correlation coefficient of extreme precipitation indices, as measured by CHIRPS and station observations (1985-2012)

The PCC values for monthly rainfall between the stations and CHIRPS datasets (Fig. 4) indicated weak to moderate correlations with a mean value of 0.65 and a maximum value of 0.94 observed at station AL0005 for the November, In fact, November and December had the highest correlation coefficients, 0.83 and 0.78, respectively, compared to May and October, which had 0.29 and 0.53, respectively. In general, the highest PCC values were observed from November to April.

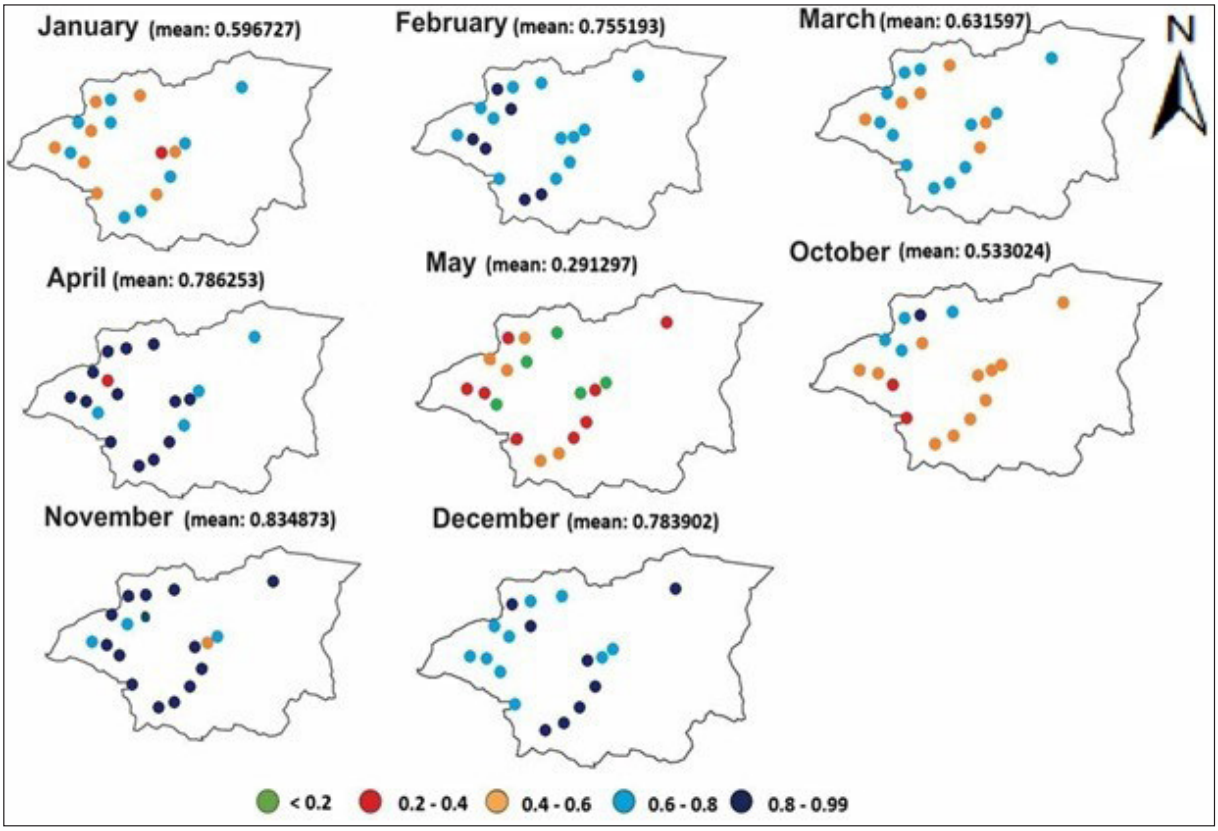

Figure 4. Spatial distribution of Pearson's linear correlation coefficient for monthly precipitation between CHIRPS and station observations (1985-2012)

These results are partially consistent with those of Al Shamayleh et al. (2024), who found that May had the lowest average correlation coefficient (0.24) among all months in the Wala Basin, Jordan. Also, they are consistent with the findings of Saeidizand et al., who showed that the CHIRPS data are reasonably correlated with the observed data during the spring months. The AL0026 station, located in the northeast of ZRB, had the highest average monthly correlation of 0.74, while AL0066 had the lowest average PCC. The AL0066, station demonstrated negative PCC values for May. It has been reported that CHIRPS performance depends on climate conditions and geographic location (Alejo et al., 2024, Du et al., 2024). In fact, during the winter months, CHIRPS may provide better rainfall estimates due to the prevalence of dense clouds, which allow sufficient time for the sensors to detect them, whereas detection opportunity is smaller due to the rapid disappearance of clouds (Mianabadi et al., 2022). The AL0004, AL0005, AL0019, AL0022 and AL0026 stations, which are about 100 meters (m) higher than other stations, demonstrated reasonable agreement between the stations and the CHIRPS dataset, where the average PCC values ranged from 0.71 to 0.73, in contrast to the other stations, where the PCC values were below 0.70. Several research studies found that CHIRPS performed slightly better in high-altitude stations. Gebrechorkos et al. (2018) reported similar findings. Research in Saudi Arabia found that CHIRPS data performed better at altitudes between 500 and 750 m than at altitudes of 0 to 500 m (Helmi and Abdelhamed, 2022). The reason CHIRPS underperforms in low-altitude regions may be due to localized convective rainfall, combined with a sparse network of rainfall stations that does not provide enough information for CHIRPS to capture rainfall patterns (Funk et al., 2015). The lack of correlation between CHIRPS and station data sets was also observed in several other studies. Previous research has suggested that CHIRPS dataset is not suitable as a source of precipitation data in the dry and semi-arid regions (Paredes Trejo et al., 2017). Cavalcante et al. (2020) indicated that that CHIRPS data underestimated rainiest events. However, the CHIRPS data may be suitable for detecting main drought events (Das et al., 2022).

3.2 Observed and CHIRPS trends in rainfall indices

All 12 selected indices, except for CDD, determined station data (Fig. 5) and CHIRPS data (Fig. 6), showed a clear distinction between the western and eastern parts of the basin due to the higher precipitation in the western part, where the recorded mean annual rainfall values were greater than 260 mm. In contrast, below-average annual rainfall was observed in the station located in the eastern part.

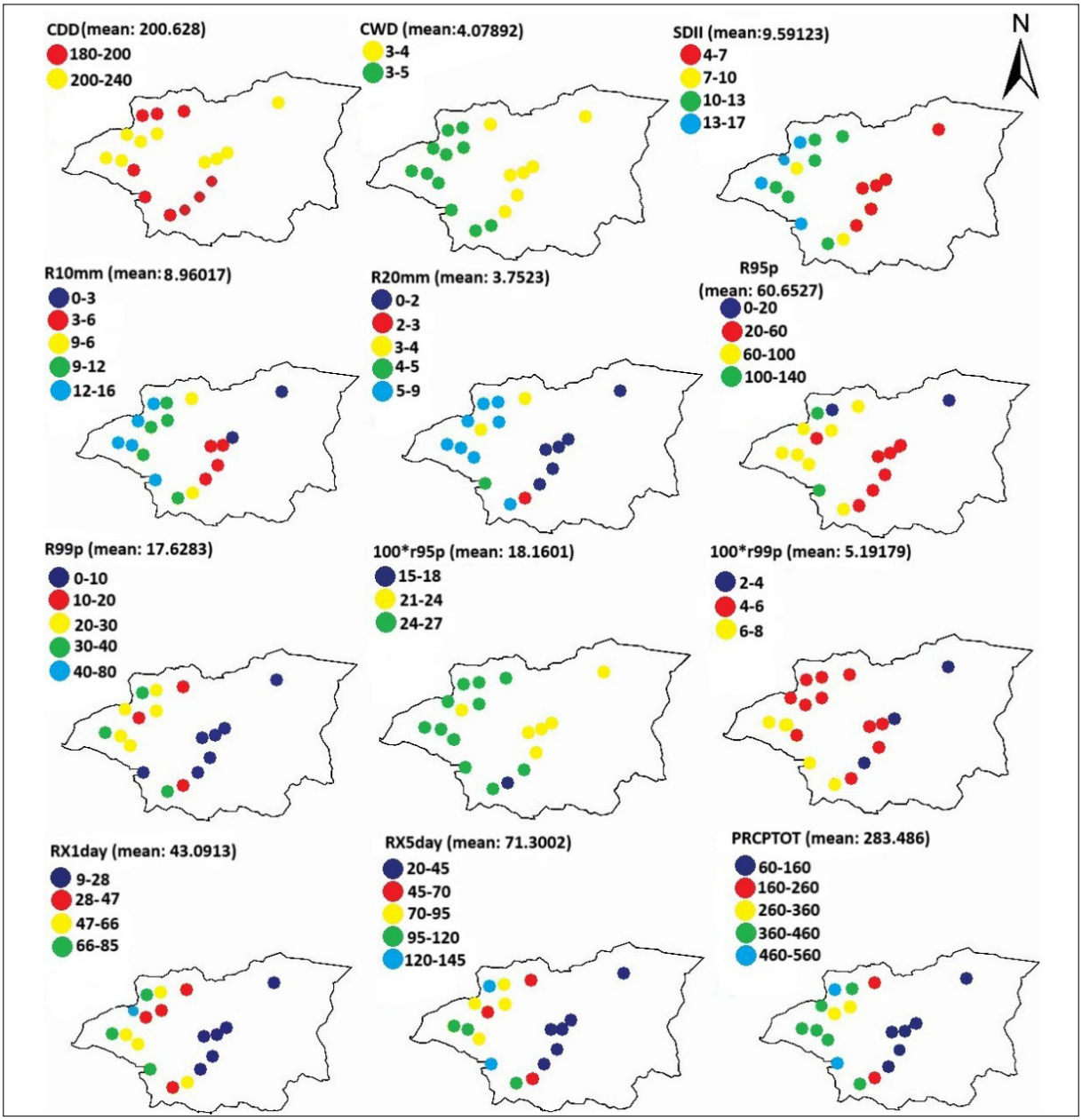

Figure 5. Extreme precipitation indices, measured by stations (1985-2012)

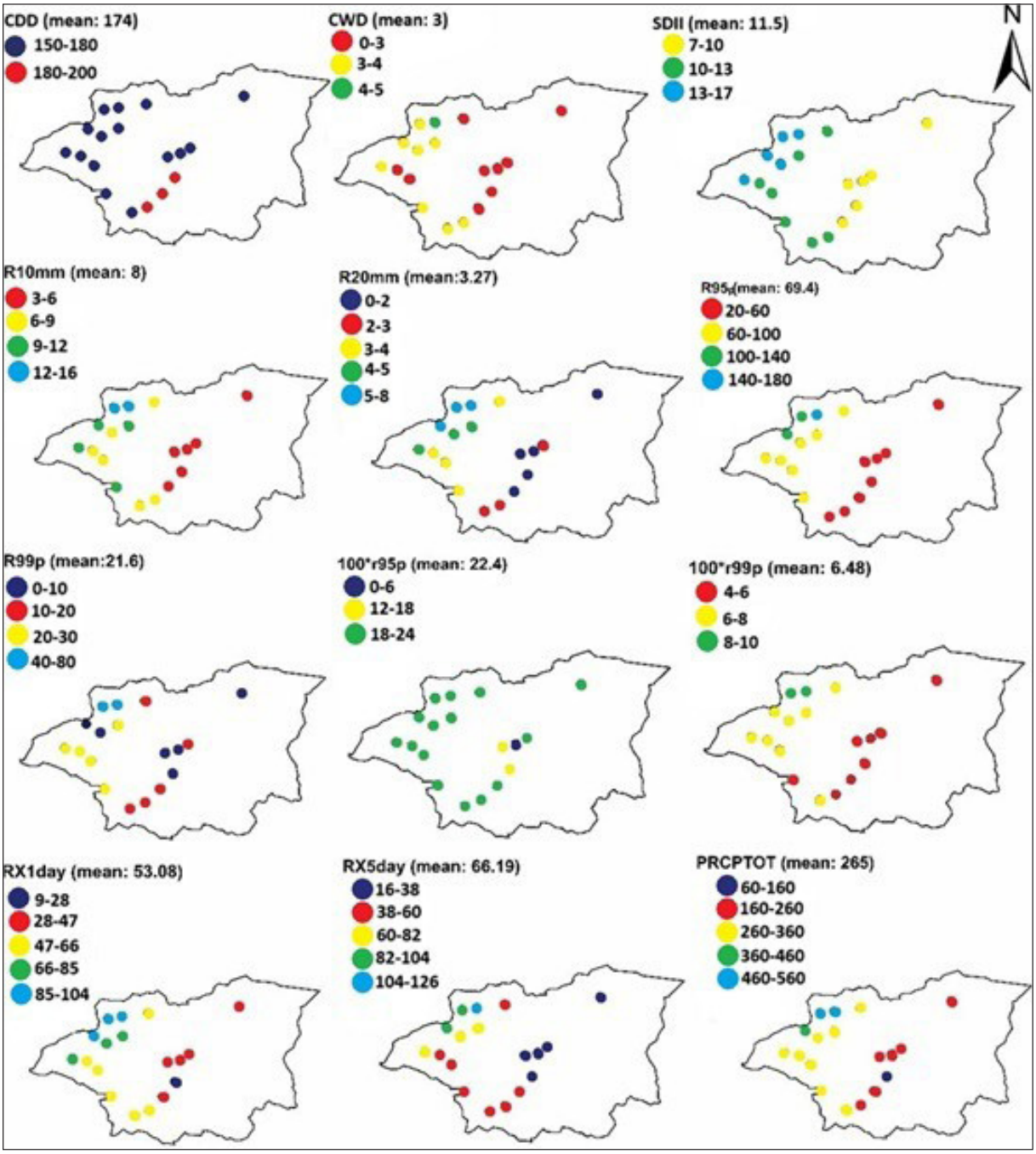

Figure 6. Extreme precipitation indices, measured by CHIRPS (1985-2012)

The results of the trend analysis obtained for observed rainfall data from 18 meteorological stations in the ZRB from 1985-2012 (Fig. 7) can be classified into three groups. The first group includes the results from stations AL0066, and AL0002, which display statistically significant (p-values < 0.05) increasing or decreasing trends across more than one index. The second group contains the results from four stations (AL0015, AL0019, AL0028, and AL0047), which show a statistically significant trend in only one indicator, which may differ across stations. As for the third group, it contains the remaining the stations that did not show any statistically significant trend, although some stations showed a high-value trend, whether upward or downward. The CWD, SDII, R20mm, R95p, RX1day, RX5day, and PRCPTOT indicators showed significant trends at AL0002. These indicators, except for CWD, trended upward, as indicated by positive slope values ranging from 0.111 for R20mm to 4.713 for PRCPTOT. Also, CWD, SDII, and R10mm trended upward, as indicated by slope values between 0.067 and 0.125 at AL0066. CWD also showed a weak downward trend at AL0019, AL0028, AL0047, and AL0015, indicated by slope values ranging from –0.044 to –0.062.

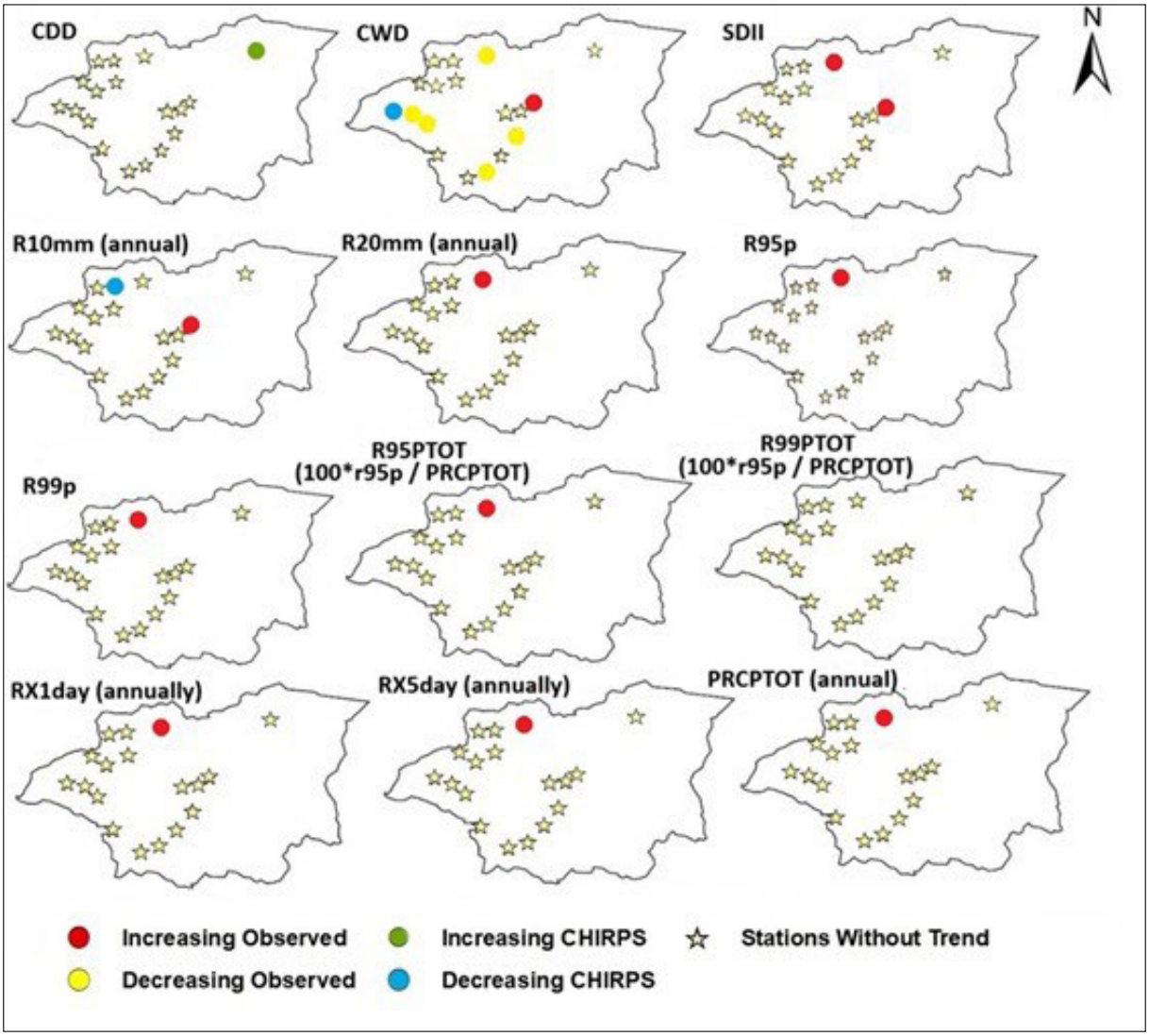

Figure 7. The significant trends for each of the precipitation indices (1985-2012)

Overall, there were 15 significant trends, or about 6 % of the total number of possible trends, which is about the same or less than the percentages obtained in similar studies (Cavalcante et al., 2020; Mubialiwo et al., 2023). Although such sporadic trends should be interpreted with caution, they can nevertheless reveal critical insights relevant to water resources management. For example, Mubialiwo et al. (2023) reported that rainfall is less frequent over the Mpologoma catchment in Uganda, East Africa, but with higher intensity. In this study, one significant and strong PRCPTOT trend (Station AL0002) points to the onset of climate change, characterized by increasing annual rainfall in the northwest part of the ZRB. This PRCPTOT trend is linked to other indices, such as increasing SDII and decreasing CWD. Increasing SDII and decreasing CWD values were also detected in the Wala basin in Jordan (Al-Shamayleh et al., 2024). The CHIRPS data sets for the same period 1985-2012 replicated the same distinction between the eastern and western parts of the watershed. However, it did not generate the same trend as the station data (Fig. 8). It produced only 3 significant trends produced by CHIRPS, or 1.2% of the total number of significant trends produced from the station data. Furthermore, none of the trends were similar to the two datasets. In fact, CHIRPS data showed a significant downward trend at AL0026 and AL0004 for the CWD and R10mm indices, recording values of -0.05 and -0.132, respectively (Tables 3 and 4), in addition to the upward trend shown in the CDD indicator, which showed a value of 1 at AL0059 station. (Tables 5 and 6). These discrepancies in trend analysis between CHIRPS and station data reaffirm the underlying shortcomings of CHIRPS data in arid regions, specifically the lack of sufficient ground rainfall data. This leads to heavy reliance on satellite data, which in turn suffers from inaccuracies due to the small window of opportunity for cloud detection (Mianabadi et al., 2022; Funk et al., 2015).

Table 3. Annual trend of extreme CHIRPS precipitation indices (AL0002, AL0004, AL0005, AL0047, AL0012, AL0015, AL0016, AL0017 and AL0019) (*: Significant at P < 0.05; NT: No trend)

Index	AL0002	AL0004	AL0005	AL0047	AL0012	AL0015	AL0016	AL0017	AL0019
CDD	−0.189	0.028	−0.025	−0.143	0.5	0.552	0.294	−0.174	1
CWD	NT	NT	NT	NT	NT	NT	NT	NT	NT
SDII	−0.046	0.063	0.103	0.06	−0.025	−0.014	0.021	−0.025	−0.048
R10mm	NT	−0.132*	−0.1	NT	NT	NT	−0.071	NT	−0.071
R20mm	NT	NT	NT	NT	NT	NT	NT	−0.05	NT
R95p	NT	NT	NT	0.571	NT	NT	NT	NT	NT
R99p	NT	NT	NT	NT	NT	NT	NT	NT	NT
R95PTOT	NT	0.109	NT	0.417	NT	NT	NT	0.007	NT
R99PTOT	NT	NT	NT	NT	NT	NT	NT	NT	NT
RX1day	−0.256	0.279	0.26	0.237	−0.089	0.008	0.292	−0.111	−0.155
RX5day	−0.641	−0.735	−0.383	−0.002	−0.309	−0.055	−0.022	−0.323	−0.344
PRCPTOT	−1.095	−1.584	−1.419	−0.753	−0.674	−0.671	−0.533	−1.274	−1.535

Table 4. Annual trend of extreme CHIRPS precipitation indices (AL0026, AL0022, AL0027, AL0028, AL0036, AL0053, AL0054, AL0059 and AL0066) (*: Significant at P < 0.05; NT: No trend)

Index	AL0022	AL0026	AL0027	AL0028	AL0036	AL0066	AL0054	AL0059	AL0053
CDD	0.775	0.5	0.092	−0.143	0.257	0.812	0.303	1*	0.155
CWD	NT	−0.05*	NT	NT	NT	NT	NT	NT	NT
SDII	−0.044	0.161	0.089	0.06	0.001	−0.06	−0.047	−0.029	0.07
R10mm	−0.077	−0.118	−0.087	NT	NT	NT	NT	NT	NT
R20mm	NT	0.02	NT	NT	NT	NT	NT	NT	NT
R95p	−0.076	3.441	0.311	0.571	NT	−0.552	NT	−0.143	NT
R99p	NT	NT	NT	NT	NT	NT	NT	NT	NT
R95PTOT	NT	0.893	0.532	0.417	0.02	−0.497	NT	NT	NT
R99PTOT	NT	NT	NT	NT	NT	NT	NT	NT	NT
RX1day	−0.128	0.185	0.272	0.237	0.275	−0.404	−0.1	−0.193	0.141
RX5day	−0.153	−0.055	−0.195	−0.002	−0.454	−0.55	−0.187	0.127	−0.172
PRCPTOT	−1.795	−1.691	−1.043	−0.753	−1.344	−0.857	−0.137	−0.402	−0.945

Table 5. Annual trend of extreme station precipitation indices (AL0002, AL0004, AL0005, AL0047, AL0012, AL0015, AL0016, AL0017 and AL0019) (*: Significant at P < 0.05; NT: No trend)

Index	AL0002	AL0004	AL0005	AL0047	AL0012	AL0015	AL0016	AL0017	AL0019
CDD	0.513	0.475	0.45	0.106	0.655	0.523	0.4	0.388	0.674
CWD	−0.071*	NT	NT	−0.062*	−0.044	−0.054*	NT	NT	−0.045*
SDII	0.288*	0.064	0.009	0.153	0.053	−0.008	0.024	0.072	−0.014
R10mm	0.156	NT	NT	−0.044	NT	NT	NT	−0.186	NT
R20mm	0.111*	0.048	−0.054	NT	NT	NT	NT	−0.093	NT
R95p	3.072*	0.535	0.542	1.462	NT	NT	NT	NT	NT
R99p	NT	NT	NT	NT	NT	NT	NT	NT	NT
R95PTOT	1.056*	0.28	0.333	0.522	NT	NT	NT	0.033	NT
R99PTOT	NT	NT	NT	NT	NT	NT	NT	NT	NT
RX1day	1.667*	0.46	0.394	0.757	0.161	0.008	0.17	0.343	0.032
RX5day	1.448*	0.533	0.278	0.414	0.342	−0.16	−0.021	−0.634	0.224
PRCPTOT	4.713*	1.321	−1.07	−1.163	−0.033	−1.032	−0.736	−3.398	−0.816

Table 6. Annual trend of extreme station precipitation indices (AL0026, AL0022, AL0027, AL0028, AL0036, AL0053, AL0054, AL0059 and AL0066) (*: Significant at P < 0.05; NT: No trend)

Index	AL0026	AL0022	AL0027	AL0028	AL0036	AL0053	AL0054	AL0059	AL0066
CDD	−0.321	0.293	0.05	0.793	0.265	0.864	1.183	−0.23	1
CWD	NT	−0.044	−0.053	−0.044*	NT	NT	NT	NT	0.091*
SDII	−0.021	0.053	0.147	0.127	−0.064	0.026	0.027	−0.031	0.067*
R10mm	0.129	NT	0.1	−0.061	−0.111	−0.091	NT	NT	0.125*
R20mm	NT	NT	0.062	NT	−0.063	NT	NT	NT	NT
R95p	0.049	0.333	2.243	0.149	NT	−0.5	NT	NT	0.25
R99p	NT	NT	NT	NT	NT	NT	NT	NT	NT
R95PTOT	0.336	0.244	0.194	0.151	NT	0.168	NT	NT	0.017
R99PTOT	NT	NT	NT	NT	NT	NT	NT	NT	NT
RX1day	0.149	0.667	1.096	0.491	−0.269	−0.211	0.107	−0.221	0.25
RX5day	0.731	0.252	1.156	0.635	−0.812	0.043	0.183	−0.085	0.669
PRCPTOT	1.637	−0.478	3.919	−0.981	−3.981	−2.415	−1.01	−0.833	1.533

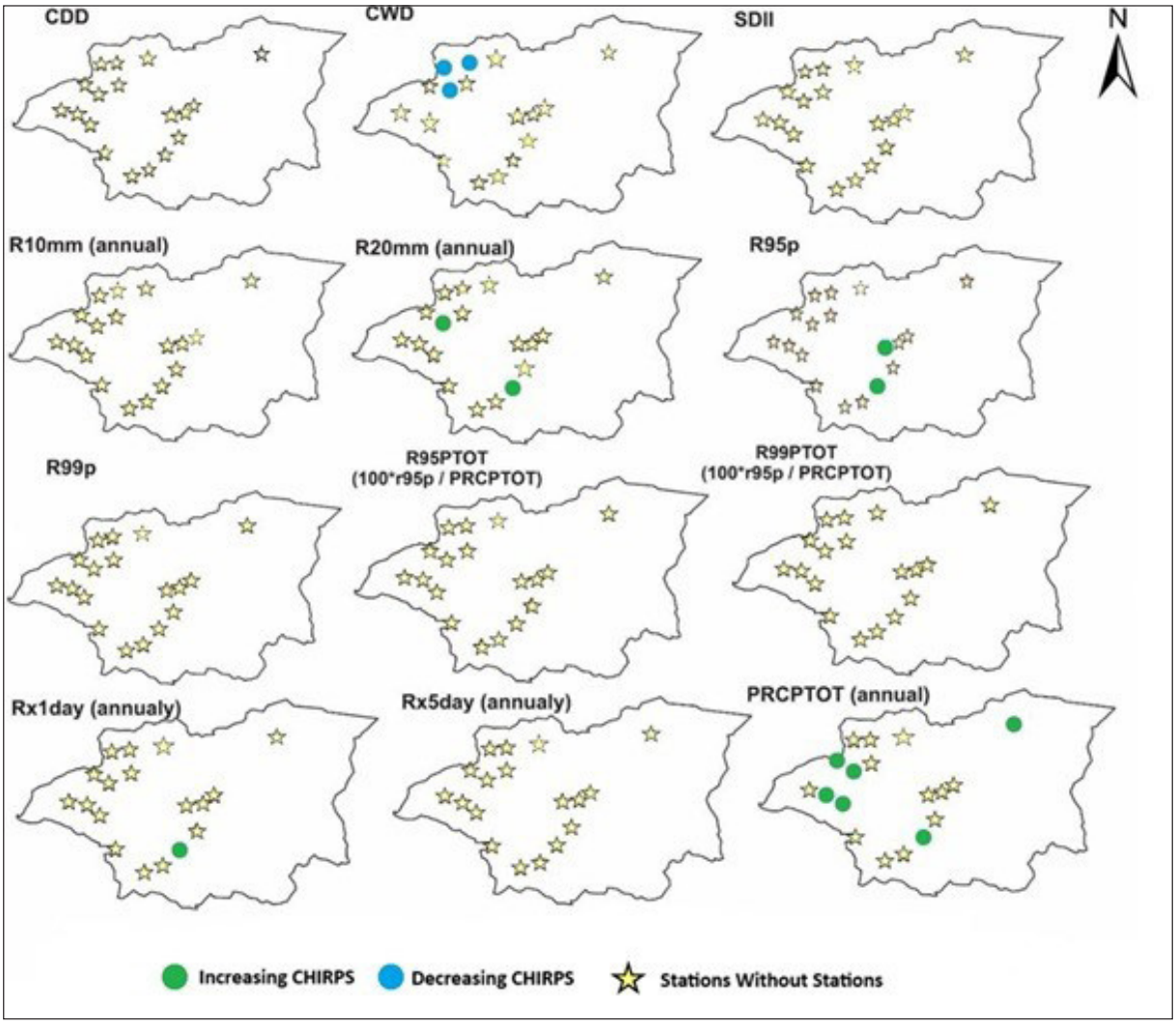

Figure 8. The significant trends for each of the precipitation indices (1992-2023 CHIRPS)

Furthermore, the results of the trend analysis obtained for CHIRPS rainfall data from 1992 to 2023 (Fig 8) from 18 stations showed a strong upward trend for PRCPTOT indicators at stations AL0059, AL0053, AL0026, AL0028, AL0047 and AL0016 as indicated by slope values of 1.707, 2.909, 5.366, 2.691, 2.691, 2691 and 1.709, respectively. Significant trends for R95p were found at AL0012 and AL0016 with slope values of 1.136 and 1.244, respectively. The remaining trends are weak downward for CWD, as indicated by slope values ranging from -0.041 to -0.034 at AL0053, AL004, and AL005, respectively. Also, a weak upward trend for R20, with slope values of 0.091 and 0.04 at AL0053 and AL0016, respectively.

In addition, rainfall trends were analyzed at five stations with available records spanning 1998 to 2023 (Fig 9).

Significant trends detected for R20mm: weak upward slope of 0.067 at AL0019 and strong downward slope of -35.809 for PRCPTOT at AL0059. On the other hand, the results for the same five stations were analyzed using CHIRPS data, and differences were revealed. Contrary to the trend in the observed rainfall data, an upward trend in PRCPTOT was observed at station AL0059 with a slope value of 1.92. Also, upward trends appeared in the same indicator PRCPTOT at stations AL0026 and AL0028, with values of 7.947 and 2.993 respectively. Also AL0053 showed a slight upward trend in the R20mm indicator with a value of 0.1.

Three stations showed a downward trend in the CDD indicator with values between 1 and 1.5 for AL0019, AL0028 and AL0059. Thus, the total number of trends in the results of CHIRPS data is 7 significant trends while the total number of trends in the observed data results is only 2 significant trends.

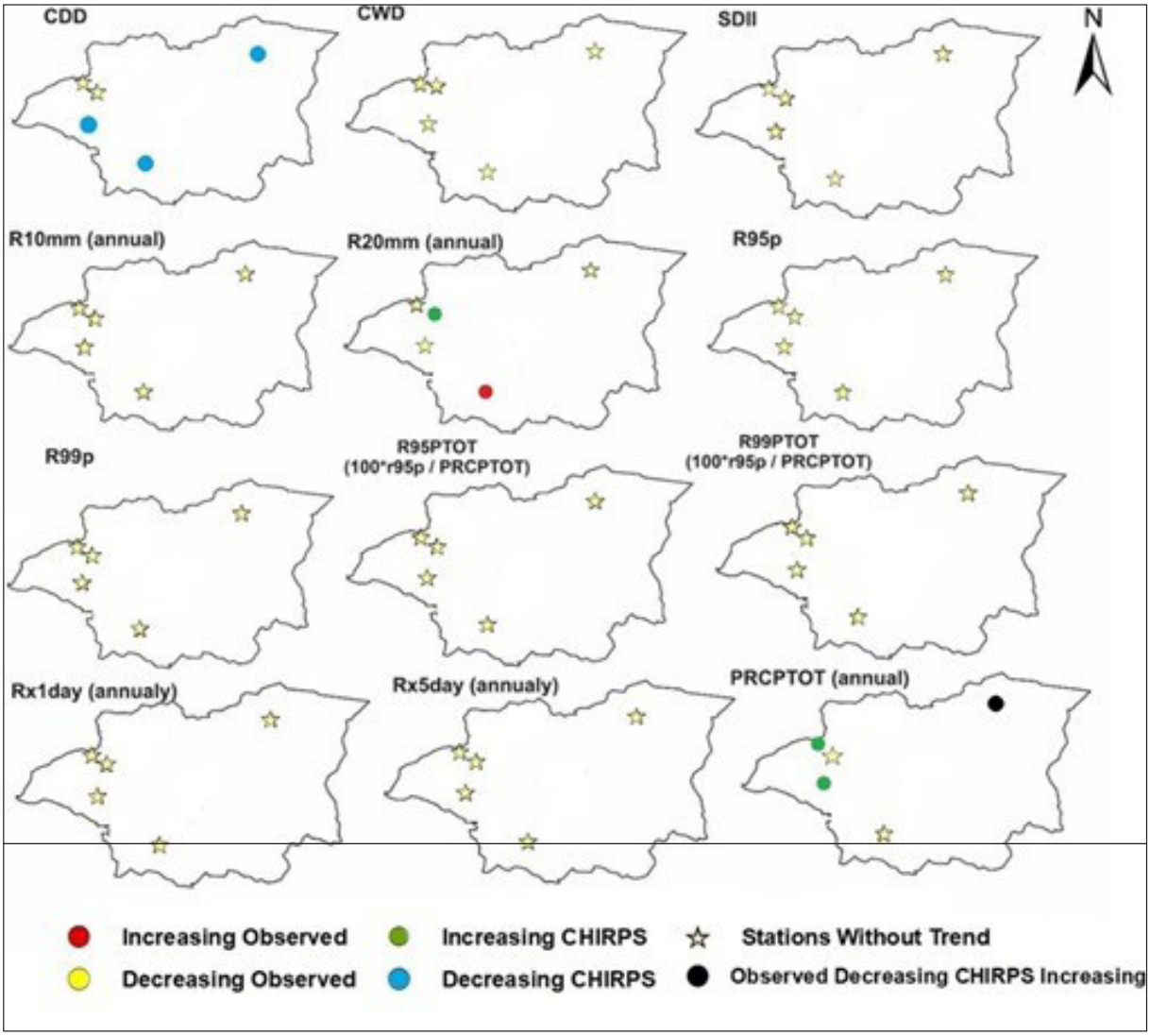

Figure 9. The significant trends for each of the precipitation indices (1998-2023 for both observed and CHIRPS data groups)

3.3 Implications for water resources management

The weak monthly and annual correlations between station and CHIRPS, and discrepancies in trend identification between the two datasets, pose serious challenges for using CHIRPS data in hydrological and water resources assessments, such as runoff modelling and frequency analysis. This is particularly true in low-altitude areas during autumn or late spring months, as observed in annual and monthly precipitation (Du et al., 2024). However, CHIRPS's better performance in high-altitude areas and during winter months offers potential for assessing rainfall patterns and making informed decisions on land and water resource sustainability and seasonal water allocation (Al-Shamayleh et al., 2024). Nonetheless, CHIRPS should always be used with caution due to divergent trends in extreme rainfall indices between the stations and the CHIRPS data. For example, the mismatch in rainfall trends between CHIRPS and station data underscores the need to strengthen the existing network of rainfall stations, especially in lower-altitude areas of the ZRB, to better monitor rainfall patterns and enhance the bias correction and validation of CHIRPS data.

Mismatches between CHIRPS and station trends, combined with delayed or missed flood warnings and spatial bias in low-altitude zones, reduce the accuracy of extreme rainfall detection. These discrepancies lead to errors in rainfall peak timing, resulting in underestimation or overestimation of flood forecasts and distorted

hydrographs, thereby compromising timely warnings and emergency preparedness. Similarly, inaccuracies in trend detection hinder the correct identification of drought onset and recovery. The weak performance of CHIRPS during transitional seasons (spring and autumn) obscures intermediate drought phases, yielding ineffective mitigation policies and poor water allocation strategies. Moreover, these discrepancies complicate calibration and validation of runoff simulation models. Input uncertainty and divergence in extreme rainfall indices can skew runoff volumes and timing, since such models are susceptible to precipitation accuracy.

4. Conclusion

This study, conducted in three parts, assessed precipitation trends over 27, 25, and 31 years in Jordan's Zarqa River Basin (ZRB) using ground station and CHIRPS data. The analysis examined variability, CHIRPS reliability, and implications for water resource management and climate adaptation. Results show that CHIRPS performs relatively well in high-elevation areas and during the wet season (November–April), but underperforms in arid, low-elevation zones and dry months. Correlation analysis indicated weak to moderate agreement with ground data at monthly and annual scales, with mean PCCs of 0.65 and 0.69, respectively.

Trend analysis revealed distinct differences between datasets: station data (1985–2012) showed 15 significant trends, mostly upward in the northwest and downward in the east, while CHIRPS detected only three, including mismatches and additional signals. In the 1998–2023 period, station data showed one strong downward and one upward trend, while CHIRPS alone identified three downward and 11 upward trends. These findings highlight both the potential and the limitations of CHIRPS for long-term climate trend detection in complex terrains. In arid regions, limited opportunities to detect clouds, reinforcing the need for calibration and validation.

For practical application, CHIRPS should be used only after bias correction and integration with validated ground-station data. Policymakers and practitioners should expand and modernize rainfall monitoring networks, particularly in low-altitude zones, to improve calibration and strengthen climate datasets. A hybrid data approach will enhance hydrological modelling, support resilient infrastructure design, and strengthen climate adaptation planning. Accurate precipitation data are especially critical for dam development and operation, which play a central role in water security, groundwater recharge management, and sustainable harvesting projects. Strengthening monitoring systems and adopting integrated datasets will ensure more reliable water resource planning and climate-resilient strategies across the ZRB.

Author Contributions

N.H. Alnizami played a central role in the study, contributing to the conceptualization and methodology design. M. Rahbeh oversaw project administration, provided supervision, and prepared the original draft. M.M. Zoubi was instrumental in the investigation, performing the formal analysis and drafting the manuscript. Q.Y. Abu-Afifeh contributed by managing data curation. T.A. Qutishat was responsible for the visualization aspects. M.R. AlHalaigah contributed by providing resources. H. Al-Jawaldeh was responsible for the software aspects. B. Al Qarallah handled manuscript editing.

Conflict Of Interest

The authors declare that there is no conflict of interest regarding the publication of this manuscript.

References

Abu-Afifeh, Q., Rahbeh, M., Al-Afeshat, A., Al-Omari, S., Qutishat, T. A., Brezat, A., and Alkayed, A. (2023). Dam sustainability's interdependency with climate change and dam failure drivers. Sustainability. 15(23): 1-19

Ajjur, S. B., and Riffi, M. I. (2020). Analysis of the observed trends in daily extreme precipitation indices in Gaza Strip during 1974–2016. International Journal of Climatology, 40(14): 6189-6200

Al Shamayleh, S., Leong Tan, M., Samat, N., Rahbeh, M., and Zhang, F. (2024). Performance of CHIRPS for estimating precipitation extremes in the Wala Basin, Jordan. Journal of Water and Climate Change. 15(3): 1349–1363

Al-Addous, M., Bdour, M., Alnaief, M., Rabaiah, S., and Schweimanns, N. (2023). Water resources in Jordan: a review of current challenges and future opportunities. Water. 15(21): 1-34

Al-Afeshat, A., Zoubi, M. M., Abu Afifeh, Q. Y., Al-Jawaldeh, H., Qutishat, T. A., Masoud, A. M. N., and Rahbeh, M. (2025). Interrelation of dams sustainability with the local communities and water quality. Global Journal of Environmental Science and Management, 11(1): 157-176

Alejo, L.A., and Alejandro, A.S. (2021). Validating CHIRPS ability to estimate rainfall amount and detect rainfall occurrences in the Philippines. Theoretical and Applied Climatology, 145(3-4): 967–977

Alexander, L., and Herold, N. (2016). World climate programme world climate services programme ClimPACT2 indices and software a document prepared on behalf of the commission for climatology (CCl) expert team on sector-specific climate indices (ET-SCI).

Al-Houri, Z.M. (2014). Detecting variability and trends in daily rainfall characteristics in Amman-Zarqa Basin, Jordan. International Journal of Applied Science and Technology, 4(6): 11-25

Al-Qinna, M.I., Hammouri, N.A., Obeidat, M.M., and Ahmad, F.Y. (2010). Drought analysis in Jordan under current and future climates. Climate Change. 106(3): 421–440

Alsalal, S., Tan, M. L., Samat, N., Al-mehr, J. T., and Zhang, F. (2024). Temperature and precipitation changes under CMIP6 projections in the Mujib Basin, Jordan. Theoretical and Applied Climatology, 155(8): 7703–7720

Alsilibe, F., Bene, K., Bilal, G., Alghafli, K., and Shi, X. (2023). Accuracy assessment and validation of multi-source CHIRPS precipitation estimates for water resource management in the Barada Basin, Syria. Remote sensing, 15(7): 1778

Baez-Villanueva, O. M., Zambrano-Bigiarini, M., Beck, H. E., McNamara, I., Ribbe, L., Nauditt, A., Birkel, C., Verbist, K., Giraldo-Osorio, J. D., and Xuan Thinh, N. (2020). RF-MEP: A novel random forest method for merging gridded precipitation products and ground-based measurements. Remote Sensing of Environment, 239: 111606

Beyene, T. D., Zimale, F. A., Tekleab, S., and Nedaw, D. (2023). Evaluation of a multi-staged bias correction approach on CHIRP and CHIRPS rainfall product: A Case Study of the Lake Hawassa Watershed. Journal Water Climate Change, 14(6): 1847–1867

Chen, Y., Zhang, X., Fang, G., Li, Z., Wang, F., Qin, J., and Sun, F. (2020). Potential risks and challenges of climate change in the arid region of Northwestern China. Regional Sustainability. 1 (1): 20–30

Das, P., Zhang, Z., Ren, H., (2022). Evaluating the accuracy of two satellite-based quantitative precipitation estimation products and their application for meteorological drought monitoring over the Lake Victoria Basin, East Africa. Geo-spatial Information Science, 25(3): 500–518

Dede, M., Sunardi, S., Lam, K.C., and Withaningsih, S. (2023). Relationship between landscape and river ecosystem services. Global Journal of Environmental Science and Management, 9(3): 637-652

Du, H., Tan, M.L., Zhang, F., Chun, K.P., Li,L., and Kabir, M.H. (2024). Evaluating the effectiveness of CHIRPS data for hydroclimatic studies. Theoretical and Applied Climatology, 155: 1519–1539

El-Mahroug, S. E., Suleiman, A. A., Zoubi, M. M., Al-Omari, S., Abu-Afifeh, Q. Y., Al-Jawaldeh, H. F., Alta'any, Y. A., Al-Nawaiseh, T., Obeidat, N., Alsoud, S. H., Alshoshan, A. M., Al-Shibli, F. M., and Ta'any, R. (2025). Predictive Modeling of Climate-Driven Crop Yield Variability Using DSSAT Towards Sustainable Agriculture. AgriEngineering, 7(5), 156–156

Funk, C., Peterson, P., Landsfeld, M., Pedreros, D., Verdin, J., Shukla, S., Husak, G., Rowland, J., Harrison, L., Hoell, A., and Michaelsen, J. (2015). The climate hazards infrared precipitation with stations—a new environmental record for monitoring extremes. Scientific Data. 2(1): 1-22

Gebrechorkos, S. H., Hülsmann, S., and Bernhofer, C. (2018). Evaluation of multiple climate data sources for managing environmental resources in East Africa. Hydrology and Earth System Sciences, 22(8): 4547–4564

Hamed, M. M., Kyaw, A. K., Nashwan, M. S., and Shahid, S. (2023). Spatiotemporal changes in universal thermal climate index in the Middle East and North Africa. Atmospheric Research, 295: 107008

Hasibuan, H.S., Elizandri, B.N., Asrofani, F.W., and Putra, G.A.Y. (2025). Potential application of rain water harvesting technology as an alternative clean water source to mitigate land subsidence. Global Journal of Environmental Science and Management, 11(1): 277-294

Helmi, A. M., Abdelhamed, M. S., (2022). Evaluation of CMORPH, PERSIANN-CDR, CHIRPS V2.0, TMPA 3B42 V7, and GPM IMERG v6 satellite precipitation datasets in arabian arid regions. Water. 15(1): 92

Hroub, H. A., Rahbeh, M., Zoubi, M. M., Abu-Afifeh, Q. Y., Al-Jawaldeh, H., and Obeidat, N. (2025). Projection of future temperature variations in river basins under climate change scenarios using general circulation models. Global Journal of Environmental Science and Management, 11(2): 1-24

Javier, F., Barbosa, A., Peñaloza-Murillo, M. A., Moreno, M. A., Farías, A., Javier, F., Barbosa, A., Peñaloza-Murillo, M. A., Moreno, M. A., and Farías, A. (2016). Intercomparison of improved satellite rainfall estimation with CHIRPS Gridded product and rain gauge data over Venezuela. Atmósfera. 29(4): 323–342

Justus Reymond, D., and Sudalaimuthu, K. (2023). Geospatial visualization and seasonal variation of heavy metals in river sediments. Global Journal of Environmental Science and Management, 9(2): 309-322

Katsanos, D., Retalis, A., and Michaelides, S. (2016). Validation of a high-resolution precipitation database (CHIRPS) over Cyprus for a 30-year period. Atmospheric Research, 169: 459–464

Kundzewicz, Z.W., Mata, L.J., Arnell, N.W., Doll, P., Kabat, P., Jimenez, B., Miller, K., Oki, T., Zekai, S., and Shiklomanov, I. (2007). Freshwater resources and their management. In: Parry, M.L., Canziani, O.F., Palutikof, J.P., van der Linden, P.J, and Hanson, C. E., (eds.) Climate Change 2007: impacts, adaptation and vulnerability. Cambridge University Press. 173-210

Lelieveld, J., Proestos, Y., Hadjinicolaou, P., Tanarhte, M., Tyrlis, E., and Zittis, G. (2016). Strongly Increasing Heat Extremes in the Middle East and North Africa (MENA) in the 21st Century. Climatic Change. 137(1-2): 245–260

Masih, I., Maskey, S., Mussá, F. E. F., and Trambauer, P. (2014). A Review of droughts on the African continent: a geospatial and long-term perspective. Hydrology and Earth System Sciences, 18 (9): 3635–3649

Mentaschi, L., Besio, G., Cassola, F., and Mazzino, A. (2013). Problems in RMSE-based wave model validations. Ocean Modelling, 72: 53-58

Mianabadi, A., Salari, K., and Pourmohamad, Y. (2022). Drought monitoring using the long-term CHIRPS precipitation over southeastern Iran. Applied Water Science, 12(8): 183

Mubialiwo, A., Abebe, A., and Onyutha, C. (2023). Changes in extreme precipitation over Mpologoma catchment in Uganda, East Africa. Heliyon. 9(3): e14016

Obeidat, N., Abu Awwad, A., Al-Salaymeh, A., Bresciani, R., Masi, F., Rizzo, A., AlBtoosh, J., and Zoubi, M. M. (2025). Ground-based green façade for enhanced greywater treatment and sustainable water management. Water. 10(1): 1–24

Obeidat, N., Abu-Awwad, A., Al-Salaymeh, A. S., AlBtoosh, J., Zoubi, M. M., Abu-Afifeh, Q. Y., Seif, M. A., Hroub, H., and Arabiat, O. (2025). Social acceptance of water quality through decentralized greywater treatment using green wall system. Global Journal of Environmental Science and Management, 11(3): 1-14

Ocampo-Marulanda, C., Fernández-Álvarez, C., Cerón, W. L., Canchala, T., Carvajal-Escobar, Y., and Alfonso-Morales, W. (2022). A spatiotemporal assessment of the high-resolution CHIRPS rainfall dataset in southwestern Colombia using combined principal component analysis. Ain Shams Engineering Journal, 13(5): 101739

Paredes-Trejo, F. J., Barbosa, H. A., and Lakshmi Kumar, T. V. (2017). Validating CHIRPS-based satellite precipitation estimates in Northeast Brazil. Journal of Arid Environment, 139: 26–40

Prakash, S. (2019). Performance assessment of CHIRPS, MSWEP, SM2RAIN-CCI, and TMPA precipitation products across India. Journal of Hydrology., 571: 50–59

Rahman, K., Gorelick, S.M., Dennedy-Frank, P.J., Yoon, J., and Rajaratnam, B. (2015). Declining rainfall and regional variability changes in Jordan. Water Resources Research, 51 (5): 3828–3835

Rosane, c., Batista, D., Paulo, P., Tedeschi, R. G., Priscila, C., and Barreiros, E. (2020). Evaluation of extreme rainfall indices from CHIRPS precipitation estimates over the Brazilian Amazonia. Atmospheric Research, 238: 104879–104879

Saeidizand, R., Sabetghadam, S., Tarnavsky, E., and Pierleoni, A. (2018), Evaluation of CHIRPS rainfall estimates over Iran. Quarterly Journal of the Royal Meteorological Society, 144(S1): 282–291

Salman, S. A., Shahid, S., Ismail, T., Chung, E.-S., and Al-Abadi, A.M. (2017). Long-term trends in daily temperature extremes in Iraq. Atmospheric Research, 198: 97–107

Shatanawi, K., Mohammad, A.H., Odeh, T., Arafeh, M, Halalsheh, M., and Kassab, G. (2022). Analysis of historical precipitation in semi-arid areas – case study of Amman Zarqa Basin. Journal of Ecological Engineering, 23 (8): 100–110

Shen, Z., Yong, B., Gourley, J. J., Qi, W., Lu, D., Liu, J., Ren, L., Hong, Y., and Zhang, J. (2020). Recent global performance of the climate hazards group infrared precipitation (CHIRP) with stations (CHIRPS). Journal of Hydrology, 591: 125284

Suharyanto, A., Maulana, A., Suprayogo. D., Devia, Y.P., and Kurniawan, S. (2023). Land surface temperature changes

caused by land cover/land use properties and their impact on rainfall characteristics. Global Journal of Environmental Science and Management, 9(3): 353-372

Teweldebrihan, M.D., and Dinka, M.O. (2024). The impact of climate change on the development of water resources. Global Journal of Environmental Science and Management, 10(3): 1359-1370

Trenberth, K.E., (2011). Changes in precipitation with climate change. Climate Research, 47(1): 123–138

Wu, W., Li, Y., Luo, X., Zhang, Y., Ji, X., and Li, X. (2019). Performance evaluation of the CHIRPS precipitation dataset and its utility in drought monitoring over Yunnan Province, China. Geomatics, Natural Hazards and Risk, 10(1): 2145–2162

Zeleňáková, M., Abd-Elhamid, H. F., Krajníková, K., Smetanková, J., Purcz, P., and Alkhalaf, I. (2022). Spatial and temporal variability of rainfall trends in response to climate change—a case study: Syria. Water. 14 (10): 1670

JJEES

JJEES (2026) 17 (1): 97-105
ISSN 1995-6681

Jordan Journal of Earth and Environmental Sciences

Using the SAMS Stochastic Program for Analysis and Modeling Climate Data in Nineveh Governorate

Hasan Jamal Al-Bazaz[1*], Omar M.A. Mahmood Agha[2] and Mohammed Awni Khattab[2]

[1] Department of Climate Change, College of Environmental Sciences, University of Mosul, Iraq.
[2] Department of Dams and Water Resources Engineering, College of Engineering, University of Mosul, Iraq.

Received on 23 June 2025; Accepted on 14 September 2025

Abstract

Hydrological data is considered essential information in the design of water resource projects. Therefore, stochastic simulation of hydrological time series based on mathematical models is necessary to estimate the generated statistical properties. In this study, SAMS 2010 software was used to fit four models: ARMA, BB, ISM, and KGK, for generating statistical properties of monthly rainfall data and maximum and minimum temperatures for Mosul, Tal Afar, Rabia, and Sinjar stations in Nineveh Governorate for the time period 1985-2021. The results revealed that the nonparametric disaggregation model is capable of producing the statistical properties of hydrological time series and preserve the correlation structure between historical and generated models. The ISM model excelled in preserving the basic annual statistical properties. Meanwhile, other models showed agreement between historical and generated monthly data in representing general trends of rainfall and temperatures with slight differences not exceeding ±5%. The ARMA model recorded the lowest ability to preserve the temporal correlation structure in most stations. The study concluded that nonparametric disaggregation models for hydrological time series represent an effective tool among stochastic generation methods, making them an effective choice and tool for water resources management and future planning.

Keywords: *Disaggregation model, Nonparametric, Nineveh, Rainfall, SAMS, Temperature.*

1. Introduction

Rainfall and temperature are among the most important climatic elements , and predicting them is difficult. Nevertheless, they remain of great importance and are highly beneficial in the management of water resources and agricultural projects. Moreover, the impacts of global warming are increasingly evident, as extreme events such as prolonged droughts, heavy rainfall, and rising temperatures have begun to affect agriculture and socio-economic development worldwide. Therefore, a comprehensive understanding of rainfall and its past and future fluctuations has become necessary in light of current climate change in to develop effective adaptation and mitigation strategies (Dai et al., 2024). As the primary source of fresh water, rainfall plays a fundamental role in agriculture and the economy. Consequently, fluctuations in rainfall patterns directly influence water availability, agricultural production, and economic stability, making climate change a central factor in managing water resources (Vetrithangam et al., 2025; Al-Bazaz & Agha, 2023). In this context, climate change involves long-term shifts in climatic elements such as rainfall and temperature, occurring at both local and global scales (Hussain et al., 2025).

Furthermore, climate change represents one of the most serious challenges facing humanity. Alterations in rainfall and temperature disturb the environmental balance and the hydrological cycle, increasing the vulnerability of ecosystems. This situation highlights the urgent need for accurate predictions and advanced modeling techniques to support and improve the management of natural disasters, such as droughts and floods (Al-Bazaz & Agha, 2023; Wang & Liu, 2023).

In the last decade, Nineveh Governorate has been significantly exposed to climate change (UNCCD, 2022), as there has been a change in the pattern of rainfall and a difference in temperatures, and this has affected water resources and agricultural projects, as the study area is characterized as a farming region (Al-Bazaz and Mahmood Agha, 2024).

Based on the foregoing, it has become necessary to employ simulation and analysis techniques, foremost among them hydrological software models, as these are considered vital tools for water resources management. Numerous models and techniques are available to assess and predict hydrological elements, and each differs in terms of accuracy, duration, and scope of work (Makridakis et al., 1984).

SAMS 2010 is a software package specialized in stochastic analysis, modeling, and simulation of hydrological time series, developed as a collaborative effort between Colorado State University and the U.S. Bureau of Reclamation in Denver, Colorado, to meet hydrological research needs in the analysis of climatic and water data. The SAMS program provides a set of options and tools, including three main options: first, statistical analysis of data; second, stochastic model construction; and third, generating synthetic series

* Corresponding author e-mail: hasanalbazaz@uomosul.edu.iq

for future estimation. The program also allows application to annual, seasonal, and monthly data. In addition, the program includes parametric models, such as linear decomposition models and multivariate autoregressive models, as well as nonparametric techniques, which are essential for analyzing data that do not follow a probability distribution (Qassem, 2021). The program's capabilities include historical data analysis, parameter estimation, and data generation (Saada et al., 2019). Saada (2015) indicated that the use of stochastic models for climatic time series to generate synthetic time series by demonstrating the statistical properties (mean, variance, and skewness) of the generated data is one of the modeling problems represented in finding a model capable of preserving historical properties. Saada (2014) also confirmed the possibility of using modeling models for monthly rainfall forecasting in arid and semi-arid regions, which is the climate that characterizes the study area. Moreover, Jöckel and Pflaumer (2024) indicated that the temporal dependence on previous values in the data significantly affects risk assessment, and that using ARMA models helps make variance estimation more accurate. Consequently, by utilizing ARMA models, decision-makers can obtain a more precise assessment of risks. In this way, the ability to make such predictions is of utmost importance in improving the effective management of water resources (Hamdi et al., 2008).

Researchers (Abdullah et al., 2019) tested the capabilities of the SAMS program by applying four stochastic models to monthly and annual rainfall data and the SPI drought index for sites in Jordan and Saudi Arabia. The researchers showed that the models succeeded in preserving the statistical properties of the climatic data at each site.

In Iraq, Al-Mohseen (2010) analyzed the annual flow status using three stochastic models with the SAMS 2007 stochastic model analysis system program. He showed that there is variation in the models' ability to preserve the statistical properties of generated time series and confirmed that the SAMS program is effective for analyzing, modeling, and generating hydrological data. Moreover, Qassem (2021) used five linear models (ARMA, GAR1, BB, ISM, and KGK) to regenerate monthly data. It was found that there is strong convergence between historical and generated statistical properties, and it was confirmed that the nonparametric approach has a high ability to regenerate observed data with a preference using the ISM model based on statistical criteria. Furthermore, in their study of the flow conditions at the Kut Dam on the Tigris River, Al-Youdawi and Al-Badranee (2025) used a univariate ARMA model in the SAMS program, relying on 21 years of dam discharge data. Their findings highlighted the model's effectiveness in capturing the underlying patterns in discharge data, leading to more accurate predictions of flow. Their results demonstrated the feasibility of using the SAMS program with the ARMA model to analyze observed Tigris River discharges at the Kut Dam and predict future discharges.

The objective of this study is to investigate the possibility of using the nonparametric disaggregation model on climatic data (rainfall, maximum and minimum temperatures) for Mosul, Rabia, Sinjar, and Tal Afar stations in Nineveh Governorate for the period 1985-2021 and to demonstrate the extent to which the nonparametric model can succeed in preserving the generated statistical properties using SAMS 2010 software. Also, this paper is the first study to use nonparametric disaggregation of climatic data in the study area and Iraq.

2. Materials and methods

2.1 Study Area and Data Used

The historical monthly rainfall data used in this study extend for 37 years (1985-2021). Four meteorological stations were selected in Nineveh Governorate: Mosul, Rabia, Tal Afar, and Sinjar. Climatic data were obtained from the Iraqi General Authority for Meteorology and Seismology, part of the Iraqi Ministry of Transport. The selected meteorological stations cover the north and northwest of Nineveh Governorate, an area of strategic importance because it mainly comprises agricultural lands dependent on rain-fed agriculture. This area is also considered one of the areas affected by climate change. Figure 1 shows the geographical location of meteorological stations in Nineveh Governorate.

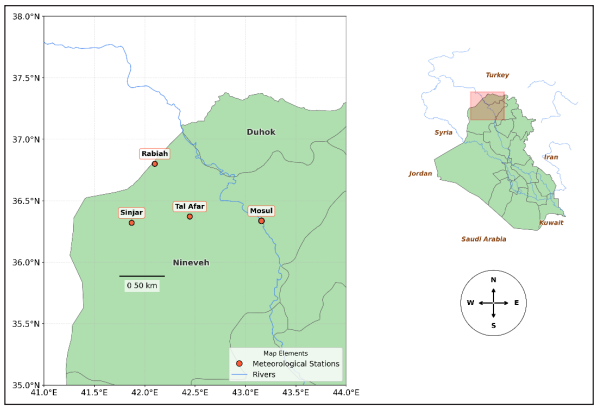

Figure 1. Locations of meteorological stations in the study area.

2.2 Methods

Four nonparametric disaggregation models were used to generate climatic data without making any assumptions, and their statistical properties, such as mean and standard deviation, were compared.

2.2.1 Autoregressive Moving Average Model (ARMA)

The ARMA (p,q) model was used. This model links autocorrelation parameter p to moving-average parameter q. The best model is chosen from several tests based on the Akaike Information Criterion (AICC) (Akaike, 1974) and Schwarz Information Criterion (SIC) (Hurvich and Tsai, 1989). The best model is the one with the lowest values for both criteria (Sveinsson et al., 2011).

$$Z_t = \sum_{i=1}^{p} \varphi_i Z_{t-i} + \varepsilon_t - \sum_{j=1}^{q} \theta_j \varepsilon_{t-j} \quad \text{..... (1)}$$

Where:

Zt: Climatic parameter at year t, Zt−i: Climatic parameter at previous time points, εt: White noise term, φj: Autoregressive (AR) coefficient, θj: Moving average (MA) coefficient, p: Order of the autoregressive coefficient, q: Order of the moving average coefficient.

2.2.2 Index Sequential Model (ISM)

This model involves sequentially reordering the observed data (Ouarda et al. 1997). In this model, the observed data

are reordered from the first observed point to the end of the observed time record.

$$Y = [y_1 + y_2 + y_3 + \text{--------} + y_n] \quad \text{..... (2)}$$

$$\acute{Y}_i = [y_i + y_{i+1} + y_{i+2} + \text{--------} + y_{n+i-1}] \quad \text{..... (3)}$$

Where: $\acute{Y}i$: Sum of the reordered data, i: Step size between years, n: Number of years (length of the time series).

2.2.3 Block Bootstrapping (BB) Model

It is an algorithm for nonparametric time series resampling (Vogel and Shallcross, 1996). In this model, historical data are resampled as blocks with replacement. The time series must be long enough to ensure the preservation of its correlation structure. The model steps are as follows:

1. Define the block length i The candidate overlapping blocks are:

$$y_{B1} = [y_1, y_2, y_3, \ldots\ldots, y_l] \quad \text{..... (4)}$$

$$y_{B2} = [y_2, y_3, \ldots\ldots, y_{l+1}] \quad \text{..... (5)}$$

$$y_{BN-l+1} = [Y_{n-l+1}, y_{N-l+2}, \ldots\ldots, y_N] \quad \text{..... (6)}$$

2. One of the (N-l+1) blocks is selected by generating a discrete uniform random number from 1 to N-l+1. If c is chosen from the random numbers, [Y1 ,Y2 ,…,Yi]=[Yc ,Yc+1 ,…,Yc+l−1], where Yj is the generated number. In this case, the required block is resampled.

3. The following values to be resampled [Yl+1,yl+2 ,…,y2l] are obtained in the same way as in Step 2.

4. These steps continue until the generated series is obtained.

2.2.4 K-Nearest Neighbor with Gamma Kernel Estimation (KGK) Model

It is a nonparametric method that resamples data using a Gamma distribution. Furthermore, the determination of gamma parameters leads to some bias in variance and arithmetic mean (Lee and Salas, 2008).

$$\boldsymbol{Y}_{x^2/h^2, h^2/x}(t) = \frac{t^{x^2/h^2 - 1} e^{-t/(h^2/x^2)}}{(h^2/x)^{x^2/h^2} \Gamma(x^2/h^2)} \quad \text{..... (7)}$$

Where: h: Smoothing parameter, It can be calculated through Least Squares Cross-Validation (LSCV) proposed by Chen (2000), t: Generated random number, x: Historical data

The four models (ARMA, BB, ISM and KGK) were applied using SAMS 2010 software, developed as a collaborative effort between Colorado State University and the U.S. Bureau of Reclamation in Denver, Colorado (Sveinsson et al., 2011), to disaggregate monthly climatic data (rainfall and maximum and minimum temperatures), extract historical and generated statistical properties, and generate 100 time series of data for 37 years at the four selected stations.

3. Results and Discussion

Time series generation is an essential tool in operations research, as this data serves as the basis for decision-makers in many studies. This study examines the efficiency of nonparametric models for generating time series and preserving their statistical properties. The Stochastic Analysis, Modeling, and Simulation (SAMS, 2010) program, widely used in hydrology for time series modeling, was adopted. It is a specialized software tool for stochastic modeling and simulation of hydrological data due to its high ability to preserve the statistical properties of generated time series. This capability makes it an important tool in hydrological analysis, as it helps simulate the future behavior of hydrological systems under random climatic conditions. In this study, four models (ARMA, ISM, BB and KGK) were applied to analyze hydrological data comprising rainfall and maximum and minimum temperatures collected from four meteorological stations in areas famous for rain-fed agriculture. These are Mosul, Tal Afar, Sinjar, and Rabia stations in Nineveh Governorate. Statistical tests (arithmetic mean and standard deviation) were calculated from 100 time series over 37 years, yielding accurate results that showed convergence between historical and generated values. Its ability to preserve statistical properties when generating synthetic data makes it particularly useful for areas with limited historical records or for assessing future scenarios under different climatic conditions.

Table 1 shows the results of the ARMA test analysis for rainfall, maximum, and minimum temperatures at the four climatic stations: Mosul, Sinjar, Rabia, and Tal Afar. The optimal ARMA models were selected based on statistical criteria represented by AICC and SIC values, where the model with the lowest values is considered the best for both requirements, providing reliable measures for model selection (Sveinsson et al., 2011). These results are consistent with hydrological studies that emphasize the importance of appropriate model identification for accurate time series analysis. This approach leads to a better model that more accurately represents the data. (Al-Youdawi & Al-Badranee, 2025; Hamdi et al., 2008; Hussain et al., 2025).

Table 1. Results of the ARMA tests for the rain, T max, and T min in all stations

Stations		Rain		T max		T min	
Mosul	AICC	398.492	1-1	217.259	0-2	217.436	1-0
	SIC	398.986		217.753		216.694	
Sinjar	AICC	402.608	1-0	203.352	0-1	228.261	0-2
	SIC	401.886		202.61		228.756	
Rabiah	AICC	390.882	1-0	233.452	0-2	201.839	0-2
	SIC	390.140		233.946		202.333	
Tal-Afar	AICC	395.960	1-0	218.468	0-2	213.407	0-1
	SIC	395.218		218.962		212.665	

For rainfall data, three stations (Rabia, Tal Afar, and Sinjar) showed compatibility with the ARMA (1,0) model, while the Mosul station showed an ARMA (1,1) pattern. As for maximum temperatures, most stations followed the ARMA (0,2) pattern, while the Sinjar station showed an ARMA (0,1) model. ARMA models for minimum temperatures showed clear variation among climatic stations, with ARMA (1,0) in Mosul, ARMA (0,2) in both Sinjar and Rabia, and ARMA (0,1) in Tal Afar.

Through the comparison between historical data and data generated via the four stochastic models (ARMA, BB, ISM, KGK), the effectiveness of these methods in preserving the statistical properties of climatic data is evident, as shown in Figure 2. Tables (2-4) show a comprehensive comparison between observed and generated values for annual and monthly rainfall and maximum and minimum temperatures across all stations. The close agreement between historical and generated statistical parameters (arithmetic mean and standard deviation) demonstrates the strength of the stochastic generation process. The results showed strong convergence between the means of historical and generated rainfall data for the ISM, BB, and KGK models, outperforming the ARMA model. As for maximum and minimum temperatures, the BB and ISM models outperformed the ARMA and KGK models in the time-series comparison. Also, the ISM (the improved semi-parametric model) showed superior performance across most stations and parameters, confirming Saada's (2015) earlier findings on the effectiveness of nonparametric methods in modeling hydrological data. This result aligns with Abdullah et al. (2019), who found that SAMS models successfully preserve the statistical properties of climatic data for sites in Jordan and Saudi Arabia, which share climatic characteristics similar to those of the study area.

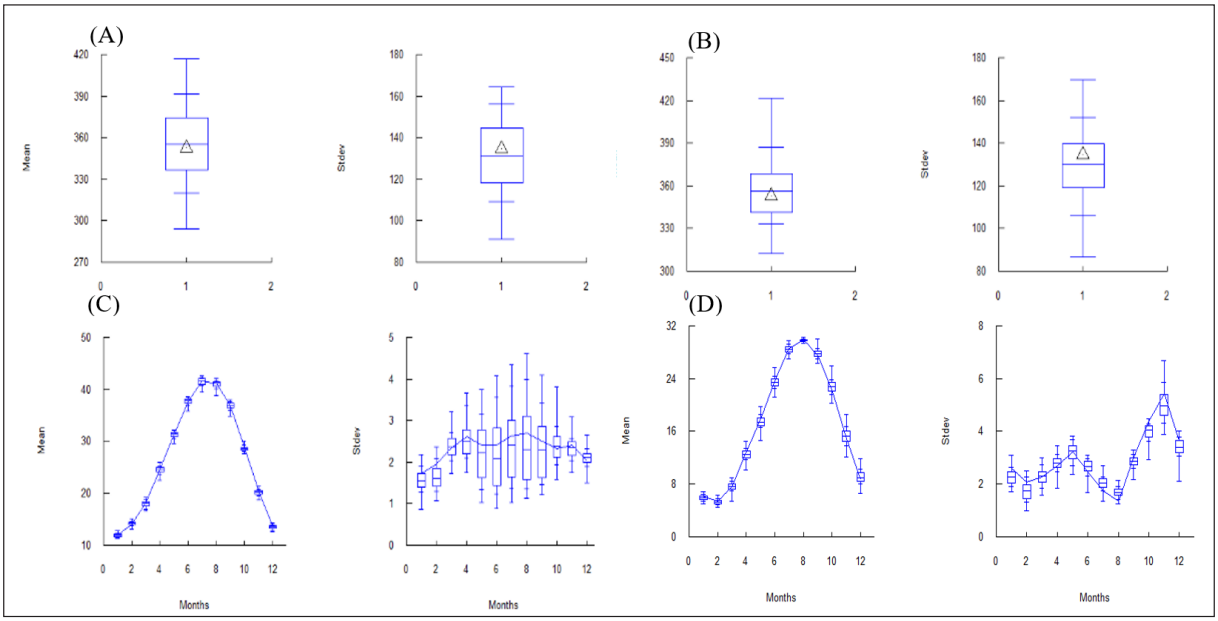

Figure 2. Statistical characteristics (A) ARMA model for rainfall at the Mosul station, (B) BB model for rainfall at the Mosul station, (C) KGK model for maximum temperatures at Rabia station, and (D) ISM model for minimum temperatures at the Sinjar station

Table 2. Comparison of Observed and Generated Values in Models for Annual and Monthly Rain in Stations

		Historical		ARAM		BB		ISM		KGK	
		Mean	St.Dev	Mean	St.Dev	Mean	St.Dev	Mean	St.Dev	Mean	St.Dev.
Mosul Station	Annual	352.7	134.5	354.4	132.3	357.9	129.5	352.7	134.5	346.5	152.6
	M 1	61.46	43.57	64.07	45.25	64.52	45.62	62.78	46.34	64.35	47.12
	M 2	55.62	32.5	56.37	36.12	58.03	35.61	56.63	35.38	58.08	36.63
	M 3	60.22	48.18	61.87	48.56	58.81	46.16	59.89	46.07	58.27	46.74
	M 4	42.4	41.49	37.6	33.01	38.52	35.55	37.89	36.26	39.48	36.31
	M 5	14.72	27.12	11.28	19.44	13.36	21.75	12.76	21.73	13.38	22.2
	M 10	13.76	19.02	14.78	20.59	14.85	20.43	15.04	20.75	14.42	19.39
	M 11	40.82	38.27	42.8	36.66	43.81	38.6	43.26	38.63	42.27	39.13
	M 12	61.76	38.38	61.5	37.08	63.16	38.96	62.45	38.34	63.29	40.65
Sinjar Station	Annual	334.6	132.3	323.5	136.1	341	125.3	334.6	132.3	327	153
	M 1	64.67	50.3	60.6	44.31	62.22	44.7	61.12	44.95	61.56	47.27
	M 2	52.79	36.75	49.93	38.16	53.17	37.89	51.92	38	51.9	39.46
	M 3	57	46.46	51.04	46.68	55.04	45.84	53.63	45.26	54.37	46.56
	M 4	29.24	26.87	30.4	28.03	29.3	26.4	29.62	27.43	29.79	26.57
	M 5	14.89	24.7	13.98	22.2	14.9	24.22	15.34	26	16	27.93
	M 10	17.62	22.47	21.07	28.94	19.36	24.97	20	24.98	19.57	25.35
	M 11	38.01	37.99	39.35	37.21	42.05	39.7	39.55	39.13	38.25	39.5
	M 12	58.56	46.8	58.19	47.99	63.29	48.04	61.53	47.91	62.36	48.99
Rabiah Station	Annual	341.4	113.4	340.4	111.8	348.3	107.6	341.4	113.4	358.4	130.3
	M 1	63.27	46.49	60.29	41.02	60.51	41.93	59.33	40.05	67.05	45.4
	M 2	51.35	29.7	51.3	31.7	53.34	31.37	52.72	32.13	55.58	33.31
	M 3	56.8	42.06	55.47	43.79	56.08	43.92	54.48	41.24	57.3	44.57
	M 4	36.44	33.17	37.84	35.1	36.78	33.14	35.52	31.69	38.16	33.47
	M 5	20.51	22.31	21.24	22.78	21.68	22.99	21.79	23.74	24.22	25.82
	M 10	21.23	27.13	22.084	29.39	22.96	29.38	22.22	28.8	24.78	31.5
	M 11	31.15	25.93	31.53	25.38	33.61	26.44	33	26.76	34.67	27.39
	M 12	57.3	42.23	57.99	43.15	60.1	42.39	59.68	42.25	62.6	44.46
Tal-Afar Station	Annual	305.9	123.3	304.2	120.9	311.7	118.2	305.9	123.3	295.4	136.8
	M 1	59.66	49.82	56.15	42.8	60.51	46.14	58.86	44.79	59.62	47.09
	M 2	42.91	26.29	42.41	27.52	42.87	27.44	41.77	27.38	42.68	27.99
	M 3	55.57	47.67	56.24	54.44	55.4	47.46	53.21	47.76	52.39	47.17
	M 4	32.36	31.74	29.7	27.82	29.88	28.18	29.91	29.54	29.68	28.84
	M 5	15.46	26.54	15.24	23.45	15.27	25.06	16.31	26.18	16.28	27.11
	M 10	12.17	15.35	13.65	17.93	13.29	17.69	13.11	16.85	12.74	16.8
	M 11	35.67	36.25	40.83	38.63	39.77	37.7	39.59	37.54	37.91	38.22
	M 12	49.96	35.72	48.94	33.47	51.89	35.4	50.59	34.72	49.57	35.71

Table 3. Comparison of Observed and Generated Values in Models for Annual and Monthly T max in Stations

		Historical		ARAM		BB		ISM		KGK	
		Mean	St.Dev	Mean	St.Dev	Mean	St.Dev	Mean	St.Dev	Mean	St.Dev.
Mosul Station	Annual	341.3	13.64	341.40	13.03	341.0	13.04	341.3	13.64	331.00	52.20
	M 1	13.09	1.67	13.11	1.46	12.99	1.45	13.03	1.54	13.04	1.62
	M 2	15.48	1.93	15.60	1.58	15.51	1.60	15.57	1.67	15.49	1.81
	M 3	19.8	2.25	19.70	2.17	19.71	2.13	19.74	2.21	19.48	2.26
	M 4	26.01	2.23	26.07	2.20	26.02	2.20	26.04	2.29	25.92	2.26
	M 5	33.51	1.77	33.63	1.66	33.56	1.57	33.58	1.66	33.44	1.88
	M 6	39.82	1.15	39.87	1.33	39.85	1.37	39.84	1.37	39.67	1.47
	M 7	43.37	1.90	43.51	1.90	43.54	1.88	43.51	2.01	43.29	2.13
	M 8	43.34	1.19	43.30	1.55	43.30	1.57	43.30	1.48	43.13	1.60
	M 9	38.64	1.50	38.71	1.62	38.60	1.63	38.63	1.64	38.54	1.64
	M 10	31.78	3.61	31.35	2.67	31.29	2.54	31.43	2.85	31.30	2.95
	M 11	31.78	3.61	21.64	2.23	21.68	2.29	21.70	2.28	21.43	2.31
	M 12	14.92	2.08	14.94	2.16	14.90	2.20	14.91	2.13	14.66	2.16
Sinjar Station	Annual	257.1	10.9	257.1	10.5	257	10.61	257.1	7.537	253.4	39.16
	M 1	7.53	1.39	7.57	1.24	7.55	1.25	10.9	1.28	7.60	1.29
	M 2	9.29	1.66	9.43	1.35	9.38	1.37	257.1	7.53	9.55	1.31
	M 3	13.52	2.10	13.5	2.0	13.56	1.94	10.9	1.28	13.81	1.90
	M 4	19.24	1.98	19.28	1.95	19.34	1.99	257.1	7.53	19.6	1.91
	M 5	25.88	1.49	25.88	1.42	25.92	1.39	10.9	1.28	26.11	1.32
	M 6	31.85	1.09	31.79	1.19	31.85	1.20	257.1	7.53	32.07	1.15
	M 7	35.53	1.19	35.63	1.27	35.61	1.32	10.9	1.28	35.88	1.29
	M 8	35.05	1.07	34.92	1.24	34.94	1.3	257.1	7.53	35.17	1.23
	M 9	30.71	1.26	30.77	1.38	30.68	1.4	10.9	1.28	30.89	1.41
	M 10	23.53	1.95	23.44	1.86	23.41	1.86	257.1	7.53	23.7	1.78
	M 11	15.24	1.91	15.19	1.79	15.21	1.77	10.9	1.28	15.44	1.76
	M 12	9.68	1.7	9.64	1.73	9.611	1.79	257.1	7.53	9.82	1.75
Rabiah Station	Annual	320.1	17.45	320.20	20.90	319.9	17.26	320.10	17.45	311.30	51.48
	M 1	11.91	1.723	11.89	1.93	11.94	1.51	0.25	1.57	11.87	1.54
	M 2	14.06	1.943	14.15	2.01	14.23	1.66	14.22	1.66	14.19	1.68
	M 3	18.15	2.33	18.08	2.47	18.10	2.31	18.09	2.33	17.98	2.37
	M 4	24.51	2.614	24.45	2.52	24.54	2.47	24.59	2.50	24.41	2.53
	M 5	31.3	2.4	31.32	2.32	31.38	2.17	31.38	2.18	31.32	2.24
	M 6	37.71	2.402	37.84	2.19	37.80	2.17	37.79	2.17	37.75	2.26
	M 7	41.55	2.639	41.60	2.38	41.65	2.37	41.72	2.40	41.61	2.49
	M 8	41.12	2.697	41.25	2.53	41.13	2.41	41.15	2.39	41.04	2.53
	M 9	36.89	2.514	36.96	2.35	36.91	2.32	36.98	2.32	36.89	2.41
	M 10	28.92	2.328	28.84	2.89	28.65	2.49	28.65	2.39	28.68	2.46
	M 11	20.3	2.404	20.12	2.71	20.04	2.30	20.06	2.28	20.13	2.26
	M 12	13.64	2.041	13.60	2.29	13.48	2.10	13.52	2.09	13.46	2.04
Tal-Afar Station	Annual	331.5	14.64	331.70	13.87	331.2	14.09	331.5	14.64	325.3	51.42
	M 1	12.11	1.70	12.16	1.67	12.09	1.47	12.08	1.55	12.20	1.63
	M 2	14.19	2.01	14.27	1.66	14.34	1.60	14.29	1.63	14.42	1.67
	M 3	18.77	2.60	18.89	2.75	18.77	2.72	18.75	2.73	18.95	2.71
	M 4	25.45	2.42	25.53	2.45	25.47	2.39	25.46	2.41	25.66	2.45
	M 5	32.67	1.85	32.69	1.78	32.66	1.62	32.72	1.71	32.85	1.75
	M 6	38.86	1.16	38.87	1.41	38.87	1.37	38.88	1.41	39.03	1.41
	M 7	42.62	1.41	42.64	1.56	42.65	1.56	42.69	1.62	42.81	1.62
	M 8	42.26	1.21	42.17	1.48	42.17	1.56	42.17	1.51	42.33	1.54
	M 9	37.64	1.59	37.65	1.75	37.55	1.75	37.65	1.84	37.80	1.80
	M 10	32.04	4.74	31.58	3.58	31.69	4.13	31.85	4.06	32.09	4.31
	M 11	20.76	2.37	20.92	2.43	20.75	2.35	20.80	2.36	20.99	2.39
	M 12	14.13	2.17	14.34	2.17	14.14	2.22	14.20	2.22	14.35	2.21

Table 4. Comparison of Observed and Generated Values in Models for Annual and Monthly T min in Stations

		Historical		ARAM		BB		ISM		KGK	
		Mean	St.Dev	Mean	St.Dev	Mean	St.Dev	Mean	St.Dev	Mean	St.Dev.
Mosul Station	Annual	161	12.64	161.70	12.23	160.7	11.93	161.00	12.64	159.10	24.53
	M 1	2.661	1.76	2.62	1.75	2.59	1.71	2.65	1.71	2.62	1.71
	M 2	3.93	1.76	4.04	1.75	3.93	1.75	3.98	1.76	4.05	1.73
	M 3	7.392	1.92	7.61	1.65	7.47	1.67	7.53	1.74	7.66	1.68
	M 4	11.55	1.50	11.61	1.47	11.60	1.52	11.59	1.49	11.72	1.49
	M 5	16.68	1.58	16.67	1.58	16.62	1.57	16.64	1.62	16.81	1.60
	M 6	21.79	1.51	21.77	1.60	21.76	1.59	21.76	1.61	21.93	1.61
	M 7	25.53	1.40	25.54	1.49	25.52	1.52	25.51	1.54	25.70	1.56
	M 8	24.87	1.39	24.78	1.64	24.78	1.64	24.81	1.61	24.95	1.64
	M 9	20.02	1.61	20.06	1.65	20.00	1.65	20.03	1.66	20.23	1.64
	M 10	14.6	1.70	14.68	1.59	14.58	1.59	14.61	1.64	14.78	1.61
	M 11	7.89	1.69	7.90	1.68	7.87	1.67	7.89	1.74	8.00	1.68
	M 12	4.12	2.07	4.10	2.12	4.06	2.12	4.07	2.15	4.14	2.10
Sinjar Station	Annual	205.1	14.25	205.2	13.79	205	14.06	205.10	14.25	201.20	31.35
	M 1	5.957	2.602	5.998	2.359	5.883	2.139	5.83	2.26	5.92	2.26
	M 2	5.335	2.063	5.145	1.981	5.354	1.976	5.31	1.88	5.27	1.91
	M 3	7.638	2.27	7.456	2.296	7.493	2.353	7.59	2.34	7.51	2.30
	M 4	12.76	2.699	12.39	2.77	12.39	2.83	12.51	2.82	12.42	2.80
	M 5	17.86	3.209	17.2	3.232	17.2	3.275	17.39	3.23	17.36	3.24
	M 6	23.72	2.461	23.39	2.753	23.4	2.714	23.47	2.67	23.40	2.59
	M 7	28.61	1.732	28.38	2.072	28.41	2.011	28.46	2.06	28.43	2.00
	M 8	29.88	1.334	29.92	1.734	29.81	1.674	29.88	1.69	29.92	1.69
	M 9	27.53	2.984	27.86	2.773	27.84	2.74	27.76	2.87	27.97	2.80
	M 10	22.38	4.357	23	3.781	22.82	3.807	22.78	4.02	23.05	3.81
	M 11	14.8	5.438	15.49	4.958	15.36	4.877	15.23	5.01	15.50	4.92
	M 12	8.638	3.659	9.138	3.308	8.969	3.435	8.98	3.50	9.14	3.34
Rabiah Station	Annual	129.4	10.5	129.50	10.17	129.5	10.55	129.40	10.53	126.20	21.80
	M 1	0.956	1.58	0.73	1.53	0.78	1.47	0.81	1.47	0.78	1.51
	M 2	1.73	1.45	1.60	1.38	1.60	1.40	1.68	1.39	1.67	1.40
	M 3	4.84	1.74	4.92	1.42	4.91	1.46	4.93	1.44	4.97	1.43
	M 4	9.34	1.41	9.50	1.29	9.48	1.35	9.45	1.36	9.50	1.31
	M 5	13.8	1.06	13.86	1.23	13.82	1.23	13.82	1.25	13.79	1.25
	M 6	18.5	1.32	18.61	1.58	18.55	1.54	18.51	1.55	18.53	1.52
	M 7	21.84	1.31	22.01	1.45	22.03	1.51	21.98	1.48	21.98	1.51
	M 8	21.08	1.16	21.08	1.27	21.10	1.29	21.10	1.32	21.10	1.33
	M 9	16.54	1.45	16.54	1.38	16.55	1.40	16.56	1.45	16.54	1.44
	M 10	12.07	1.41	12.05	1.26	12.04	1.25	12.06	1.32	12.08	1.33
	M 11	6.25	1.55	6.26	1.54	6.24	1.54	6.20	1.54	6.23	1.53
	M 12	2.41	1.65	2.38	1.52	2.38	1.51	2.31	1.54	2.27	1.58
Tal-Afar Station	Annual	186.8	12.52	186.80	12.06	186.5	11.90	186.80	12.52	181.20	28.34
	M 1	3.81	2.41	3.85	2.28	3.88	2.42	3.92	2.31	3.65	2.48
	M 2	4.93	2.10	5.03	1.90	4.97	1.98	5.08	1.94	4.88	2.05
	M 3	8.11	1.92	8.22	1.73	8.23	1.65	8.27	1.69	8.13	1.72
	M 4	12.69	2.35	12.72	2.35	12.64	2.43	12.66	2.39	12.56	2.34
	M 5	18.64	1.64	18.57	1.72	18.58	1.67	18.55	1.70	18.43	1.70
	M 6	24.54	1.39	24.47	1.56	24.47	1.47	24.45	1.54	24.35	1.52
	M 7	28.24	1.48	28.30	1.55	28.28	1.56	28.29	1.59	28.19	1.61
	M 8	27.97	1.33	27.85	1.62	27.80	1.55	27.82	1.60	27.71	1.61
	M 9	23.90	1.58	23.90	1.58	23.90	1.58	23.90	1.58	23.90	1.58
	M 10	17.86	1.60	23.87	1.60	23.83	1.63	23.87	1.64	23.77	1.70
	M 11	10.40	1.73	17.89	1.57	17.86	1.54	17.88	1.58	17.82	1.57
	M 12	5.68	1.66	10.35	1.69	10.30	1.65	10.37	1.65	10.37	1.65

Finally, when evaluating the performance of the four models (ARMA, ISM, BB, and KGK), it was found that they were effective at generating hydrological time series. Using nonparametric simulation, synthetic time series were generated from these four models, resulting in 100 time series spanning 37 years. Statistical analyses of historical data (mean and standard deviation) revealed a strong correlation with the generated data, indicating that the models preserve the correlation structure. A test of different (which relies on taking two random samples from two normal populations) was conducted on the historical and generated data for all stations. The results of this test showed that the p-value was greater than 0.05, indicating no significant difference between the arithmetic mean and standard deviation, and thus the generated models simulated the original data well.

4. Conclusion

This study represents the first application of nonparametric disaggregation of climatic data in Iraq. The study showed that, when applied to parametric models (ARMA, BB, ISM, and KGK), the ISM model performed well at preserving the statistical properties of both historical and generated climatic data across the four meteorological stations. This finding was confirmed by the difference test (p-value > 0.05), indicating that the generated models accurately simulate the historical data, with no significant differences in means, effectively replicating the original data and enhancing the reliability of the results. Researchers in the field can use the most effective ARMA models identified. Finally, the importance of this study lies in the demonstrated potential to apply nonparametric models to climatic data for hydrological modeling, with the possibility of extending this application to other areas, especially those with limited historical data or that require assessment of future scenarios and decision-making to address climate change.

Acknowledgments

The authors express their gratitude to the College of Environmental Sciences and the College of Engineering at the University of Mosul for their assistance in carrying out the current research.

Conflicts of Interest

The authors declare no conflict of interest.

References

Akaike, H. (1974). A new look at the statistical model identification. IEEE Transactions on Automatic Control, 19(6), 716–723. https://doi.org/10.1109/TAC.1974.1100705

Al-Bazaz, H. J., & Agha, O. M. A. M. (2023). A study of the homogeneity of climatic data for rain, temperature, and humidity for Nineveh Governorate. Al-Rafidain Engineering Journal, 28(2), 173–185. https://doi.org/10.33899/rengj.2023.137763.1225

Al-Bazaz, H. J., & Agha, O. M. A. M. (2024). Climate change and the behaviour of meteorological drought and its impact on wheat yield. Engineering and Applied Science Research, 51(2), 248–258. https://doi.org/10.14456/easr.2024.24

Al-Mohseen, K. A. (2010). Frequency analysis of hydrologic drought (case study). Al-Rafidain Engineering Journal, 18(6). https://doi.org/10.33899/rengj.2010.35187

Al-Youdawi, G. R., & Al-Badranee, L. B. (2025). Predicting annual Tigris River streamflow at Kut Barrage using the SAMS program. Wasit Journal of Engineering Sciences, 13(1), 39–49.

Al-Zakar, S. H., Şarlak, N., & Agha, O. M. A. (2017). Disaggregation of annual to monthly streamflow: A case study of the Kizilirmak Basin (Turkey). Advances in Meteorology, 2017, Article 3582826. https://doi.org/10.1155/2017/3582826

Amin, D., & Lotfy, A. (2019). Future generation of multi-daily rainfall time series for hydrological analysis in wadi systems. International Research Journal of Engineering and Technology, 6(5), 1–6.

Chen, S. X. (2000). Probability density function estimation using gamma kernels. Annals of the Institute of Statistical Mathematics, 52, 471–480. https://doi.org/10.1023/A:1004165218295

Dai, Y., Abhishek, Li, L., Gong, Y., Wu, X., Sheng, B., & Zhao, W. (2024). Variations in present and future hourly extreme rainfall: Insights from high-resolution data and a novel temporal disaggregation model. Water, 16(23), 3463. https://doi.org/10.3390/w16233463

Hamdi, M. R., Bdour, A. N., & Tarawneh, Z. S. (2008). Developing reference crop evapotranspiration time-series simulation model using Class A pan: A case study for the Jordan Valley, Jordan. Jordan Journal of Earth and Environmental Sciences, 1(1), 33–44.

Hurvich, C. M., & Tsai, C.-L. (1989). Regression and time series model selection in small samples. Biometrika, 76(2), 297–307.

Hussain, K., Farooq, F. J., Salim, M. N., Farooq, S. U., & Altaf, I. (2025). Time-series analysis for forecasting climate parameters of the Kashmir Valley using ARIMA and seasonal ARIMA models. Jordan Journal of Earth and Environmental Sciences, 16(1), 83–95.

Jöckel, K.-H., & Pflaumer, P. (2024). Using ARMA models in stochastic enterprise valuation. SEFBIS Journal, 1–8. https://doi.org/10.14267/SEFBIS.2024.02

Lee, T. S., Salas, J. D., Keedy, J., Frevert, D., & Fulp, T. (2007). Stochastic modeling and simulation of the Colorado River flows. In Proceedings of the World Environmental and Water Resources Congress 2007 (pp. 1–10). ASCE. https://doi.org/10.1061/40927(243)423

Lee, T. S., & Salas, J. D. (2008). Multivariate simulation modeling with the combination of intermittent and non-intermittent monthly time series: KNN match moving block bootstrap with genetic algorithm and perturbation gamma KDE. Conference/technical paper.Makridakis, S., Wheelwright, S. C., & McGee, V. E. (1984). Forecasting: Methods and applications. Wiley.

Ouarda, T. B. M. J., Labadie, J. W., & Fontane, D. G. (1997). Index sequential hydrologic modeling for hydropower capacity estimation. Journal of the American Water Resources Association, 33(6), 1337–1349.

Qassem, A. M. Y. (2021). Temporal and spatial disaggregation of inflow into the site of a proposed Makhol Dam reservoir (‘Master’s thesis). University of Mosul, College of Engineering.

Saada, N. (2014). Time series modeling of monthly rainfall in arid areas: Case study for Saudi Arabia. American Journal of Environmental Sciences, 10(3), 277–282. https://doi.org/10.3844/ajessp.2014.277.282

Saada, N. (2015). Simulation of long-term characteristics of annual rainfall in selected areas in Saudi Arabia. Computational Water, Energy, and Environmental Engineering, 4(2), 18–24. https://doi.org/10.4236/cweee.2015.42003

Saada, N., Abdullah, M. R., Hamaideh, A., & Abu Romman, A. (2019). Application of stochastic analysis, modeling and simulation (SAMS) to selected hydrologic data in the Middle East. Engineering, Technology & Applied Science Research, 9(3), 4261–4264. https://doi.org/10.48084/etasr.2750

Sveinsson, O. G. B., Lee, T. S., Salas, J. D., Lane, W. L., & Frevert, D. K. (2011). Stochastic analysis, modeling, and simulation (SAMS) version 2010: ‘User’s manual. Computing

Hydrology Laboratory, Colorado State University.

United Nations Convention to Combat Desertification. (2022). Drought in numbers 2022 [PDF]. UNCCD. https://www.unccd.int/sites/default/files/2022-05/Drought%20in%20Numbers.pdf

Vetrithangam, D., Arunadevi, B., Pegada, N. K., Kaur, S., & Krishna Prasad, B. (2025). Cloud-based rainfall–runoff model for assessment of long-term rainfall variability and trends using Google Earth Engine. Jordan Journal of Earth and Environmental Sciences, 16(1), 35–49.

Vogel, R. M., & Shallcross, A. L. (1996). The moving blocks bootstrap versus parametric time series models. Water Resources Research, 32(6), 1875–1882.

Wang, X., & Liu, L. (2023). The Impacts of Climate Change on the Hydrological Cycle and Water Resource Management. Water, 15(13), 2342. https://doi.org/10.3390/w15132342.

Yahya, A. M., Al-Zakar, S. H. D., & Al-Mohseen, K. A. (2024). Disaggregation model of Tigris River inflow into a proposed Makhol Reservoir using a parametric approach. Tikrit Journal of Engineering Sciences, 31(1), 172–181. https://doi.org/10.25130/tjes.31.1.15

JJEES

JJEES (2026) 17 (1): 106-110
ISSN 1995-6681

Jordan Journal of Earth and Environmental Sciences

Agricultural Consideration of the Effects of Biofertilizers and Boron on Desertified Soils: A Sustainable Strategy for Enhancing Soil Chemical Properties

Mohammed Rahim Ajeel

Department of Soil and Water Techniques, Al-Musayyab Technical College, Al-Furat Al-Awsat Technical University, Iraq

Received on 10 May 2025; Accepted on 17 September 2025

Abstract

This study explored a practical approach to restoring degraded agricultural soils in Iraq›s arid regions by combining biofertilizers (Azotobacter chroococcum and Bacillus megaterium) with boron supplementation. Conducted over 120 days using a randomized complete block design with four treatments: control, biofertilizer alone, boron alone, and a biofertilizer-boron combination, the research aimed to improve soil health and provide tangible benefits for farmers facing infertile, desertified lands. Results showed that the combined treatment improved soil properties, reducing pH from 8.40 ± 0.05 to 8.20 ± 0.06 and electrical conductivity (EC) from 3.10 ± 0.08 to 2.80 ± 0.09 dS m^{-1} ($P < 0.05$), while increasing organic carbon from 0.30 ± 0.02% to 0.50 ± 0.04%, nitrogen (N) from 33 ± 2.0 to 58 ± 3.0 mg/kg, phosphorus (P) from 5.0 ± 0.3 to 11.0 ± 0.6 mg/kg, potassium (K) from 82 ± 3.5 to 90 ± 4.5 mg/kg, and boron (B) from 0.20 ± 0.02 to 1.10 ± 0.06 mg/kg (all mean ± SE, $n = 3$, $P < 0.05$). Using biofertilizers together with boron-enhanced soil fertility more effectively than either treatment alone. This approach offers farmers a low-cost, environmentally friendly method to improve crop growth and restore soil health. The observed improvements over 120 days demonstrate that even short-term interventions can support agricultural productivity, enhance soil quality, and help communities adapt to desertification. Long-term monitoring is recommended to confirm the sustainability of these benefits.

Keywords: *Soil Chemical Properties, Biofertilizers, Boron, Sustainable Agriculture, Desertified Soils, Nutrient Dynamics.*

1. Introduction

Desertification is a major environmental issue, characterized by the deterioration of dryland ecosystems due to human activities and climate fluctuations. According to the United Nations Convention to Combat Desertification (UNCCD, 2020), more than one-third of the Earth›s land area is affected by desertification, threatening the livelihoods of over a billion people living in these regions. Soils in these areas suffer from low organic matter, nutrient deficiencies, increased salinity, and unstable pH levels. These conditions not only reduce agricultural productivity but also impair essential soil functions, such as nutrient cycling and water retention, thereby complicating efforts to sustainable land management (Lal, 2015; Smith et al., 2019).

The use of chemical fertilizers to improve soil fertility in degraded lands raises sustainability concerns due to environmental impacts, including groundwater pollution, soil acidification, and long-term degradation (Johnson, 2021). Excessive fertilizer use also decreases soil biodiversity and overall soil health, highlighting the need for more sustainable alternatives (Tilman et al., 2022).

Among these alternatives, biofertilizers containing beneficial microorganisms—such as nitrogen-fixing bacteria and phosphate-solubilizing fungi—can enhance soil fertility and support plant growth. These biofertilizers improve nutrient availability and strengthen interactions between plants and soil, helping to rehabilitate degraded soils (Nguema-Ona et al., 2021).

Boron is an essential micronutrient that plays a crucial role in plant functions, including cell wall formation, reproductive development, and crop productivity. Degraded soils often lack adequate boron due to leaching and reduced organic matter content, limiting the ‹ ‹soil›s capacity to retain this nutrient (Thompson, 2023). Recent studies suggest that combining biofertilizers with essential nutrients such as boron can produce synergistic effects, improving both soil fertility and plant productivity in degraded environments (Vessey, 2003).

Although the individual benefits of biofertilizers are well established, their combined effects on degraded soils remain underexplored. Understanding the interactions between microbial activity and nutrient availability can provide practical solutions to improve both chemical and biological soil qualities (Barea et al., 2005).

This study aimed to evaluate the effectiveness of an integrated approach using biofertilizers and boron to improve soil chemical properties and functions in arid desert areas. It also sought to demonstrate how this approach can offer practical, eco-friendly solutions to restore degraded ecosystems, enhance agricultural productivity, and mitigate soil deterioration. The findings are expected to help local communities achieve more sustainable land management and contribute to global understanding of soil restoration under changing climatic conditions, supporting sustainable development goals.

* Corresponding author e-mail: mohammed.rahim@atu.edu.iq

2. Materials and Methods:

2.1 Study Site:

The field test was conducted in the desert region in southern Iraq, which has a dry climate, with an average annual rainfall of 150 mm and an average annual temperature of 25°C. Before starting the experiment, the soil samples were collected from random sites at a depth of 0-30 cm. Samples were air-dried under controlled conditions, crushed with a hammer, and passed through a 2 mm sieve to obtain homogeneous material. After that, Composite samples were then prepared for the analysis of soil chemical, physical, and biological properties (Table 1).

Table 1. Some Chemical and Physical Properties of the Studied Soil

Attributes		Values	Units of measurement
Soil pH (pH)		8.5	
Electrical conductivity (ECe)		3.2	dS m-1
Organic Carbon		0.3	%
Gypsum		1.5	
Lime		12	
Cation exchange capacity (CEC)		8	cmol kg-1
Available nitrogen		30.43	mg kg-1 soil
Available phosphorus		5.36	
Available potassium		80.32	
Available boron		0.22	
Exchangeable Calcium		1500	
Exchangeable Sodium		200	
Bulk density		1.6	g cm^{-3}
Porosity		40	%
Soil horizons	Sand	65	%
	Silt	25	
	Clay	10	
soil texture		Sandy Loam	

**The analyses were conducted at the laboratory of the Directorate of Agriculture in Karbala, Iraq.*

2.2 Biofertilizers:

A commercial biofertilizer containing Azotobacter chroococcum (AZ1), a nitrogen-fixing bacterium, and Bacillus megaterium (BM2), a phosphate-solubilizing bacterium, was used. Seeds of Pennisetum glaucum L. were coated with 20 g of biofertilizer per kilogram of seeds. The biofertilizer contained 1×10^8 CFU g^{-1} of Azotobacter chroococcum and 1×10^8 CFU g^{-1} of Bacillus megaterium to ensure sufficient microbial activity. Microbial strains were obtained from reputable culture collections to ensure their validity under experimental conditions. Colony-forming units (CFU g^{-1}) were standardized to ensure uniform application. Seed coating was chosen as the application method to enhance microbial colonization of roots, which is particularly effective in the arid environment of the study site.

2.3 Boron Application:

Boron was used in the form of boric acid (H3Bo3 contains 17% boron), with the rate of adding 2 kg per hectare. The rate corresponds to 0.34 kg elemental B ha^{-1}. Boric acid was dissolved in water and evenly applied to the soil surface. Application volume per plot was standardized, and no additional insecticides were used to avoid contamination. The soil was then lightly tilled to incorporate the mixture into the top 5 cm, ensuring uniform distribution. This percentage was determined by the initial experiments to ensure the availability of adequate boron in sandy loam soils while avoiding potential toxicity.

2.4 Experimental Design:

The experiment was conducted according to a Randomized Complete Block Design (RCBD), consisting of four treatments, each repeated three times. Each replicate represents an independent field plot (biological replicate) to account for spatial variability within the field. The treatments were: (1) control without biofertilizer or boron, (2) only biofertilizer, (3) boron only, and (4) a mixture of fertilizers and boron. The area of each piece was 4 m 2 (2 m x 2 m), and the adjacent pieces were separated by a barrier of 1 m to prevent mutual pollution. Each plot measured 2 × 2 m (4 m^2) and was separated by 1 m buffer zones to prevent cross-contamination. Pennisetum Glaucum L. Drip irrigation was used to simulate desert conditions while supporting plant growth. Soil moisture was maintained at 50% field capacity, monitored with a tensiometer. The experiment lasted for a 120-day growth season.

2.5 Soil Sampling:

Soil samples were collected from each plot at a depth of 0–15 cm on two occasions: prior to treatment application (baseline) and at the ‹ ‹experiment›s conclusion (120 days post-sowing). Five soil cores were randomly sampled per plot, then combined into a composite sample. These samples were air-dried, ground, and passed through a 2 mm sieve to prepare them for chemical analysis.

2.6 Soil Chemical Analysis:

Soil chemical properties were assessed using established laboratory protocols (Table 2). Soil pH and electrical conductivity (EC) were measured in a 1:2 soil-to-water suspension using a glass electrode pH meter and a conductivity meter, respectively, according to the methods by Jackson (1973). Organic carbon content was determined via the Walkley-Black chromic acid wet oxidation method (Walkley & Black, 1934). Available nitrogen was quantified using the alkaline permanganate distillation technique as outlined by Subbiah and Asija (1956). Available phosphorus was extracted with sodium bicarbonate and measured colorimetrically using the Olsen method (Olsen et al., 1954). Exchangeable potassium was extracted with 1 N ammonium acetate and analyzed by flame photometry, as described by Hanway and Heidel (1952). Available boron was extracted with hot water and determined colorimetrically using the azomethine-H method (Berger & Truog, 1944). All analyses were conducted in triplicate (n = 3) and reported as mean ± standard deviation (SD) to show replicate variability.

Table 2. Soil chemical properties after 120 days

Treatment	pH	EC (dS/m)	Organic C (%)	Available N\ (mg/kg)	Available P (mg/kg)	Available K (mg/kg)	Available B (mg/kg)
Control	8.40 ± 0.05	3.10 ± 0.08	0.30 ± 0.02	33 ± 2.0	5.0 ± 0.3	82 ± 3.5	0.20 ± 0.02
Biofertilizer	8.30 ± 0.06	2.90 ± 0.07	0.40 ± 0.03	48 ± 2.5	10.0 ± 0.5	84 ± 4.0	0.20 ± 0.02
Boron	8.40 ± 0.05	3.00 ± 0.08	0.30 ± 0.02	35 ± 1.8	6.0 ± 0.3	83 ± 3.2	1.00 ± 0.05
Biofertilizer + Boron	8.20 ± 0.06	2.80 ± 0.09	0.50 ± 0.04	58 ± 3.0	11.0 ± 0.6	90 ± 4.5	1.10 ± 0.06

**Note: Values represent mean ± standard deviation of three replicates (n=3).*

2.7 Statistical Analysis:

The obtained data were analyzed using one-way analysis of variance (ANOVA) with SPSS software (version 26.0). ANOVA assumptions were checked, and exact P-values were reported for significant effects. All results are expressed as mean ± standard deviation (SD). The SD values indicate the variability among replicates. Differences among treatments were evaluated by comparing mean values and their associated standard deviations.

3. Results and Discussion:

The summary in the accompanying schedule showed the effects of fertilizers and boron processors applied alone or in conmbination on the chemical properties of the soil in the region. All values are presented as mean ± standard deviation (SD) of three independent field replicates (n = 3) to show the variability among replicates

3.1 Soil pH

The soil has a pH of 8.5, indicating strong alkalinity, which is typical for desert soils in Iraq (Qadir and Azeez, 2020). In the control treatment, the pH slightly decreased to 8.40 ± 0.05, perhaps due to the accumulation of alkaline cations during irrigation (Richards, 1954). The ± SD values indicate variability among independent plots (biological replicates). The application of mineral fertilizers alone reduced the soil pH to 8.30 ± 0.06. The combined treatment of biofertilizers and boron fertilizers resulted in the greatest decrease, lowering the pH to 8.20 ± 0.06. This decrease may be related to the production of organic acids by Chroococcum and Bacillus Megaterium, which release H^+ ions during microbial metabolism (Marschner, 1995; Ajeel & Al-Hakeim, 2024; Ajeel et al., 2025). The decrease in pH during joint treatment might suggest an interventional reaction, which could be driven by boron. These results support previous studies showing that boron enhances microbial activity in alkaline soil (Tariq et al., 2017).

3.2 Electrical Conductivity (EC)

The primary conductivity of the 3.2 dS m^{-1} soil, which reflects a moderate salinity that corresponds to the conditions of the Iraqi desert (Abdulrahman, 2025). After treatment, the conductivity decreased slightly to 3.10 ± 0.08 dS m^{-1} in the control group, and to 2.90 ± 0.07 dS m^{-1} and 3.00 ± 0.08 dS m^{-1} with biomed fertilizers alone and boron alone, respectively. The joint treatment achieved the lowest electric conductivity of 2.80 ± 0.09 dS m^{-1}. The ± SD values indicate variability among independent plots (biological replicates).

These declines might suggest a potential improvement in salt filtration and soil structure, which could be related to increases in organic materials and microbial activity, thus possibly promoting water leakage (Nguema-Ona et al., 2021). Boron can reduce salt stress by stabilizing cell membranes, thereby improving the soil›s ability to resist salt accumulation (Shorrocks, 1997; Tariq et al., 2017). This is consistent with evidence that integrated nutrient strategies enhance soil physical properties in salt environments (Six et al., 2006).

3.3 Organic Carbon

Organic carbon levels remain fixed at 0.30 ± 0.02% in the control and boron treatments alone, indicating a slight contribution to soil organic matter (SOM). In comparison, biofertilizer alone increased organic carbon to 0.40 ± 0.03%, whereas the joint treatment increased it to 0.50 ± 0.04%. This improvement may be due to the use of biofertilizers that stimulate increased microbial mass and root secretions (the main components of SOM) (Lal, 2009). The superior results of the common treatment might reflect the combined growth of plants and root biomass with biotechnology and boron, which could increase carbon inputs (Smith et al., 2019; Ajeel & Al-Hakeim, 2024; Ajeel et al., 2025). These results suggest that integrated nutrient management likely contributes to increased organic materials in deteriorating soil (Six et al., 2006).

3.4 Available Nitrogen (N)

The nitrogen available modestly increased from 30 mg kg^{-1} to 33 ± 2.0 mg kg^{-1} in the control group, which may reflect natural variation. The application of fertilizers increased available nitrogen to 48 ± 2.5 mg kg^{-1}, possibly due to nitrogen fixation by Chroococcum (Mahdi et al., 2010). The common treatment also increased it to 58 ± 3.0 mg kg^{-1}, suggesting that boron may promote plant growth and root nodulation, thereby enhancing nitrogen fixation efficiency (Blevins & Lukaszewski, 1998; Thompson, 2023). This result is consistent with studies showing that boron may improve nitrogen absorption in alkaline soil (Tariq et al., 2017).

3.5 Available Phosphorus (P)

Available phosphorus in the control group remained unchanged at 5.0 ± 0.3 mg kg^{-1}, while boron alone increased it slightly to 6.0 ± 0.3 mg kg^{-1}. The application of biofertilizers increased phosphorus availability to 10.0 ± 0.5 mg kg^{-1}, and the joint treatment reached the highest level at 11.0 ± 0.6 mg kg^{-1}. This increase may be associated with phosphate solubilization by Bacillus megatherium, converting insoluble phosphate into a plant-available form (Adesemoye & Kloepper, 2009). The improvement in joint treatment might result from boron-stimulated root growth, thereby expanding the soil volume available for phosphorus

absorption (Marschner, 1995; Tariq et al., 2017). These results highlight the potential of synergistic interactions between microorganisms and micronutrients to improve phosphorus availability.

3.6 Available Potassium (K)

Potassium gradually increased from the initial dose of 80 mg kg^{-1} to 82 ± 3.5 mg kg^{-1} in the control group, 84 ± 4.0 mg kg^{-1} in biotechnology alone, 83 ± 3.2 mg kg^{-1} in boron alone, and 90 ± 4.5 mg kg^{-1} in the joint treatment. Although biofertilizers do not directly solubilize potassium, improving soil structure and microbial activity can enhance nutrient cycling and reduce extraction losses (Nguema-Ona et al., 2021). The increase in joint treatment might reflect improvements in root distribution and nutrient absorption efficiency, as suggested by similar studies (Lal, 2009; Smith et al., 2019).

3.7 Available Boron (B)

Available boron in the control group was 0.20 ± 0.02 mg kg^{-1} and was similar to that with biofertilizer alone (0.20 ± 0.02 mg kg^{-1}). Boron alone increased availability to 1.00 ± 0.05 mg kg^{-1}, while the combined treatment increased it to 1.10 ± 0.06 mg kg^{-1}. Direct boron supplements (supposed to be 2 kg B ha^{-1}) may help correct boron deficiency and bring levels within the optimal range for plant growth (0.5–2.0 mg kg^{-1}) (Gupta, 1993). The measured values are above the critical deficiency threshold (~0.5 mg kg^{-1}) and well below the toxicity level (~5 mg kg^{-1}), suggesting safe and agronomically effective supplementation (Brdar-Jokanović, 2020). The slight increase in joint treatment might be related to increased boron retention due to higher organic matter content (Thompson, 2023; Tariq et al., 2017), reflecting complementary effects of organic and inorganic amendments.

4. Conclusion:

This study demonstrates that combining microbial fertilizers with boron supplements provides an effective and sustainable strategy for rehabilitating chemically degraded soils in arid environments. This integrated approach significantly improves key soil properties, including stabilizing pH, reducing salinity, increasing organic carbon, and enhancing the availability of nitrogen, phosphorus, potassium, and boron. By simultaneously addressing nutrient imbalances and microbial activity, this dual treatment strengthens efforts to restore soil health while minimizing environmental harm.

The novelty of this approach lies in its combination of biological interventions with essential micronutrients, which reactivates nutrient cycles and enhances soil resilience against alkalinity-induced deterioration. These findings offer practical guidance for expanding environmentally friendly land management strategies and contribute directly to achieving global sustainable development goals, particularly SDG 15.3, which focuses on combating land degradation. By linking agricultural productivity with environmental sustainability, this research supports climate-resilient solutions for drylands at risk.

Statements and Declarations:

The author confirms no conflict of interest. This study was conducted independently, and all findings are based solely on experimental results. No financial, personal, or professional relationships exist that could influence the research, ensuring its integrity and objectivity.

Acknowledgments

The researcher wishes to express heartfelt gratitude to the Department of Soil and Water Techniques, Al-Musayyab Technical College, Al-Furat Al-Awsat Technical University, Iraq, for constant support. Deep appreciation is also extended to Assistant Lecturer Mohammed Rahim Ajeel, for his generous guidance and encouragement throughout the research journey.

References

Abdulrahman, S. A. (2025). ‹ ‹Iraq›s desertification: The complication of environmental security issues. Natural Built Social Environment Health, 1(1), 83–103. https://doi.org/10.63095/NBSEH.25.720252

Adesemoye, A. O., & Kloepper, J. W. (2009). Plant–microbe interactions in enhanced fertilizer-use efficiency. Applied Microbiology and Biotechnology, 85(1), 1–12. https://doi.org/10.1007/s00253-009-2196-0

Ajeel, M. R., & Al-Hakeim, M. S. (2024). The influence of biological and organic fertilization and boron spraying on some soil characteristics. IOP Conference Series: Earth and Environmental Science, 1371, 082022. https://doi.org/10.1088/1755-1315/1371/8/082022

Ajeel, M. R., Hamid, M. M. H., & Al-Shahbani, I. R. (2025). The impact of biofertilizers, organic fertilizers, and foliar application of boron on yield characteristics of maize (Zea mays L.). Basrah Journal of Agricultural Sciences, 38(1), 312–323. https://doi.org/10.37077/25200860.2024.38.1.24

Barea, J. M., Pozo, M. J., Azcón, R., & Azcón-Aguilar, C. (2005). Microbial cooperation in the rhizosphere. Journal of Experimental Botany, 56(417), 1761–1778. https://doi.org/10.1093/jxb/eri197

Berger, K. C., & Truog, E. (1944). Boron tests and determination for soils and plants. Soil Science, 57(1), 25–36. https://doi.org/10.1097/00010694-194401000-00003

Blevins, D. G., & Lukaszewski, K. M. (1998). Boron in plant structure and function. Annual Review of Plant Physiology and Plant Molecular Biology, 49, 481–500. https://doi.org/10.1146/annurev.arplant.49.1.481

Brdar-Jokanović, M. (2020). Boron toxicity and deficiency in agricultural plants. International Journal of Molecular Sciences, 21(4), Article 1424. https://doi.org/10.3390/ijms21041424

Gupta, U. C. (1993). Boron and its role in crop production. CRC Press.

Hanway, J. J., & Heidel, H. (1952). Soil analysis methods as used in the Iowa State College Soil Testing Laboratory. Iowa State College.

Jackson, M. L. (1973). Soil chemical analysis. Prentice Hall of India.

Johnson, K., & Lee, S. (2021). Environmental impacts of chemical fertilizers in dryland agriculture: A review. Environmental Management, 67(4), 789–802. https://doi.org/10.1007/s00267-021-01452-7

Lal, R. (2009). Soils and sustainable agriculture: A review. Agronomy for Sustainable Development, 29(1), 57–64.

Lal, R. (2015). Restoring soil quality to mitigate soil degradation. Sustainability, 7(5), 5875–5895. https://doi.org/10.3390/su7055875

Mahdi, S. S., Hassan, G. I., Samoon, S. A., Rather, H. A., Dar, S. A., & Zehra, B. (2010). Bio-fertilizers in organic agriculture. Journal of Phytology, 2(10), 42–54.

Marschner, H. (1995). Mineral nutrition of higher plants (2nd ed.). Academic Press.

Nguema-Ona, E., Vicré-Gibouin, M., Cannesan, M. A., & Driouich, A. (2021). Biofertilizers in arid and semi-arid ecosystems: Improving soil fertility and crop productivity. Agronomy, 11(9), Article 1784. https://doi.org/10.3390/agronomy11091784

Olsen, S. R., Cole, C. V., Watanabe, F. S., & Dean, L. A. (1954). Estimation of available phosphorus in soils by extraction with sodium bicarbonate. USDA Circular, 939, 1–19.

Qadir, M. H. S. F., & Azeez, D. R. (2020). Assessment and mapping of desertification using soil quality indicators for some parts of Iraq. Iraqi Journal of Agricultural Sciences, 51(5), 1290–1299. https://doi.org/10.36103/ijas.v51i5.1136

Richards, L. A. (1954). Diagnosis and improvement of saline and alkali soils (USDA Handbook No. 60). U.S. Government Printing Office.

Shorrocks, V. M. (1997). The occurrence and correction of boron deficiency. Plant and Soil, 193(1–2), 121–148. https://doi.org/10.1023/A:1004216126069

Six, J., Conant, R. T., Paul, E. A., & Paustian, K. (2002). Soil organic matter, biota and aggregation in temperate and tropical soils: Effects of no-tillage. Agronomie, 22(7–8), 755–775. https://doi.org/10.1051/agro:2002043

Smith, P., House, J. I., Bustamante, M., Sobocká, J., Harper, R., Pan, G., West, P. C., Clark, J. M., Adhya, T., Rumpel, C., Paustian, K., Kuikman, P., Cotrufo, M. F., Elliott, J. A., McDowell, R., Griffiths, R. I., Asakawa, S., Bondeau, A., Jain, A. K., … Pugh, T. A. M. (2019). Global change pressures on soils from land use and management. Global Change Biology, 25(3), 1008–1028. https://doi.org/10.1111/gcb.14502

Subbiah, B. V., & Asija, G. L. (1956). A rapid procedure for the estimation of available nitrogen in soils. Current Science, 25, 259–260.

Tariq, M., Mottaleb, S. A., & Rashid, A. (2017). Boron application mitigates salinity stress in wheat by improving plant growth and ionic homeostasis. Journal of Plant Nutrition, 40(15), 2135–2145. https://doi.org/10.1080/01904167.2017.1346672

Thompson, J. (2023). Boron deficiency in dryland soils: Causes and remediation strategies. Soil Science Society of America Journal, 87(1), 45–56. https://doi.org/10.1002/saj2.20456

Tilman, D., Cassman, K. G., Matson, P. A., Naylor, R., & Polasky, S. (2002). Agricultural sustainability and intensive production practices. Nature, 418(6898), 671–677. https://doi.org/10.1038/nature01014

United Nations Convention to Combat Desertification. (2020). The global land outlook. UNCCD Secretariat.

Vessey, J. K. (2003). Plant growth-promoting rhizobacteria as biofertilizers. Plant and Soil, 255(2), 571–586. https://doi.org/10.1023/A:1026037216893

Walkley, A., & Black, I. A. (1934). An examination of the Degtjareff method for determining soil organic matter, and a proposed modification of the chromic acid titration method. Soil Science, 37(1), 29–38. https://doi.org/10.1097/00010694-193401000-00003

JJEES

JJEES (2026) 17 (1): 111-117
ISSN 1995-6681

Jordan Journal of Earth and Environmental Sciences

Estimation of Channel Oscillation Pattern of Lower Kopili River Using Geospacial Technology, Assam, India

Shanku Ghosh[1], C Prakasam[1*]

1Department of Geography, School of Earth Sciences, Assam University Diphu Campus, (A Central University), Diphu, Karbi Anglong, Assam 782462, India

Received on 29 November 2024; Accepted on 25 September 2025

Abstract

This study attempts to study the course change or channel migration of the Lower Kopili River (LKR) between 1980 and 2020. Spatially, the study is mostly focused on the Nagaon district section, where the river is experiencing the highest shifting compared to other parts. The planform, surrounding land use land cover, and channel sinuosity have been measured, and their temporal variation has also been studied. Satellite data from Landsat MSS, TM, and LISS III have been used to generate LULC maps and to extract channel planform for different decades. Channel central lines for all planforms were drawn in GIS, and the channel migration toolbox from the Department of Ecology, State of Washington, was used as the primary tool for measuring the decadal extent of channel migration. Following the channel central lines, cross sections were drawn at-500 meters intervals. To study the land use land cover maps (LULC) dynamics of the study area, five LULC maps were generated across all five decades (1980-2020). The results of the study show that the highest average migration has occurred at 99.16 meters per transect between 1980-1990, followed by 44.58 meters/transect between 1990-2000, and 94.51 and 63.25 meters per transect between 2000-2010 and 2010-2020, respectively. The section-wise sinuosity index reveals that between sections 4 and 7, the river follows a highly meandering path with an average sinuosity index of 2.08. It has been observed that the river frequently changes its flow path through channel avulsion, creating several oxbow lakes.

Keywords: *Channel shifting, Kopili River, LULC, river shifting, meandering.*

1. Introduction

Channel shifting, migration, and avulsion are defined as when the river changes its course or abandons the old one and starts flowing along a new course. This is a common characteristic of meandering streams, where the river flows along a meandering path, generates cut-offs and migrates in the floodplain (Brizga & Finlayson, 1990). Through this process of meandering and floodplain formation, the river channel migrates across its floodplain. Point bar deposition along the inner banks of meander loops increases sheer stress and accelerates erosion on the outer bank (Dietrich et al., 1979; Zhu et al., 2022). Continuous sedimentation on the point bar pushes the channel outward and causes it to migrate laterally across its floodplain (Dietrich & Whiting, 1989; Zhu et al., 2022). A river channel becomes straight or decreases local sinuosity by formingof cut-offs. Cut-offs are mainly of two types: neck cut-offs and chute cut-offs (Howard and Knutson, 1984). Cut-off formation results in the abandonment of the old meander loop, and the river starts to flow through a newly created straight path; simultaneously, the abandoned loop exists as an oxbow lake. In the process of channel avulsion Bank failure is an integral part. River hydraulic erosion develops cantilevered soil blocks through undercutting along the banks, which overhang without any basal support; during high-flow times (floods), increased shear stress and accelerated erosion cause these blocks to collapse (Debnath et al., 2023; Chakraborty and Saha, 2021). River discharge, flow velocity, bank lithology, stratigraphy, channel geometry, and human influence are important factors in river bank failure. Based on the degree, magnitude, intensity and frequency of flood occurrence there are changes in channel width due to bank scouring, sedimentation, etc. (Gupta and Fox, 1974). Stream gradient plays an important role in controlling velocity; a high stream gradient results in a higher flow velocity and increased erosivity. The presence of loose bank material, along with lateral, sequential erosion and deposition, Causes the River channel to shift across its floodplain and adjust its geometry (Debnath et al., 2017). River planforms exist in equilibrium with three fundamental components: energy, sediment supply, and vegetation. Any changes in these components result in channel planform morphological changes, in some cases shifting from one planform to another (Gurnell et al., 2009). Vegetation, sediment supply and river discharge are directly related to the land use land cover (LULC) of the river basin catchment areas as well as downstream channel planform riparian areas. River channels respond differently to watershed LULC change over space and time. Changes in upstream LULC have a direct impact on the downstream channel form and shape, depending on the time lag between upstream LULC change and the downstream channel›s response to it, because it might take a long time to transport coarse bed load to the downstream (Kondolf et al. 2002). The volume of discharge from the river is altered by changing LULC. According to Schilling et al., there has been an increase in Mississippi

* Corresponding author e-mail: cprakasam@gmail.com

River discharge from 1890-2003 due to agricultural activity-induced LULC change in the upper Mississippi River basin (Schilling et al., 2010). Watershed LULC is an important factor that influences watershed hydrology, rainfall, runoff, discharge, and sediment yield. LULC modification or decreased vegetation cover in the watershed influences river channel pattern, response, and results in channel avulsion, bank erosion, and channel migration in the downstream floodplain. This further modifies the channel planform and riparian vegetation (Thakur et al., 2012). Vegetation has significant control over the flow resistance, bank strength, bar formation, log-jam formation and concave bank bench deposition. Lateral stability and channel form of the river are significantly influenced by the root density and soil-binding properties of the bank/channel riparian vegetation (Hickin and Nanson, 1984). Most historical studies addressing the relationship between vegetation cover and channel response conclude that high vegetation cover in fluvial systems results in decreased channel width and form ratio (Turner, 1974; Hickin and Nanson, 1984). The control of bank/channel riparian vegetation on channel form can be seen in the study conducted by Nevins, 1969; where a highly braided pattern channel (Turdnganui River channel in New Zealand) was converted into a meandering pattern through the planned planting of willow shrubs at selected bends (Nevins, 1969). Another Study conducted by Hickin & Nanson on Western Canadian Rivers reveals that, compared to unvegetated alluvial exposed banks, river banks with high vegetation cover and root density offer high resistance to channel migration and lateral erosion (Hickin and Nanson, 1984). Anthropogenic influence in river floodplains is an important agent of river channel change. Human-induced changes in river channels are a longstanding practice, but scientific exploration of such impacts began after 1956 (Gregory, 2006). According to Kesel, to improve and maintain navigation, the lower Mississippi River was channelized and shortened by 245 km (1929-1942), which resulted in the chute cut-off of 15 meandering bands, and the river was additionally shortened by 88 km (between 1939 and 1955) (Kesel, 2003).

In the present era combined impact of climate change and anthropogenic activities making bank erosion and channel widening a mounting issue across the major river systems i.e. Ganga, Brahmaputra, Indus, Amu darya, Irrawaddy, Amazon, Yukon, Lower Mississippi, Middle-Lower Nizer, Lower Congo etc. the Ganga and Brahmaputra are the two major rivers In India, bank erosion in along the Ganga and Brahmaputra and their tributaries are persistent issue (Ghosh & Sahu, 2019; Ghosh, 2022; Ghosh & Sahu, 2023; Rahman et al., 2025; Mosselman, 2025; Bhuyan, et al, 2024) . The Kopili River, one of the major south bank tributaries of the Brahmaputra River follows a highly meandering flow path in the selected location downstream and changes its course over timewhich influences the riparian settlements and agricultural practice. So, it is important to closely examine the river channel-shifting pattern and its controlling factors. With bank erosion, flooding is another significant issue in the study area. Though the flood issue is addressed in some studies (Shivaprasad Sharma and Roy, 2018a; Shivaprasad Sharma and Roy, 2018b), the bank erosion remains untouched. The main objectives of the study are to analyze the channel planform riparian LULC pattern, meandering dynamics, and lateral erosion extent to demarcate LKR planform avulsion-vulnerable locations.

2. Study Area:

The Kopili River, after originating from the Barail range (1800 M.) near the Jayantia hills of Meghalaya flows for almost 300 Km across Assam, Meghalaya. ‹ ‹a major south bank tributary of the Brahmaputra River, which contributes approximately 1.47% of the Brahmaputra River›s discharge (Sharma et al., 2019). Major tributaries of the Kopili are Diyung, Jamuna, Borpani, and the Kolong River. The river basin has a total geographical area of 15921.72 Km², covering the Dima Hasao, West Karbi Anglong, Karbi Anglong, Nagaon, and Marigaon districts of Assam. The present study selects a 117.8 km section of the Lower Kopili River, which lies mostly under the Nagaon district (Figure 1). With a total 2287 km² geographical area and drained by 23 large and small rivers Nagaon is majorly dominated by agricultural activity and highest crop producing district of Assam, due to lack of agricultural infrastructure and irrigation facilities fellow agriculture also practiced here, where during the winter seasons croplands are kept as fellow land in some places of the district (Bhuyan & Deka, 2024). The district is located in the floodplain of the Brahmaputra and Kopili River. Kopili is the largest river flowing through the middle of the district. From a Lithological perspective, the district is composed of Quaternary fluvial sediment deposits (Geological Resource Map, 1998) with a gentle gradient towards the Brahmaputra River.

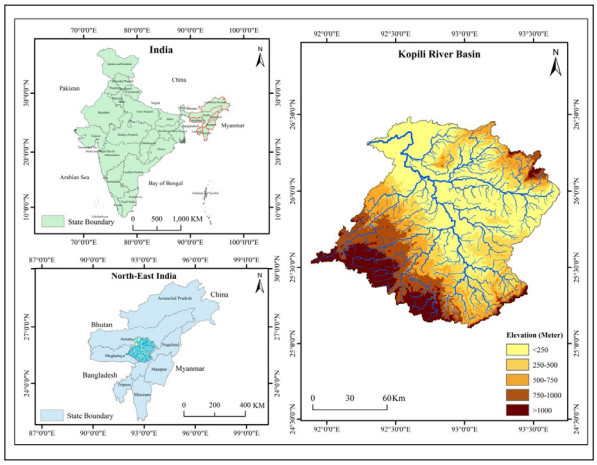

Figure 1. Study area map showing geographical location of the study area.

3. Methodology:

The tools, techniques, and database used in the study are in the methodological flowchart (Figure 2). Different temporal satellite images (Table 1) were collected and preprocessed (layer stacking, noise removal, and haze reduction) for analysis. The four-kilometer buffer area was created on both sides of the channel thalweg along the 117.8 km stretch of the river. Further, the study area was extracted from the satellite images using a buffer. Satellite images were resampled to address differences in spatial resolution. In the next stage, five LULC maps were generated from

the resampled images using the Maximum Likelihood supervised classification method. Following the major land use and land cover types, the entire area was classified into six classes (dense vegetation, sparse vegetation, agricultural land, water body, built-up area, and sand bar). The river channel planform shapes were extracted from satellite images for overlay analysis and to study spatiotemporal variation over the five decades. To study the channel planform dynamics the sinuosity index was used. Here, the river study area was divided into nine sections, and the Sinuosity index was calculated for each section. The primary objective of the study is to estimate channel migration and its spatial-temporal variation. The rate of channel shifting was calculated for each successive decade (1980-1990, 1990-2000, 2000-2010, and 2010-2020). The entire reach was divided into cross-sections at 500-meter intervals. The decadal rate and direction (eft bank & right bank) were further plotted in a graph.

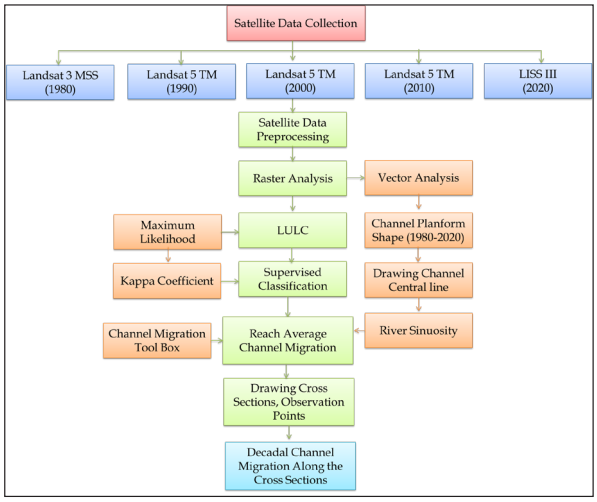

Figure 2. Methodological flowchart showing the tools, techniques, and database used in the study.

Table 1. Description of the collected satellite images.

SL. No.	Satellite	Sensor	Spatial Resolution	Date of Acquisition	Path and Row
1	Landsat-3	MSS	60M.	01-02-1980	146/042
2	Landsat-5	TM	30M.	08-05-1990	136/042
3	Landsat-5	TM	30M.	27-12-1999	136/042
4	Landsat-5	TM	30M.	10-11-2011	136/042
5	Resourcesat-I	LISS-III	24M.	10-10-2018	111/053

4. Results:

4.1. Land Use Land Cover (LULC):

As defined by the Food and Agricultural Organization (FAO), land cover is the physical feature of the Earth›s surface, and the addition of economic activity and modification of land cover is known as land use. In the present study, channel riparian LULC dynamics (1980-2020) have been analyzed to examine channel migration in the Lower Kopili River. Five LULC maps were prepared for each decade (1980 to 2020). The study area comprises six major LULC types (Figure 3), namely dense vegetation, sparse vegetation or bushes, agricultural land, built-up area, sandbar (channel bars), and water body (pond, lake, river, wetlands). The results of the LULC analysis (table 2) show that throughout the study period (1980-2020), agricultural land occupied the highest proportion (>30%) of the study area. Here, the agricultural land represents both the recent crop lands and current fallow lands. In 1980, agricultural land constituted 40.42›% of the study area among all the decades. In 2010, agricultural land constituted the highest proportion (56.20%), adding an additional 10%. Both the dense and sparse canal riparian vegetation have shown negative growth of 12.54% and 54%, respectively. The dense vegetation covered 56.53 km² in 1980, which reduced to 49.44 km² in 2020; the same trend was observed for sparse vegetation, which reduced from 277.86 km² in 1980 to 127.81 km² in 2020. Water bodies (natural and artificial) and built-up areas (rural and urban) have seen the highest positive growth of 141.48 and 324.37 percent respectively. The area occupied by the water body has grown from 42.7 km² to 103.11 km². Built-up area has seen the highest increase from 52.97 km² to 224.79 km² over the five decades, mainly due to the expansion of areas occupied by sparse and dense vegetation. Sandbar represents channel-bar deposition (mid-channel, point, lateral) and bank-surface sand splay due to sedimentation. This area constitutes approximately 5% of the total study area (1980-2020).

Table 2. Decadal area distribution of each LULC class and their growth rate.

	Area (Km²)				
LULC Type	1980	1990	2000	2010	2020
Sand Bar	2.42	5.62	2.57	12.45	2.87
Dense Vegetation	56.53	105.08	113.08	62.33	49.44
Sparse Vegetation	277.86	222.88	178.97	101.52	127.81
Water body	42.7	88.52	96.97	40.77	103.11
Agricultural Land	293.42	233.9	243.65	407.99	217.88
Built Up Area	52.97	69.9	90.66	100.84	224.79
Total Area	725.9	725.9	725.9	725.9	725.9

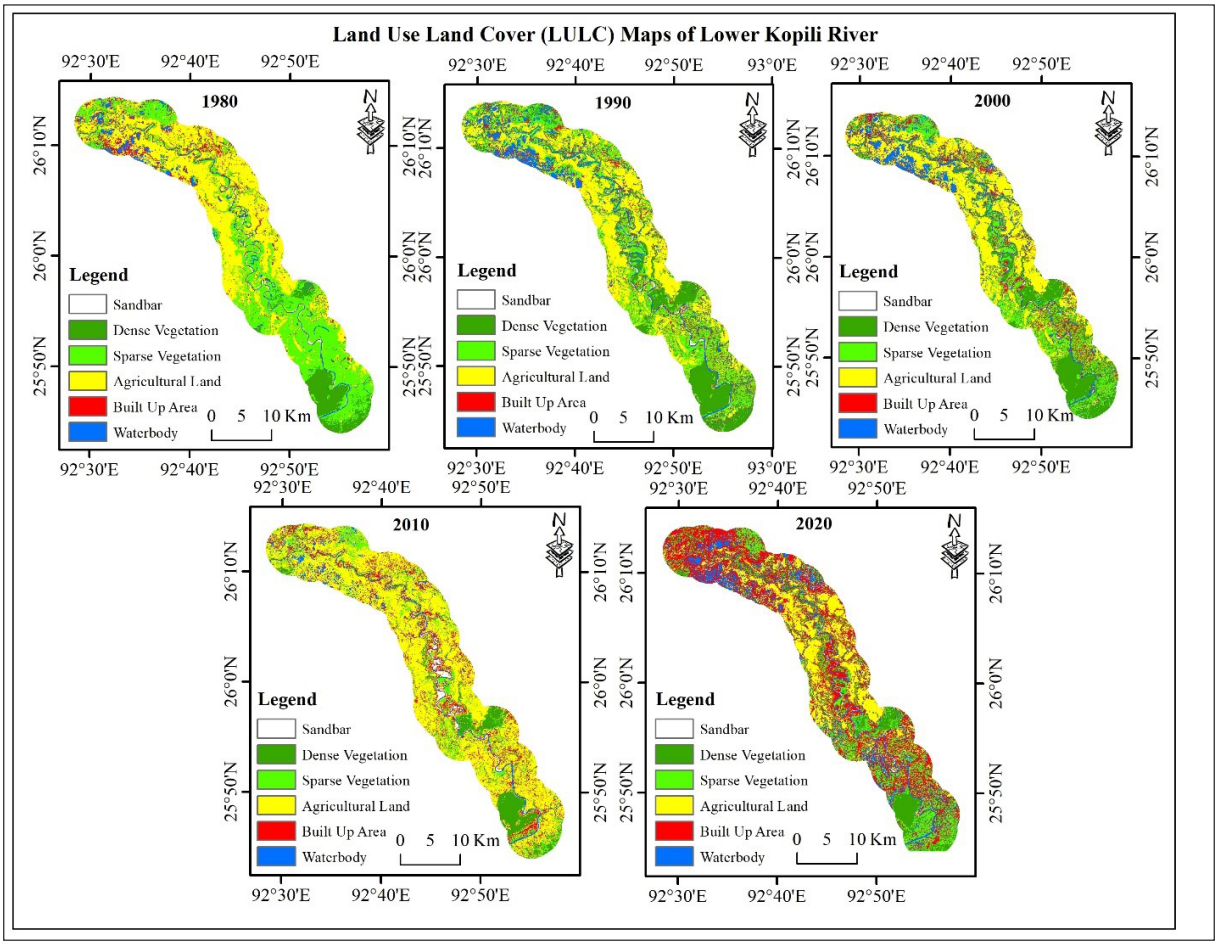

Figure 3. LULC maps, showing decadal LULC dynamics in the study area.

4.2. Channel Meandering:

The sinuosity index (SI) is a measure of how much river channels deviate from a straight line path; ‹ ‹it›s an important parameter of measuring river channel stability, while a high sinuosity value indicates a meandering channel, a tendency of more channel widening through bank erosion and course change. Since the present study concerns channel sifting of the LKR, the sinuosity index was considered an important parameter for analysis. The total stretch of the river has been classified into nine sections to identify areas with dynamic meandering adjustment and migration. As mentioned in Table 3 & Figure 4, the LKR sinuosity index varies from the lowest 1.29 to the highest 3.19, while the river carries an overall SI of 1.78, which confirms a high channel meandering nature. Among the nine created sections, significant spatio-temporal variation has been noticed. sections 4, 5, and 6 demarcate the zone of high sinuosity and dynamic channel adjustments. The channel flows with an average SI of 2.16 through this zone, and across the remaining section, the channel contains a relatively lower SI of 1.58. Section 6 has the highest sinuosity index of 2.56, followed by section 4 with 2.05 sinuosity index and section 5 (1.88). A lower SI value along the channel stretch of sections 1, 2, 3, 7, 8, and 9 indicates channel stability and less dynamic sifting, and vice versa.

Table 3. Section-wise decadal sinuosity index of Lower Kopili River.

Section	1980	1990	2000	2010	2020	Sum
1	1.8	1.79	1.8	1.76	1.76	1.78
2	1.38	1.31	1.31	1.29	1.3	1.32
3	1.66	1.65	1.67	1.64	1.64	1.65
4	2.18	2.06	2.03	2.02	1.97	2.05
5	1.81	1.85	1.94	1.76	2.05	1.88
6	2.21	2.38	2.51	3.19	2.55	2.57
7	2.05	1.85	1.9	1.78	1.52	1.82
8	1.44	1.45	1.51	1.3	1.58	1.46
9	1.52	1.49	1.48	1.49	1.52	1.50
Sum	1.78	1.76	1.79	1.80	1.77	1.78

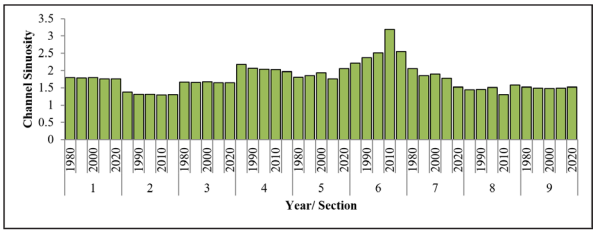

Figure 4. Bar diagram showing the section wise sinuosity index graph.

4.3. Channel Migration & Channel Avulsion:

As mentioned in the methodology, to estimate the extent of channel migration, multiple cross-sections were drawn along the valley central line with 500 meters spacing. Following the extent of the meander loops, the length of the cross-sections was kept at 5000 meters. To measure the extent and direction of channel migration for all five decades (1980-1990, 1990-2000, 2000-2010 & 2010-2020), channel planforms were extracted from satellite images (Table 1), and the valley central line was drawn using the planform shapefile. Specifically, the channel migration extent was measured in both the left- and right-bank directions, as shown in the graph (figure 5). Between 1980 and 1990, the highest right-bank migration was observed at 989 meters along the 132nd cross section and 834 meters along the 120th cross section towards the left bank. Between 1990 to 2020, the channel migrated 470.15 meters along the 69th cross section towards the right bank and 353 meters along the 132nd cross section towards the left bank. Between 2000-2010, the channel migrated 1077.26 meters (121st cross section) towards the left bank and 598 meters (102nd cross section) along the right bank, and between 2010-2020, 715.31 meters migrated following the 102nd cross section and 308.99 meters migrated along the 76th cross section towards the right and left bank respectively. The overall highest average migration of 99.16 meters was observed between 1980 and 1990, followed by 94.51 meters between 2000 and 2010, 63.26 meters/transect between 2010 and 2020, and the lowest of 44.58 meters/transect between 1990 and 2000. As per the direction (left and right) of channel migration, over all decades, nearly the same number of transects have seen migration on both sides of the valley central line. The graph (Figure 6) representing overall channel migration (1980-2020) indicates that, along the studied reach, the highest channel migration has occurred between the 65th and 70th cross sections and the 100th to 140th cross sections; these zones are highly vulnerable to channel migration.

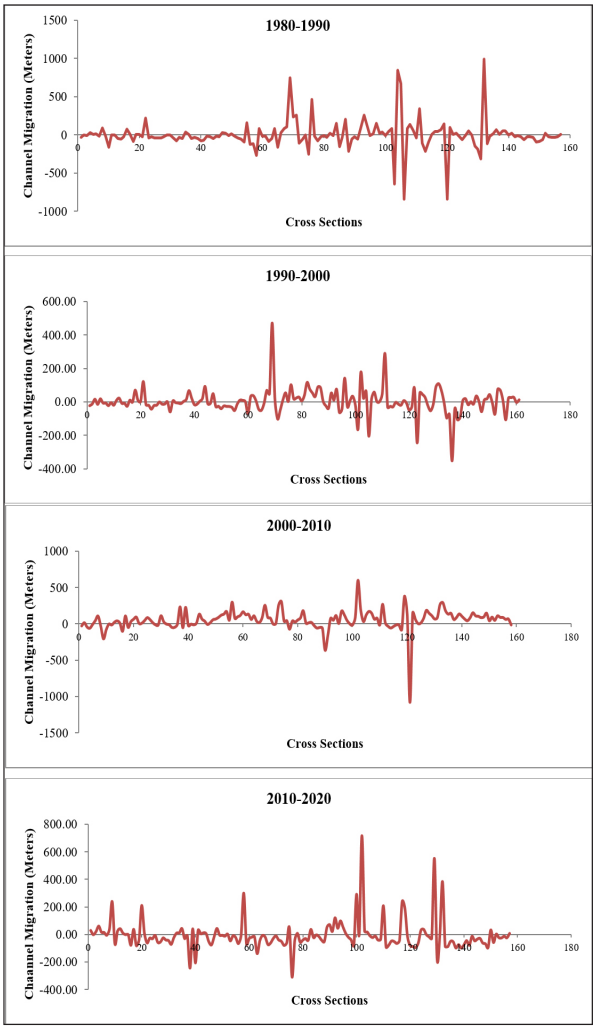

Figure 5. Channel migration graph showing the extent of channel migration

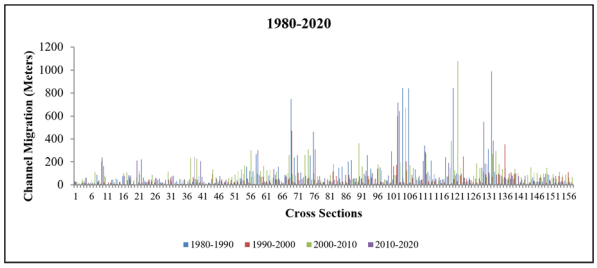

Figure 6. Combined channel migration graph (1980-2020).

5. Discussion:

The above discussion focuses on the derived results, including the analyses of channel riparian land use and land cover (LULC) patterns and their dynamic changes, channel sinuosity, and measurements of channel migration and avulsion. The LULC analysis is focused on the created buffer area (4 km) on both sides of the channel›s central line. The Kopili River channel and surrounding area are covered by agricultural land, which occupies the highest proportion of the area. Both dense forests and sparse vegetation areas have seen significant decreases over the decades. Riparian vegetation cover is a crucial factor in maintaining channel stability, which increases the strength of bank materials, and deforestation reduces root density and canopy cover, promotes greater runoff generation, elevates sediment supply, and increases infiltration loss (Yu et al., 2015; Loch, 2000). As discussed earlier, the second-highest average channel migration occurred between 2000 and 2010, at 94.51 meters per transect. Notably, this period also witnessed the greatest reduction in both dense and sparse vegetation cover, as shown in Table 2. In the following decade (2010–2020), the average migration rate declined to 63.26 meters per transect, while the area covered by sparse vegetation increased, as indicated in the table.

The section-wise channel sinuosity index indicates significant variation in channel sinuosity across specific segments—particularly sections 4, 5, 6, and 7—where the river exhibits extreme meandering patterns (sinuosity > 1.8). In these areas, the channel continuously adjusts its flow path, and a notable meander cutoff occurred between 1990 and 2000 at coordinates 25°55›13»N, 92°50›41»E (Figure 7). The channel migration graph (Figure 6) shows that lateral migration is not uniform across the study area. There is considerable variation in the extent of migration. Certain cross sections—specifically the 65th, 70th, and 100th to 140th—experience high decadal migration, while others show low to very low migration rates. It has been observed that cross sections experiencing high accretion are located within zones of elevated channel sinuosity. This result suggests a direct relationship between the sinuosity index and channel migration. Overall, the analysis of channel meandering and migration indicates that localized channel migration has been occurring consistently throughout the study period in the Lower Kopili River.

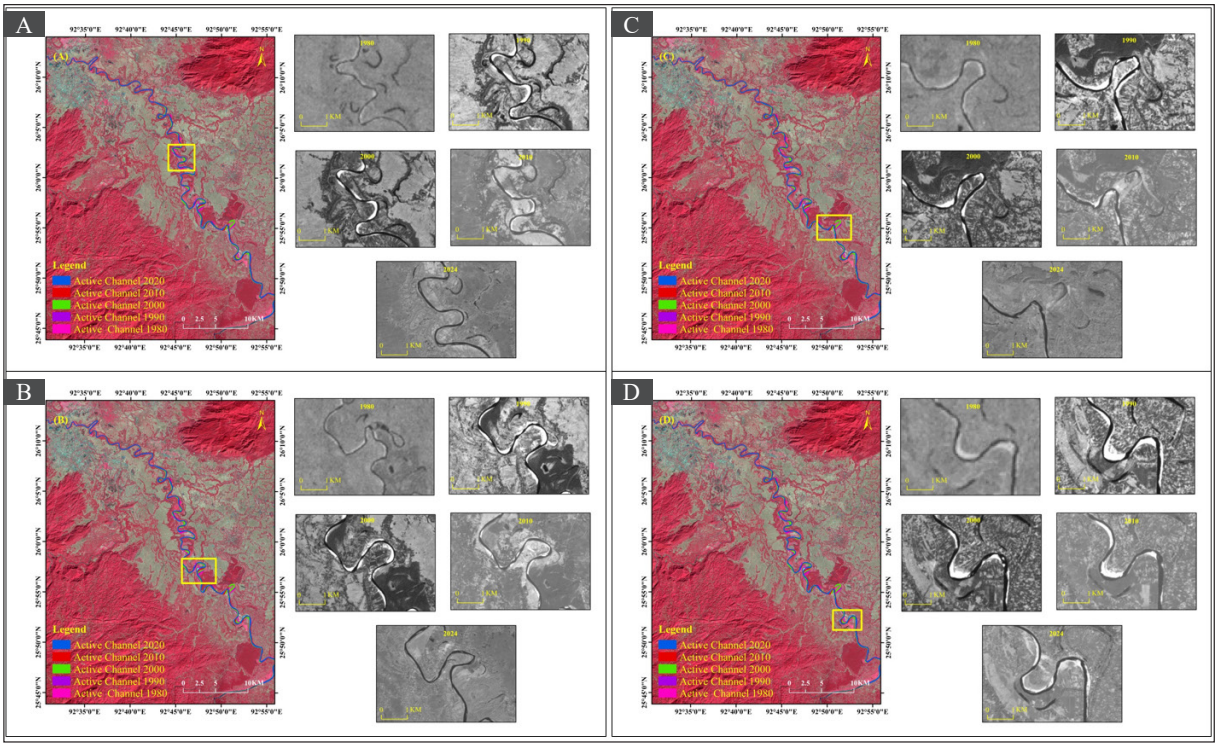

Figure 7. (A), (B), (C), (D): channel migration/avulsion vulnerable zones.

6. Conclusion:

The present study investigates channel shifting in the Lower Kopili River. It includes an analysis of Land Use and Land Cover (LULC), channel sinuosity, and decadal-scale channel migration. The findings reveal that channel shifting is occurring in specific locations that are significantly more vulnerable than other areas along the river. In these zones, the river continuously adjusts its meandering loops, and several oxbow lakes have formed over time. Riparian LULC analysis indicates a rapid decline in vegetation cover surrounding the channel, which has been replaced by settlements, agricultural land, and water bodies. This shift in channel planform has direct implications for land use and the livelihoods of riparian communities. These vulnerable areas require targeted attention and mitigation strategies to address the ongoing channel migration. The current study is based entirely on satellite imagery; however, future research should incorporate field-based investigations, including assessments of soil characteristics, lithology, and geological conditions, to gain deeper insights into the dynamics of channel shifting in these regions.

Acknowledgement:

The authors sincerely express their gratitude to the University Grant Commission (UGC), New Delhi, for providing the UGC-JRF fellowship during the research period.

References

Bhuyan, M. J., and Deka, N. (2024). Delineation of groundwater potential zones at micro-spatial units of Nagaon district in Assam, India, using GIS-based MCDA and AHP techniques. Environmental Science and Pollution Research 31: 54107-54128.

Bhyan, N., Sajjad, H., Rahaman, M. H., & Ahmed, R. (2025). Riverbank erosion-induced vulnerability in India: A review and future research framework. Natural Hazards, 121(1), 1–30.

Brizga, S. O., & Finlayson, B. L. (1990). Channel avulsion and river metamorphosis: The case of the Thomson River, Victoria, Australia. Earth Surface Processes and Landforms, 15, 391–404.

Chakraborty, K., & Saha, S. (2022). Assessment of bank erosion and its impact on land use and land cover dynamics of the upper Mahananda River basin, Sub-Himalayan North Bengal, India.

SN Applied Sciences, 4, Article 1–17.

Debnath, J., Pan, N. D., Ahmed, I., & Bhowmik, M. (2017). Channel migration and its impact on land use/land cover using remote sensing and GIS: A study of the Khowai River, Tripura, Northeast India. The Egyptian Journal of Remote Sensing and Space Science, 20, 197–210.

Debnath, J., Sahariah, D., Lahon, D., Nath, N., Chand, K., Meraj, G., & Farooq, M. (2023). Assessing the impacts of current and future planform changes of the Brahmaputra River on land use–land cover. Geoscience Frontiers, 14, Article 101328.

Dietrich, W. E., & Whiting, P. (1989). Boundary shear stress and sediment transport in river meanders of sand and gravel. In River meandering (Vol. 12, pp. 1–50).

Dietrich, W. E., Smith, J. D., & Dunne, T. (1979). Flow and sediment transport in a sand-bedded meander. The Journal of Geology, 87, 305–315.

Ghosh, D. (2022). Identification of prime factors of active riverbank erosion in the lower course of the Ganga–Bhagirathi River. Bulletin of Geography: Physical Geography Series, (23), 71–83.

Ghosh, D., & Sahu, A. S. (2019). Bankline migration and its impact on land use and land cover change: A case study of the Jangipur Subdivision, Murshidabad District, West Bengal. Journal of the Indian Society of Remote Sensing, 47(12), 1969–1988.

Gregory, K. J. (2006). The human role in changing river channels. Geomorphology, 79, 172–191.

Gupta, A., & Fox, H. (1974). Effects of high-magnitude floods on channel form: A case study in the Maryland Piedmont. Water Resources Research, 10, 499–509.

Gurnell, A., Surian, N., & Zanoni, L. (2009). Multi-thread river channels: A perspective on changing European alpine river systems. Aquatic Sciences, 71, 253–265.

Hickin, E. J., & Nanson, G. C. (1984). Lateral migration rates of river bends. Journal of Hydraulic Engineering, 110, 1557–1567.

Howard, A. D., & Knutson, T. R. (1984). Sufficient conditions for river meandering: A simulation approach. Water Resources Research, 20, 1659–1667.

Kesel, R. H. (2003). Human modifications to the sediment regime of the lower Mississippi River floodplain. Geomorphology, 56, 325–334.

Kondolf, G. M., Piégay, H., & Landon, N. (2002). Channel response to increased and decreased bedload supply from land-use change: Contrasts between two catchments. Geomorphology, 45, 35–51.

Loch, R. J. (2000). Effects of vegetation cover on runoff and erosion under simulated rain and overland flow on a rehabilitated mine site, Queensland. Soil Research, 38(2), 299–312.

Mosselman, E. (2025). Sustainable stabilisation of the Brahmaputra–Jamuna River in India and Bangladesh. International Journal of River Basin Management, Advance online publication, 1–9.

Nevins, T. H. F. (1969). River training—The single-thread channel. New Zealand Engineering, 24, 367–373.

Rahman, M., Islam, R., Bushra, F., Hossain, I., & Sobnam, M. (2025). Brahmaputra riverbank morphodynamic changes: A multi-temporal geospatial assessment of erosion processes in northern Bangladesh. Progress in Disaster Science, Article 100452.

Schilling, K. E., Chan, K. S., Liu, H., & Zhang, Y. K. (2010). Quantifying the effect of land use and land cover change on increasing discharge in the Upper Mississippi River. Journal of Hydrology, 387, 343–345.

Sharma, S. V. S. P., Roy, P. S., & Chakravarthi, V. (2018a). Assessment of social vulnerability to flood hazards: A case study of the Kopili River Basin, Assam, India. The International Archives of the Photogrammetry, Remote Sensing and Spatial Information Sciences, 42, 455–460.

Sharma, S. V. S. P., Roy, P. S., Chakravarthi, V., & Srinivasa Rao, G. (2018b). Flood risk assessment using multi-criteria analysis: A case study of the Kopili River Basin, Assam, India. Geomatics, Natural Hazards and Risk, 9, 79–93.

Sharma, S. V. S. P. (2019). Flood risk assessment using multi-criteria analysis in a geospatial framework: A case study of the Kopili River Basin, Assam, India (Doctoral dissertation, University of Hyderabad).

Thakur, P. K., Laha, C., & Aggarwal, S. P. (2012). Riverbank erosion hazard study of the Ganga River upstream of the Farakka Barrage using remote sensing and GIS. Natural Hazards, 61, 967–987.

Yu, M., Zhang, L., Xu, X., Feger, K. H., Wang, Y., Liu, W., & Schwärzel, K. (2015). Impact of land-use change on soil hydraulic properties of Calcaric Regosols on the Loess Plateau, Northwest China. Journal of Plant Nutrition and Soil Science, 178(3), 486–498.

Zhu, L., Chen, D., Hassan, M. A., & Venditti, J. G. (2022). Influence of riparian vegetation on sinuosity and lateral stability of meandering channels. Geophysical Research Letters, 49, Article e2022GL098765.

JJEES

JJEES (2026) 17 (1): 118-129
ISSN 1995-6681

Jordan Journal of Earth and Environmental Sciences

Rock Typing, Diagenesis and Paleoenvironment of Middle Jurassic Tethys Ramp Carbonates, Sub-Himalayas, Pakistan

Syed Haroon Ali[1*], Abdur Rauf Nizami[2], Yasir Bashir[3], Noureen Shoukat[4], Numair Ahmed Siddiqui[4], Razzaq Abdul Manan[5], Muhammad Abid[6], Naveed Rehman[7], Shahid Ali[8]

[1]*Department of Earth Sciences, University of Sargodha, Punjab, Pakistan 40100.*
[2]*Institute of Geology, University of the Punjab, Lahore, Pakistan.*
[3]*Department of Geophysical Engineering, Faculty of Mines, İstanbul Technical University, 34469 İstanbul, Türkiye*
[4]*Department of Geosciences, Universiti Teknologi PETRONAS, 32610 Tronoh, Perak, Malaysia*
[5]*Centre of Excellence in Mineralogy, University of Balochistan, Quetta, Pakistan*
[6]*School of Earth Sciences and Engineering, Hohai University, Nanjing, China*
[7]*School of Earth Resources, China University of Geosciences, 430079 Lumo Road, Wuhan, P.R. China*
[8]*Institute of Geology, University of the Punjab, Lahore, Pakistan*

Received on 11 July 2025; Accepted on 25 September 2025

Abstract

The Samana Suk Formation is extensively exposed across the Sub-Himalayan region of Pakistan, notably within the Salt Range and the Trans-Indus Ranges, where Jurassic carbonates dominate the stratigraphy. Although localized studies have been conducted, a comprehensive understanding of the link between exposures in these two regions has remained elusive. This study identifies five primary lithologies: limestone (78%), marl/shale (10%), dolomite (9.5%), irregular quartz-bearing limestone (1.5%), and sandstone (1%). Limestones in the Salt Range exhibit a range of textures, including fine- to coarse-grained, nodular, skeletal, micritic, oolitic, and intraclastic varieties. Seven distinct microfacies have been classified: mudstone, dolo-mudstone, bioclastic peloidal wackestone, bioclastic intraclastic grainstone, sandy echinoderm packstone, ooidal peloidal bioclastic grainstone, and peloidal grainstone. Stratigraphic sections in the Trans-Indus Ranges reveal considerable variability in thickness, facies composition, dolomitization intensity, quartz content, and diagenetic features. X-ray diffraction and scanning electron microscopy analyses confirm a predominantly carbonate mineralogy with well-developed microporosity. Above this Jurassic carbonate platform, the upper Paleocene Hangu Formation records a shift to subaerial depositional conditions. These findings collectively highlight the Samana Suk Formation as a valuable archive of Middle Jurassic paleoenvironments and suggest its potential as a hydrocarbon reservoir and a source of raw materials for the cement and construction industries.

Keywords: *Sedimentology; Sequence; Paleogeography; Salt Range; Depositional Environment*

1. Introduction

Several studies conducted by reservoir modellers have recognized the application of conceptual geological models (Abd El Aal et al., 2023; Teles et al., 2023; Brandano et al., 2022). The recent conjectural shift began with the application of conventional field data for on-site documentation of depositional structures and facies geometries, combined with paleogeographic datasets that were previously difficult to obtain. The deposition of the Samana Suk Formation was influenced by paleogeography, regional tectonics, and fluctuations in sea level. The formation has been recognized for approximately a hundred years, with (Cotter 1933; Davies 1993; Gee 1947) the Samana Suk Formation previously referred to as the Kioto Limestone, the Samana Suk Limestone, and the Baroch Limestone, respectively. Samana Suk Formation. exhibits extensive basinal distribution, extending from the Salt Range to the Surghar and Marwat Ranges within the Upper Indus Basin (Shah 1977), as illustrated in Figure 1. This formation is present across various basins and ranges (Sajjad 2020; Saboor et al., 2022; Wadood et al., 2021); however, the connection between the sections in the Salt Range and those in the Trans-Indus Ranges remains unexplored. This entity is extensively distributed across various basins, including the Trans Indus, Kohat, Samana, Hazara, and Kala Chitta Ranges.

Significant events that occurred before and following the breakup of Pangea are described in Figure 1. During the Permo-Triassic period, Gondwanaland initiated rifting, leading to the formation of an Atlantic-type passive continental margin (Searle 1983). The beginning of rifting of the Indo-Australian plate during the Cretaceous period, originating from Madagascar and Africa. An examination of the Tethys Sea reveals its formation during the Paleocene, resulting from the collision of the Indian Plate with the Eurasian Plate as the latter moved in a counterclockwise direction. Consequently, various geological features are situated across their respective locations within the geological formations of Pakistan (Qadri et al., 2010; Mateen et al., 2022; Ali et al., 2022a; Ali et al., 2022b; Naseem et al., 2023). The formation is exposed in the Trans Indus, Western Salt, Kohat, Kala Chitta, and Hazara ranges. The thickness of the

* Corresponding author e-mail: haroon.ali@uos.edu.pk

Samana Suk Formation varies based on the paleogeographic location of the lithostratigraphic section (Ghazi et al., 2015; Ghazi et al., 2020; Ahmed et al., 2020; Ali et al., 2021; Wahid et al., 2022), which dated back to the Middle Callovian (Ali et al., 2021; Figure 2). The fauna indicates that the formation dates back to the Middle Jurassic period (Wahid et al., 2022).

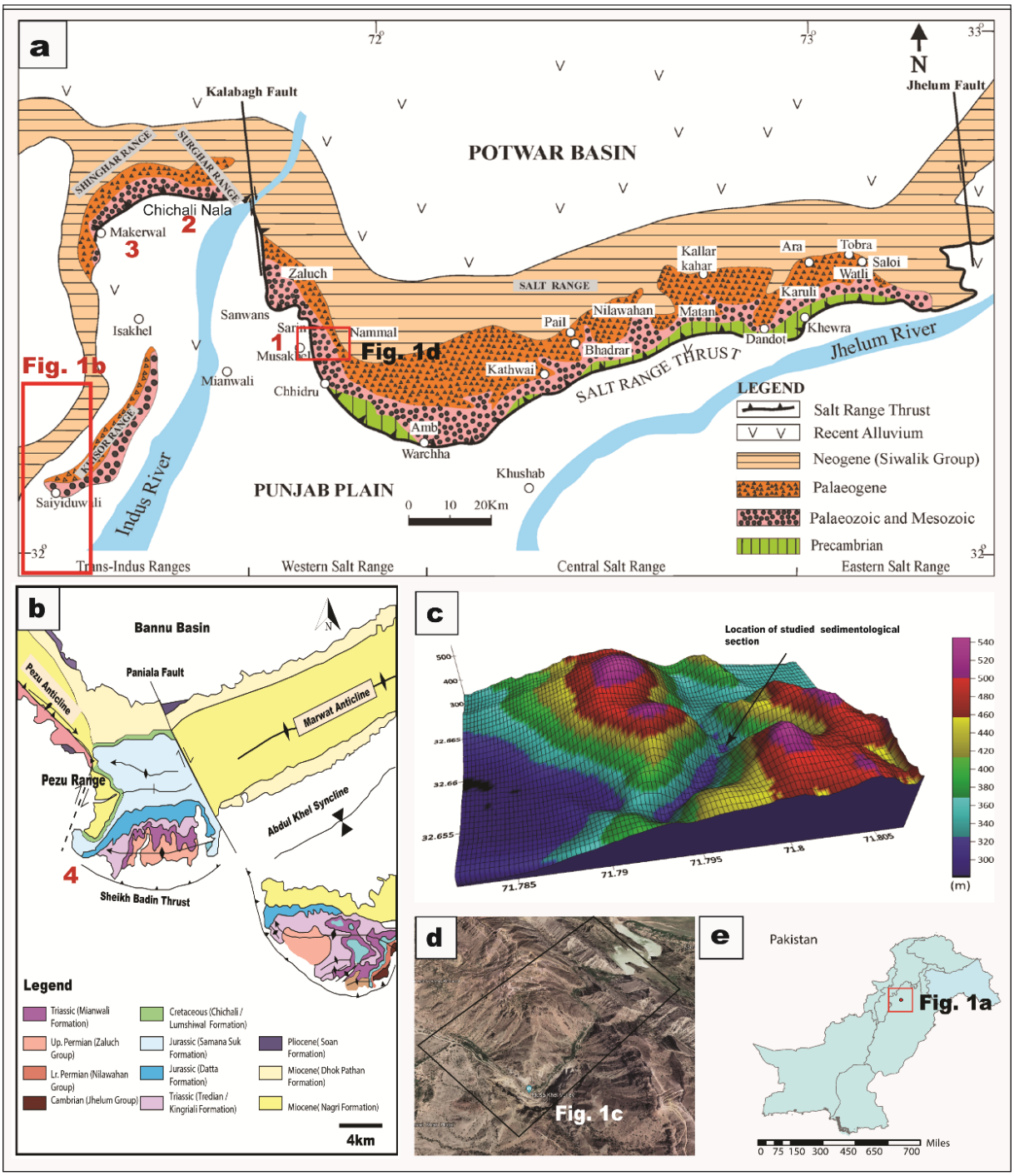

Figure 1. a) Location map of the researched geographical area in the Salt Range, Sub Himalayas, Pakistan: 1-Nammal Gorge, Western Salt Range; 2-Chichali Nala, Surghar Range; 3-Makerwal Section, Surghar Range (Ghazi et al., 2015); (b) Geological map of Marwat Range, 4-Sheikh Badin Hills; (c) Digital Elevation Model (DEM) of Nammal Gorge, indicating the position of the examined stratigraphic section; (d) It marks the DEM location and gorge can be seen, a water reservoir can be noticed near the top; (e) The location of the research area is depicted in the inset.

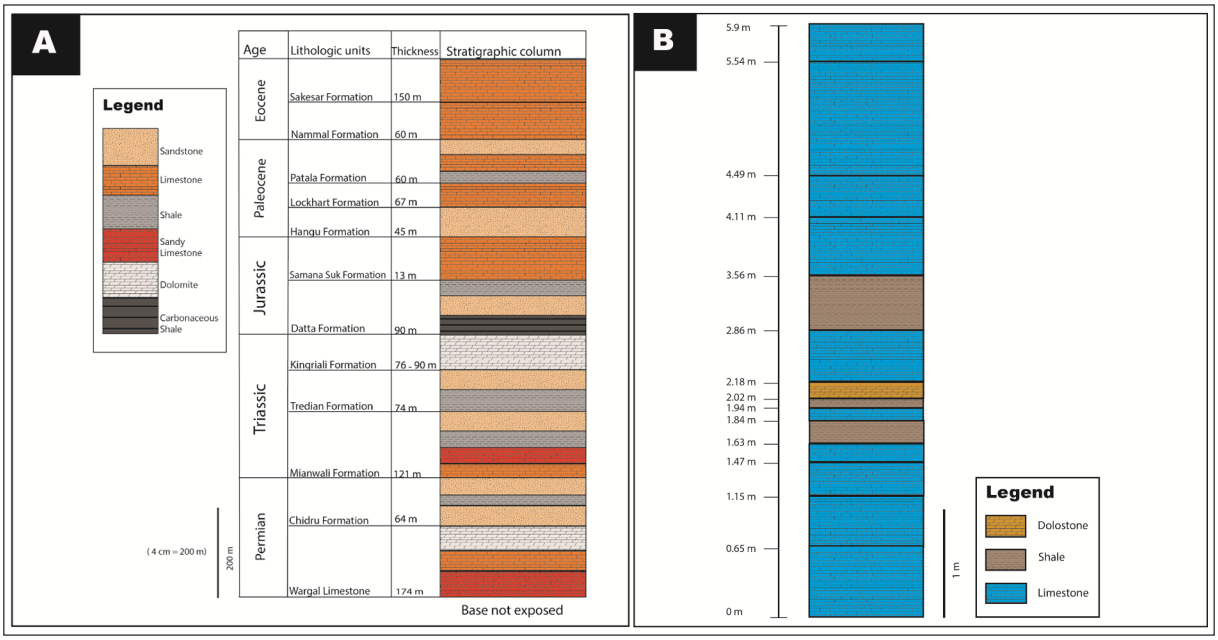

Figure 2. (a) Stratigraphic column of the Western Salt Range, encompassing rocks from the Permian to Eocene epochs; (b) Comprehensive sedimentological log of the Samana Suk Formation, detailing diverse rock types including limestone, shale, and dolomite.

- The Permo-Triassic epoch saw the first rifting of Gondwanaland and the development of a passive continental margin resembling the Atlantic coast.
- Initiation of rifting of the Indo-Australian Plate from Madagascar and Africa during the Cretaceous.
- An in-depth analysis of the Tethys Sea that emerged from the Indian Plate's northward migration, anticlockwise rotation, and eventual collision with the Eurasian Plate during the Paleocene.

The tectonic characteristics have led to various product features being situated in their respective locations within Pakistan. At the transform fault plate boundary, it is essential to highlight the rifled structures, fold-and-thrust belts linked to a foreland depression, and wrench faults. The foreland fold-and-thrust belts have developed from north to south on the Indian Plate, forming the Himalayan Collision Zone in the northwest of Pakistan. The active belts include the Kashmir Mountains, the Salt Range, the Trans Indus Ranges, the Sulaiman Range, and the Kirthar Range. The Kohat and Potwar Plateaus, Salt Range, and Trans Indus Ranges are located on the southern margin of the Himalayan Collision Zone, formed as a result of the underthrusting of the Indian Plate beneath its Phanerozoic sedimentary strata. The decollement of low-strength Pre-Cambrian evaporites from the Salt Range Formation enabled the southward extension zones of this underthrusting over the foreland. The northern fold and thrust belts converge with the Sulaiman Range to the south. The Indian Shield exists in this region as a remnant of Gondwanaland. The Chaman and Ornach-Nal faults define the western boundary of this shield. The extension reaches, at a minimum, the Indus Ophiolitic Belt located beneath the Himalayas in the northeast (Yasin et al., 2021). The stratigraphic column of rocks along the northern boundary of the Indian Plate lies within the southern shelf of the Tethys Ocean.

Tectonic set-up of the Himalayas

The Himalayan orogeny occurred during the Eocene and is defined by a compressional tectonic regime. The Proto-Himalayan zone experienced the emergence of convergent tectonics. A foreland fold and thrust belt developed on the southern margin of this zone due to underthrusting and crustal shortening. According to Kazmi and Jan (1997), the Himalayan orogenic band in northwest Pakistan was formed as a result of the collision between the Indian and Eurasian Plates, which began around 55 million years ago. East-west is the direction of the Himalayas and the related mountain ranges.

The Himalayan Collision Zone, located in northwestern Pakistan, is one of the most extensive active collision zones globally. Active foreland thrusting is taking place on a continental scale, with the Indian Plate underthrusting the Eurasian Plate along its northern margin. This process results in the formation of a series of north-dipping, south-verging thrusts. The process of crustal shortening has led to the development of various folds and thrust belts.

This study incorporated three sections for correlation and comparison regarding basin configuration, thickness, facies changes, and heterogeneity within the facies of the Samana Suk Formation. Two sections are located in the Chichali Nala Section and the Makerwal Section, while one section on Sheikh Budin Hill (7 kilometers from Pezu Pass) is positioned in the Marwat Ranges (Figure 1b).

The objectives of the paper are the following:

- To analyze the rock types and microfacies of the Samana Suk Formation, establish a correlation between the heterogeneity observed from the Salt Range to the Trans-Indus Ranges
- To investigate the paleogeography and depositional environment of the Samana Suk Formation.

2. Database, Materials and Methods

Field Observation and Laboratory Analysis

Three separate geological portions make up the Samana Suk Formation. These are the Sheikh Budin Hill Section in the Marwat Range, the Makerwal Section in the Surghar Range, the Chichali Nala Section in the Surghar Range, and Nammal Gorge in the Western Salt Range. Each image was geo-referenced using high-resolution images. Characteristics of rocks observed in the field include lithology, color, texture, and bed thickness (Figure 1a-c). All samples have been recorded and tagged in the field. Thin sections were prepared in the lab, and microphotographs were taken along with detailed petrographic examination. Thin sections were examined under a Nikon LV100ND polarizing microscope equipped with a digital camera at Quaid-E-Azam University. Photomicrographs were digitized and described. Samples were selected and analyzed by XRD, SEM-EDS, and standard thin-section preparation.

This section's Samana Suk Formation has a measured thickness of 37.98 meters. 114 samples in all were taken from 92 different beds. Most bedding planes in this section exhibit a planar nature, and the bedforms are consistently even. However, some beds exhibit a wavy bedform. The thickness of the bedding ranges from thinly bedded to massive bedding. The large beds, however, are limited in quantity. The section primarily consists of a medium-bedded succession. This section also notes small-scale shallowing-upward sequences (Figure 2b). In this measured section, the count of argillaceous horizons is greater, totaling nine. A significant quantity of dolomite beds has been documented in this section, located at depths of 2.8m, 3.4m, 4.5m, 5.5m, 6.85m, 18.7m, 21.1m, and 28.2m, with the final dolomite bed observed at 29m. The dolomites exhibit thin to medium bedding, pale grey to yellowish grey hues.

The well-developed mud-cracked surfaces, indicative of brief exposure periods and hardened ground conditions, have been documented in this section. The beds indicate the complete retreat of marine water and the occurrence of regressive cycles, resulting in the subaerial exposure of newly deposited carbonate sediments. Two documented instances of older and younger hard grounds from the Makarwal Section are located at depths of 23.8m and 38m, respectively, from the base. The hardgrounds exhibit bioturbation and consist of coarse-grained limestones with iron encrustations, which impart a reddish-grey coloration. The upper, young hard ground delineates the upper stratigraphic boundary of the Chichali Formation. The bioturbated beds observed in certain locations indicate an environment favorable to marine life during their deposition. Skolithos were identified within the strata located in the upper section of the Samana Suk Formation. The presence of these vertical burrows suggests that carbonate deposition occurred in a very shallow aquatic environment, characterized by periodic exposure in the subtidal zone. The occurrence of large fossils, including bivalves, brachiopods, and gastropods, in the uppermost layers indicates a high-energy environment conducive to carbonate sedimentation. Oolitic beds are observed at two distinct levels: 2.4 meters and 9.7 meters. These beds indicate a high-energy environment and are representative of grainstone facies. The sole occurrence of sandstone in this section of the Trans Indus Ranges is located at a depth of 4.7 meters. The depositional synthesis log of the Samana Suk Formation located at the Makarwal Section, accompanied by a comprehensive field description, is illustrated in Figure 2b.

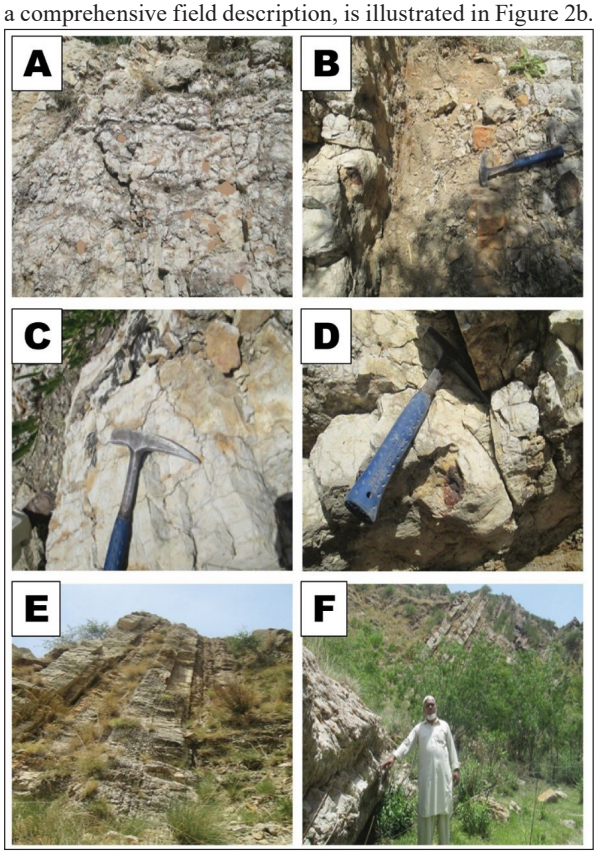

Figure 3. a) Thick-bedded fractured gray limestone with numerous dolomitic patches, showcasing a normal fault and joints; (b) A thick-bedded fractured gray limestone featuring multiple dolomitic patches that illustrate a normal fault and joints; (c) A gray limestone stylolite with a few dolomite patches; (d) The field section displaying iron nodules/concretions; (e) Panoramic view of the outcrop of Samana Suk Formation, Nammal Gorge Section; (f) The Nammal Gorge Section of Pakistan's Western Salt Range demonstrates the lower contact between the Samana Suk Formation and the Lower Jurassic Datta Formation.

3. Results and Discussion

Lithostratigraphy

This study identifies five distinct rock types: limestone (78%), marl/shale (10%), dolomite (9.5%), limestone with irregular quartz (1.5%), and sandstone (1%).

Sheikh Budin Hill Section, Khisor Range

The Sheikh Budin Hill Section is located at a Latitude of 32°17′11" N, and longitude of 70°43′51" E, situated seven kilometers from Pezu Pass in the District of Laki Marwat (see Figure 1). The overall thickness of this section measures 87.57 meters. The formation consists of thick limestone beds, as well as medium- to thick- and thin-bedded limestone, located at Sheikh Budin Hill in the Khisor Range. The bedding geometry, architecture, and heterogeneity of this formation are characterized by vertical stacking, as evidenced by the uneven, wavy beds. This section is characterized by the presence of coarse-grained limestone horizons, indicating the overall grain size. This section is characterized by a

predominance of limestone, comprising 86%, followed by dolomite at 8%, and marl/shale at 6%.

Makarwal Section, Surghar Range

The Makarwal section is situated at Latitude of 32°55′35” N, and longitude of 71°08′50” E, along the Mianwali-Bannu Road. The composition consists of thick, medium-to-thick, and thin limestone/dolomite layers, with an approximate thickness of 37.98 meters. This section exhibits heterogeneity through erosive surfaces in the vertical arrangement and the occurrence of different rock types. This section consists of 70% limestone, 15% dolomite, 10% marls/shales, 3% irregular quartz limestone, and 3% sandstone.

Chichali Nala Section, Surghar Range

The Chichali Nala Section of the Surghar Range is approximately located at Latitude of 33°00′38” N, and longitude of 71°24′13” E. The thickness is approximately 43.27 meters, consisting of substantial limestone beds that vary in thickness from medium to thick. This section consists of 86% limestone, 10% marls/shales, and 4% dolomite.

Nammal Gorge Section, Western Salt Range

The Nammal Gorge section, situated at Latitude of 32°39′34” N, and longitude of 71°48′1” E, is situated in proximity to Nammal Dam within the Western Salt Range (refer to Figure 1). This section has a measured length of 5.9 meters (see Figures 3e and 3f). This section exhibits wavy bedforms in certain areas, accompanied by thin to massive beds. Shale breaks, which are typically found in very thin beds, occur at multiple levels within this section (Figure 3e). The observation included the deposition of thin and occasionally very thin layers of shale interspersed within limestone beds, characterized by numerous shale punctuations. The initial shale break is located at a depth of 1.63 meters from the base. The final shale layer is observed at a depth of 2.86 meters. In this section, the older, lower hard ground is observed at depths of 0.6 m and 30.6 m. Several oolitic horizons have been observed, specifically at depths of 26.5 m and 29.6 m within this section. Dolomitization has occurred at two specific levels, ranging from 2.02 m to 2.18 m (Figure 3a, c). Figure 2b presents the depositional synthesis log of this formation, accompanied by a comprehensive field description from the Nammal Gorge section.

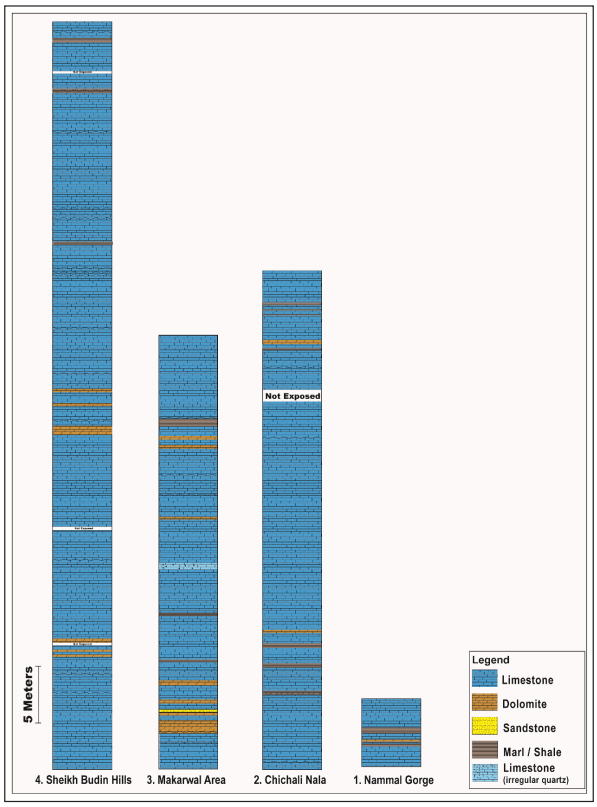

Figure 4. Stratigraphic sections of the Samana Suk Formation in the Upper Indus Basin, Pakistan: 1- Nammal Gorge Section, 2- Chichali Nala Section, 3- Makarwal Area Section, 4- Sheikh Budin Hills Section.

Table 3. Section-wise decadal sinuosity index of Lower Kopili River.

Section Name	Location (Lat- Long)	Thickness (m)	Main Lithology (%)	Features
Sheikh Budin Hill	32°17′11” N, 70°43′51” E	87.57	Limestone (86%), Dolomite (8%), Marl/Shale (6%)	Coarse-grained limestone, vertical stacking, wavy beds
Makarwal Section	32°55′35” N, 71°08′50” E	37.98	Limestone (70%), Dolomite (15%), Marls/Shales (10%), Quartz Limestone (3%), Sandstone (2%)	Erosive surfaces, lithological heterogeneity
Chichali Nala	33°00′38” N, 71°24′13” E	43.27	Limestone (86%), Marls/Shales (10%), Dolomite (4%)	Medium to thick limestone beds
Nammal Gorge	32°39′34” N, 71°48′1” E	5.9	Mainly Limestone with Shale Interbeds	Thin to massive beds, shale breaks (1.63 m to 2.86 m), oolitic horizons, dolomitization (2.02–2.18 m)

Microfacies Analysis

Using 30 thin sections of rock types, textures, pore properties, matrix composition, and mud percentages, the microfacies of the Samana Suk Formation were analyzed. Embry and Klovan’s (1971) enlarged framework for further subdividing boundstone microfacies and coquina limestone, as well as Dunham’s (1962) method for carbonate rocks, are followed in the classification of microfacies. To examine the coquina limestone facies, Embry and Klovan (1971) further subdivided Dunham’s boundstone microfacies. As seen in Figure 4, the microfacies consist of mudstone, bioclastic mudstone, bioclastic wackestone, ooidal grainstone, peloidal grainstone, ooidal packstone, peloidal packstone, bioclastic packstone, and bioclastic mudstone.

Grainstones

Petrographic analysis revealed the subsequent submicrofacies of the grainstone:

- Bioclastic Intraclastic Grainstone

Intraclasts, peloids, cortoids, and ooids may occur together with the skeletal remains of various marine organisms in carbonate sediments. These components are commonly found in shallow marine depositional environments, indicating active reworking and sediment transport. Among these, intraclasts are particularly significant as they are fragments of pre-existing sedimentary material that have been eroded, transported, and redeposited within the same basin. Their presence suggests episodes of sediment disruption and early lithification processes within the depositional setting.

- Peloidal Grainstones

This location exhibits multiple stratigraphic levels where peloidal grainstones are prominently developed. The associated microfacies are primarily composed of fecal pellets and peloidal grains, indicating a high-energy, shallow marine environment with active biogenic reworking. In addition to these components, foraminifera have been observed in close association with the grainstones, further supporting a marine depositional setting. The presence of foraminifera, along with the abundance of peloids, suggests a well-oxygenated environment favorable for benthic organisms.

- Ooidal Peloidal Bioclastic Grainstone

These grainstones are characterized by ooids, peloids, and skeletal fragments from a variety of marine organisms. The ooids typically exhibit microfabrics with distinct radial concentric symmetry, reflecting their formation in high-energy, agitated water conditions. Their nuclei often consist of quartz grains or skeletal debris, around which concentric layers of carbonate have been deposited. These ooidal structures usually appear in a tightly packed arrangement, indicating minimal matrix and a well-sorted, mature grain-supported texture.

Interpretation

These limestones were deposited in a high-energy, shallow marine environment, most likely associated with oolitic shoals, bars, and beach settings. The abundance of ooids, peloids, and well-preserved skeletal grains indicates strong water agitation, typical of wave- and current-dominated zones. The tightly packed nature of the grainstones and the radial concentric cortices of ooids further support deposition under energetic conditions. Fecal pellets and foraminifera within the peloidal grainstones suggest active bioturbation and continuous reworking by benthic organisms. Collectively, these microfacies reflect a dynamic carbonate platform setting favorable for the formation of grain-supported limestone (Ali et al., 2013).

- Packstones

According to ‘ ‘Dunham’s classification, packstone microfacies are defined by the presence of more than 50% grains supported by a fine-grained carbonate matrix. These grains typically include a mix of skeletal fragments, peloids, and occasionally ooids, reflecting deposition in moderately energetic environments. The matrix indicates lower-energy conditions than in grainstones, allowing finer material to accumulate between grains. Several distinct packstone microfacies have been identified and documented based on their grain composition and textural features.

- Sandy Echinoderm Packstone

Observations indicate that these packstone microfacies contain echinoderm fragments, including plates and spines, as seen in Figure 5a. Quartz grains are frequently present within the matrix, suggesting some siliciclastic input during deposition. Although echinoderm grains and biodebris are generally present, their occurrence ranges from infrequent to rare across different samples. Peloidal packstone microfacies also include abundant peloids, often associated with skeletal shell fragments and foraminiferal tests, reflecting a mixed biogenic and detrital origin.

- Interpretation:

The depositional environment represented by these Sandy Echinoderm Packstone microfacies is interpreted as a shallow marine shelf setting. This shelf was characterized by moderate water circulation, allowing the accumulation of both bioclastic grains and fine carbonate mud. The presence of diverse skeletal components and peloids suggests a biologically active environment with intermittent energy conditions. Such settings typically lie between high-energy shoals and deeper, low-energy lagoonal areas on the carbonate platform (Flügel 2004).

- Wackestones

Wackestones are carbonate microfacies characterized by more than 10% allochems or grains within a micritic matrix, according to Dunham (1962). These microfacies typically reflect low-energy depositional conditions, with fine carbonate mud dominating. Within the Samana Suk Formation, wackestones are observed at multiple stratigraphic levels. Their distribution is similar to that of other associated microfacies in the formation.

- Bioclastic Peloidal Wackestone

Bioclastic wackestone is characterized by the presence of more than 10% skeletal grains embedded within a micritic matrix (Figure 5b, f, j). In addition to bioclasts, peloids are also observed, indicating a mixed origin of carbonate components. These wackestones exhibit notable faunal diversity, with a fossil assemblage that includes gastropods, pelecypods, sponges, and brachiopods. The studied area contains well-preserved skeletal shells and fragmented remains, reflecting low-energy depositional conditions that favored fossil preservation.

- Interpretation:

The interpreted depositional environment for the wackestone and bioclastic wackestone facies is a shelf lagoon setting. This environment is characterized by low-energy water circulation, allowing the accumulation of fine micrite and delicate skeletal remains. The presence of diverse faunal assemblages and well-preserved shells supports a calm, protected setting with limited reworking. Such conditions

are consistent with inner platform lagoons as described by Flügel (2004).

- Mudstone

In this region, mudstones occur at various stratigraphic levels within the Samana Suk Formation. In certain areas, these mudstones exhibit significant fracturing and are infilled with calcite. A heavily fractured mudstone is interpreted as post-dating the fractures, as indicated by a medium-amplitude stylolite that intersects them. Some mudstones also display evidence of at least two stages of fracturing. This microfacies is characterized by unlaminated, homogeneous, unfossiliferous pure micritic limestone.

- Interpretation:

The mudstone facies is interpreted to have been deposited in a low-energy, restricted environment such as a hypersaline tidal pond. The absence of fossils, presence of pure micrite, and lack of lamination support this calm, evaporative setting. Such conditions are consistent with lagoonal-to-supratidal environments described by Flügel (2004), Scholle et al. (2003), and Tucker (2003).

- Dolomudstone

Description:

The mudstone submicrofacies is present at multiple stratigraphic levels within the measured section of the Samana Suk Formation. In certain locations, dolomudstones display fractures that are infilled with calcite, indicating post-depositional diagenetic processes. Bioclastic mudstones, as shown in Figures 5h and 5i, contain minor skeletal components within a micritic matrix.

Interpretation:

These facies are interpreted to have developed near the wave base in shallow marine settings with open water circulation. The presence of bioclastic components suggests periodic faunal activity in a relatively calm but oxygenated environment. Open circulation would have allowed the influx of marine waters, limiting hypersalinity and favoring the preservation of bioclasts. This interpretation aligns with the model proposed by Wright (1992) for inner shelf depositional systems.

- Facies Associations (FA)

Microfacies analysis has led to the identification of four distinct facies associations, each reflecting specific depositional environments as inferred through a comparative study with standard microfacies (SMFs). These include lagoonal and tidal flat facies, hypersaline tidal pond facies, oolitic bar facies, and marine subtidal facies. The depositional settings span a moderate-water-circulation shelf, a low-energy lagoonal shelf, and an intertidal zone influenced by open circulation near the wave base. Within this framework, lime mudstones, bioclastic peloidal wackestones, and peloidal grainstones were deposited.

The limestone facies generally present a fresh, slightly darker coloration compared to their weathered surfaces. Their lithology is typically composed of thinly bedded, unlaminated, homogeneous, and unfossiliferous micritic limestone, interpreted to have formed in restricted, hypersaline tidal ponds. Oolitic limestone occurs at two distinct stratigraphic levels in the upper portion of the studied section, marking high-energy shoal environments. Additionally, facies such as bioclastic wackestone, sandy echinoderm packstone, and grainstone reflect a rich and varied assemblage of benthic fauna and flora. The open marine subtidal zone provided ideal ecological conditions for marine life, as evidenced by the diverse skeletal remains of echinoderms, foraminifera, gastropods, pelecypods, corals, sponges, brachiopods, bryozoans, and calcareous algae preserved within these microfacies.

Petrographic Analysis

The comprehensive petrographic analysis reveals the existence of ooids, peloids, echinoids, intraclasts, and bioclasts. Non-skeletal grains are more prevalent than skeletal grains. Calcite cements are the primary type of cement, with dolomite and pyrite cements following in prevalence. Certain sections are composed of micrite. Dolomite is a well-preserved material recognized as a secondary phase, commonly observed in matrix, fracture filling, and veins. The cementation of carbonate sediments plays a crucial role in providing strength and stability to microfacies, enabling them to endure both physical and chemical compaction.

- Micritic envelopes

Micritic envelopes are typically found on both skeletal and non-skeletal grains within various grainstones and packstones. The cement described in this document includes micritic envelopes, syntaxial overgrowth, poikilotopic cement, blocky cement, drusy cement, fabric-preserved dolomite, fine dolomite cement, dedolomite cement, iron cement, and pyrite.

- Syntaxial rim cement

The syntaxial rim cement forms in optical continuity above the host grain. It generally develops in optical continuity on the shells of echinoderms (crinoids and echinoids) and can be identified by synchronous extinction. Observations have been made on various crinoids and echinoid shells at specific depths within the studied area.

- Blocky to Drusy calcite cement

This material serves to fill cavities and may include sparry calcite as a component. The crystals are located in different microfacies of this formation, beginning small at the cavity boundaries and increasing in size towards the cavity center as accommodation space becomes available.

- Poikilotopic cement

This cement develops after the creation of intergranular cement and extensive dolomitization. This type of cement features fine grains that are encapsulated by larger cement crystals. This phenomenon typically takes place within a burial regime and evolves in a phreatic environment.

- Mechanical compaction

During this phase, the sediments undergo compaction, leading to the initial formation of grain-to-grain contacts. These basic interactions between grains then evolve into sutured grain contacts. The interlocking of one grain with another is sometimes observed as well. Dissolution of grains

initiates at these contacts, ultimately leading to the formation of dissolution seams.

- Stylolitization

The formation of stylolites occurs as a later stage in the diagenetic evolution of limestones (Figure 6a). Stylolites represent a diagenetic process characterized by pressure-dissolution or chemical compaction, which can be induced by tectonic pressures, enhanced compaction due to overburden, or a combination of these factors.

- Dolomitization

The dolomitization of limestones during diagenetic processes is a prevalent characteristic of the Samana Suk Formation. This area is developed on various levels, serving both as a substitute and as a binding agent. Dolomitization has been noted in association with stylolites.

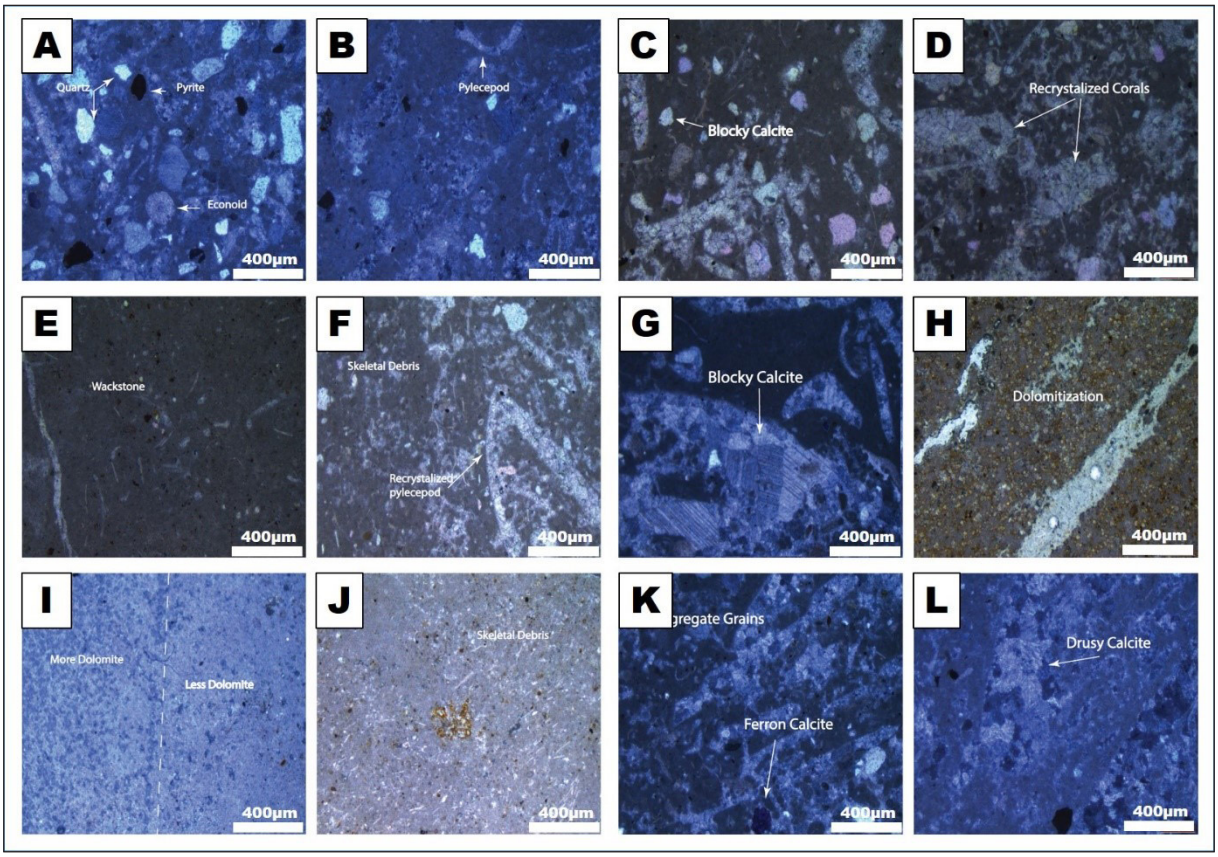

Figure 5. (a) Sandy echinoderm packstone featuring syntaxial overgrowth cements, quartz, and pyrite; (b) Bioclastic peloidal wackestone characterized by blocky calcite cement in pelecypods; (c) Bioclastic peloidal wackestone where most fossils exhibit recrystallization by blocky to drusy calcite cements; (d) Recrystallized corals present in the section, accompanied by large drusy calcitic cements; (e) Dolomudstone containing scattered skeletal debris; (f) Bioclastic peloidal wackestone with recrystallized pelecypods; (g) Poikilotopic cement alongside blocky calcitic cement; (h) Micro-dolomitization observed with very fine crystals of dolomite in dolo-mudstone facies; (i) Dolomudstone facies illustrating the transition between less and more dolomite zones; (j) Skeletal debris found in bioclastic wackestone facies, with visible iron cements; (k) Blocky to drusy calcitic cement within a micritic matrix; (l) Poikilotopic calcite combined with drusy calcitic cements, with minor pyrite also present.

Pervasive dolomitization

This material forms as a result of the prolonged dolomitization of limestones. This process of dolomitization affects the rock's fabric rather than its texture, resulting in complete dolomitization.

- Microdolomitization

During this diagenetic process, dolomite crystals form at very small sizes, requiring higher magnification to observe them effectively.

- Dedolomitization

Certain thin sections that are abundant in dolomite demonstrate dedolomitization processes. During diagenesis, a common reversal process, dolomite undergoes calcitization. This process is considered one of the last stages of diagenesis.

- Fractures

Frequent fractures are observed in the measured section across various levels. The late voids and microfracture-filling spar are associated with deep burial conditions, precipitating between the spalled-off cortices of the ooids.

XRD, SEM, and EDS Analyses

X-ray diffraction (XRD) and scanning electron microscopy (SEM) showed that calcite is the dominant mineral phase within the Samana Suk Formation. The mineralogical composition suggests extensive dedolomitization, as indicated by the presence of calcitic crystal overgrowths and altered textures. Supporting evidence includes minor clay content, intergranular porosity, and hollow grains, as shown in Figure 6c, f, and i. These features reflect post-depositional diagenetic processes that have modified the original dolomitic fabric.

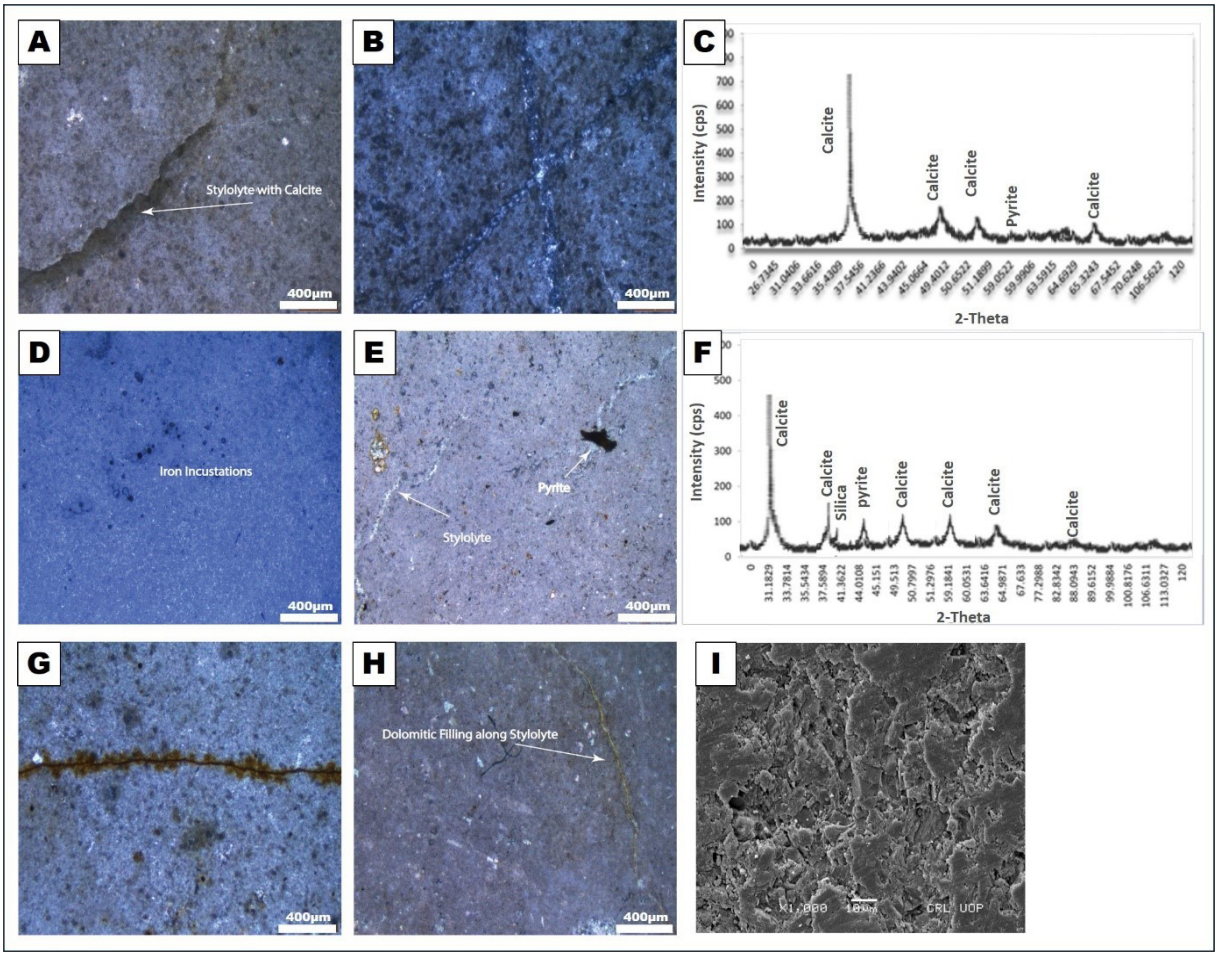

Figure 6. (a) Stylolite observed in mudstone facies; (b) fractures infilled with microdolomite matrix; (c) X-ray diffraction analysis indicates a predominance of calcite in the Samana Suk Formation, with minor pyrite; (d) iron cements identified in the dolomudstone facies; (e) stylolite and pyrite present in the dolomudstone facies; (f) XRD results reveal the presence of calcite, silica, and pyrite; (g) fractures filled with iron mineral growth; (h) Dolomitic mudstone exhibiting dolomite-rich stylolites; (i) Scanning Electron Microscope (SEM) analysis reveals calcitic cements with minor pores, predominantly micropores.

4. Discussion

The Samana Suk Formation represents one of the most extensive and well-preserved Jurassic carbonate successions in northern Pakistan. Deposited along the northern passive margin of the Tethys Ocean, it developed as part of a widespread carbonate platform system, highlighting its significance in the broader context of sedimentology, paleogeography, and tectonic evolution (Shah, 2009; Kassi et al., 2015). The formation predominantly consists of carbonate rocks interbedded with minor siliciclastic components such as marl and shale, suggesting deposition across a range of shallow marine settings, from inner to outer-shelf environments (Kazmi & Jan, 1997; Flügel, 2004). Tectonic activity during the Early Cretaceous, marked by seafloor spreading and rifting, transitioned into a compressional regime in the mid to late Cretaceous, driven by the subduction of Neo-Tethyan oceanic crust (Bender & Raza, 1995). The Samana Suk Formation is characterized by a variety of bioclastic microfacies, including mudstone, wackestone, packstone, and grainstone, indicating dynamic depositional conditions across the carbonate shelf. Key measured sections such as the Chichali Nala, Makerwal, Sheikh Budin Hills, and Nammal Gorge provide a detailed record of lithofacies variability. These include lagoonal and tidal flat lithofacies, hypersaline tidal pond facies, oolitic bar complexes, and open marine subtidal facies, with additional facies such as high-energy tidal channels, restricted shelves, and winnowed platform deposits particularly well-represented in the Makerwal and Sheikh Budin Hill sections (Nizami et al., 2009; Ali & Windley, 2009). Diagenetic processes affecting the Samana Suk Formation are equally diverse and include micritization, dolomitization, mechanical and chemical compaction, as well as the development of ferroan calcite and dolomite phases (Wright, 1992; Flügel, 2004). These features are particularly prominent in the Makarwal and Chichali Nala sections, where multiple stages of diagenetic overprinting have been documented and linked to burial history and tectonic reactivation.

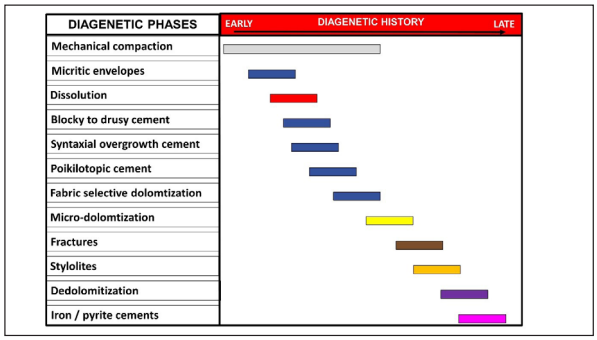

Figure 7. Generalized diagenetic sequence that represents the dominance of mechanical compaction to various types of cements, to fractures, and stylolites.

Deltaic facies replaced the shelf facies of the Mianwali Formation as a result of the tectonic and depositional history of the Indian Plate from the Permian to the Jurassic periods, as shown in Figures 8a and 8 b. This transition is characterized by regressive parasequence sets that indicate a shift from underfill to overfill conditions (Gaetani and Garzanti 1991). The process of dolomitization abruptly halted after the Triassic period, leading to a notable shift towards global cooling and increased humidity (Valdiya and Valdiya 2016). The limited accommodation space and insufficient sediment supply facilitated the formation of laterite beds and their exposure to the atmosphere (Ali et al., 2013). The Jurassic Samana Suk Formation (Figure 8c), along with the Chiltan and Takatu Limestones, represents important sedimentary units within the Sulaiman Foldbelt located in western Pakistan. The Chiltan Limestone consists of substantial layers of light-grey limestone, characterized by a thick, white appearance, and is covered by a thin stratum of dark shale (Siddiqui 2012; Basit et al., 2023). The argillaceous components within the marl/shale are formed by periodic influxes of clay into the area, driven by tectonic uplift, erosion, or small-scale, remote-past climate variations. Cyclic deposition is absent, and the intercalations along with shale/marl fractures, found at various levels, occur randomly. Correlations between them are feasible based on their respective lithologies, thicknesses, and depositional environments.

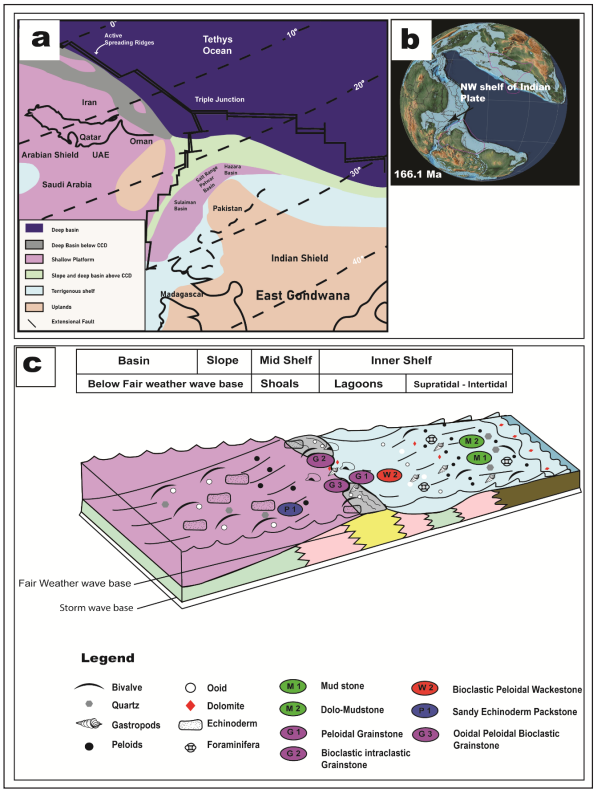

Figure 8. (a) The paleogeographic position of the northwestern section of the Indian Plate; (b) A paleogeographic image produced by Gplates Software illustrates the location of the northwestern shelf of the Indian Plate and the submerged portion of the plate during the Middle Jurassic; (c) The depositional setting of the Samana Suk Formation, featuring proximal mudstone facies adjacent to the outer segments of the oolitic shoals (after Sallam and Ruban, 2020; Wilson 1997).

5. Conclusions

This study investigates the Jurassic carbonates of the Samana Suk Formation (5.9–87.57 m) in the Salt Range, Pakistan, revealing a complex shallow-shelf depositional system characterized by shallowing-upward successions, diverse microfacies, and multiple diagenetic phases. Seven microfacies were identified, representing environments from tidal flats and lagoons to sand shoals and mid-ramp settings, deposited under both restricted- and open-marine conditions. Petrographic and geochemical analyses highlight an intricate paragenetic sequence, including various cement types, dolomitization, dedolomitization, and stylolitization, reflecting a dynamic post-depositional history. Field observations across all four measured sections, from the coarse, vertically stacked limestone beds of Sheikh Budin to the shale-interrupted carbonate layers of Nammal Gorge, reveal a consistent dominance of limestone with variable admixtures of dolomite and marl, highlighting the complex depositional heterogeneity and localized diagenetic overprints that characterize the paleogeographic transitions in northwestern Pakistan. These findings enhance our understanding of Middle Jurassic Tethyan carbonates and demonstrate the Samana Suk Formation's potential as a raw material for cement, construction aggregate, and as a reservoir candidate in petroleum exploration.

Acknowledgments

We want to express our sincere appreciation to the Department of Earth Sciences, University of Sargodha, for providing the facilities for this research. Furthermore, to the Geophysical Engineering Department at Istanbul Technical University in Turkey for collaboration.

References

Abd El Aal, A., Abdullah, G. M., Radwan, A. E., El-Azab, H. S., El-Habashi, M., & Al-Amri, S. (2023). Linking sedimentary cyclicity with mechanical and physical properties of limestone and marl rocks, Dam Formation, eastern Saudi Arabia: Implications for hydrocarbon exploration and reservoir development. Journal of Asian Earth Sciences, 251, Article 105656. https://doi.org/10.1016/j.jseaes.2023.105656

Ahmed, N., Ali, S. H., Ahmad, M., Zamin, H., & Khan, I. A. (2020). Subsurface structural investigation based on seismic data of the northeastern Potwar Basin, Pakistan. Indian Journal of Geo-Marine Sciences, 49(7), 1258–1268.

Ali, F., Haneef, M., Anjum, M. N., Hanif, M., Shah, S. M. A., & Ahmad, S. (2013). Microfacies analysis and sequence stratigraphic modeling of the Samana Suk Formation, Chichali Nala, Trans-Indus Ranges, Punjab, Pakistan. Journal of Himalayan Earth Sciences, 46(1), 1–15.

Ali, S., & Windley, B. F. (2009). Evolution of the Himalayan foreland basin in northwest Pakistan. Journal of Asian Earth Sciences, 34(2), 147–160.

Ali, S. H. (2009). Reservoir characteristics of the Early–Middle Cambrian Baghanwala Formation, eastern Salt Range, Pakistan. In Proceedings of the SPE–PAPG Annual Technical Conference: Maximize Reserves—Optimize Exploitation. Islamabad, Pakistan.

Ali, S. H., Ahmad, B., Hamza, M., Ali, F., & Iqbal, S. (2022b, June). Facies and sedimentary structures of the Sharaban Formation, Neoproterozoic Kirana Complex, Sargodha, Punjab, Pakistan. In Proceedings of the 6th International Conference on Earth Sciences Pakistan 2022. Abbottabad, Pakistan.

Ali, S. H., Shoukat, N., Bashir, Y., Ghazi, S., Ahmed, S. A., & Hussain, M. (2022a). Sedimentology and depositional environment of Neoproterozoic stromatolitic limestones of the Langrial and Miranjani areas, Lesser Himalayas, Pakistan. In Proceedings of the International Conference on Applied Pure Science. Kelaniya, Sri Lanka.

Ali, S. H., Shoukat, N., Bashir, Y., Ghazi, S., Asim, S., & Abid, S. (2021). Lithofacies and sedimentology of the Baghanwala Formation (Early–Middle Cambrian), eastern Salt Range, Pakistan. Pakistan Journal of Scientific and Industrial Research, Series A: Physical Sciences, 65A(2), 159–168.

Basit, A., Umar, M., Jamil, M., Usman, M., Munaver, K., Hafeez, M. A., & Ashraf, N. (2023). Facies analysis and depositional framework of Late Permian–Jurassic sedimentary successions, western Salt Range, Pakistan: Implications for sequence stratigraphy and Neo-Tethys paleogeography. Kuwait Journal of Science, 50(1B), 1–18.

Bender, F., & Raza, H. A. (1995). Geology of Pakistan. Gebrüder Borntraeger.

Brandano, M., Mateu-Vicens, G., & Baceta, J. I. (2022). Understanding carbonate factories through palaeoecological and sedimentological signals: Tribute to Luis Pomar. Sedimentology, 69(1), 5–23.

Cotter, G. D. (1933). The geology of part of the Attock District west of longitude 72°45′ E. Memoirs of the Geological Survey of India, 55(2), 63–161.

Davies, L. M. (1993). The fossil fauna of the Samana Range and neighboring areas: Palaeocene foraminifera. Memoirs of the Geological Survey of India: Palaeontologia Indica, New Series, 15, 1–15.

Dunham, R. J. (1962). Classification of carbonate rocks according to depositional textures. In W. E. Ham (Ed.), Classification of carbonate rocks: A symposium (pp. 108–121). American Association of Petroleum Geologists.

Embry, A. F., & Klovan, J. E. (1971). A late Devonian reef tract on northeastern Banks Island, NWT. Bulletin of Canadian Petroleum Geology, 19(4), 730–781.

Flügel, E. (2004). Microfacies of carbonate rocks: Analysis, interpretation and application. Springer.

Gaetani, M., & Garzanti, E. (1991). Multicyclic history of the northern Indian continental margin (northwestern Himalaya). AAPG Bulletin, 75(9), 1427–1446.

Gee, E. R. (1947). The age of the Saline Series of the Punjab and Kohat. National Science Proceedings, Section B, 14, 269–310.

Ghazi, S., Ali, S. H., Sahraeyan, M., & Hanif, T. (2015). Tectono-sedimentary framework of the Salt Range, northwestern Himalayan fold-and-thrust belt, Pakistan. Arabian Journal of Geosciences, 8, 1635–1651.

Ghazi, S., Ali, S. H., Shahzad, T., Ahmed, N., Khalid, P., Akram, S., & Sami, J. (2020). Sedimentary, structural, and salt tectonic evolution of the Karoli–Nilawahan area, central Salt Range, Pakistan. Himalayan Geology, 41(2), 145–156.

Javed, A., Wahid, A., Mughal, M. S., Ahmad, M. U., & Ali, S. H. (2021). Geological and petrographic investigations of Miocene molasse deposits, Sub-Himalayas, Pakistan. Arabian Journal of Geosciences, 14, Article 1032.

Kassi, A. M., Khan, A., & Khan, S. (2015). Lithostratigraphy and depositional environments of Jurassic rocks in Pakistan. Journal of Himalayan Earth Sciences, 48(1), 21–36.

Kazmi, A. H., & Jan, M. Q. (1997). Geology and tectonics of Pakistan. Graphic Publishers.

Mateen, A., Wahid, A., Janjuhah, H. T., Farooqi, Z. U. R., Ali, S. H., & Naseer, A. (2022). Petrographic and geochemical analysis of Indus sediments: Implications for placer gold deposits, Peshawar Basin, NW Himalaya, Pakistan. Minerals, 12(8), Article 1059.

Mertmann, D., & Ahmad, S. (1994). Shinawari and Samana Suk formations of the Surghar and Salt Ranges, Pakistan: Facies and depositional environments. Zeitschrift der Deutschen Geologischen Gesellschaft, 145(2), 305–317.

Naseem, A. A., Anjum, M. N., Yaseen, M., Ahmad, S., Munes, A., Haider, M. S., Younus, M., & Siddiqui, M. N. (2023). Preliminary geoheritage assessment of the Gharam Chashma Granitic Batholith, NW Pakistan. Geoheritage, 15(1), Article 31.

Nizami, A. R. (2009). Microfacies analysis and diagenetic settings of the Middle Jurassic Samana Suk Formation, Trans-Indus Ranges, Pakistan. Geological Bulletin of the Punjab University, 44, 69–84.

Nizami, S. M., Shah, M. T., & Kassi, A. M. (2009). Diagenetic alterations in Jurassic limestones of Pakistan. Pakistan Journal of Geology, 14(2), 45–60.

Rehman, N., Ali, D. S. H., Ullah, Z., Khan, A. K., Shah, M., & Ahmad, N. (2022). Evaluation of Khyber limestone for use as road aggregate based on geotechnical properties. Iranian Journal of Earth Sciences, 14(4), 252–262. https://doi.org/10.30495/IJES.2022.1939526.1650

Saboor, A., Khan, N., Hanif, M., Mehmood, S., Ali, F., & Sajjad, U. (2022). Paleo-depositional and sequence stratigraphic setting of the Middle Jurassic Samana Suk Formation, Lesser Himalayas, Pakistan. Himalayan Geology, 41(2), 121–132.

Sallam, E. S., & Ruban, D. A. (2020). Facies analysis and depositional environments of Miocene syn-rift carbonate–siliciclastic successions, Gulf of Suez, Egypt. Carbonates and Evaporites, 35, Article 73.

Scholle, P. A., & Ulmer-Scholle, D. S. (2003). A color guide to the petrography of carbonate rocks. American Association of Petroleum Geologists.

Searle, M. P. (1983). On the tectonics of the western Himalaya. Episodes, 6(4), 21–26.

Shah, S. M. I. (1977). Stratigraphy of Pakistan (Memoir 12). Geological Survey of Pakistan.

Shah, S. M. I. (2009). Stratigraphy of Pakistan (Memoir 22). Geological Survey of Pakistan.

Siddiqui, N. K. (2012). A prospective Neoproterozoic–Cambrian hydrocarbon play in the Kirthar Fold Belt, Pakistan. Geological Society, London, Special Publications, 366(1), 123–130.

Teles, V., Hamon, Y., Deschamps, R., Arrouy, G., & Duguet, M. (2023). Modelling coupled heterogeneities in lacustrine microbialite-bearing carbonate reservoirs of the Yacoraite Formation, Argentina. Comptes Rendus Géoscience, 355(S1), 1–20.

Tucker, M. E. (2003). Sedimentary rocks in the field (3rd ed.). John Wiley & Sons.

Valdiya, K. S. (2016). Later Proterozoic and Early Cambrian of the Himalaya. In The making of India: Geodynamic evolution (pp. 335–371). Springer.

Wadood, B., Khan, S., Li, H., Iqbal, M., Wang, Y., & Ullah, K. (2021). Sequence stratigraphic framework of the Jurassic Samana Suk Formation, North Pakistan: Implications for reservoir potential. Arabian Journal for Science and Engineering, 46(1), 525–542.

Wahid, A., Rauf, A., Ali, S. H., Zamin, H., Jamil, M., Ghani, S., & Khan, I. A. (2022). Impact of complex tectonics on the development of geopressured zones: A case study from the Sub-Himalayan Basin, Pakistan. Geopersia, 12(1), 89–106.

Wilson, J. L. (1997). Carbonate depositional environments and diagenesis. In R. F. Lindsay, J. C. Green, & J. R. W. Cartwright (Eds.), Carbonate seismology (pp. 9–28). Society of Exploration Geophysicists.

Wright, V. P. (1992). A revised classification of limestones. Sedimentary Geology, 76(3–4), 177–185.

Yasin, Q., Baklouti, S., Khalid, P., Ahmad, S., Arslan, M., & Mehmood, H. (2021). Evaluation of shale gas reservoirs in complex structural settings: A case study of the Patala Formation, Kohat–Potwar Plateau, Pakistan. Journal of Petroleum Science and Engineering, 198, Article 108225.

المملكة الأردنية الهاشمية

صندوق دعم البحث العلمي

الجامعة الهاشمية

المجلة الأردنية
لعلوم الأرض والبيئة

JJEES

مجلة علمية عالمية محكمة

المجلد (١٧) العدد (١)

http:// jjees.hu.edu.jo/

ISSN 1995-6681

المجلة الأردنية لعلوم الأرض والبيئة

مجلة علمية عالمية محكمة

المجلة الأردنية لعلوم الأرض والبيئة: مجلة علمية عالمية محكمة ومفهرسة ومصنفة، تصدر عن عمادة البحث العلمي في الجامعة الهاشمية وبدعم من صندوق البحث العلمي - وزارة التعليم العالي والبحث العلمي، الأردن.

ترسل البحوث إلكترونيا إلى البريد الإلكتروني التالي:

رئيس تحرير المجلة الأردنية لعلوم الأرض والبيئة

jjees@hu.edu.jo

لمزيد من المعلومات والأعداد السابقة يرجى زيارة موقع المجلة على شبكة الانترنت على الرابط التالي:

www.jjees.hu.edu.jo

المملكة الأردنية الهاشمية صندوق دعم البحث العلمي الجامعة الهاشمية

Indexed by Scopus ELSEVIER

JJEES

المجلة الأردنية لعلوم الأرض والبيئة

المجلد (17) العدد (1)

مجلة علمية عالمية محكمة تصدر بدعم من صندوق دعم البحث العلمي

ISSN 1995-6681 jjees.hu.edu.jo آذار 2026